Development of High Performance Filtration System Using Composite Bed Filter and Multi-element Structured Array

by

Guomin Xu

A dissertation submitted to Graduate Faculty of
Auburn University
in partial fulfillment of the
Doctor of Philosophy

Auburn, Alabama
August 1, 2015

Keywords: wet laid process, microfibrous entrapped sorbent, mass transfer, fuel cell, filtration, composite bed filter, removal efficiency

Approved by

Bruce J. Tatarchuk, Chair, Professor of Chemical Engineering
W. Robert Ashurst, Professor of Chemical Engineering
Allan E. David, Professor of Chemical Engineering
Bart Prorok, Professor of Material Engineering

Abstract

A composite nonwoven (CNW) material, activated carbon fiber enhanced microfibrous entrapped sorbent (ACF-MFES) , was prepared by incorporating micro sized (100-500μm) sorbent particulates into the blended microfiber (10-20μm bicomponent polymer fiber and ACF) webs via wet-lay process. This novel fibrous sorbent media is characterized by its small particulates, high voidage and uniform structure. The manufacturing process of ACF-MFES is similar with the industrial nonwovens production and thereby it can be readily scaled up. The application of ACF-MFES nonwovens materials in the air cleaning systems can provide considerable advantages over traditional packed bed design; these advantages include higher single pass removal efficiency, lower pressure drop, higher bed utilization and lightweight.

The first part of this work is the development of ACF-MFES, including the formation of recipe and process optimization. For the recipe, self-bonding bicomponent fiber, activated carbon fiber, sorbent particulates and various process additives was used. For the process optimization, each process step, including the fiber selection, wet-end chemistry, web formation technology, and web bonding technology, was optimized. In this study, for the first time, ACF was added to create a blended fiber web; it was found that only small portion of ACF effectively improved the nonwoven's quality including the softness, strength, resilience, and the homogeneity of particle distribution.

The second part is the performance test of ACF-MFES. Hexane adsorption is used to demonstrate the media's adsorption rate and capacity; the performance is compared with traditional granular packed bed sorbent. Bench scale experiments were firstly conducted in a

2.54cm (1.0”) diameter stainless steel pipe setup, and then full scale tests were conducted in a 24x24” HVAC filter test rig. The hexane breakthrough curve showed that the ACF-MFES media has much faster adsorption kinetics compared to packed bed sorbent. This enhancement in adsorption rate is resulted from ACF-MFES media’s high contacting efficiency due to its small particulates and high surface area.

The third part is the kinetics study of adsorption in ACF-MFES. Hexane adsorption onto activated carbon is a strong physisorption process, which is usually in mass transfer control rather than in intrinsic reaction control. Therefore, the kinetics study of adsorption is actually the study of mass transport between fluid and solid. The mass transfer of hexane molecule from the bulk of fluid to the specific adsorption site on the interior surface of activated carbon involves two steps: external mass transport and internal mass transport. The external mass transport mainly carried out through film diffusion, whereas the internal mass transport is more complicated because some different mechanisms are involved in this step, including molecular and Knudsen diffusion in the fluid phase, and surface diffusion in the solid phase. In this work, these four mass transfer coefficients are lumped into one overall mass transfer coefficient k_G by analogy to the electrical resistance model.

Acknowledgements

Many people have helped me on my way to the successful completion of this dissertation. Firstly, I would like express my sincere gratitude to Dr. Bruce Tatarchuk for his financial support and academic guidance. I would like to acknowledge Dr. Robert Ashurst, Dr. Allan David, Dr. Marko Hakovirta, and Dr. Bart Prorok for serving on my committee. I express my appreciation to all the members of Center for Microfibrous Material Manufacturing for their suggestion and helps, especially, Dr. Don Cahela, Dr. Hongyun Yang, Dr. Wenhua Zhu, Mr. Dwight Cahela, Ms. Kimberly Dennis, Mr. Ron Putt. I am also thankful to Amogh Karwa, Abhijeet Phalle, Qiang Gu, Sabrina Wahid, Shahadat Hussain, Achintya Sujan, Pengfei Zhao, Peng Cheng and many others. I am also grateful to Sue Ellen Abner, Elaine Manning, and Karen Cochran for the administrative support throughout my graduate studies.

I would like to thank my family. Without their encouragement and love, this dissertation would not have been possible.

Table of Contents

List of Tables

List of Figures

Nomenclature

C, adsorbate concentration in fluid phase (mol/m^3)

C_0, inlet concentration of adsorbate (mol/m^3)

C_s, gas phase adsorbate concentration at particle surface (mol/m^3)

d_p, diameter of particle (m)

d_c, characteristic length of system (m)

D_e, effective internal diffusivity (m^2/s)

D_m, molecular diffusivity (m^2/s)

D_s, surface diffusivity (m^2/s)

D_z, effective axial dispersion coefficient (m^2/s)

E_0, filter's initial removal efficiency

f, fanning friction factor

k_f, fluid-to-particle mass transfer coefficient (m/s)

$k_G\alpha$, overall volumetric mass transfer coefficient (1/s)

k_p, intrapellet mass transfer coefficient (1/s)

K'- adsorption rate constant (1/s)

K_e, Freundlich isotherm constant

L, length of bed (m)

n, exponent in Freundlich isotherm

q_0, solid phase adsorbate concentration in equilibrium with C_0 (mol/m^3 adsorbent)

$\bar{q}$, volume-averaged solid phase adsorbate concentration (mol/m^3)

q_s, solid phase adsorbate concentration at particle surface (mol/m^3)

Q, volumetric flow rate (m^3/s)

Re, Reynolds number

Sc, Schmidt number

Sh, Sherwood number

t, time (s)

t_b, breakthrough time (s)

T, temperature

u_0, superficial gas velocity (m/s)

W_b, weight of adsorbent bed (kg)

W_e, solid phase adsorbate concentration in equilibrium with C_0 (kg/kg adsorbent)

z, axial length (m)

Greek letters

α, external surface area per volume of bed (m^2/m^3)

ΔP, pressure drop (Pa)

ε_b, bed voidage

ε_p, porosity of particle

η, heterogeneous contacting efficiency

μ, fluid viscosity (m^2/s)

ρ, fluid density (kg/m^3)

ρ_b, packing density of sorbent bed (kg/m^3)

ρ_p, density of particle (kg/m^3)

τ, saturation capacity of bed (s)

τ_p, particle's pore tortuosity

τ_s, particle's surface tortuosity

Chapter 1

Introduction and Literature Review

1.1. Background and introduction to microfibrous material

Nonwovens are fabric-like materials that are made from fibers/filaments (not converted to yarns), which are bonded by mechanical, thermal or chemical methods. Nonwovens products are widely used in medical and hygiene products, filtration, automobiles, geotextiles, etc. [1]. In 2010 alone, global nonwovens production reached 7 million tons and sales exceeded $25 billion according to the data from INDA.

Composite nonwovens (CNW), which use a combination of two or more materials or manufacturing technologies to create the desired product with enhanced performance or multifunction, or reduction of cost, are the new trend in the nonwovens industry. Generally, they can be classified into the following categories: laminated CNW, coated CNW, blended CNW, technology-combined composite CNW, and CNW with particulates. Most recently, researchers have attempted to incorporate a new class of fibers, such as nanofiber [2, 3] super-adsorbent fibers [4], and conductive polymer fiber into the base fibers to create high performance composites. For instance, Karwa et al [5-7] developed a novel carbon nanofiber CNW using the chemical vapor deposition (CVD) method, and found that the nanofiber remarkably enhanced the media’s aerosol filtration efficiency without any significant pressure drop penalty.

However, most researchers, either in academic or industry, have focused on the CNW without particulates; CNW with particulates are rarely reported. Ramkumar et al [8] developed a nonparticulate dry nonwoven pad for chemical warfare agent decontamination using a needle-punching nonwoven technology. Qian et al [9] developed a three-layer nonwoven composite using two different materials by a spun-lacing method. For the CNW with particulates, Lukic et al [10] developed a novel abrasive composite nonwoven material using latex as the bonding agent and alumina particles as the abrasive components.

For the CNW without particulates, the functional properties, such as aerosol filtration, gas removal, and water absorption, are provided by the fibers. In contrast, CNW with particulates are quite different heterogeneous nonwovens, in which the fibers merely act as the support or carrier material while the particulates act as the functional component. The incorporation of particulates into the webs can greatly expand the application spectrum of nonwoven materials because many industrial materials, such as catalysts, adsorbents, abrasive grains are in the form of particulates.

Bruce Tatarchuk et al [11-14] developed a novel catalyst structure, microfibrous entrapped catalyst (MFEC), by incorporating catalyst particulates into microfiber webs via the wet-lay process. MFEC is distinct in its small characteristic dimensions and high surface-area-to-volume ratio when compared to the traditional packed bed or monolithic reactor; these two factors are primarily responsible for the process intensification (enhanced heat and mass transport) in heterogeneous contact systems.

1.2. Application of microfibrous materials

1.2.1. Fuel and air purification for fuel cell

CO is the most concerning contaminant in the reformate gas stream for the PEM fuel cell application. Preferential oxidation of CO is one of the methods used to remove the CO. Chang et al [15] used Ni fiber to entrap 150-250 µm Pt-Co/Al_2O_3 catalyst and studied the CO removal efficiency by experimentation. It was found that this microfibrous entrapped catalyst was very effective in the removal of the CO in H_2 in the temperature range of 25 to 200 ˚C. H_2S is another important contaminant in the fuel stream for PEM fuel cell. Lu et al. [16] used Ni fiber entrapped ZnO/SiO_2 sorbent to adsorb the H_2S in the H_2 stream. The experimental result showed that at 1.2 cm/s face velocity and 400 ˚C, only a 1mm thick MFES sheet is required reduce the H_2S concentration from 2% to 0.00006%. Compared to the commercial 1-2 mm size of ZnO pellet sorbent, the breakthrough capacity is improved 2-3 fold. In addition to anode fuel purification, the microfibrous material was also utilized to purify the cathode air. Kennedy et al. [17] used composite bed filter (a combination of packed bed and microfibrous bed filter) to remove the VOCs in the air stream. They also developed a programmable algorithm to optimize the filter design by carefully studying the tradeoffs between two factors of power loss: parasitic power loss due to the pressure drop from the additional filter, and the power loss caused by the contamination effects of impurities.

1.2.2. Air purification

Air purification is an area with many applications for microfibrous materials. Kalluri et al. [18] used microfibrous entrapped Pd/γ-Al_2O_3 to decompose the ozone in the air. The performance of this material was compared with the traditional packed bed and monolith catalysts. The microfibrous material outperformed the other two traditional catalyst systems in terms of heterogeneous contacting efficiency and in pressure drop. Wahid et al.[19] utilized Ni fiber entrapped mixed metal oxide Pd-Mn/ γ-Al_2O3 catalyst to remove VOCs in the air at high face velocity (ca. 3-30 m/s) and low temperature (<200 ˚C). The microfibrous bed system exhibited high conversion in a very short contact time (ca. 100 µs). They also used the multi element structured array (MESA) to adjust the pleat factor (PF) of a contact system. It was found that increasing the PF can significantly reduce the pressure drop and increase the contact time, consequently increasing the conversion. In addition to the MFEC, microfibrous entrapped sorbents (MFES) were also developed for air purification. Kalluri et al. [20] used microfibrous entrapped activated carbon adsorbent to remove VOCs. The MFES significantly increase the single pass removal efficiency and sorbent bed utilization before the occurrence of breakthrough.

1.2.3. Fisher-Tropsch reaction

Fisher-Tropsch synthesis (FTS) is a highly exothermic catalytic reaction, and hence thermal management is an important issue for steady-state operation. Metal fibers formed from materials such as Cu have excellent thermal conductivity, making it reasonable to use metal microfibrous entrapped catalysts to improve the thermal property of catalyst beds. Sheng et al [21-23] used Cu fiber entrapped Co/Al_2O_3 as the catalyst of FTS. It was found that the maximum temperature deviation from the centerline to the reactor wall in a 41 mm ID reactor was reduced to 6.4 ˚C for Cu fiber MFEC bed, a much smaller value than the 460 ˚C associated with a traditional packed bed. The hot spot and runaway states were effectively prevented by using metal MFEC. In addition, the Cu MFEC bed can quickly (in several minutes) reach steady state in the startup period of FTS, while the traditional packed bed needs about 1.5 day to reach the steady state. Due to the improved the thermal conductivity of catalyst bed, it is possible to use larger size reactor (such as 15 cm ID) to replace the common 3 cm tubular reactor without losing the thermal stability of reactor.

1.2.4. Research of microfibrous material in China

The success of microfibrous materials in many application areas has drawn much attention from other researchers. One group led by Dr. Lu in East China Normal University has made a lot of effort to extend the applications of microfibrous materials. They have published more than 20 articles within diversified areas [24-48].

1.2.4.1. Steam reforming catalyst for H_2 production

Catalytic steam reforming is one the main methods for H_2 production. The steam reforming process requires high temperature and a high pressure atmosphere, therefore thermal management is usually critical for steady state operation and the prevention of catalyst deactivation. It was found that the MFEC could significantly improve the performance of the reaction when compared to the traditional packed bed system. Ling et al. [35] developed a miniature methanol fuel processer using Ni fiber (8μm) entrapped Pd-ZnO/Al_2O_3 catalyst. They found that the processor with the microfibrous catalyst exhibited 4-fold improvement in weight hourly space velocity (WHSV) compared to the traditional packed bed catalyst when high conversion (>98%) was required. A prototype fuel processor using MFEC as catalyst (as shown in Figure 1.1) was fabricated, and it was capable of producing 1700 standard cubic centimeters per minute (sccm) of PEMFC-grade H_2. Chen et al. [31] developed a Cu microfibrous entrapped Ni/Al_2O_3 catalyst for dry reforming of methane. The CFD simulation illustrated that the use of Cu fiber significantly enhanced the heat transfer in the catalyst bed. The CH_4 conversion was increased from 84% to 89% on the packed bed catalyst in the same conditions, while the carbon deposition rate was reduced 4-fold.

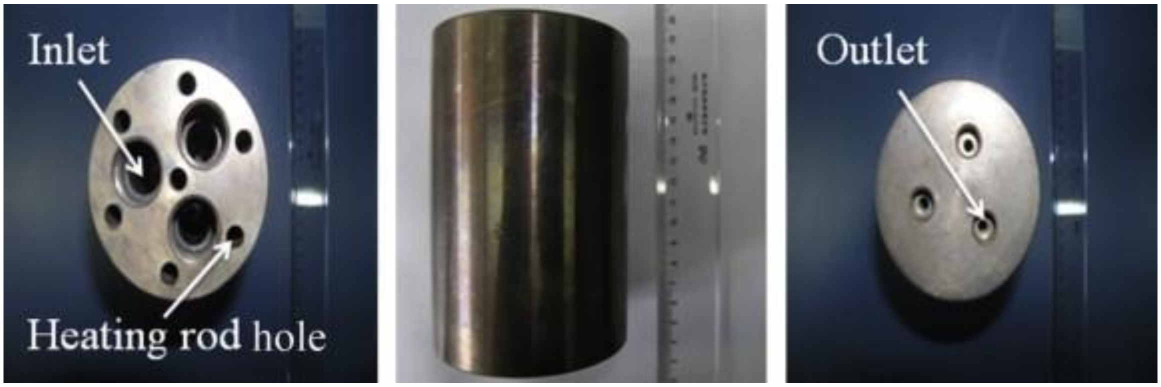

Figure 1.1 Prototype methanol fuel process using Ni microfibrous material as catalyst

1.2.4.2. Low temperature selective oxidation of alcohols

The oxidation of alcohols to form carbonyl compounds is an important reaction in organic chemistry. Gas phase oxidation of alcohols is a strong exothermic reaction; heat transfer is a big limitation to the overall reaction rate. Ag catalyst has good heat conductivity, but its catalytic activity is low at low temperatures. In contrast, oxide supported catalysts such as Au/SiO_2 have good low temperature activity, but poor heat conductivity [49]. The MFEC with high heat transport ability provides an opportunity to address this problem. Zhao et al. [26, 34, 36, 38] developed a microstructured Ni fiber Au catalyst using galvanic deposition approach. This catalyst is very effective for oxidizing acyclic, benzylic, and polynary alcohols. The catalyst showed high performance in terms of low temperature activity, selectivity, stability and heat transfer capability. For benzyl alcohol, 95% conversion was achieved with more than 98% selectivity to benzaldehyde in a 660 h test. A low temperature deviation (<10 ˚C) between the catalyst bed and the reactor wall was also observed due to the high thermal conductivity of the metal fiber web. The uniform temperature distribution in the catalyst bed significantly improved the selectivity of reactions. In addition, interesting results were found that indicated that the formation of NiO nano particles around Au particles during the Au galvanic deposition step significantly promoted the low temperature activity of the catalyst. Mao et al. [37] also reported a highly efficient microfibrous structured silver catalyst for gas-phase oxidation of alcohols.

1.2.5. Process intensification

Development of process intensification technologies to improve chemical process efficiency has gained a lot of attention in recent years [50, 51]. In David Reay's monograph "Process Intensification: Engineering for Efficiency, Sustainability and Flexibility" [52], some major intensification technologies and their applications are discussed. These technologies include a microreactor [53, 54], a monolithic reactor, rotating packed beds (HIGEE) [55, 56], and other structured catalysts or reactors such as porous anodic alumina plate monolithic catalysts [57-59]. Structured catalysts and reactors (SC&R) are important chemical process intensification technologies. Compared to the conventional tubular reactor and packed bed catalyst, the SC&R is an integration of reactor and catalyst. Knitted packings and corrugated open/close cross-flow packings are widely used in distillation columns, and significantly improve the separation efficiency [60, 61]. Cordierite monoliths have been widely used in automobile exhaust converters. However, those SC&R typically use the washcoat method to load micro-sized catalyst particles onto the surface of the substrate, and thereby the total catalyst load is limited. In contrast, MFEC is a novel SC&R technology whose catalyst load is not limited by the washcoat method. This advantage makes MFEC technology an attractive alternative to other SC&R technologies in many process intensification applications. In addition, since MFEC is a nonwoven material, it is ready to be corrugated to further increase the catalyst loading and reduce the bed's pressure drop.

In addition to the many chemical applications in which process intensification is involved (or desired), the MFEC technology also has great potential in catalyst screening, catalyst testing, and kinetics studies due to its unique mass and heat transport characteristics. A lot of heterogeneous catalytic reactions involve mass/heat transfer limitations, a coupling of reaction kinetics with mass/heat transport, and a slowness to reach steady state operation (FTS reaction takes days to reach steady state). These issues make the fast catalyst screening, and reaction kinetics studies very difficult. The MFEC uses micro-sized particles, eliminating the mass transport limitation, and high thermal conductivity metal fibers, eliminating heat transport limitations and reaching steady state in a short period. On the other hand, in the MFEC system the mass and heat transport factors are typically decoupled with the intrinsic reaction kinetics. These features of MFEC make it ideal for application in catalyst screening and kinetics studies.

1.3. Composite Nonwoven Sorbent Media

Filtration is one of the largest application areas for nonwovens, but they are typically limited in the number of possibilities for particulate filtration applications. Molecular filters such as activated carbon filters typically come in the form of granular beds containing large size particulates (2-5mm) to allow for air permeability. The packed bed filters suffer from poor intrabed and intraparticle mass transfer, low bed utilization, and non-uniform packing in a way that leads to bed/wall channeling or bypass flow. In addition, their large volume and heavy weight are not satisfactory for compact/miniature applications. In contrast, fibrous sorbent media such as ACF felt, CNW containing sorbent particulates are high efficiency, very uniform in structure, and suitable for miniature applications.

In this study, a novel fibrous CNW, activated carbon fiber enhanced microfibrous entrapped sorbent (ACF-MFES), was developed and prepared via a wet-laid process. The addition of ACF into the polymeric fiber significantly improved the web forming and sintering process, effectively preventing the hot spot that leads to over sintering and making the resulting media more fluffy (low flow resistance) and resilient. The presence of ACF also further improved the adsorption kinetics and the total chemical capacity. The ACF-MFES is characterized by its super thin critical bed length and high removal efficiency. It is capable of achieve 3-log (99.9%) gas removal using media only a couple mm thick, within decades of µs contacting time.

The ACF-MFES media typically consists of 1-4 vol% microfiber (10-20µm) and 10-20 vol% sorbent particles (100-250µm) with rest being void. The choice of fiber could be metal or glass fiber for durable and regenerative product, or polymer fiber for disposable product. The choice of adsorbent can be activated carbon, silica, or alumina, depending upon the application. Due to the use of micro sized particulates and additional fine ACF, the external surface area of sorbent in ACF-MFES can reach up to 3×10^4 m^2/m^3. The high surface area to volume ratio of ACF-MFES material significantly enhances the mass transport in adsorption. Figure 1.3 (a) and (b) show the SEM images of unsintered media with 180-250µm activated carbon particles entrapped in nickel fiber web. Figure 1.4 (a) and (b) show the SEM images of ACF-MFES media.

1.4. Synthesis of ACF-MFES and process optimization

The basic steps for manufacturing nonwovens include: (a) fiber or polymer selection, (b) web formation, (c) web bonding, and (d) finishing. To develop a high quality ACF-MFES media, all these four steps need to be carefully studied and optimized.

The first step is the selection of fibers. There are two concerns when selecting the proper fiber for ACF-MFES materials: (a) all sorbent particles in the web need be bonded firmly and (b) the surface of the particles will not be covered by bonding agent, which will reduce the adsorption capacity. The use of a chemical bonding agent or polymer binder cannot satisfy these two requirements because they cannot provide uniform bonding throughout the entire web matrix, and are readily able to cover the surface of the sorbent particles. In this respect, a self-bonding fiber is desired. A bicomponent fiber with a low melting temperature sheath is a fiber that can be self-bonded through the thermal bonding process. In this study, a concentric sheath-core structure bicomponent fiber, linear low density polyethylene on polyethylene terephthalate (LLDPE/PET), was used as the base fiber.

The diameter of fiber is another important factor with significant influence on the particulates retention and the media's permeability. A small dimensional fiber is beneficial for particulate retention, but unfavorable for media permeability. The optimization of fiber dimension for ACF-MFES will be discussed in the media pressure drop section.

1.4.1. Web formation technology and wet end chemistry

The second step in the process is the web formation. In the nonwovens industry, for staple fibers, the webs are formed through dry-lay or wet-lay process, whereas for direct polymer input, the webs are formed by spunbond and meltblown process. In order to incorporate the sorbent particles into the webs and gain uniform particle distribution, the wet-lay process was selected as the primary web formation technology. The advantage of the wet lay process lies in its ability to form a suspension stock, where fibers and particulates are well dispersed and mixed in the water medium. Since the particles and fibers are premixed in the stage of suspension, the particles are well distributed in the final formed web. This characteristic is essential to achieve a high contacting efficiency, and prevents channeling flow from occuring in ACF-MFES.

In suspension preparation and the web formation process, the fiber length, the consistency of suspension, and the wet-end chemistry are important to the formation of a good quality web. The fiber length suitable for nonwovens is 6-25 mm. Since flocculation of fibers in the suspension increases with the increase in fiber length, short fibers (6mm cut length) were used for preparing ACF-MFES. The consistency, which is the weight ratio of dry material to the total weight of suspension, has substantial influence on the web formation. In the pulp and paper industry, a typical consistency is 0.3% - 0.7%, however, the nonwovens use a much lower consistency (0.005% - 0.05%) to enhance the dispersion of the fibers. The low consistency means that more water must be removed in the web formation, and hence requires more energy. Tradeoffs must be taken to balance these two conflicting factors. After a lot of experimental investigation, the ideal consistency was determined to be 0.02%.

The use of wet-end chemistry in nonwovens is inspired by the papermaking industry. They can be divided into three categories by their functions: dispersion aids, retention aids, and formation aids. To improve the retention of particles in the web, the water viscosity was modified by adding a certain amount of Hydroxy Ethyl Cellulose (HEC). The high viscosity water can reduce the settling speed of solid particles (which settle faster than fibers) and hence reduce the loss of particles in the web formation process. Poor dispersion of fibers and lack of suspension stability would result in web defects like log, rope and dumbbell [1]. To address this issue, a dispersant (Cruwik Syn) was added.

1.4.2. Web bonding

The third step in the process is web bonding. The resulting wet web from the web formation step is called a preform in our study. The fibers in the preform are not bonded and the web lacks the necessary strength or structure stability for specific applications. Common bonding technologies include mechanical bonding, thermal bonding and chemical bonding. As discussed above, the selected bicomponent fiber can be self-bonded through thermal bonding. Naturally, the thermal bonding method is chosen for this study. Thermal bonding can be divided into three categories based on the means of heat transfer: heat conduction (heated calendar or plate), heat convection (hot through air), and radiation (infrared or ultrasonic).

A heated calendar is one of the most widely used means of thermal bonding in the nonwoven industry and was therefore attempted first. It was found that the fibers tended to adhere to the heated plate and the resulting web lacked strength due to the polymer degradation in the presence of moisture [62]. Heat transport using a convection method (such as in the home baking oven) is slower, but the result is more uniform than when conduction is used. The experiments showed that the webs can be well bonded in the oven by air stream. To optimize the operation conditions, the bicomponent fiber was first analyzed by a differential scanning calorimeter (DSC) via a heat/cool/heat cycle method; the melting point for the sheath and core were determined to be 125˚C and 250˚C, respectively. Based on the thermal properties of the bicomponent fiber, the best sintering temperature was found to be 130-140 ˚C. Through a lot experiments and observation, the optimized bonding process was determined as follows: first dry at 110˚C for 15min, then raise the temperature to 145˚C at a ramping rate of 10˚C/min, and sinter at this temperature for 5min, and finally cool down to 110 ˚C and dry for 1 hour.

The last step, web finishing is not required for ACF-MFES media.

1.4.3. Multi-forming processes

Multi-forming processes are an effective way to create layered composite nonwovens; it consists of more than one web forming section where the web forms, and then combines together in a later stage. The multi-card process, multi-forming box air-lay and wet-lay process [63, 64], multi-beam spunbond process, and combined forming process [65, 66] are some common multi-forming processes.

One of the most successful cases using multi-forming processes is the spunbond-meltblown-spunbond (SMS) process as shown in Figure 1.2. In a typical SMS media, the meltblown layer acts as the functional layer, whereas the spunbond layer provides mechanical strength and protection to the meltblown layer [1].

Hong et al [67] reported an air–water hybrid former that was comprised of a head-box with three stock flow channels; the outer channels were used to convey the aqueous stock while the inner channel was used to convey airborne fibers. This hybrid former can be used to produce composite materials by combining air-lay and wet-lay webs. This technology brings promise for manufacturing the next generation of two-in-one filter media by combining the wet-lay ACF-MFES media with traditional air-lay filter media. The resulting composite media is capable to remove both particulate and molecular contaminants.

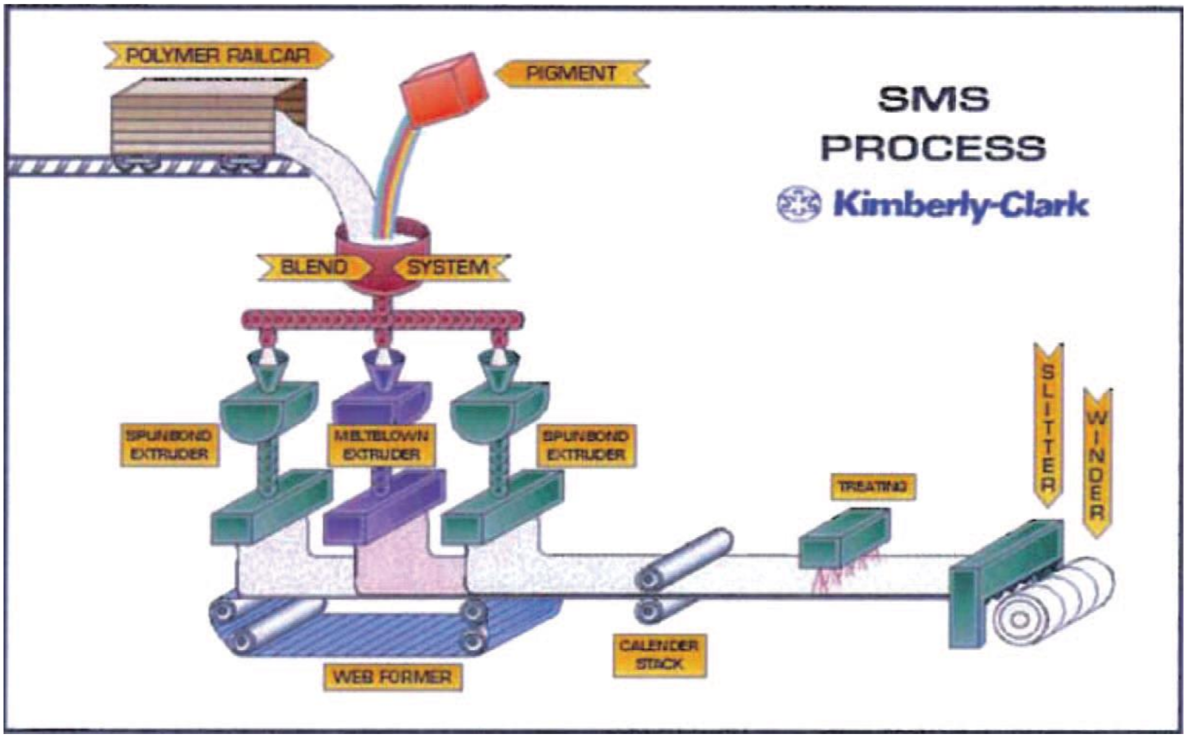

Figure 1.2 Scheme of spunbond-meltblown-spunbond (SMS) process [1]

1.5. Application of MFES

The high efficiency, low cost polymeric MFES has great potential to be used in commercial or industrial HVAC systems as a substitution for current packed bed carbon filters. Due to the high cost of carbon filters, most of the current HVAC systems haven't installed any molecular filter, so they are not capable to deal with gas phase contaminants. With the rise in concern about indoor air quality and molecular contaminants, installation of molecular filters for future's HVAC systems has become a common trend. The widespread use of molecular filters is dependent on the advancement of technologies and a reduction in cost; the current price gap between molecular filters and common particulate filters is still large. Compared to packed bed carbon filters, the ACF-MFEC filters use a much lower sorbent mass (while still providing considerable removal efficiency and protection time) and therefore remarkably reduces the cost of the molecular filters. The price of ACF-MFES filters can be very close to that of the normal air filters due to the use of cheap raw materials, and a mature manufacturing process. A preliminary exploration of the application of MFES media in HVAC systems has been conducted by Luna et al [62].

Air purification for fuel cells systems is another important application for MFES media. The effect of anode contaminants, including CO, CO_2, H_2S, ammonia, chloride, and hydrocarbons on the performance of fuel cells has been extensively reported [15, 68-70]. The anode contamination effects were also reviewed by Cheng [71] and Zamel [72]. Compared to the anode contamination, the cathode contamination was overlooked and siginficantly fewer studies were reported [72-78]. The major contaminants in the air include nitrogen oxides (NO and NO_2), sulfur oxides (SO_2 and SO_3), carbon oxides (CO and CO_2), ozone, and hydrocarbons. These air contaminants can poison the cathode catalyst and the membrane electrode assembly (MEA), causing substantial performance degradation. The most economic and effective way to remove the air contaminants is to use adsorptive filters or cleaners. However, the use of cleaners in fuel cells will reduce the net power output due to the parasitic power. The current adsorptive filters, due to low contacting efficiency, require a thick bed to achieve the required removal efficiency (high removal efficiency is required due to the low tolerance of PEMFC to contaminants). The MFES media and the component bed (packed bed + MFES) have improved contacting efficiency, and hence improved removal efficiency, allowing for a thinner critical bed length compared to the packed bed filter. Use of MFES media or component bed can effectively reduce the total length of the bed, the total mass of sorbent, and the required parasitic power for the filter.

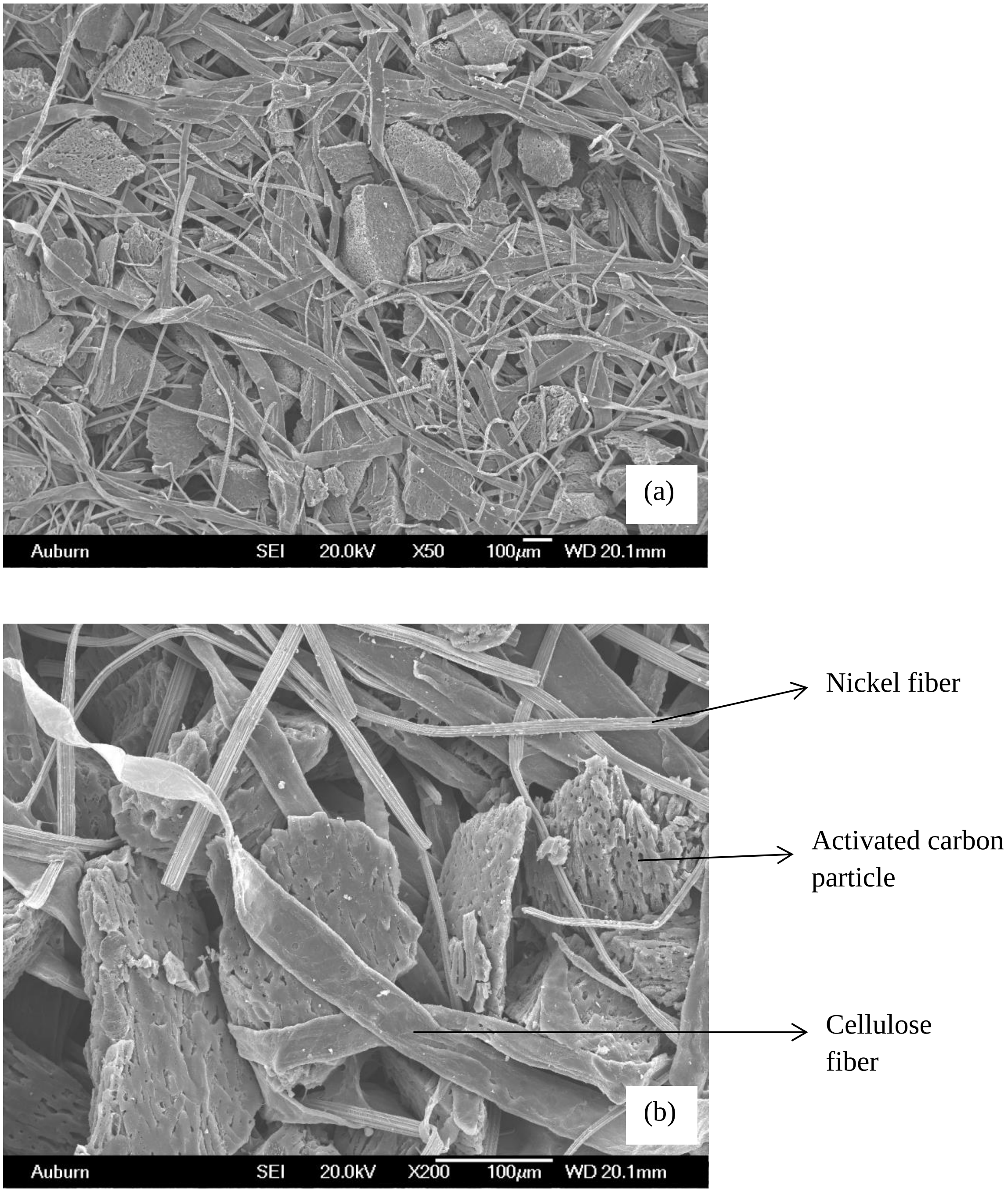

Figure 1.3 (a) & (b) SEM image of 180-250μm activated carbon particles entrapped in 8μ nickel fiber web

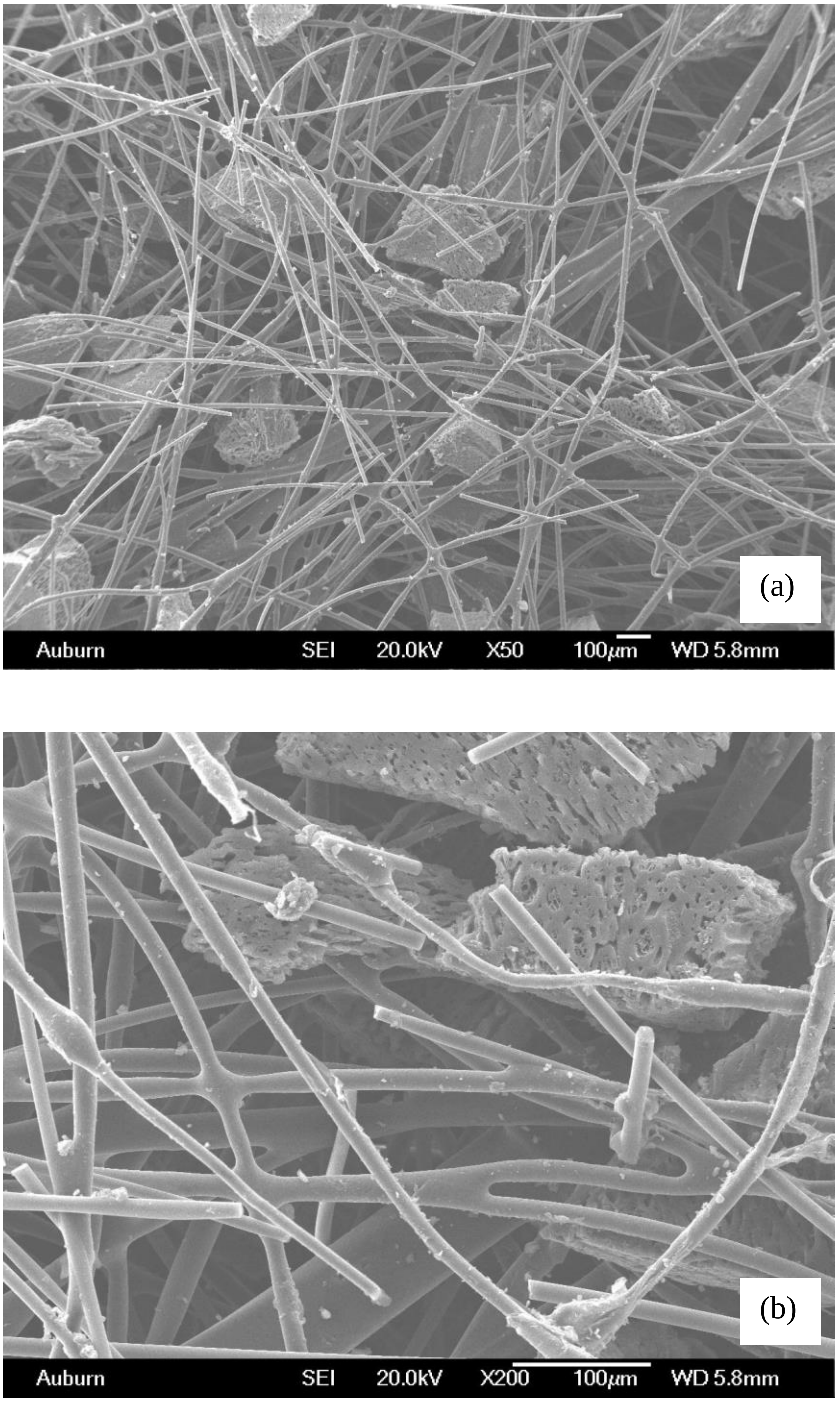

Figure 1.4 (a) & (b) SEM image of 180-250 μm activated carbon particles entrapped in bicomponent polymer and activated carbon fiber blended fiber web

1.6. Heterogeneous contacting systems.

The most important feature of MFES media is its high contacting efficiency. To further explain this concept, this section gives a brief review of various traditional heterogeneous contacting systems in use in industry, and compares them with the MFES system.

1.6.1. Packed beds

Packed beds are the most widely used contacting system in industry. They consist of structured or un-structured packing (such as Raschig ring) or particles (such as catalyst and adsorbent particles). The particles in packed beds are packed in a random and loose way; the particles touch each other to maintain the stability of structure. Because of this feature, the voidage of a packed bed is not adjustable, typically ranging from 0.4-0.5. Use of small particles (such as 200 µm) in packed beds leads to very high pressure drops at normal operating velocity for most industrial applications. As we know, decreasing the particle size can directly increase the surface area to volume ratio, and hence improve the system’s contacting efficiency; however, in packed beds, the use of small particles is limited by its high pressure drop. This limitation makes the packed bed a low contacting efficiency system in many applications. The heat transfer becomes another important limitation of packed beds when strong exothermic or endothermic reactions are involved. Packed bed systems are the most common contacting system, and the knowledge about their characteristics has been well established. The mass transport performance of packed beds has been extensively researched [79-83]; a good review can be found in Wakao’s work [84]. The pressure drop model of packed beds was well reviewed by Dullien [85].

1.6.2. Microreactors (Microchannel reactors)

A microreactor, also known as a microchannel reactor or microstructure reactor, is a device with typical lateral dimensions below 1.0 mm. Microreactors, together with other micro devices such as micro heat exchangers and micro mixers, have been applied in many areas, such as high throughput catalyst screening and kinetics studies [54, 86, 87], photochemical platforms [88], portable power generators [89], synthesis of special compounds and solid products [90, 91], etc. The heat and mass transport behavior in microchannel reactors has been studied using experimental and theoretical methods by many authors [53, 92-94]. A good review of microreactor technology can be found in Oliver and Ehrfeld's books [95, 96].

Microreactors are characterized by their small characterized dimension (typically several orders of magnitude smaller than traditional tubular reactor) and high surface area to volume ratio. This small scale enables the reagent to be mixed in a very short time. For a binary system, the mixing time in the microchannel can be described by equation 1.2 [97]. Equation 1.2 shows that the mixing time is proportional to the square hydraulic diameter of reactor; this means that one order of magnitude reduction in dimension will lead two orders of magnitude decrease in mixing time. In addition, the small scale of microreactors also reduces the diffusion distance of molecules from bulk fluid to the wall (catalyst layer), which significantly reduces the mass transfer resistance. On the other hand, the high surface area to volume ratio provides a large contacting interface for mass/heat transfer and hence effectively increases the overall volumetric mass/heat transfer coefficient; the value of the coefficients are typically several orders of magnitude greater than conventional reactors. In conclusion, the underlying reason for enhancement in mass/heat transport is the small dimension (scale) of microreactors. The MFEC/MFES materials' characteristic dimension is on the same scale as microreactors, therefore they share many charasterics (attributes) with microreactors in transport behavior. Due to the similarity between MFEC/MFES and microreactors, the knowledge (such as transport phenomenon, application areas, etc.) developed in the study of microreactors is also useful for studying the characteristics of MFEC/MFES system and exploiting suitable applications.

$$t = \frac{d_h^2}{D_{AB}} \tag{1.2}$$

1.6.3. Monolithic reactor

Monolithic catalysts were introduced in the mid-1970s, and they are mainly used in environmental applications, such as the automotive converter and DeNOx catalysts[100]. The major advantage of monoliths is their high ratio of geometric surface area to pressure drop. However, the mass transfer in the channel of monoliths is limited by its relatively large hydraulic diameter (d_h). The dimension of d_h in monoliths is generally one order of magnitude larger than that in the microreactor. The typical dimensions of a monolithares shown in Table 1.1. The substrates of monoliths are mostly made of ceramics (such as cordierite). The catalyst support is typically coated on the walls of channels using the wash coating technique. Since the coated catalyst layer is typically thin (tens to hundreds of microns), the catalyst load is very limited in monoliths. Heat transport is another big limitation for monoliths. Due to the poor thermal conductivity of ceramic materials, and heavy thermal mass (because of its large mass and volume) of monolith substrates, quick warm-up of monoliths is very difficult. The quick start-up feature is very important in catalytic converter application. A remarkably large amount of toxic gas is emitted to the atmosphere during the initial 60 second start-up period due to the slow warm-up of catalytic converters.

Table 1.1 Typical Dimension of Monolithic catalysts

Applications	cell density (cpsi)	d_h (mm)	ε (%)
Automotive converter	400	1	70-80
Stationary emission control	64	2.9	82

Although most monoliths are used in catalysis applications, it has been reported that activated carbon monoliths are used to adsorb VOCs in the large volume of effluent gas in order to decrease the pressure drop or operation cost [101-104]. Figure 1.5 shows the monolithic activated carbon honeycomb.

The major advantage of the monolithic structure, low pressure drop, is relied on its high open and parallel channels, however, the open structure also results in poor external (fluid-to-wall) mass transfer [105]. The mass transfer coefficient in monoliths can be estimated by Equation 1.3[98]. From equation 1.3, we can find that increasing the channel dimension (d) will decrease the mass transfer coefficient.

$$Sh = 2.43\left(1 + \left(\frac{Gz}{132}\right)^{0.835}\right) \tag{1.3}$$

where,

$$Gz = Re \cdot Sc\frac{d}{L} \tag{1.4}$$

Figure 1.5 Monolithic activated carbon honeycomb [99]

References

[1] Das D, Pradhan AK, Chattopadhyay R, Singh SN. Composite Nonwovens. Textile Progress. 2012;44(1):1-84.

[2] Huang Z-M, Zhang YZ, Kotaki M, Ramakrishna S. A review on polymer nanofibers by electrospinning and their applications in nanocomposites. Composites Science and Technology. 2003;63(15):2223-53.

[3] Kosmider K, Scott J. Polymeric nanofibres exhibit an enhanced air filtration performance. Filtration & Separation. 2002;39(6):20-2.

[4] Kim Y-J, Yoon K-J, Ko S-W. Preparation and properties of alginate superabsorbent filament fibers crosslinked with glutaraldehyde. Journal of Applied Polymer Science. 2000;78(10):1797-804.

[5] Karwa AN, Tatarchuk BJ. Aerosol filtration enhancement using carbon nanostructures synthesized within a sintered nickel microfibrous matrix. Separation and Purification Technology. 2012;87(0):84-94.

[6] Karwa AN, Davis VA, Tatarchuk BJ. Carbon Nanofiber Synthesis within 3-Dimensional Sintered Nickel Microfibrous Matrices: Optimization of Synthesis Conditions. Journal of Nanotechnology. 2012;2012.

[7] Karwa AN, Barron TJ, Davis VA, Tatarchuk BJ. A novel nano-nonwoven fabric with three-dimensionally dispersed nanofibers: entrapment of carbon nanofibers within nonwovens using the wet-lay process. Nanotechnology. 2012;23(18):185601.

[8] Ramkumar SS, Love AH, Sata UR, Koester CJ, Smith WJ, Keating GA, et al. Next-Generation Nonparticulate Dry Nonwoven Pad for Chemical Warfare Agent Decontamination. Industrial & Engineering Chemistry Research. 2008;47(24):9889-95.

[9] Qian C. Development of a New Non-woven Composite and its Properties. Textile Research Journal. 2007;77(6):397-402.

[10] Lukić S, Jovanić P. Structural analysis of abrasive composite materials with nonwoven textile matrix. Materials Letters. 2004;58(3–4):439-43.

[11] Cahela DR, Tatarchuk BJ. Permeability of sintered microfibrous composites for heterogeneous catalysis and other chemical processing opportunities. Catalysis Today. 2001;69(1–4):33-9.

[12] Kohler DA, Krishnagopalan A, Rose MF, Tatarchuk BJ, Zabasajja JN, University A, inventors; Mixed fiber composite structures high surface area-high conductivity mixtures. 1992 1992-1-14.

[13] Krishnagopalan A, Rose MF, Tatarchuk BJ, University A, inventors; Mixed fiber composite structures. 1992 1992-4-7.

[14] Kohler DA, Krishnagopalan GA, Rose MF, Tatarchuk BJ, Zabasajja JN, University A, inventors; Preparation of mixed fiber composite structures. 1994 1994-4-19.

[15] Chang B-K, Lu Y, Tatarchuk BJ. Microfibrous entrapment of small catalyst or sorbent particulates for high contacting-efficiency removal of trace contaminants including CO and H2S from practical reformates for PEM H2–O2 fuel cells. Chemical Engineering Journal. 2006;115(3):195-202.

[16] Microreactor Technology and Process Intensification (ACS Symposium): American Chemical Society; 2005.

[17] Kennedy DM, Cahela DR, Zhu WH, Westrom KC, Nelms RM, Tatarchuk BJ. Fuel cell cathode air filters: Methodologies for design and optimization. Journal of Power Sources. 2007;168(2):391-9.

[18] Kalluri RR, Cahela DR, Tatarchuk BJ. Comparative heterogeneous contacting efficiency in fixed bed reactors: Opportunities for new microstructured systems. Applied Catalysis B: Environmental. 2009;90(3–4):507-15.

[19] Wahid S, Tatarchuk BJ. Catalytic Material with Enhanced Contacting Efficiency for Volatile Organic Compound Removal at Ultrashort Contact Time. Industrial & Engineering Chemistry Research. 2013.

[20] Kalluri RR, Cahela DR, Tatarchuk BJ. Microfibrous entrapped small particle adsorbents for high efficiency heterogeneous contacting. Separation and Purification Technology. 2008;62(2):304-16.

[21] Sheng M, Yang H, Cahela DR, Tatarchuk BJ. Novel catalyst structures with enhanced heat transfer characteristics. Journal of Catalysis. 2011;281(2):254-62.

[22] Sheng M, Yang H, Cahela DR, Yantz Jr WR, Gonzalez CF, Tatarchuk BJ. High conductivity catalyst structures for applications in exothermic reactions. Applied Catalysis A: General. 2012;445–446(0):143-52.

[23] Sheng M, Cahela DR, Yang H, Gonzalez CF, Yantz Jr WR, Harris DK, et al. Effective thermal conductivity and junction factor for sintered microfibrous materials. International Journal of Heat and Mass Transfer. 2013;56(1–2):10-9.

[24] Zhao G, Hu H, Jiang Z, Zhang S, Lu Y. NiO-doped Au/Ti-powder: A catalyst with dramatic improvement in activity for gas-phase oxidation of alcohols. Applied Catalysis A: General. 2013;467(0):171-7.

[25] Zhao G, Deng M, Jiang Y, Hu H, Huang J, Lu Y. Microstructured Au/Ni-fiber catalyst: Galvanic reaction preparation and catalytic performance for low-temperature gas-phase alcohol oxidation. Journal of Catalysis. 2013;301(0):46-53.

[26] Zhao G, Huang J, Jiang Z, Zhang S, Chen L, Lu Y. Microstructured Au/Ni-fiber catalyst for low-temperature gas-phase alcohol oxidation: Evidence of Ni2O3–Au+ hybrid active sites. Applied Catalysis B: Environmental. 2013;140–141(0):249-57.

[27] Chen W, Zhao G, Xue Q, Chen L, Lu Y. High carbon-resistance Ni/CeAlO3-Al2O3 catalyst for CH4/CO2 reforming. Applied Catalysis B: Environmental. 2013;136–137(0):260-8.

[28] Zhao G, Hu H, Chen W, Jiang Z, Zhang S, Huang J, et al. Ni2O3-Au+ hybrid active sites on NiOx@Au ensembles for low-temperature gas-phase oxidation of alcohols. Catalysis Science & Technology. 2013;3(2):404-8.

[29] Lu X, Zhao G, Lu Y. Propylene epoxidation with O2 and H2: a high-performance Au/TS-1 catalyst prepared via a deposition-precipitation method using urea. Catalysis Science & Technology. 2013;3(11):2906-9.

[30] Fang Y, Jiang F, Liu H, Wu X, Lu Y. Free-standing Ni-microfiber-supported carbon nanotube aerogel hybrid electrodes in 3D for high-performance supercapacitors. RSC Advances. 2012;2(16):6562-9.

[31] Chen W, Sheng W, Zhao G, Cao F, Xue Q, Chen L, et al. Microfibrous entrapment of Ni/Al2O3 for dry reforming of methane: a demonstration on enhancement of carbon resistance and conversion. RSC Advances. 2012;2(9):3651-3.

[32] Chen W, Sheng W, Cao F, Lu Y. Microfibrous entrapment of Ni/Al2O3 for dry reforming of methane: Heat/mass transfer enhancement towards carbon resistance and conversion promotion. International Journal of Hydrogen Energy. 2012;37(23):18021-30.

[33] Li Y, Fang Y, Liu H, Wu X, Lu Y. Free-standing 3D polyaniline-CNT/Ni-fiber hybrid electrodes for high-performance supercapacitors. Nanoscale. 2012;4(9):2867-9.

[34] Zhao G, Hu H, Deng M, Lu Y. Microstructured Au/Ni-fiber catalyst for low-temperature gas-phase selective oxidation of alcohols. Chemical Communications. 2011;47(34):9642-4.

[35] Ling M, Zhao G, Chen W, Wang M, Xue Q, Lu Y. Microfibrous structured catalytic packings for miniature methanol fuel processor: Methanol steam reforming and CO preferential oxidation. International Journal of Hydrogen Energy. 2011;36(20):12833-42.

[36] Zhao G, Hu H, Deng M, Lu Y. Galvanic Deposition of Au on Paperlike Cu Fiber for High-Efficiency, Low-Temperature Gas-Phase Oxidation of Alcohols. ChemCatChem. 2011;3(10):1629-36.

[37] Mao J, Deng M, Chen L, Liu Y, Lu Y. Novel microfibrous-structured silver catalyst for high efficiency gas-phase oxidation of alcohols. AIChE Journal. 2010;56(6):1545-56.

[38] Zhao G, Hu H, Deng M, Ling M, Lu Y. Au/Cu-fiber catalyst with enhanced low-temperature activity and heat transfer for the gas-phase oxidation of alcohols. Green Chemistry. 2011;13(1):55-8.

[39] Gao L, Xue Q, Liu Y, Lu Y. Base-free catalytic aerobic oxidation of mercaptans for gasoline sweetening over HTLcs-derived CuZnAl catalyst. AIChE Journal. 2009;55(12):3214-20.

[40] Jiang F, Fang Y, Liu Y, Chen L, Xue Q, Lu Y, et al. Paper-like 3-dimensional carbon nanotubes (CNTs)-microfiber hybrid: A promising macroscopic structure of CNTs. Journal of Materials Chemistry. 2009;19(22):3632-7.

[41] Mao J, Deng M, Xue Q, Chen L, Lu Y. Thin-sheet Ag/Ni-fiber catalyst for gas-phase selective oxidation of benzyl alcohol with molecular oxygen. Catalysis Communications. 2009;10(10):1376-9.

[42] Tang Y, Liu Y, Zhu P, Xue Q, Chen L, Lu Y. High-performance HTLcs-derived CuZnAl catalysts for hydrogen production via methanol steam reforming. AIChE Journal. 2009;55(5):1217-28.

[43] Xue Q, Gao L, Lu Y. Sulfur-tolerant Pt/Gd2O3–CeO2–Al2O3 catalyst for high efficiency H2 production from autothermal reforming of retail gasoline. Catalysis Today. 2009;146(1–2):103-9.

[44] Wang M, Li J, Chen L, Lu Y. Miniature NH3 cracker based on microfibrous entrapped Ni-CeO2/Al2O3 catalyst monolith for portable fuel cell power supplies. International Journal of Hydrogen Energy. 2009;34(4):1710-6.

[45] Lu Y, Wang Y, Gao L, Chen J, Mao J, Xue Q, et al. Aerobic Oxidative Desulfurization: A Promising Approach for Sulfur Removal from Fuels. ChemSusChem. 2008;1(4):302-6.

[46] Lu Y, Chen J, Liu Y, Xue Q, He M. Highly sulfur-tolerant Pt/Ce0.8Gd0.2O1.9 catalyst for steam reforming of liquid hydrocarbons in fuel cell applications. Journal of Catalysis. 2008;254(1):39-48.

[47] Liu Y, Wang H, Li J, Lu Y, Wu H, Xue Q, et al. Monolithic microfibrous nickel catalyst co-modified with ceria and alumina for miniature hydrogen production via ammonia decomposition. Applied Catalysis A: General. 2007;328(1):77-82.

[48] Liu Y, Wang H, Li J, Lu Y, Xue Q, Chen J. Microfibrous entrapped Ni/Al2O3 using SS-316 fibers for H2 production from NH3. AIChE Journal. 2007;53(7):1845-9.

[49] Della Pina C, Falletta E, Rossi M. Highly selective oxidation of benzyl alcohol to benzaldehyde catalyzed by bimetallic gold–copper catalyst. Journal of Catalysis. 2008;260(2):384-6.

[50] Pangarkar K, Schildhauer TJ, van Ommen JR, Nijenhuis J, Kapteijn F, Moulijn JA. Structured Packings for Multiphase Catalytic Reactors. Industrial & Engineering Chemistry Research. 2008;47(10):3720-51.

[51] Kapteijn F, Nijhuis TA, Heiszwolf JJ, Moulijn JA. New non-traditional multiphase catalytic reactors based on monolithic structures. Catalysis Today. 2001;66(2–4):133-44.

[52] Reay D, Ramshaw C, Harvey A. Process Intensification, Second Edition: Engineering for Efficiency, Sustainability and Flexibility (Isotopes in Organic Chemistry): Butterworth-Heinemann; 2013.

[53] Chen J-F, Chen G-Z, Wang J-X, Shao L, Li P-F. High-throughput microporous tube-in-tube microreactor as novel gas–liquid contactor: Mass transfer study. AIChE Journal. 2011;57(1):239-49.

[54] Ajmera SK, Delattre C, Schmidt MA, Jensen KF. Microfabricated cross-flow chemical reactor for catalyst testing. Sensors and Actuators B: Chemical. 2002;82(2–3):297-306.

[55] Rao DP, Bhowal A, Goswami PS. Process Intensification in Rotating Packed Beds (HIGEE): An Appraisal. Industrial & Engineering Chemistry Research. 2004;43(4):1150-62.

[56] Zhang D, Zhang P-Y, Zou H-K, Chu G-W, Wu W, Zhu Z-W, et al. Application of HIGEE process intensification technology in synthesis of petroleum sulfonate surfactant. Chemical Engineering and Processing: Process Intensification. 2010;49(5):508-13.

[57] Zhou L, Guo Y, Yagi M, Sakurai M, Kameyama H. Investigation of a novel porous anodic alumina plate for methane steam reforming: Hydrothermal stability, electrical heating possibility and reforming reactivity. International Journal of Hydrogen Energy. 2009;34(2):844-58.

[58] Zhang Q, Xu J, Fan F, Sun D, Xu G, Zhang S, et al. Application of porous anodic alumina monolith catalyst in steam reforming of dimethyl ether: Cu/γ-Al2O3/Al catalyst degradation behaviors and catalytic activity improvement by pre-competition impregnation method. Fuel Processing Technology. 2014;119(0):52-9.

[59] Zhang Q, Fan F, Xu G, Ye D, Wang W, Zhu Z. Steam reforming of dimethyl ether over a novel anodic γ-Al2O3 supported copper bi-functional catalyst. International Journal of Hydrogen Energy. 2013;38(25):10305-14.

[60] Spiegel L, Meier W. Distillation Columns with Structured Packings in the Next Decade. Chemical Engineering Research and Design. 2003;81(1):39-47.

[61] Laso M, de Brito MH, Bomio P, von Stockar U. Liquid-side mass transfer characteristics of a structured packing. The Chemical Engineering Journal and the Biochemical Engineering Journal. 1995;58(3):251-8.

[62] Luna E, Tatarchuk B. Improvement of Indoor Air Quality Through The Development of Polymeric Microfibrous Material. dissertation, 2009.

[63] Bunyard C, Qin J, Waldroup DE, Zhang JG, Bunyard C, Qin J, et al., inventors; Bulk Enhancement For Airlaid Material. 2011 2011-6-30.

[64] Wood DE, Corp. C, inventors; Apparatus for manufacturing nonwoven textile articles. 1970 1970-10-20.

[65] Boich H-H, Kirsch A, Knitsch G, Gmbh C, inventors; Fibrous spun-bonded non-woven composite patent US5685757. 1997 1997-11-11.

[66] Yahiaoui A, Charles EBI, Bell DS, Secen NA, Kimberly-Clark Worldwide I, inventors; Coform material having improved fluid handling and method for producing patent 6296936 B1. 2001.

[67] Hong SH, Nuttall DA, Corporation K-C, inventors; Air/water hybrid former. 1982 1982-8-17.

[68] Qi Z, He C, Kaufman A. Effect of CO in the anode fuel on the performance of PEM fuel cell cathode. Journal of Power Sources. 2002;111(2):239-47.

[69] Li H, Wang H, Qian W, Zhang S, Wessel S, Cheng TTH, et al. Chloride contamination effects on proton exchange membrane fuel cell performance and durability. Journal of Power Sources. 2011;196(15):6249-55.

[70] Kortsdottir K, Lindström RW, Lindbergh G. The influence of ethene impurities in the gas feed of a PEM fuel cell. International Journal of Hydrogen Energy. 2013;38(1):497-509.

[71] Cheng X, Shi Z, Glass N, Zhang L, Zhang J, Song D, et al. A review of PEM hydrogen fuel cell contamination: Impacts, mechanisms, and mitigation. Journal of Power Sources. 2007;165(2):739-56.

[72] Zamel N, Li X. Effect of contaminants on polymer electrolyte membrane fuel cells. Progress in Energy and Combustion Science. 2011;37(3):292-329.

[73] Ma X, Yang D, Zhou W, Zhang C, Pan X, Xu L, et al. Evaluation of activated carbon adsorbent for fuel cell cathode air filtration. Journal of Power Sources. 2008;175(1):383-9.

[74] Jing F, Hou M, Shi W, Fu J, Yu H, Ming P, et al. The effect of ambient contamination on PEMFC performance. Journal of Power Sources. 2007;166(1):172-6.

[75] Nagahara Y, Sugawara S, Shinohara K. The impact of air contaminants on PEMFC performance and durability. Journal of Power Sources. 2008;182(2):422-8.

[76] Yang D, Ma J, Xu L, Wu M, Wang H. The effect of nitrogen oxides in air on the performance of proton exchange membrane fuel cell. Electrochimica Acta. 2006;51(19):4039-44.

[77] Gould BD, Baturina OA, Swider-Lyons KE. Deactivation of Pt/VC proton exchange membrane fuel cell cathodes by SO2, H2S and COS. Journal of Power Sources. 2009;188(1):89-95.

[78] Mohtadi R, Lee Wk, Van Zee JW. Assessing durability of cathodes exposed to common air impurities. Journal of Power Sources. 2004;138(1–2):216-25.

[79] Thoenes Jr D, Kramers H. Mass transfer from spheres in various regular packings to a flowing fluid. Chemical Engineering Science. 1958;8(3–4):271-83.

[80] Pfeffer R. Heat and Mass Transport in Multiparticle Systems. Industrial & Engineering Chemistry Fundamentals. 1964;3(4):380-3.

[81] Edwards MF, Richardson JF. Gas dispersion in packed beds. Chemical Engineering Science. 1968;23(2):109-23.

[82] El-Kaissy MM, Homsy GM. A Theoretical Study of Pressure Drop and Transport in Packed Beds at Intermediate Reynolds Numbers. Industrial & Engineering Chemistry Fundamentals. 1973;12(1):82-90.

[83] Langer G, Roethe A, Roethe KP, Gelbin D. Heat and mass transfer in packed beds—III. Axial mass dispersion. International Journal of Heat and Mass Transfer. 1978;21(6):751-9.

[84] Wakao N. Heat and Mass Transfer in Packed Beds; 1982.

[85] Dullien FAL. Porous media: fluid transprot and pore structure; 1992.

[86] Keybl J, Jensen KF. Microreactor System for High-Pressure Continuous Flow Homogeneous Catalysis Measurements. Industrial & Engineering Chemistry Research. 2011;50(19):11013-22.

[87] McMullen JP, Jensen KF. Rapid Determination of Reaction Kinetics with an Automated Microfluidic System. Organic Process Research & Development. 2011;15(2):398-407.

[88] Pimparkar K, Yen B, Goodell J, Martin V, Lee W-H, Porco J, et al. Development of a Photochemical Microfluidics Platform. Journal of Flow Chemistry. 2011;1(2):53-5.

[89] Marton CH, Haldeman GS, Jensen KF. Portable Thermoelectric Power Generator Based on a Microfabricated Silicon Combustor with Low Resistance to Flow. Industrial & Engineering Chemistry Research. 2011;50(14):8468-75.

[90] Kuhn S, Noel T, Gu L, Heider PL, Jensen KF. A Teflon microreactor with integrated piezoelectric actuator to handle solid forming reactions. Lab on a Chip. 2011;11(15):2488-92.

[91] Noël T, Kuhn S, Musacchio AJ, Jensen KF, Buchwald SL. Suzuki–Miyaura Cross-Coupling Reactions in Flow: Multistep Synthesis Enabled by a Microfluidic Extraction. Angewandte Chemie International Edition. 2011;50(26):5943-6.

[92] Vennela N, Mondal S, De S, Bhattacharjee S. Sherwood number in flow through parallel porous plates (Microchannel) due to pressure and electroosmotic flow. AIChE Journal. 2012;58(6):1693-703.

[93] Jiang P-X, Fan M-H, Si G-S, Ren Z-P. Thermal–hydraulic performance of small scale micro-channel and porous-media heat-exchangers. International Journal of Heat and Mass Transfer. 2001;44(5):1039-51.

[94] Wang Q-A, Wang J-X, Yu W, Shao L, Chen G-Z, Chen J-F. Investigation of Micromixing Efficiency in a Novel High-Throughput Microporous Tube-in-Tube Microchannel Reactor. Industrial & Engineering Chemistry Research. 2009;48(10):5004-9.

[95] Oliver G. Microsystem Engineering of Lab-on-a-chip Devices. 2nd ed; 2008.

[96] Ehrfeld W. Microreactors: new technology from modern chemistry. 1st ed; 2000.

[97] Hartman RL, McMullen JP, Jensen KF. Deciding Whether To Go with the Flow: Evaluating the Merits of Flow Reactors for Synthesis. Angewandte Chemie International Edition. 2011;50(33):7502-19.

[98] van Male P, de Croon MHJM, Tiggelaar RM, van den Berg A, Schouten JC. Heat and mass transfer in a square microchannel with asymmetric heating. International Journal of Heat and Mass Transfer. 2004;47(1):87-99.

[99] ACMC. [cited; Available from: http://www.appliedcatalysts.com/product_ACMC.htm

[100] Boger T, Heibel AK, Sorensen CM. Monolithic Catalysts for the Chemical Industry. Industrial & Engineering Chemistry Research. 2004;43(16):4602-11.

[101] Gadkaree KP. Carbon honeycomb structures for adsorption applications. Carbon. 1998;36(7–8):981-9.

[102] Fuertes AB, Marbán G, Nevskaia DM. Adsorption of volatile organic compounds by means of activated carbon fibre-based monoliths. Carbon. 2003;41(1):87-96.

[103] Crittenden B, Patton A, Jouin C, Perera S, Tennison S, Echevarria J. Carbon Monoliths: A Comparison with Granular Materials. Adsorption. 2005;11(1):537-41.

[104] Yates M, Blanco J, Avila P, Martin MP. Honeycomb monoliths of activated carbons for effluent gas purification. Microporous and Mesoporous Materials. 2000;37(1–2):201-8.

[105] Patton A, Crittenden BD, Perera SP. Use of the Linear Driving Force Approximation to Guide the Design of Monolithic Adsorbents. Chemical Engineering Research and Design. 2004;82(8):999-1009.

Chapter 2

Adsorption Experiments in Bench Scale

2.1. Introduction

Catalytic reactions and chemisorption are activated processes that require a minimum energy, i.e., activation energy (E_a), to allow the chemical process occur. In this case, the surface reaction rate plays an important role in determining the overall reaction rate. In most reaction systems, the surface reaction is usually coupled with the mass and heat transport process and together they determine the apparent order of reaction and reaction rate. Unlike the chemical reaction, the physisorption is not an activated process, and its surface adsorption and reaction rates are adequately high so that the overall rate of adsorption is always controlled by mass transfer, rather than by the intrinsic kinetics [1]. In other words, in the physisorption process, the mass transport is decoupled with the surface reaction; in addition, for trace gas adsorption, the heat effect is also negligible. This characteristic makes the physisorption a more appropriate process (when compared with the reaction process) to investigate the mass transport efficiency of a contacting system via analysis of the transient adsorbent uptake curve (i.e., breakthrough curve). The slope or sharpness of the breakthrough curve directly reflects the mass transfer efficiency of sorbent systems.

In this work, n-hexane was selected as the adsorbate to conduct breakthrough tests. The breakthrough data was fitted by the Modified Wheeler-Jonas model to obtain the mass transfer coefficient. Breakthrough tests for ACF-MFES, packed bed, and composite beds were conducted, and their performances were compared. Various factors, such as the particle size, fiber size, void fraction, etc., that influence the overall adsorption rate in the packed bed and ACF-MFES were investigated. The mechanism that enhances the contacting efficiency of ACF-MFES was examined by experimental and theoretical analysis.

2.2. Experimental details

2.2.1. Material

Bi-composite polymeric fiber (linear low density polyethylene on polyethylene terephthalate) was obtained from Invista Company. The ACF was obtained from Toyobo Co., Ltd., and the activated carbon particulates (ACP) were purchased from PICA (now Jacobi Carbon). The bulk density of the ACP is 0.54g/cc, while the bulk density of the ACF felt is 0.05 g/cc. The ACP was received in the form of 6×12, 12×20, and 60×140 mesh size particles. The coarse particles were ground and sieved using a set of standard sieves to obtain the following particle size ranges: 20×35 (0.84-0.50 mm), 35×50 (0.50-0.30 mm), and 50×60 (0.30-0.25 mm) mesh fractions. The fine particles (60×140mesh) were directly sieved to 60×80 (0.25-0.18 mm) and 80×140 (018-0.10 mm) mesh size particles. Glass beads (Biospec products) were used as the bed support media. γ-Al_2O_3 (Alfa-Aesar) was used as an inert diluent to adjust the dilution ratio of the packed bed. The dispersant, Cruwik Syn, was obtained from Crucible Chemical Company. The hexane gas cylinder (0.75% Hexane in nitrogen) and breathing air cylinder were obtained from Airgas Inc.

2.2.2. Characterization

The properties of ACF and ACP were analyzed with the N_2 adsorption method using Autosorb-1 (Quantachrome Instruments), and the results are presented in Table 2.1. The ACF's

BET surface area and pore volume are higher than PICA carbon, while the average pore diameter of ACF is smaller than that of PICA carbon. The micropore size distribution of activated carbon was also analyzed by the Dubinin–Astakhov (D-A) method. The pore size distribution for Toyobo ACF is shown in Figure 2.1. The majority of pores in ACF are micropores (<2nm) [2], and that the pore size distribution is unimodal and quite narrow. The AC particle distribution in ACF-MFES was observed by SEM. Images of the surface and cross-section of ACF-MFES are shown in Figure 2.2 (a) and (b), respectively. The particle distribution in the entire 3-D network is uniform. The thermal properties of bicomponent polymers (LLDPE/PET) were examined by differential scanning calorimetry. The result (Figure 2.3) shows that the melting points for the sheath and core polymer materials are 125˚C and 250˚C, respectively.

Table 2.1 Properties of activated carbon product

Parameters	PICA	Toyobo ACF
Specific surface area (m^2/g)	1261	1481
Specific pore volume (cc/g)	0.6	0.71
Average pore dia. (nm)	1.92	1.76

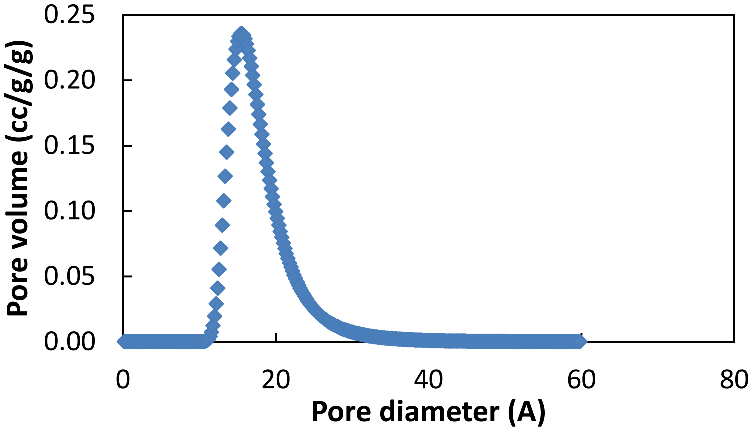

Figure 2.1 Pore size distribution for Toyobo ACF

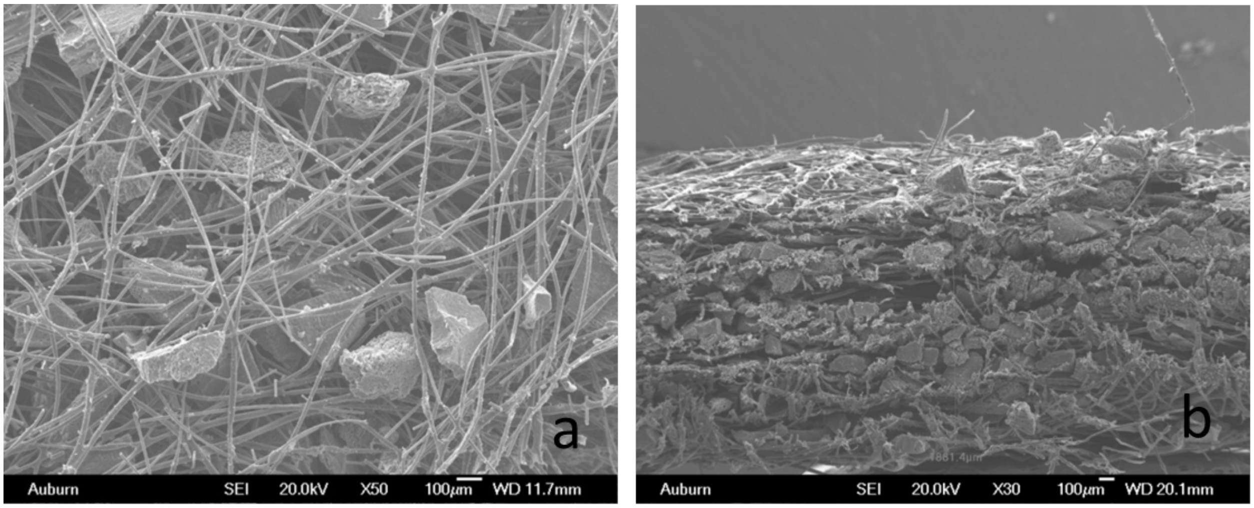

Figure 2.2 (a) The surface of ACF-MFES (b) cross-section of ACF-MFES

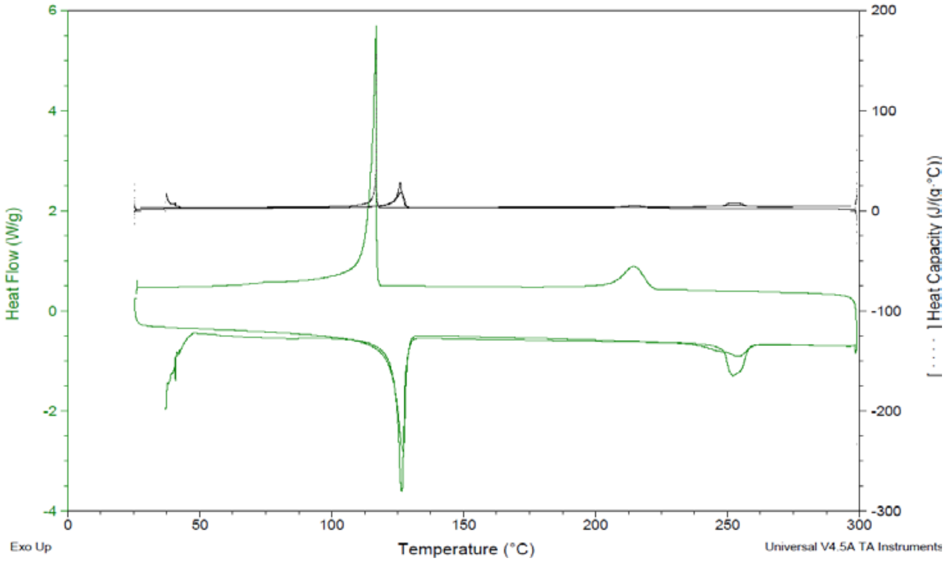

Figure 2.3 Differential scanning calorimetry (DSC) analysis of bicomponent fiber

2.2.3. Preparation of ACF-MFES

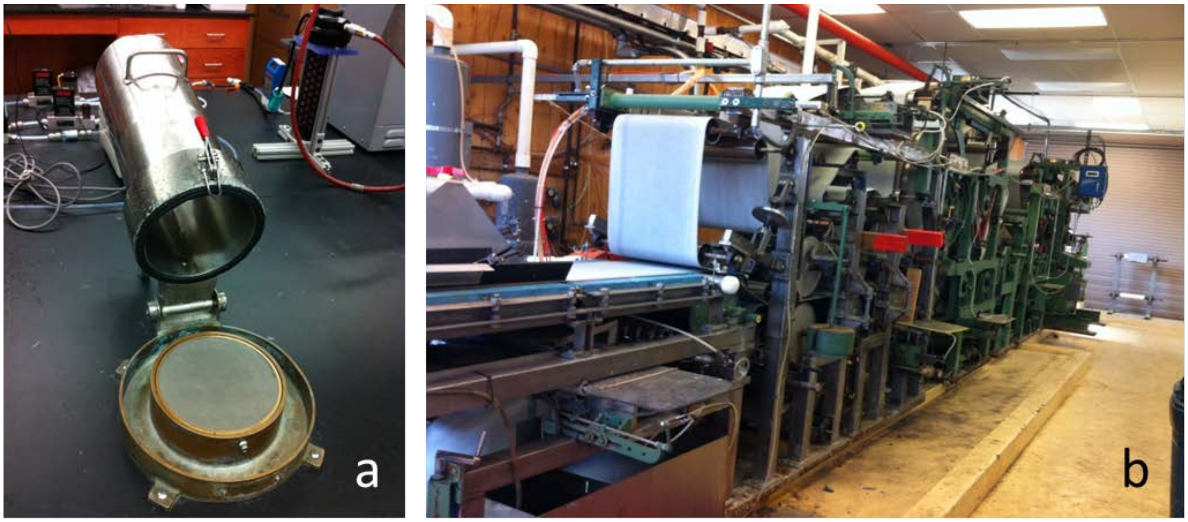

Figure 2.4 (a) 6.25” TAPPI hand sheet former; (b) 20” wide continuous paper making machine at Auburn University

The ACF-MFES was prepared by the wet lay method, which is similar to the paper-making process. Figure 2.4 (a) shows a TAPPI hand sheet former, which was used to make ACF-MFES samples in this study. Figure 2.4 (b) shows a 20” wide continuous paper making machine, which is capable of producing ACF-MFES nonwovens on a large scale.

The general process of making ACF-MFES samples using the hand former is described as follows. First, 5ml of dispersant (Cruwik Syn) was added into one liter of high viscosity water, and then 3.0g fiber (blend of polymer fiber and ACF) was added and dispersed in the water through continuous agitation. With the aid of dispersant, the fibers are well dispersed in 5min with low speed stirring. The suspension was then transferred to the head box of the hand sheet former. 6.0g ACP (0.18-0.25mm) were added to the suspension, and dispersed thoroughly with the hand dasher. The excess water was then drained, and the ACF-MFES web was formed on the wire screen. Finally, the web was dried and bonded in an oven through using a hot air stream.

The resulting ACF-MFES sheet had approximately 10-15 vol% carbon, 2-5 vol% fiber with the remaining volume being void.

2.2.4. Experimental setup

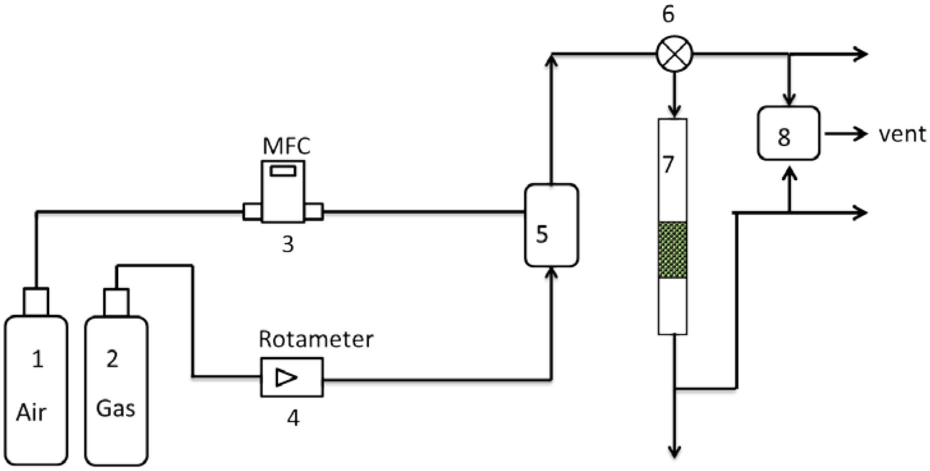

1. Compressed air; 2. Hexane gas cylinder; 3. Mass flow controller; 4. Rotameter; 5. Mixing chamber; 6. Three way valve; 7. Adsorption column; 8 MiniRae 3000 gas detector

Figure 2.5 Schematic diagram of apparatus

Figure 2.5 shows a schematic diagram of the apparatus for the breakthrough test. The setup was primarily composed of three sections: the gas generation section, adsorption section and analysis section. For gas generation, various methods such as cylinder gas, syringe injection, and liquid bubblers are available. The bubbler is the most widely used method for generating VOC gas in adsorption tests [3-5]; it uses liquid adsorbent, which is less expensive than mixture gas, but requires high-quality flow and temperature control systems. In this study, both the bubbler and cylinder gas were attempted. It was found that the gas cylinder can deliver very stable challenge gas over a long period [6, 7], whereas the bubbler method is sensitive to the temperature and pressure change in the systems, leading to a considerable concentration fluctuation. Therefore, cylinder gas was used for the hexane breakthrough tests. The flow rates of gas and dilution air were controlled by two mass flow controllers (Alicat Scientific Inc.). A 5h hour blank test through an empty or inert (Al_2O_3) filled column was conducted to verify the stability of the challenge gas; it was observed that the deviation was less than 0.5%. A large glass chamber was placed before the adsorbent column to enhance the gas and air mixing.

For the test section, the adsorbent column used was a glass reactor of 25.4cm (10") long and 1.9cm (0.75") diameter. The configuration of bed packing was as shown in Figure 2.6. A sintered glass frit located in the middle of the column acted as a sorbent support. A thin layer of ACF-MFES media was placed beneath the granular sorbent bed as a polishing layer. On the top, a glass bead layer was used to produce a uniform flow pattern as opposed to an incoming parabolic flow pattern. In the analysis section, a MiniRAE-3000 VOC detector (RAE systems Inc.) was used to measure and record the hexane concentration in the inlet and outlet. The device was calibrated with a 100ppm isobutylene calibration gas prior to each use.

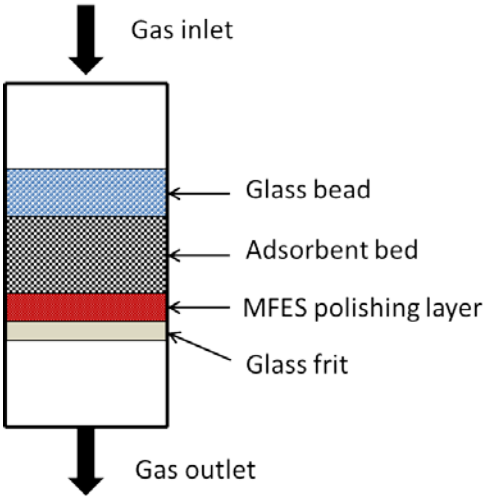

Figure 2.6 Illustration of sorbent packing in the column

2.3. Results and Discussion

2.3.1. Pressure drop of media

The air permeability is a large concern for filter media; a high pressure drop across the media can overload the air handler and reduce airflow, but more importantly, it will consume a considerable amount of energy. The inert polymeric fibers act as the support material in the ACF-MFES media, but they add extra flow resistance and thereby need be minimized. For most fibrous media, the pressure drop across the media has an inverse relationship with the fiber dimension. This is a direct result of the fact that the external surface area is inversely proportional to the fiber diameter. To investigate the effect of fiber dimension on the media's permeability, two different size of fiber (13µm and 19µm) were used. In each experiment, the media contained same amount of sorbent and fiber; the only variable was the fiber size. As shown in the Figure 2.7, with the decrease of fiber diameter, the pressure drop across the media increases significantly. Considering the pressure drop penalty, 19µm fiber was determined most appropriate for use in the later research. It is worth noting that the pressure drop across the ACF-MFES was much lower than across the packed bed with same size of particulates due to its high voidage (typically over 0.8). The pressure drop across the packed bed with particle size of 0.215mm (60×80mesh) can reach up to 3000 Pa for a 1 cm bed length at 1.5m/s face velocity.

In the fiber diameter comparison experiments, the particle diameter was kept constant at 210 µm. In the particle diameter comparison experiments, the fiber diameter kept constant at 19 µm.

	Fiber or particle diameter (µm)	Surface area to volume ratio (m^2/m^3)	Surface increment (%)	ΔP increment (%)
Fiber diameter	19	2.10×10^5	As reference	As reference
	13	3.08×10^5	46	55
Particle diameter	400	1.5×10^4	As reference	As reference
	280	2.1×10^4	40	9.5
	210	2.8×10^4	87	20.5
	140	4.3×10^4	186	35

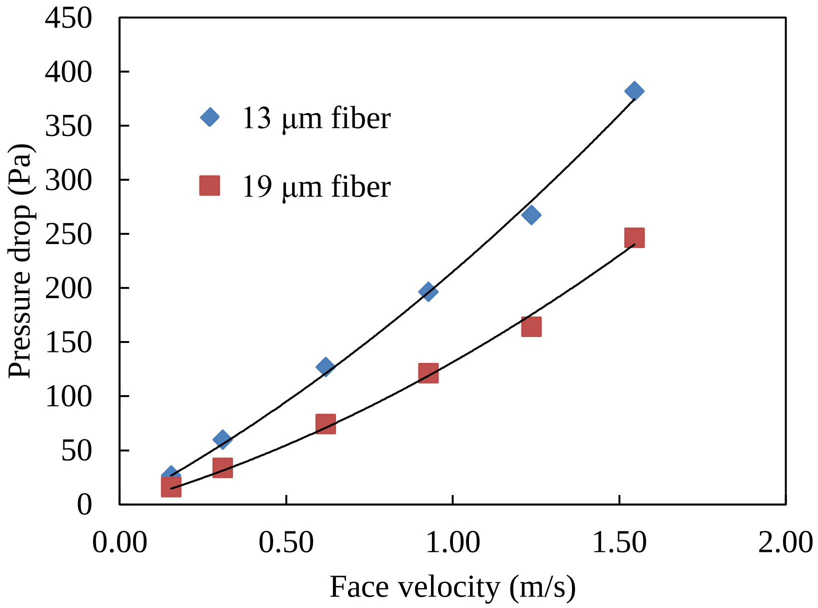

Figure 2.7 Comparison of pressure drop across the media made from different fiber diameters

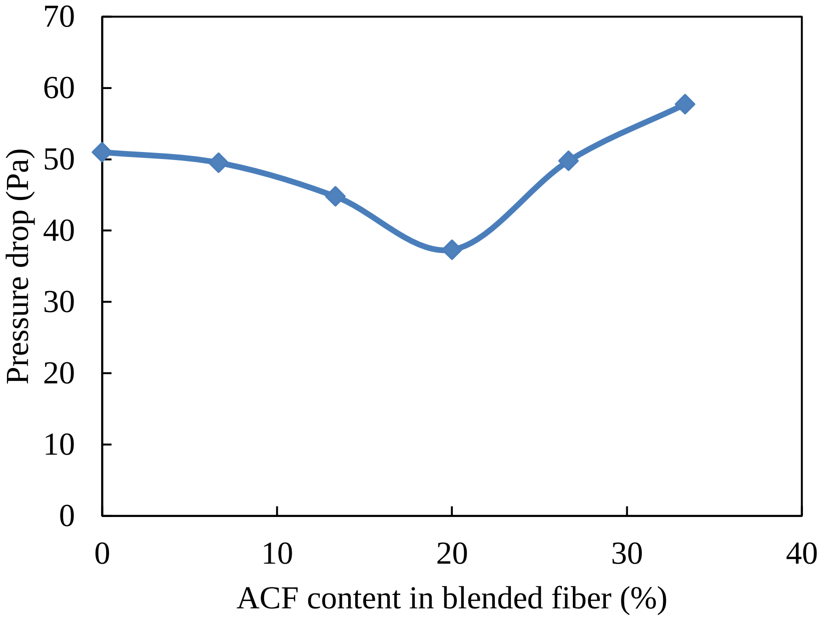

Figure 2.8 Pressure drop versus ACF content in blended fiber at face velocity of 0.5m/s

Figure 2.8 shows the effect of ACF content on the media pressure drop. In each test, the media contained the same weight of fiber (3.0g fiber) and sorbent (6.0g AC); the only variable was the content of ACF in the blended fiber. It was found that the pressure drop across the media decreased as the ACF content increased from zero to 20%, but with further increase of ACF content, the pressure drop increased. It was also found that 10-20% ACF is the optimum formula to achieve quality ACF-MFES media in the web forming and sintering steps. In future discussion, the default ratio of ACF to bicomponent fiber in ACF-MFES is 1:5, i.e., 0.5 g ACF and 2.5 g bicomponent fiber.

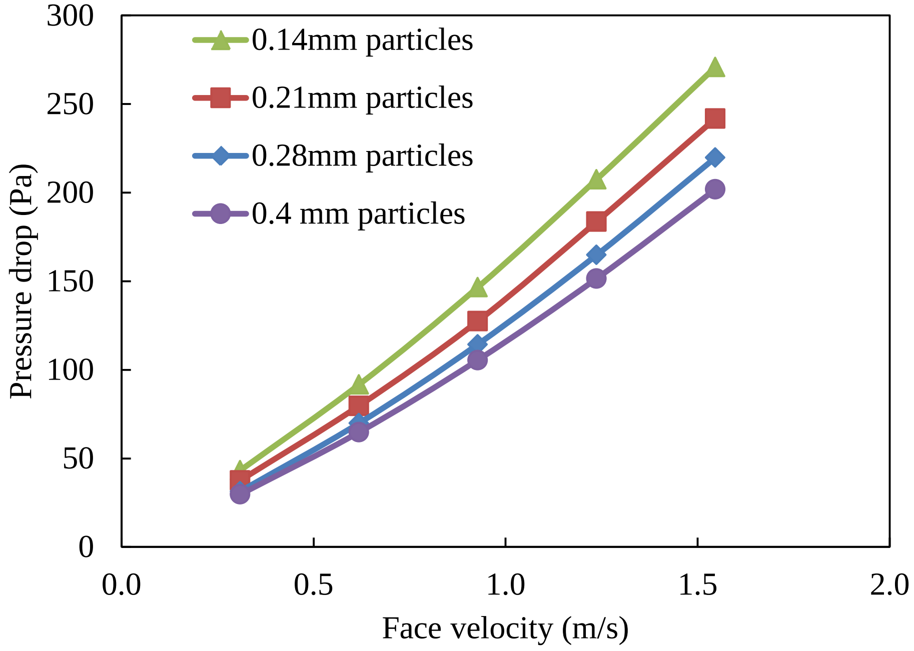

Figure 2.9. Pressure drop versus face velocity for different AC particle size

In addition to the dimension of fiber, the dimension of the particulates also has influence on the media’s permeability. However, even though the volume fraction of particulate is relatively high, the total external surface area of particulates is less than that of fiber. As we know, at laminar flow conditions (Re<10), the viscous friction force is proportional to the external surface area, while the inertia force is not significant. Therefore, it can be anticipated that the impact of particulate size on pressure drop will be smaller than that of fiber size. This was verified by a set of experiments; in each test, the only variable was the particulate size, with 0.14, 0.21, 0.28 and 0.40 mm being tested. As shown in Figure 2.9, the pressure drop only slightly increased as particulate size decreased. This indicates that the major contributor to flow resistance in ACF-MFES media is the fiber rather than the particulates at low flow rate. However, at high flow rate, the contribution of particulates will be significant because inertia loss will become an important factor.

2.3.2. Adsorption equilibrium isotherm

The adsorption isotherm was obtained by the dynamics method using the same process as the breakthrough test within a gas concentration range of 5ppm to 300ppm and at temperature of 21±1˚C. The total adsorption amount was calculated from the breakthrough curve by integrating the area above the curve using MATLA's trapezoidal numerical integration method (Matlab function: trapz). The calculation equation is as follows:

$$W_e = \frac{Q}{W_b}\int_0^{\infty}(C_0 - C)dt \tag{2.1}$$

Where W_e is the equilibrium adsorption amount in kg/kg sorbent, Q is the flow rate in m^3/min, W_b is the weight of the sorbent bed in kg, and C is the hexane gas concentration in kg/m^3.

The data is best fitted by Freundlich equation (Equation 2.2), and the fitting curve is shown in Figure 2.10. The fitting equation shows that the value of parameter n is 7.09, indicating that the isotherm of hexane adsorption onto activated carbon is highly favorable [1].

$$W_e = K_f C^{1/n} \tag{2.2}$$

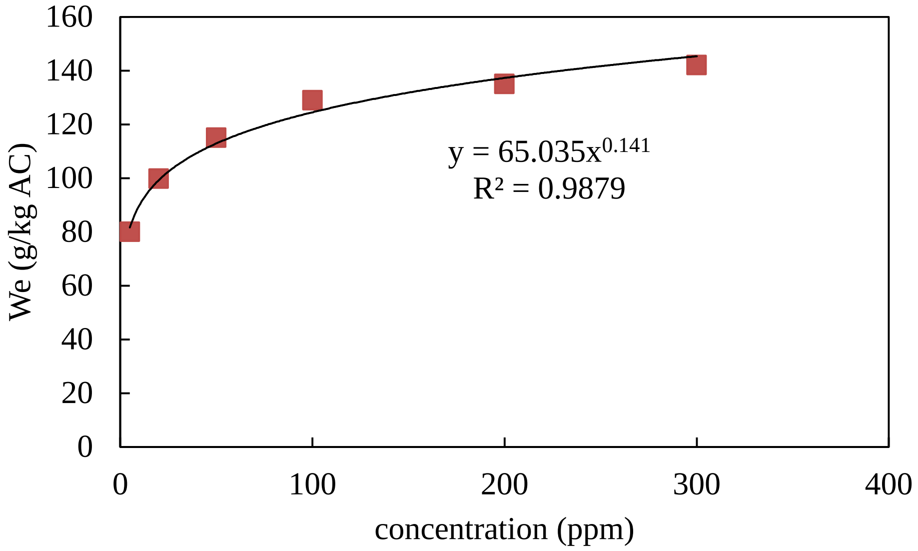

Figure 2.10 Experimental equilibrium data of hexane adsorption onto PICA activated carbon

2.3.3. Breakthrough data analysis and performance determination

Experimental breakthrough data was obtained for various ACF-MFES media, packed bed media and composite bed media. The experimental conditions and bed dimensions are summarized in Table 2.2. The composition and properties of the various beds (media) are described in Table 2.3.

Table 2.2 Experimental bed dimension and flow conditions

Parameters	Value
Bed diameter (mm)	19.05
Bed length (mm)	12.7
Weight of adsorbent (g)	1.72
Temperature (˚C)	21 (±1)
Pressure (atm)	1.0
Feed hexane concentration (ppm)	300ppm
Inlet gas flow rate (LPM)	10

Inlet gas face velocity (m/s)	0.6

Table 2.3 Summary of bed composition and properties (typical value)

Bed type	ACP vol.	Fiber vol.	Bed voidage	Basis weight (g/m^2)	Thickness (mm)	Density (kg/m^3)
PB	0.6	NA	0.4	NA	NA	480
MFES	0.1	0.05	0.85	500	4.5	130
ACF felt	NA	0.08	0.92	210	3	70
ACF cloth	NA	0.45	0.45	200	0.5	390

2.3.3.1. Performance parameters

The overall performance of sorbent media needed to be evaluated using many factors, such as the initial removal efficiency (E_0), saturation capacity (τ), breakthrough time (t_b), pressure drop, weight, and volume. In this study, the most significant factor is the contacting efficiency of the sorbent media. Two parameters, the pseudo adsorption rate constant (K') and heterogeneous contacting efficiency (η), are used to compare sorbents' contacting efficiency.

2.3.3.1.1. Adsorption rate constant

The adsorption rate constant K' is obtained by regressing the experimental breakthrough data using the modified Wheeler's equation (equation 2.4), which was first obtained by Yoon [8]. Yoon used the term $\ln\left(\frac{P}{1-P}\right)$ to replace the term ln(P) in the original Wheeler's equation, where P is the dimensionless effluent concentration defined as $P=C/C_0$. The modified equation can fit the experimental data in the entire S shape breakthrough curve, while the original only fit in the low penetration region.

$$\log\left(\frac{P}{1-P}\right) = 0.434K't - 0.434K'\tau \tag{2.4}$$

Where

$$K' = \frac{C_0}{\rho_b W_e} k_G \alpha \tag{2.5}$$

$$\tau = \frac{W_e W_b}{C_0 Q} \tag{2.6}$$

Equation 2.5 indicates that the adsorption rate constant (K') is directly proportional to the system's overall volumetric mass transfer coefficient ($k_G\alpha$). Therefore, using parameter K' to compare the contacting efficiency of different system is straightforward. However, the parameter K' does not include the pressure drop information, which is also an important factor for contacting efficiency.

2.3.3.1.2. Heterogeneous contacting efficiency

The heterogeneous contacting efficiency (η) is an important concept in this study. The parameter η combines the mass transfer and momentum transfer (pressure drop) into a single parameter. The value of η can be considered the indicator of contacting efficiency of system. The definition and derivation of η are briefly discussed below.

When a process (such as a reaction or an adsorption process) is in the mass transfer-limited regime, the gas phase mass balance for reactant A in a packed bed is given by [9]

$$u_0 \frac{dC_A}{dz} = k_G \alpha C_A \tag{2.7}$$

Integrating, with $C_A=C_0$ at z=0, yields

$$\frac{C_A}{C_0} = \exp\left(-\frac{k_G \alpha}{u_0} \cdot z\right) \tag{2.8}$$

Rearranging the equation gives

$$-log(1-E) = 0.434 \frac{k_G \alpha}{u_0} \cdot L \tag{2.9}$$

Where E is removal efficiency or conversion defined as $E = \frac{C_0 - C_A}{C_0}$, and L is the length of packed bed.

On the other hand, according to Ergun equation, the pressure drop of packed bed is

$$\frac{\Delta P}{\rho u_0^2} = \frac{2f}{d_p} \cdot L \tag{2.10}$$

Where f is the friction factor.

Eliminating the term L (which is not an inherent property of bed) by taking the ratio of equation 2.9 to 2.10 gives the expression of η

$$\eta = \frac{-\,log(1-E)}{\left(\frac{\Delta P}{\rho u_0^2}\right)} = 0.434 \frac{k_G \alpha d_p}{2 f u_0} \tag{2.11}$$

The parameter η, by definition, represents the system’s conversion ability with a certain pressure drop; it is only dependent on the bed’s inherent properties (such as particle size, voidage, structural uniformity), but is independent of the bed length. It is evident that the higher the η value the better the bed’s conversion capability, and the smaller the pressure drop penalty. Therefore, η is a useful criterion to compare the overall contacting efficiency of different systems such as packed beds, fibrous media, monolithic reactors, microchannel reactors, etc. The value of η can be readily obtained from experimental data provided that the system's conversion and pressure drop are measured.

2.3.3.2. Acquisition of performance parameters

Some important performance parameters can be obtained from the experimental breakthrough data. According to the modified Wheeler's model, the data was plotted as $\log(\frac{P}{1-P})$ versus time as shown in Figure 2.11. The data points were then fitted by linear equation, and the linear equation was expressed as y=ax-b. The linear plot of the breakthrough curve is more convenient for the acquisition of the performance parameters as shown in Figure 2.11, because most of these parameters can be directly ascertained from the figure. Table 2.4 shows the formulas or methods used to obtain the values of performance parameters from the information on the plot.

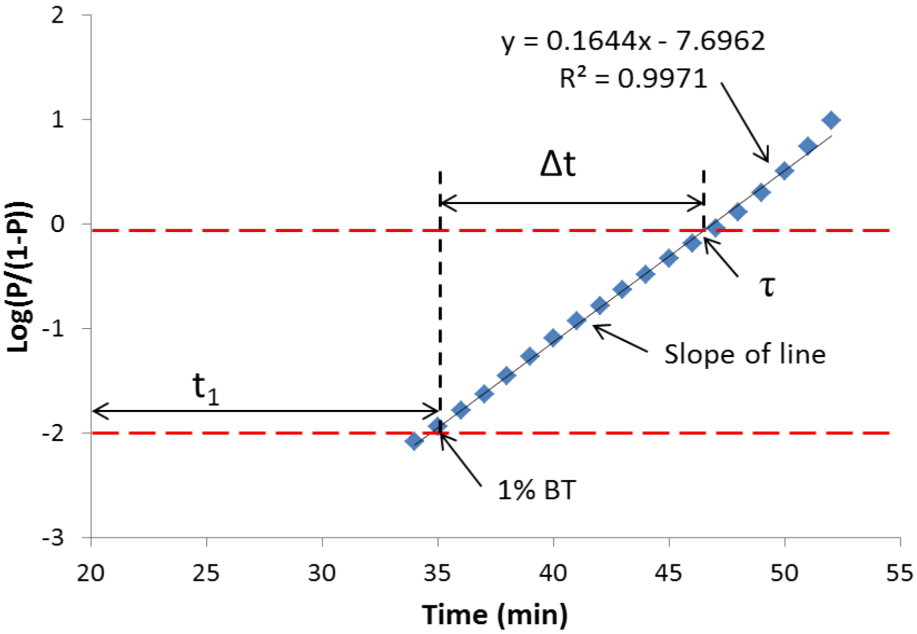

Figure 2.11 Liner plot of breakthrough data using modified Wheeler's model

Table 2.4 Calculation equations of performance parameters

Parameters	Expression
Fitting equation	y=ax-b
K'	a/0.43
τ	b/a
Bed utilization (%) [a]	$(t_1/\tau) \times 100\%$
Critical bed length [a]	Δt/τ
t_{b1} (2-log removal) [b]	Intersection of y=-2 and the fitting line
t_{b10} (1-log removal) [b]	Intersection of y=-1 and the fitting line

[a] assuming the defined breakthrough point is 1%

[b] t_{b1} denotes 1% breakthrough time, t_{b10} denotes 10% breakthrough time

2.3.4. Breakthrough test results

2.3.4.1. Comparison of various beds

To demonstrate the high contacting efficiency of the ACF-MFES bed, its breakthrough performance was compared with that of a traditional packed bed (PB) and of activated carbon fiber fabrics (ACF felt and ACF cloth), which are considered the most efficient adsorbent media. The test conditions, L=0.5” (1.27 cm), C_0= 300ppm, u_0= 0.6m/s, and T=21˚C, remained constant for each attempt.

Figure 2.12 shows the experimental breakthrough curve of the packed bed. Figure 2.14 shows the breakthrough curve of the ACF felt, ACF cloth, and ACF-MFES. For demonstration purposes, the linear plots of the breakthrough curves are shown in Figure 2. **13** and Figure 2.15. In later discussion, only the traditional breakthrough curve will be depicted, and the linear plot will be omitted. From the linear plots and the regression equations, we can see that the R^2 value is very close to unity, indicating that the experimental data agrees very closely with the model.

Table 2.5 gives a summary of the breakthrough performance of various sorbent beds. From the table, we can see that the K’ value for packed beds is small, only 0.27 min^{-1}, which is approximately 1/10 of that of ACF-MFES (3.03 min^{-1}). This ratio roughly agrees with the ratio of α_p (particle’s surface area to volume ratio) for the two beds. The ACF felt had the greatest experimental K’ value, 5.55 min^{-1}, which is 1.83 times that of the ACF-MFES. However, the fiber diameter of ACF is 0.01 mm (10 µm), which is only 1/20 of the particle size of ACF-MFES, indicating that the α_p of ACF is 20 times greater than that in ACF-MFES. This phenomenon will be explained in next section.

Another interesting result observed is that the K’ for ACF-cloth (only 1.45 min^{-1}) was much smaller than that of the ACF felt even though they are comprised of exactly the same fiber. It was determined that this difference was primarily caused by the different bed structures, and it will be discussed later in more detail.

Table 2.5 provides some other performance parameters including the breakthrough time (t_b), initial removal efficiency, and pressure drop. Overall, the ACF-MFES is the best contacting system because it has a high removal efficiency and relatively low pressure drop.

The last column in the table shows the heterogeneous contacting efficiency of four contact systems. The ACF-MFES has the greatest value of η, showing that it has a good balance between conversion and pressure drop. In addition, the ACF cloth has a surprisingly low value of η (1.11×10^{-3}), which is one order of magnitude smaller than that of ACF-MFES.

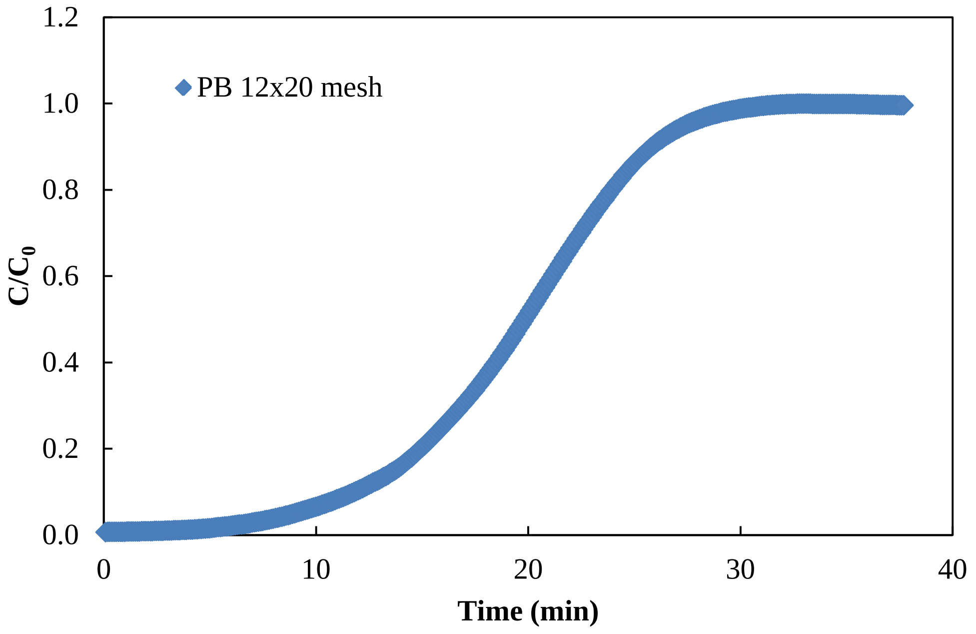

Figure 2.12 Experimental breakthrough curve of a packed bed with 12×20 mesh particle size

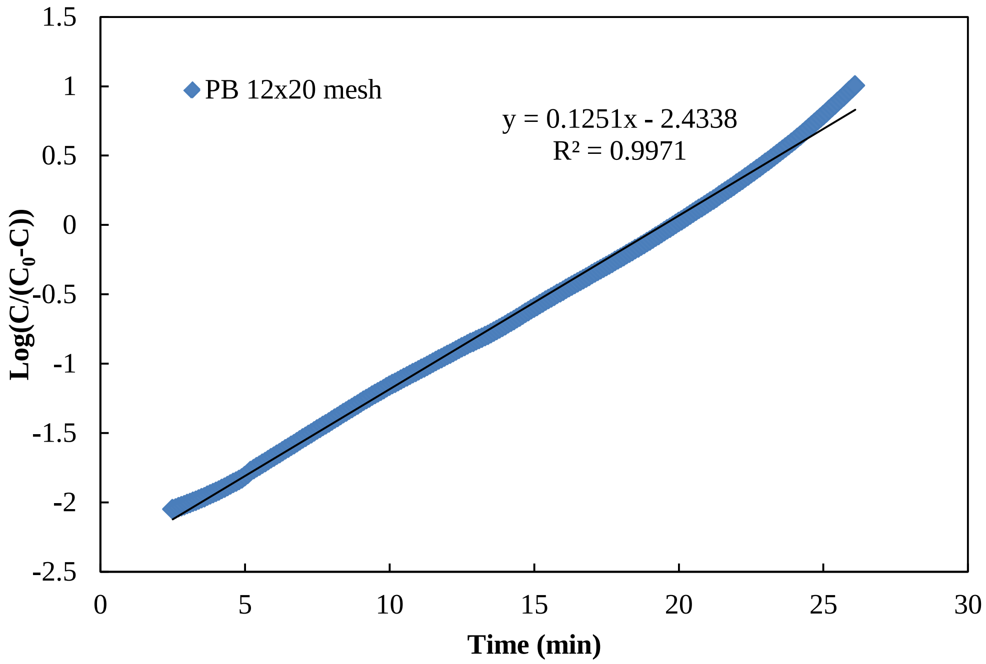

Figure 2.13 Linear plot of the breakthrough curve of a packed bed

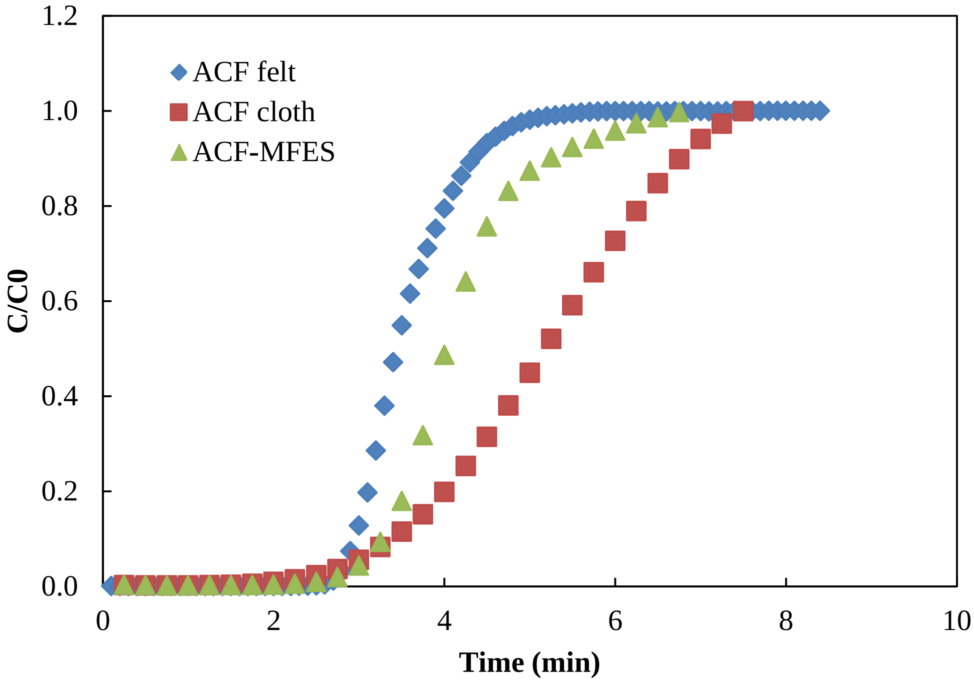

Figure 2.14 Experimental breakthrough curves of ACF felt, ACF cloth, and ACF-MFES bed

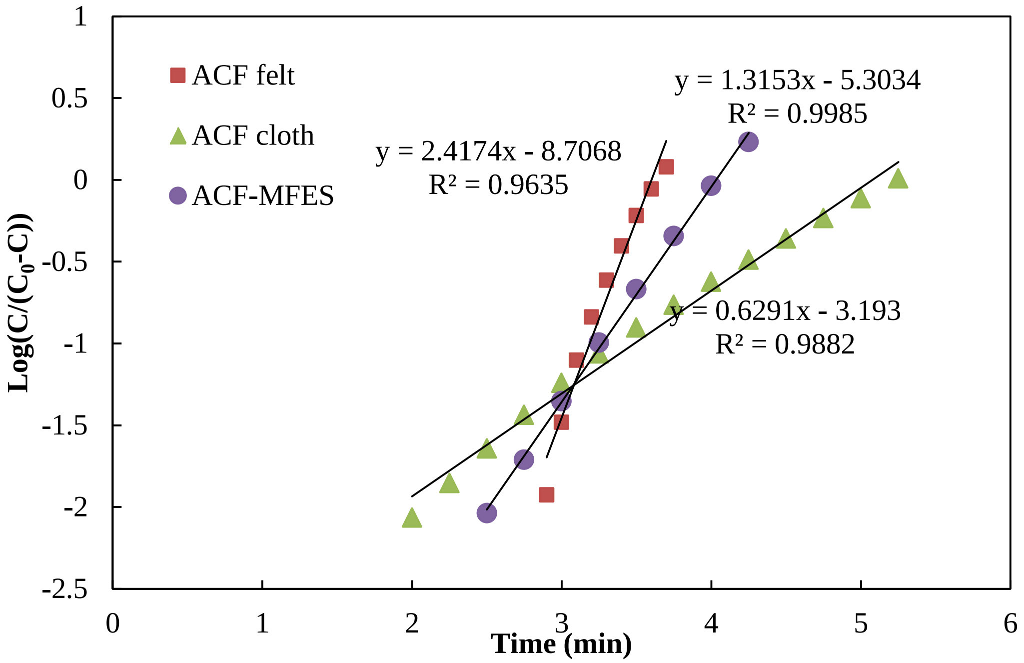

Figure 2.15 Linear plot of breakthrough curve for ACF felt, ACF cloth, and ACF-MFES

Table 2.5 Comparison of breakthrough performance of various sorbent beds

Bed type	Particle size (mm)	t_{b1} (min)	K' (min^{-1})	E_0	ΔP (Pa)	$\eta\times10^3$ (dimensionless)
PB 12×20	1.26	3.4	0.27	2.4-log	169	6.13
ACF felt	0.01	2.7	5.55	8.7-log	405	9.28
ACF cloth	0.01	1.9	1.45	3.2-log	1232	1.11
ACF-MFES	0.21	2.5	3.03	5.3-log	210	10.9

2.3.4.2. Effect of structure uniformity

The experimental results have shown that the ACF-felt and ACF-cloth have very different contact efficiencies, even though they are comprised of exactly the same fiber. The only explanation is that they have very different structures. To observe the structure of the media, SEM analysis was used.

Figure 2.16 shows the micro structures of ACF-MFES (a), ACF felt (b), and ACF cloth (c & d). The particles and fibers in ACF-MFES are randomly and uniformly distributed due to the use of the wet lay process. The fiber distribution in ACF felt is also uniform (the local fiber density in any differential space is almost same). However, in the ACF cloth, the fibers (filaments) are first converted to yard, and are then woven into the fabric. The fiber distribution in ACF cloth is not random, but shows obvious regularity. The local fiber density within the yarn is much higher than that in the void space between yarns. These differences in fiber distribution lead to different flow conditions, and hence different contacting efficiency, when a fluid flows through the ACF felt and ACF cloth beds.

When fluid flows through a uniform structure (such as ACF felt), it flows around each fiber, and has an equal chance to come in contact with each fiber. However, when the fluid flows through the ACF cloth, due to the differences in local fiber density, the fluid tends to flow through the spaces with low fiber density. A flow with this velocity profile in ACF cloth leads to significant channeling flow. The contacting chance and time between the fluid and the fibers are significantly reduced. Therefore, the nonuniformity of structure is the primary reason ACF cloth's lower contacting efficiency when compared to the ACF felt.

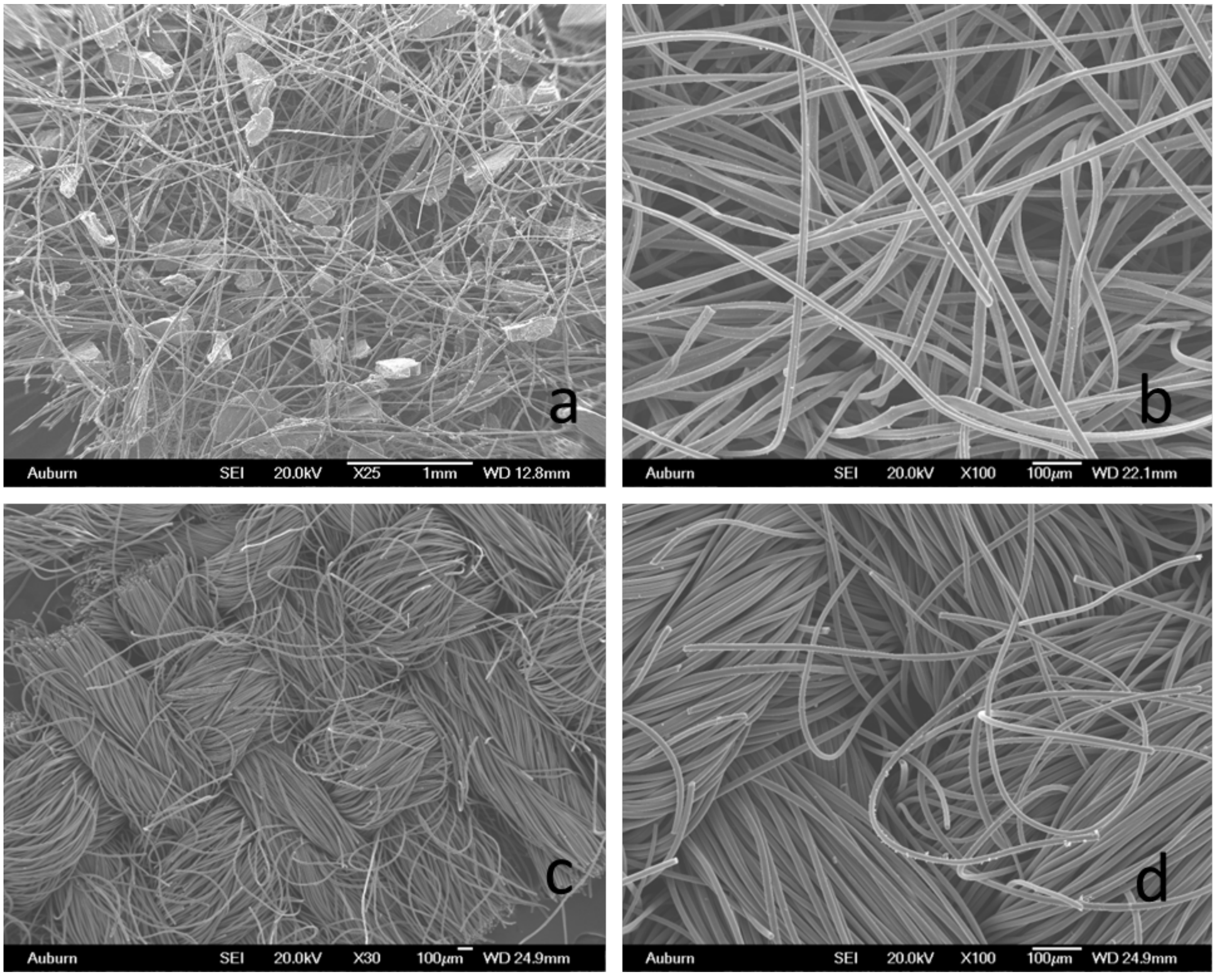

Figure 2.16 SEM image of ACF-MFES media (a), ACF felt (b), and ACF cloth (c & d)

Above discussions demonstrate that structure uniformity is a very important factor for a contact system to achieve its maximum contacting efficiency. The ACF-MFES has inherent structure uniformity due the use of the wet laid process. The particle and fiber distribution in ACF-MFES is uniform in the entire 3-D network, as shown in Figure 2.2. This structural uniformity can explain the observed experimental result that the mass transfer efficiency in ACF-MFES is higher than that in a packed bed with same particle size.

Figure 2.17 shows the experimental breakthrough curves for ACF-MFES and packed beds with same particle size (60×80 mesh). The K’ value for ACF-MFES is 2.72 min^{-1}, while it is only 1.98 min^{-1} for the packed bed. The reason that the packed bed has a lower value of K' is because the non-uniformity of structure in the packed bed causes significant channeling flow. In the packed bed, as particle size decreases, the chance of forming a particle cluster increases. This is because the small particles have a higher surface energy, so they tend to aggregate to release the energy. Another reason for cluster formation could be the higher pressure drop in small particle beds; the high pressure drop could compress the particles and make them adhere to one another [3].

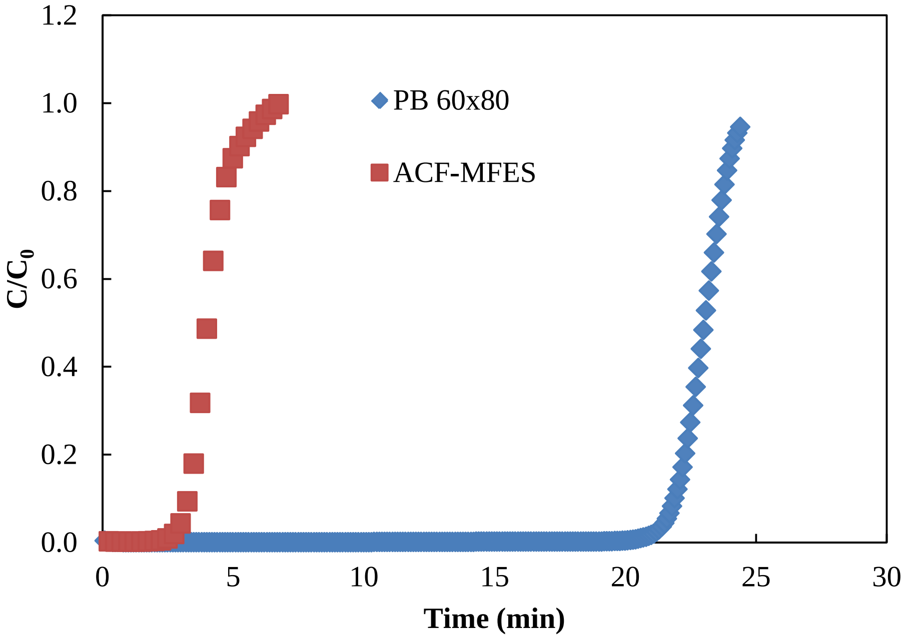

Figure 2.17 Comparison of ACF-MFES and PB with same particle size (60×80mesh)

2.3.4.3. Effect of particle size on the adsorption performance

The particle size is an important design parameter for a contacting system; it has a substantial effect on both external diffusion and internal diffusion resistance. Generally, decreasing the particle size can increase the particle's surface area to volume ratio and decrease the diffusion distance inside the particle, and therefore increase the mass transfer rate. However, the experimental results show that for a fine particle bed, further decreasing the particle size cannot achieve the expected improvement in mass transfer rate. In this study, the effect of particle size on various contact systems (PB, MFES, and ACF felt) was studied, and results were compared.

Figure 2.18 shows the experimental breakthrough curves for packed beds with various particle sizes. In this set of experiments, five different mesh size particles were used: 6×12, 12×20, 20×35, 50×60 and 60×80 mesh. The corresponding average particle sizes were 2.52, 1.26, 0.67, 0.28, and 0.22 mm, respectively. Excepting the particle size, all other experimental conditions were the same. The results are summarized in Table 2.6 . As shown in the table, as particle size decreased, the adsorption rate constant K' increased. Figure 2.19 shows the correlation between K' and d_p. The value of K' is roughly proportional to $d_p^{-1.5}$. This relationship indicates that the external diffusion resistance is the dominant resistance in the mass transport process since the volumetric external mass transfer coefficient $k_f \cdot \alpha$ has the same relationship with d_p according to the Thoenes and Kramers' correlation [9].

$$k_f \alpha \propto d_p^{-1.5} \tag{2.12}$$

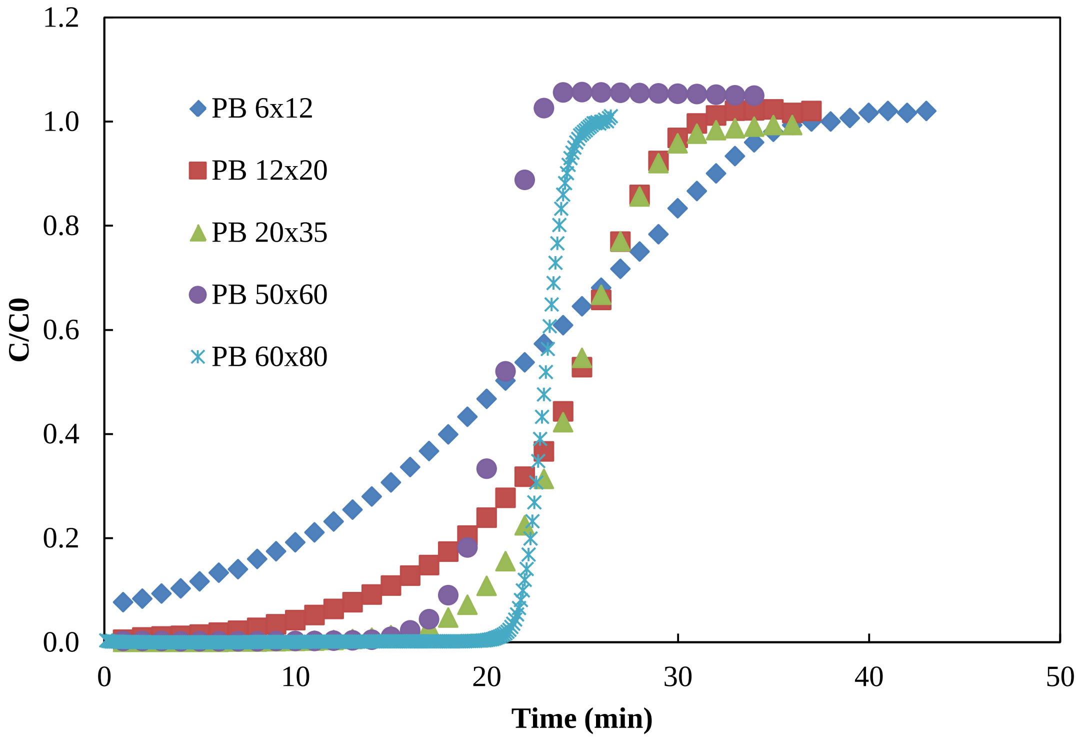

Figure 2.18, Effect of particle size on the performance of packed beds

Table 2.6 Effect of particle size on the performance of adsorption for various beds

Bed type	Mesh size	d_p (mm)	α_p (m^2/m^3)	K' (min^{-1})
PB	6×12	2.5	2,400	0.13
	12×20	1.26	4,800	0.22
	20×35	0.67	8,900	0.45
	50×60	0.28	21,400	1.3
	60×80	0.22	27,300	1.98
ACF-MFES	35×50	0.4	15,000	1.17
	50×60	0.28	21,400	2.2
	60×80	0.22	27,300	2.72
	80×140	0.14	42,800	3.95
ACF-felt	NA	0.01	400,000	5.55

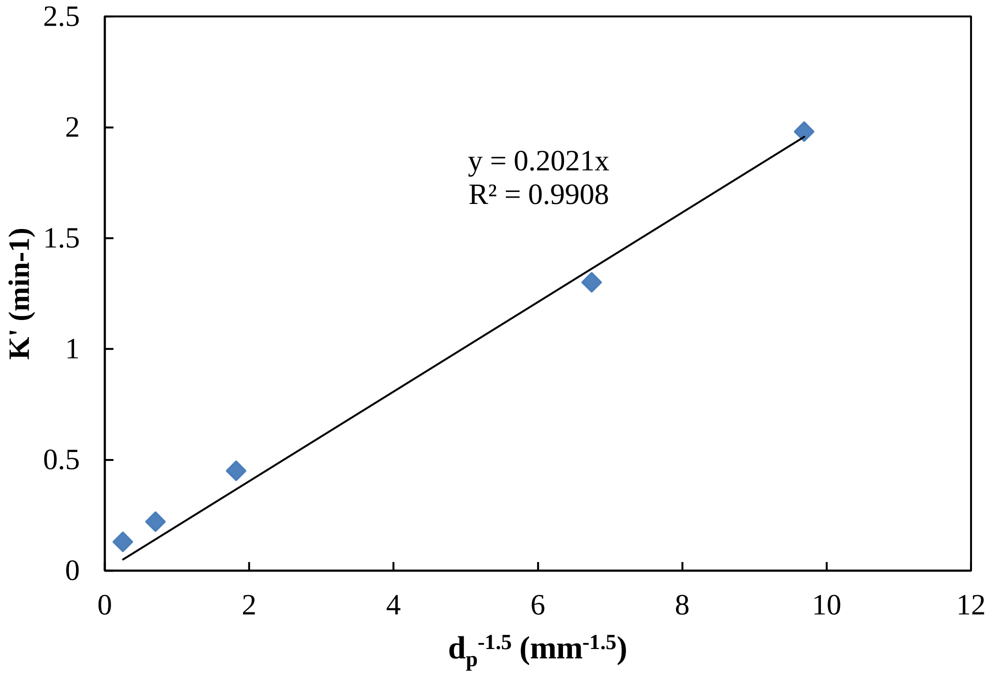

Figure 2.19 Correlation between K’ and d_p in packed bed

Figure 2.20 shows the experimental breakthrough curves for ACF-MFES beds with various particle sizes. The average diameter for 35×50, 50×60, 60×80 and 80×140 mesh particles is 0.40, 0.28, 0.22 and 0.14mm, respectively. The performance parameters are summarized in Table 2.6. As shown in the table, for the ACF-MFES bed, the K’ value also increases as particle size decreases. However, Figure 2.21 shows that the K’ is roughly inversely proportional to the particle size.

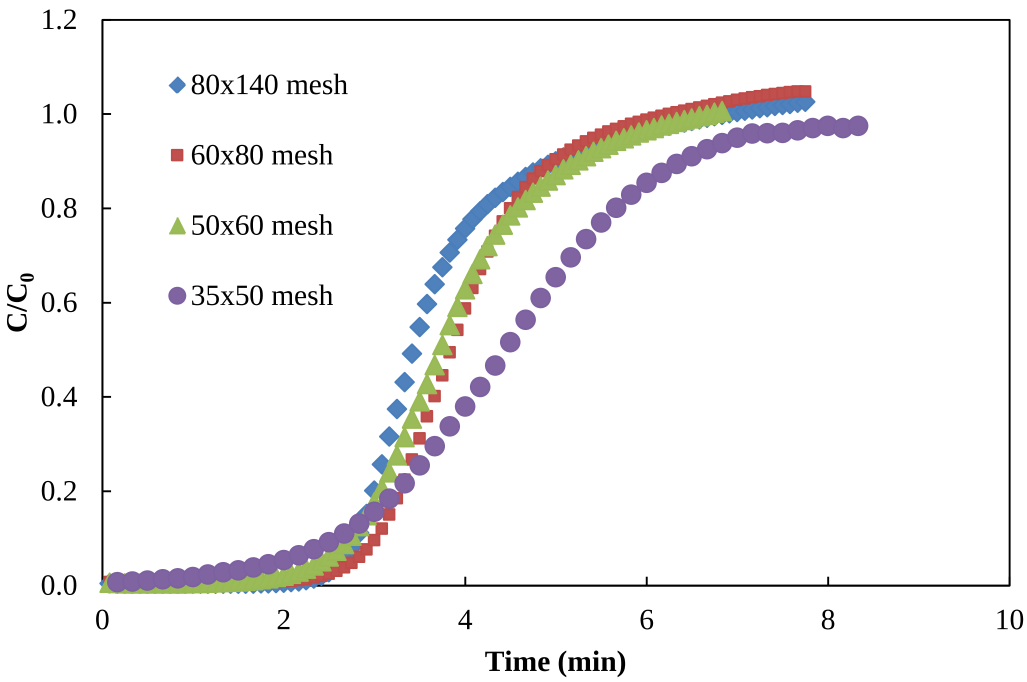

Figure 2.20 Effect of particle size on the performance of the ACF-MFES media

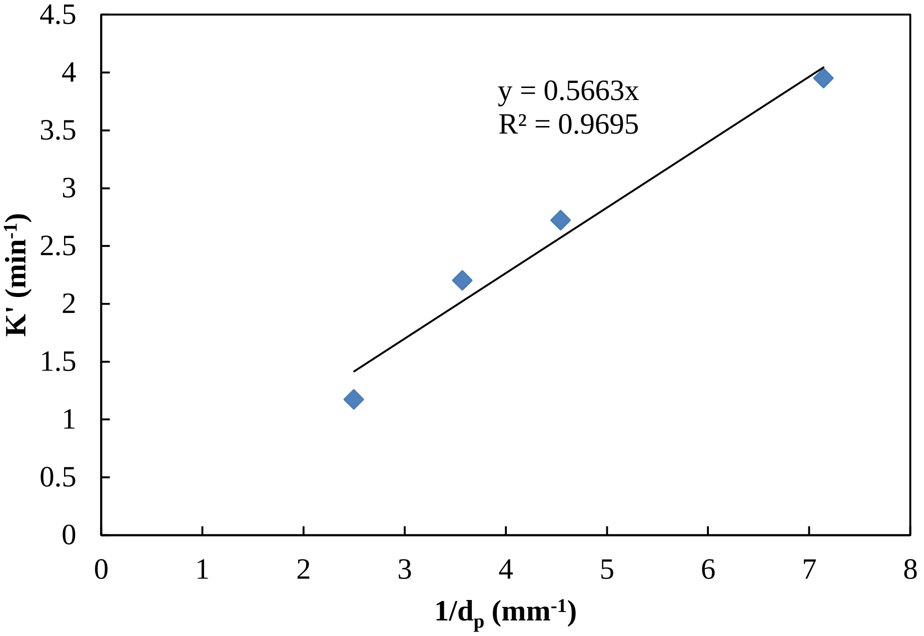

Figure 2.21 Correlation of K’ and d_p for ACF-MFES media

Table 2.6 also shows that the K’ value for ACF-felt is 5.55 min^{-1}, which only increased by 40% compared to the ACF-MFES bed with 80×140 mesh particles. However, the d_p (fiber diameter) of ACF-felt is only 0.01 mm (corresponding value of ($1/d_p$) is 100), which is more than 10 times smaller than that of the finest ACF-MFES particles (0.14 mm). If the ACF felt follows the same trend fitting line as shown in Figure 2.21, the K' value can reach up to 56.6 min^{-1}, one order of magnitude greater than the real value (5.55 min^{-1}). The particle's surface area to volume ratio (α_p) for ACF-felt can reach up to 400,000 m^2/m^3, which is also one order of magnitude greater than that of the ACF-MFES bed. Actually, due to the extremely small dimensions of ACF, the external and internal diffusion limitation is almost completely eliminated from the mass transport process. Suzuki [10] noted that in the ACF felt system, the mass transfer is axial dispersion limited.

Based on the observed experimental results above, a proposal about the concept of "limiting contacting efficiency" was addressed (see Figure 2.22). The limiting contacting efficiency for a contact system is the maximum value that can be achieved under fixed operating conditions. When the contacting efficiency is near this limiting value, further decreasing the particle size is ineffective in improving the contacting efficiency.

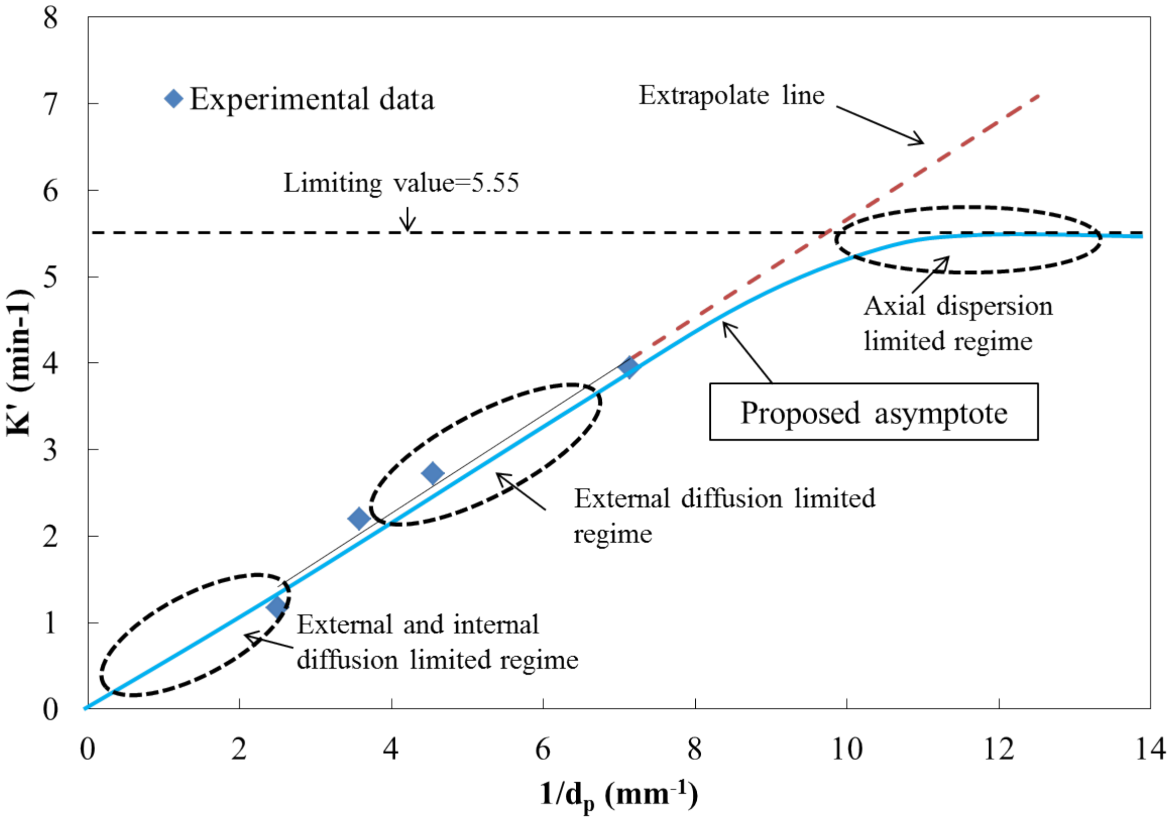

Figure 2.22 Proposed relationship between K' and d_p. The limiting value 5.55 min^{-1} is the K' value of ACF felt; the extrapolate line is the extension of the fitting line for experimental data points.

From the proposed curve shown in Figure 2.22, we can see that in the region of low values of $1/d_p$ (large particle size), both external and internal diffusion resistances are significant. Therefore, decreasing the particle size can simultaneously enhance the external and internal transfer. In the intermediate region (intermediate particle size), internal diffusion resistance is nearly eliminated, and the external diffusion resistance becomes the dominant resistance. In the region of high values of $1/d_p$ (small particle size), both external and internal diffusion resistances are nearly eliminated, and the overall mass transfer rate is limited by the axial dispersion resistance. In this region, further decreasing the particle size cannot effectively increase the overall mass transfer rate. The value of K' levels off and slowly reaches its limiting value of 5.55, which is the K' value of ACF felt.

Based on the trend of the extrapolate line (red dashed line), it can be determined that the limiting value of K' will be reached near the ($1/d_p$) value of 10 (i.e., d_p=0.1). This means that when the particle is smaller than 100 µm (0.1 mm), the dominant resistance transitions from the external diffusion resistance to axial dispersion resistance. The K' value of 5.55 can be considered the limiting contacting efficiency that can be achieved by an MFES bed, and it occurs when the particle size is down to 100 µm. This conclusion is also valid for catalytic reaction systems, where the contacting efficiency between the gas phase reactants and the solid catalyst particles has a limiting value as the particle size decreases.

The following discussion will further explain the above developed proposal. As described in Equation 2.13, the overall mass transfer resistance ($\frac{1}{k_G\alpha}$) is the summation of external diffusion resistance (1st term), internal diffusion resistance (2nd term), and axial dispersion resistance (3rd term). Since these three resistances are in a series, the greatest one dominates the overall resistance. When particles are relatively large, the external and internal diffusion resistances are large, while the axial dispersion effect is insignificant. When particles are very small, the external and internal diffusion resistances are adequately small, while the axial dispersion resistance becomes dominant.

Table 2.**7** summarizes the dependence of the three individual resistances on particle size. Both external and internal diffusion resistances have strong dependence on particle size. From the term of axial dispersion resistance ($\varepsilon_b \frac{D_z}{u_0^2}$), we can see that the axial dispersion resistance has strong dependence on u_0. However, the effect of particle size on the magnitude of axial dispersion resistance is complicated. The actual dispersion effect is a combination of axial

molecular diffusion, intraparticle velocity variation, and intrabed channeling flow or flow maldistribution. Edwards and Richardson noted that in fine particle beds, the intrabed channeling effect is enhanced, and can make the effective axial dispersion coefficient (D_z) much higher than that predicted by empirical correlation [11]. Therefore, decreasing the particle size can effectively reduce (or even eliminate) the external and internal diffusion resistance, but it cannot eliminate the axial dispersion resistance. The overall mass transfer coefficient reaches its limiting value when the process is in the axial dispersion controlled regime.

$$\frac{1}{k_G \alpha} = \frac{1}{k_f \alpha} + \frac{1}{(1-\varepsilon_b) k_p K_0} + \varepsilon_b \frac{D_z}{u_0^2} \tag{2.13}$$

Table 2.7 The dependence of three resistances on particle size

Type of resistance	Variation of resistance with d_p
External diffusion	$(d_p)^{1.5}$ [9]
Internal diffusion	$(d_p)^{2.0}$ [1][a]
Axial dispersion	Complicated

[a] According to the relationship of k_p and d_p: $k_p = \frac{60\varepsilon_p D_e}{d_p^2 K_0}$, more details see Chapter 3.

2.3.4.4. Effect of face velocity

The face velocity of a system is an important operating parameter in determining the performance of an adsorbent bed. The face velocity has significant effects on residence time and external diffusion. In this work, the effect of face velocity on the performance of ACF-MFES media was studied by varying the face velocity from 0.3 to 1.2 m/s, while remaining at a constant inlet hexane concentration of 300 ppm and a bed height of 1.27 cm.

Figure 2.23 shows the experimental breakthrough results of ACF-MFES media at various face velocities. Table 2.8 gives a summary of the breakthrough performances. As expected, both the breakthrough time and adsorption capacity (τ) decreased with an increase in face velocity. However, the adsorption rate constant K’ as well as $k_G \cdot \alpha$ increased with increasing face velocity, as evidenced by the steeper breakthrough curve for higher face velocities. An increase in u_0 can reduce the thickness of the external mass transfer boundary layer, and thus reduce the external resistance. Figure 2.24 shows the experimentally observed relationship between the overall mass transfer coefficient ($k_G \cdot \alpha$) and face velocity (u_0). The regression analysis shows that $k_G \cdot \alpha$ has a strong linear relationship (R^2=0.957) with $\sqrt{u_0}$. According to the Thoenes and Kramers correlation for flow through packed beds [13], the external mass transfer coefficient k_f also increases with the square root of the face velocity:

$$k_f \propto \sqrt{u_0} \tag{2.14}$$

This indicates that external resistance is the dominant resistance present in ACF-MFES beds over the velocity range of the experiments. The external mass transfer is usually the control step in the overall mass transfer process, due to the laminar flow behavior in ACF-MFES beds under most operating conditions.

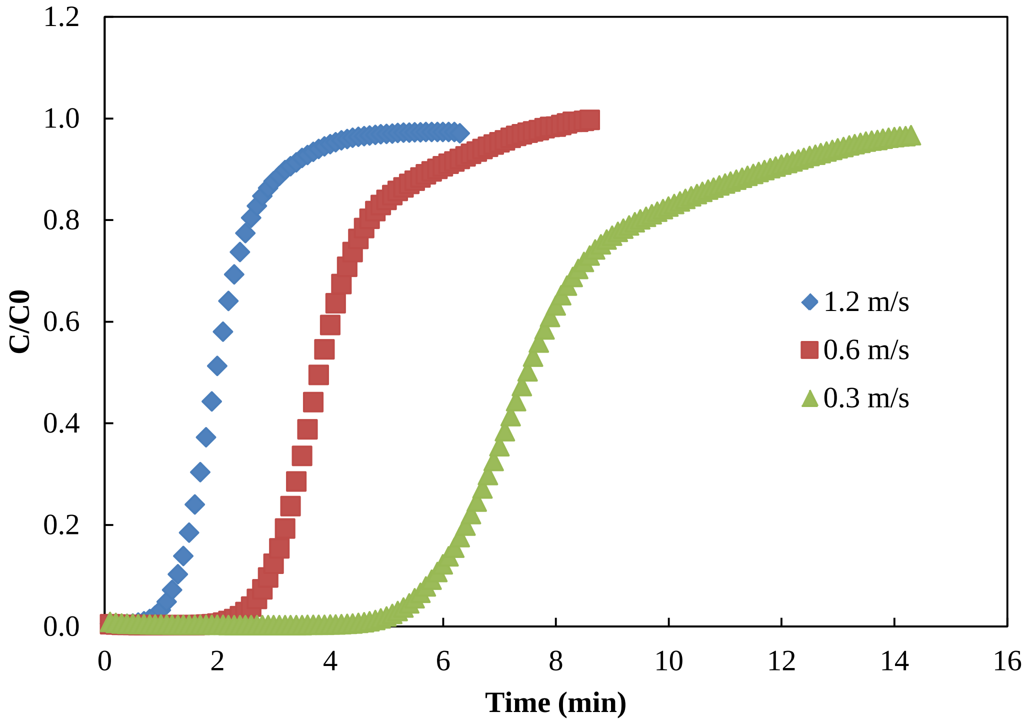

Figure 2.23 Experimental Breakthrough curve of ACF-MFES at various velocities

Table 2.8 The effect of face velocity on the performance of ACF-MFES media

Sample	u_0 (m/s)	t_b (min)	τ (min)	K' (min^{-1})	$k_G \cdot \alpha$ (min^{-1})
1	0.3	4.6	7.8	1.63	19,729
2	0.6	2.2	3.9	2.79	33,770
3	1.2	0.7	2.0	3.60	43,574

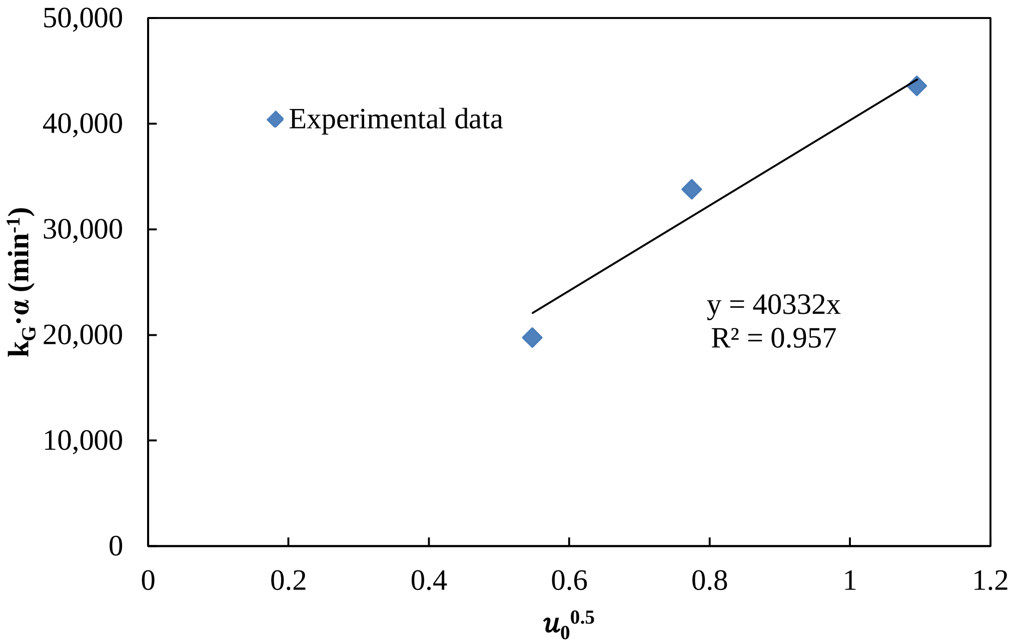

Figure 2.24 The relationship between overall mass transfer coefficient and face velocity

2.3.4.5. Effect of pleat factor

PF is a unique attribute of ACF-MFES with respect to traditional packed bed since MFES is very flexible (like paper) so that can be readily corrugated. Using corrugated media (PF>1) can increase the total load of particles in a fixed cross-section area (such as an adsorbent column or reactor) without increasing the thickness of bed, and consequently increase the capacity and conversion. On the other hand, PF can also effectively decrease the media velocity and thus increase the residence time of fluid in beds.

The media velocity is defined as the total flow rate divided by the total face area of media. For flat media (PF=1), the media velocity is equal to system velocity; for pleated media, the media velocity is equal to the system velocity divided by pleat factor (PF), where PF is defined as:

$$\mathrm{PF} = \frac{\text{Total face area of media}}{\text{Cross section area of the system}} \tag{2.15}$$

The effect of PF on the adsorption performance of ACF-MFES will be discussed in Chapter 3 where full scale pleated filter (24”×24” filter made from MFES media) will be tested and analyzed.

2.3.5. Applications of microfibrous material in heterogeneous catalytic system

When the sorbent particles in MFES are replaced by catalyst particle, the resulting bed is called microfibrous entrapped catalyst (MFEC). The MFEC bed shares the same mass transfer characteristics with MFES, so many conclusions drawn from MFES study are also valid for MFEC. In industries, many reactions are very rapid, therefore the overall rate of reactions are mass transfer or heat transfer limited. MFEC system, which has excellent heat and mass transport performance, has great promise in many heterogeneous catalytic reaction applications [14-18]. MFEC provides a unique technique to escape from the mass transfer-limited regimes into the reaction rate-limited regime, and thus maximize the use of catalyst activity.

In addition, the unique high contacting efficiency of MFEC is also valuable for intrinsic reaction kinetics study and quick catalyst screening. The following discussion will talk about these two applications in details.

Table 2.9 compares the overall mass transfer coefficient and conversion capability of MFEC with traditional packed bed and monolithic reactors. From the table, we can see that MFEC has the highest overall mass transfer coefficient ($k_G \cdot \alpha$) while the monolithic reactor’s $k_G \cdot \alpha$ is one order of magnitude smaller than MFEC. For the conversion capability, although the load of catalyst in MFEC is only 1/5 of that in packed bed, it has the highest conversion. If the catalyst in MFEC is increased to the same load with packed bed, the conversion is increased to nearly 100%, which is much higher than that of packed bed. The data clearly shows that he advantages of MFEC in contacting efficiency and conversion capability are huge compared to the packed bed and monolithic reactors.

Table 2.9 The overall mass transfer coefficient and conversion for different types of bed

type of bed	dp or d_h (mm)	$kG\cdot\alpha$	Conversion (same volume)[a]	Conversion (same catalyst load)
PB	1.26	14,528	0.55385	0.55385
MFEC	0.22	32,924	0.83944	0.99989[b]
Monolith	1.27	2,840[c]	0.14596	NA

[a] the conversion is calculated at 0.6 m/s face velocity and 2 mm thick bed assuming the reaction is mass transfer-limited

[b] MFES achieve the same particle load by increasing the thickness of bed

[c] The value of $k_G\cdot\alpha$ for monolith is calculated through Tronconi and Forzartti correlation [19]

As we know, when collecting rate law data for kinetics study, it is required to operate in the reaction-limited region. However, for the traditional packed bed reactor, the mass transfer and surface reaction are usually coupled and it is difficult to obtain the intrinsic reaction kinetics data. In contrast, the MFEC has very high mass transfer rate, and it is tunable to ensure that the reaction fall into the surface reaction control regime. In addition, due to the high contacting efficiency, the MFEC can achieve a high conversion with a thin bed length that overcomes the shortcoming of traditional differential reactor. Table 2.10 give a detailed comparison of MFEC and traditional packed bed reactor in many aspects including the conversion ability, difficulty of sampling and analysis, isothermality, channeling effect, coupling effect, and speed to reach steady-state.

Table 2.10 Comparison of MFEC and traditional packed bed reactor for kinetics study

Reactor types	Conversion	Sampling and analysis	Isothermality	Channeling effect on data interpretation	Coupling	Speed to reach steady-state
Differential (PB)	Small	Difficult [a]	Good [b]	Fatal [c]	Strong [d]	Fast
Integral (PB)	Large	Easy	Poor [b]	Small [c]	Strong [d]	Slow [e]
MFEC	Large	Easy	Good [b]	Small [c]	Weak [d]	Fast [e]

[a] Due to the small conversion in differential reactor, it is difficult to obtain the accurate conversion data.

[b] The differential reactor has a thin bed length, and there is only a small heat release in the testing. For highly endothermic or exothermic reaction, significant axial and radial temperature gradients can exist in integral reactor. MFEC has excellent heat transfer; therefore it has good isothermality for either thin or thick bed.

[c] The packed bed (especially with small particles) has great chance for channeling and bypass flow. It is fatal for differential reactor; the data interpretation will be strongly interfered by channeling flow. The integral reactor has greater length; the effect of channeling is relatively small. MFEC, due to its inherent structural uniformity, it is commonly channeling free.

[d] Traditional packed use large particle size, the surface reaction and mass/heat transport process are typically coupled. Therefore, it is difficult to study the intrinsic kinetics of reaction and the real activity of catalyst. In contrast, MFEC system use small particles; it provides super high and tunable contact efficiency and heat transfer and thus the surface reaction and transport process can be decoupled.

[e] For highly exothermic or endothermic reactions, it takes long time to reach steady state due to the hot spot and temperature gradient in the bed. However, for MFEC system, the steady-state can be reached almost immediately [12].

Based on above analysis, MFEC system, due to its excellent contacting efficiency and heat transfer efficiency, has great advantages with respect to traditional packed bed reactor (either differential or integral) in reaction kinetics study and catalyst test and screening. The

MFEC system is especially useful for rapid reactions (likely to be mass transfer limited) and highly endothermic or exothermic reactions.

For example, Sheng et al. [12] have reported the application of MFEC in Fischer-Tropsch reaction, which is a highly exothermic reaction. The traditional packed bed reactor takes long time (1.5 day as reported by Sheng et al.) to reach steady state due to the hot spot and temperature gradient along the bed. This is a serious problem for catalyst screening, because typically the catalyst's activity and selectivity data need be collected under the steady-state condition. The long time non-steady-state start-up makes the preliminary catalyst screening (according to the activity of catalyst) a time expensive process when thousands of catalyst samples need be screened. In addition, in the starting transient period, due to the hot spot and large temperature gradient in the catalyst bed, the catalyst may undergo decay or the reaction mechanism may vary in the different portion of bed. These factors significantly reduce the data's reliability and consistency. In contrast, the MFEC system can reach the steady-state condition almost immediately without hot spot and significant temperature gradient. Therefore, MFEC can provide very reliable performance data in a short time, and thus it can used to quickly screen the catalyst. In addition, the catalyst load in MFEC is much lower than packed bed. This makes the screening process more economic if noble metals are used.

2.3.6. Composite bed filter

2.3.6.1. Two-layer composite bed

Due to the high contacting efficiency of ACF-MFES media, it can be used as a polishing layer after a traditional packed bed filter to improve the overall performance of the filter. This type of filter is called "composite bed filter" in this study, and the configuration of this filter is shown in Figure 2.6.

Packed bed has the benefits of high capacity and low pressure drop, but its drawback is the low contacting efficiency (and hence thick critical bed length). In contrast, ACF-MFES has extremely high contacting efficiency but relatively low capacity. Composite bed design combines the advantages of packed bed and ACF-MFES. The composite bed possesses the benefits of high removal efficiency (due to the high contacting efficiency), high capacity, and high bed utilization (due to the reduction of critical bed length). Figure 2.25 shows the experimental breakthrough curve of packed bed, ACF-MFES, and composite bed filters. A general performance comparison is given in Table 2.11. It is evident that the composite bed significantly improved the breakthrough time as well as the adsorbent bed utilization. The t_b of composite bed (0.5" thick) was 13 min, which was much higher than the sum of individual MFES and packed bed. The bed utilization was increased to 54% by using composite bed design, compared to 12% for individual packed bed. The synergetic effect of packed bed and MFES (as polishing layer) is substantial for a thin bed requiring high removal efficiency.

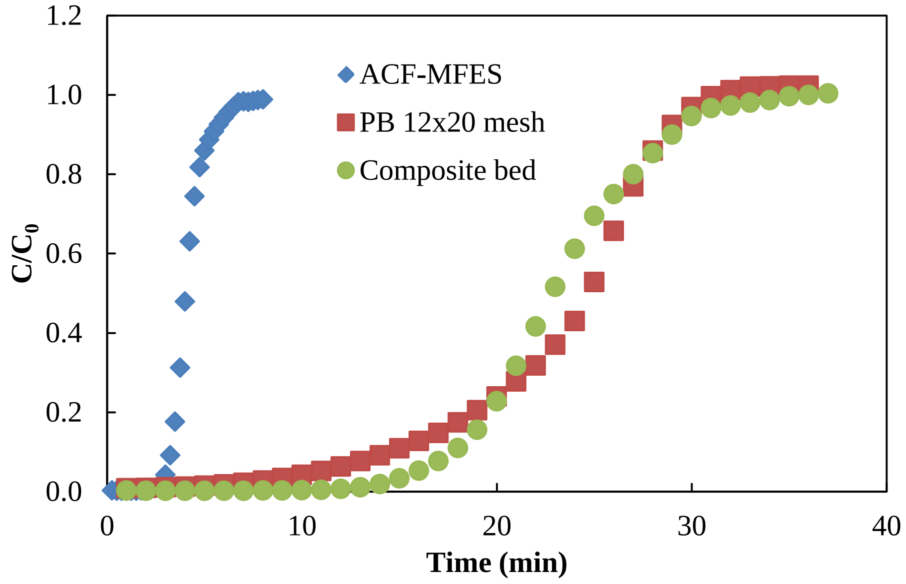

Figure 2.25 Performance comparison of the packed bed, ACF-MFES and composite bed

Table 2.11 Performance comparison of single bed (PB or MFES bed) and composite bed

Filter type	Bed depth (inch)	No. of layers	Particle mesh size	t_{b1} (min)	Bed utilization (%)	E_0 [a]
ACF-MFES	0.5	1	60x80	2.5	62.5	5.3-log
PB	0.5	1	12x20	3.0	12.0	2.2-log
Composite bed	0.5	2	12x20 & 60x80	13	54.0	4.5-log
PB	1.0	1	6x12	1.0	2.3	2.1-log
Composite bed	1.0	2	6x12 & 60x80	16.0	35.5	2.9-log
Composite bed (3-layer)	1.0	3	6x12, 20x35 & 60x80	27	58.6	4.5-log

[a] The bed's removal efficiency (E_0) is presented by log reduction, which is defined as Log reduction= $\log_{10}(C_0/C)$

2.3.6.2. Three-layer composite bed

In many industrial applications the adsorbent bed is much thicker than that described here. For a thick bed, large particles (such as 6×12 mesh) are usually used to decrease the pressure drop of bed. The critical bed length (or mass transfer zone) in this type of bed is very large, and the bed utilization is relatively low. To maximize the use of adsorbent capacity, a three-layer composite bed (illustrated in Figure 2.26) design was developed.

Figure 2.27 shows the experimental breakthrough curves of a packed bed, and two- and three-layer composite bed filters. The performance parameters are also given in Table 2.11. The total length of the bed is 1.0" for all three types. It is readily apparent that both t_b and bed unitization are significantly increased by using a three-layer composite bed design with respect to PB and two-layer composite beds.

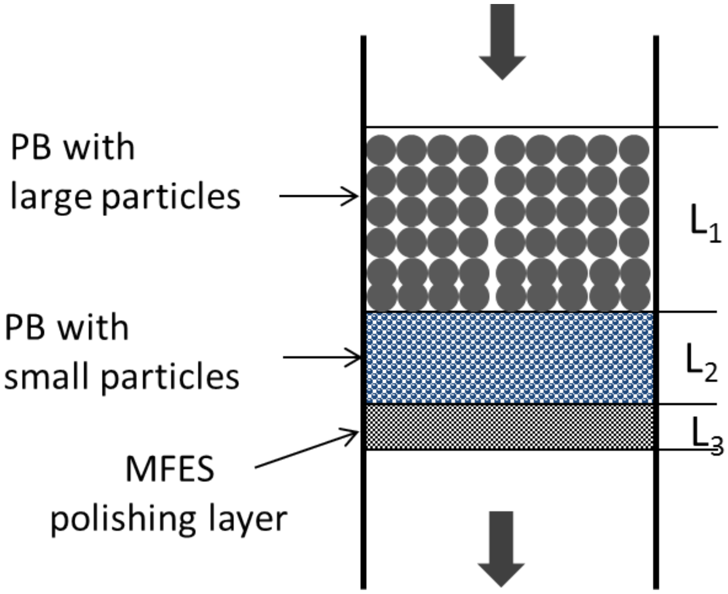

Figure 2.26 Configuration of a three-layer composite bed

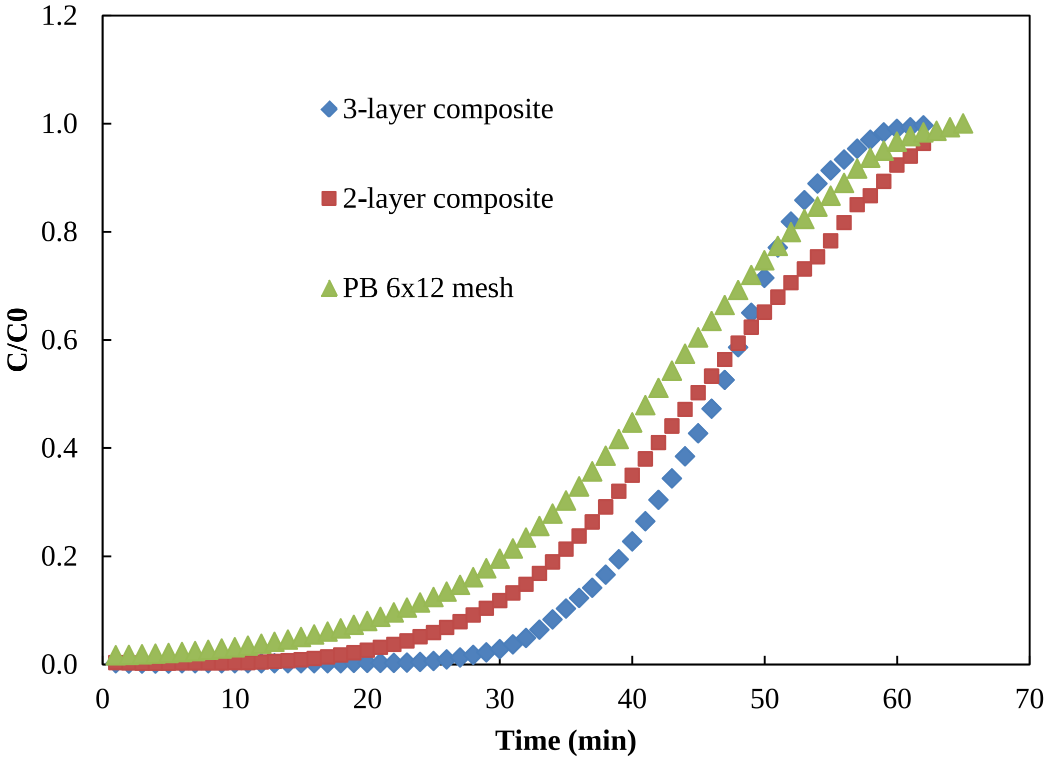

Figure 2.27 Performance comparison of composite bed filters (two- and three-layer) and a single layer packed bed filter

Table 2.12 Design essentials of three-layer composite bed filter

Layer	Name	Details	Function	Note
1st	Capacity layer	PB with large particle (4×20 mesh)	Provide the major capacity	Low pressure drop
2nd	Guard layer	PB with small particles (20×35mesh or finer)	Protect polishing layer	Keep the effluent gas in trace level
3rd	Polishing layer	ACF-MFES (60×80 mesh)	Achieve very high removal efficiency	Polishing the trace gas

The design essentials of the 3-layer composite bed are summarized in Table 2.12. As noted in the table, the first layer is called the “capacity layer”, which is a packed bed comprised of large particles (pellets). The “capacity layer” is the thickest layer among the three, and its function is to provide the major capacity of bed. Since coarse pellets are used, the pressure drop of the capacity layer is low, although the bed is thick. The second layer we called the “guard layer”, and it is a packed bed comprised of small particles. Its function is to prevent the wave front of concentration profile from entering the low capacity polishing layer prematurely, and saturating the polishing layer. Therefore, the guard layer can be considered a “buffer region” in which the mass transfer zone is preliminarily compressed before entering the final polishing layer. The existence of a guard layer guarantees that only trace level contaminants may enter the polishing layer before the capacity layer is totally saturated. The final layer, called the “polishing layer”, is comprised of the material with the highest contacting efficiency, ACF-MFES. The polishing layer can significantly improve the removal efficiency (reducing the contaminant to a ppb scale) and increase the overall bed utilization.

Focusing on the change in mass transfer zone (MTZ) along the bed, as illustrated in Figure 2.28, can further explain the principles behind the three-layer composite bed. From this figure, it can clearly be seen how the composite bed functions, and how the adsorption wave propagates along with the bed length direction. The concentration profile demonstrates a compressive propagation as the adsorption wave travels into the "guard" and "polishing" layers. This compressive propagation characteristic of composite beds (with respect to constant pattern propagation in the packed bed) significantly decreases the effective critical bed length and consequently increases overall bed utilization.

Design parameters for a 3-layer composite bed filter include:

(1) Total length of bed (L);

(2) Lengths of each layer (L_1, L_2, and L_3);

(3) Particle size of each layer

These design parameters could be optimized according to the application requirements including allowed pressure drop in the maximum air flow rate, the required removal efficiency, the protection time, etc.

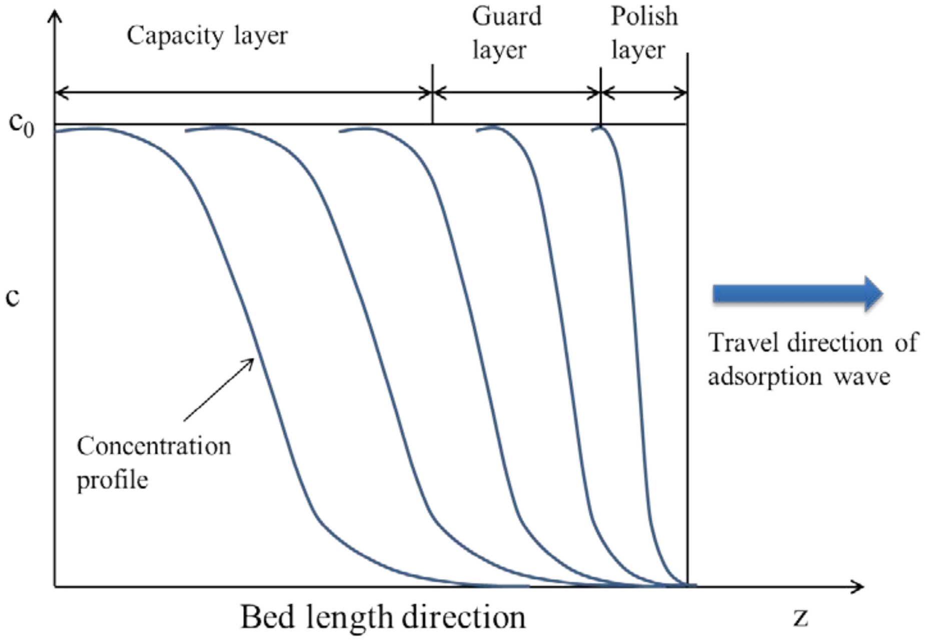

Figure 2.28 Compressive adsorption wave propagation in composite bed

2.4. Conclusion

To understand the reasons underlying this enhancement, a series of experiments was conducted to analyze each factor's unique contribution. Further research showed that the primary factor allowing for improvement was the enhancement of external mass transfer due to the use of smaller particulates, which in return provide a high surface-to-volume ratio and small diffusion distance. While the reduction of intraparticle diffusion resistance (due to decreased particle size and the uniform structure of the media) minimized axial dispersion and intrabed channeling, the enhanced radial and static mixing effects (resulting from the presence of inert fibers) were considered minor concerns.

The novel ACF-MFES nonwoven sorbent media showed significant improvement in gas phase filtration in terms of its removal efficiency and pressure drop. The excellent filtration performance, and mature, low cost manufacturing process (continuous papermaking process) make this composite sorbent media very promising for many applications including indoor air quality control, personal protective equipment, air cleaning in fuel cells stacks, and semi-conduct plant clean room.

References

[1] Ruthven DM. Principles of Adsorption and Adsorption Processes: Wiley-Interscience; 1984.

[2] Zdravkov B, Čermák J, Šefara M, Janků J. Pore classification in the characterization of porous materials: A perspective. Central European Journal of Chemistry. 2007;5(2):385-95.

[3] Kalluri RR, Cahela DR, Tatarchuk BJ. Microfibrous entrapped small particle adsorbents for high efficiency heterogeneous contacting. Separation and Purification Technology. 2008;62(2):304-16.

[4] Chiang Y-C, Chiang P-C, Huang C-P. Effects of pore structure and temperature on VOC adsorption on activated carbon. Carbon. 2001;39(4):523-34.

[5] Li L, Liu S, Liu J. Surface modification of coconut shell based activated carbon for the improvement of hydrophobic VOC removal. Journal of Hazardous Materials. 2011;192(2):683-90.

[6] Mohan N, Kannan GK, Upendra S, Subha R, Kumar NS. Breakthrough of toluene vapours in granular activated carbon filled packed bed reactor. Journal of Hazardous Materials. 2009;168(2–3):777-81.

[7] Cal MP, Rood MJ, Larson SM. Removal of VOCs from humidified gas streams using activated carbon cloth. Gas Separation & Purification. 1996;10(2):117-21.

[8] Yoon YH, Nelson JH. Application of Gas Adsorption Kinetics I. A Theoretical Model for Respirator Cartridge Service Life. American Industrial Hygiene Association Journal. 1984;45(8):509-16.

[9] Fogler HS. Elements of Chemical Reaction Engineering (4th Edition): Prentice Hall; 2005.

[10] Suzuki M. Activated carbon fiber: Fundamentals and applications. Carbon. 1994;32(4):577-86.

[11] Edwards MF, Richardson JF. Gas dispersion in packed beds. Chemical Engineering Science. 1968;23(2):109-23.

[12] Sheng M, Yang H, Cahela DR, Yantz Jr WR, Gonzalez CF, Tatarchuk BJ. High conductivity catalyst structures for applications in exothermic reactions. Applied Catalysis A: General. 2012;445–446(0):143-52.

[13] Thoenes Jr D, Kramers H. Mass transfer from spheres in various regular packings to a flowing fluid. Chemical Engineering Science. 1958;8(3–4):271-83.

[14] Chen W, Sheng W, Zhao G, Cao F, Xue Q, Chen L, et al. Microfibrous entrapment of Ni/Al2O3 for dry reforming of methane: a demonstration on enhancement of carbon resistance and conversion. RSC Advances. 2012;2(9):3651-3.

[15] Chang B-K, Lu Y, Tatarchuk BJ. Microfibrous entrapment of small catalyst or sorbent particulates for high contacting-efficiency removal of trace contaminants including CO and H2S from practical reformates for PEM H2–O2 fuel cells. Chemical Engineering Journal. 2006;115(3):195-202.

[16] Wang M, Li J, Chen L, Lu Y. Miniature NH3 cracker based on microfibrous entrapped Ni-CeO2/Al2O3 catalyst monolith for portable fuel cell power supplies. International Journal of Hydrogen Energy. 2009;34(4):1710-6.

[17] Liu Y, Wang H, Li J, Lu Y, Xue Q, Chen J. Microfibrous entrapped Ni/Al2O3 using SS-316 fibers for H2 production from NH3. AIChE Journal. 2007;53(7):1845-9.

[18] Mao J, Deng M, Chen L, Liu Y, Lu Y. Novel microfibrous-structured silver catalyst for high efficiency gas-phase oxidation of alcohols. AIChE Journal. 2010;56(6):1545-56.

[19] Tronconi E, Beretta A. The role of inter- and intra-phase mass transfer in the SCR-DeNOx reaction over catalysts of different shapes. Catalysis Today. 1999;52(2–3):249-58.

Chapter 3

Carbon Filter Test in Full Scale Apparatus

3.1. Background

The air processed by building HVAC systems and industrial processes typically contains a variety of gaseous contaminants. The gas phase filters (GPF) have been used to clean the air for many years, but few controlled tests of their performance in full-scale duct have been reported. The most common gas phase filters use sorptive active agents such as activated carbon and activated alumina. In most literature, the sorbent performance was evaluated in a bench scale test rig. The data obtained in the small-scale test (media test) is not intended to be predictive of the performance of the full-scale filter because the overall performance of the filter is also influenced by other filter components. The actual full-scale testing is straightforward and requires minimal assumptions, and thus it is preferred for critical applications, as in the air filtration system for a PEM fuel cell, which requires high performance filters. For packed bed filter, packaging sorbent media into a full-scale filter increases the chance of bypass or channeling flow, settling and leakage. For fibrous media, the pleat, the housing of the filter, will influence filter performance. The significance of all these effects on filter performance must be determined by comparing the full-scale test results with the small-scale media test results. This comparison will provide useful information for engineers to improve filter design.

The lack of full-scale test data is mainly due to cost and lack of test standards.

Although some earlier efforts were made by researchers to develop a reliable, full-scale test methodology, no standard was established until 2011 by ASHRAE. The ASHRAE Standard 145.2-2011 provides a test procedure to measure percent removal efficiency and removal capacity of gas phase filters with well-controlled conditions. The end point of the test is chemical breakthrough that exceeds a minimum removal efficiency [1]. The most useful performance data is the breakthrough curve obtained at the design air flow rate and contaminant concentration. Test results can be used to determine the filter's expected. However, since the contaminants' concentration is low in real scenarios, the test is usually conducted at elevated gas challenge concentrations.

As long as the full scale test methodology has been established, the next step is to research various impact factors that influence the performance of filters. These factors include the media type, media thickness, bed depth, sorbent media size, and pleat effect. They are typically associated with filter parameter and can be optimized via proper design. The analysis of those impact factors is the focus of this study.

3.2. Brief introduction to test standard

The ANSI/ASHRAE standard 145.2-2011, Laboratory Test Method for Assessing the Performance of Gas-Phase Air-Cleaning System: Air-Cleaning Devices, is the improved, large-scale version of ANSI/ASHARE standard 145.1-2008, Laboratory Test Method for Assessing the Performance of Gas Phase Air-Cleaning System: Loose Granular Media. The latter is a small-scale, low flow rate test standard for loose media rather than full-scale filters. Standard 145.2 provides a performance test method for both individual filters and complete filtration devices. The standard describes a test procedure with quality control constraints to measure percent removal efficiency and removal capacity of filtration devices under steady-state conditions [1]. The test duct is similar to that required for ANSI/ASHARE 52.2. The duct is a square cross-section with a dimension of 24”×24”. It differs in contaminant generation, sampling, and analytical instrumentation. The filter tests are usually conducted at flow rates between 500 and 2000 cfm.

The challenge contaminants can be either generated from a pressurized gas tank or liquid chemicals. Challenge contaminants are injected through a manifold and mixed within the test duct. The contaminant-mixing capability of ASHRAE Standard 52.2 test rig is adequate. Gas sample transport through PEFE and 316SS tube is normally very efficient with minimum surface losses. In order to minimize the environmental impact of contaminant gases, the downstream challenge scrubber needs to be installed. The scrubber should have enough removal efficiency and capacity to remove challenge gas and meet effluent requirements.

Apparatus qualification testing is an essential part of the standard. Qualification tests include test duct velocity uniformity, test duct leakage, contaminant dispersal uniformity, downstream mixing, gas contaminant generation system maximum flow rate, gas analyzer calibration, contaminant generator and duct response time, no-filter test and overall check, gas analyzer and sampling system zero, test air temperature, and test air RH. The qualification tests are important to verify that the test rig is capable of providing reliable performance data.

The test should be performed with a single gas. It is recommended that each filter be tested with a VOC, an acid gas, and another gas selected from the list of standard test gases. Some of the defined standard challenge gases are shown in Table 3.1.

The determination of performance is mainly the concentration plot, i.e., breakthrough curve. Some important performance parameters include the initial removal efficiency, breakthrough time, and total capacity.

Table 3.1 Standard Test Challenge Gases (selected gases) [1]

Chemical	MW	Low conc. (ppb)	High conc. (ppm)	NIOSH REL TWA (ppm)	OSHA PEL TWA (ppm)*	High conc. Rationale**	Capacity used***
Sulfur dioxide	64.1	50	35	2	5	AA	6%, x, 8%, y_b
Hydrogen Sulfide	34.1	100	25	10 (c)	20 (c)	CC	12%, x, 20% y_b
Formaldehyde	30	100	1	0.016	0.75	EE	3%, x
Ammonia	17	100	75	25	50	AA	5%, y_a
Ozone	48	75	0.5	0.1 (c)	0.1	BB	none
Toluene	92.1	400	50	100	200	AA	20%, z
Benzene	78.1	400	60	0.1	1	AA	20%, z
Hexane	86.2	400	25	50	500	AA	10%, z
DMMP	124.1	75	20	None	None		
Chlorine	70.9	100	30	0.5 (c)	1 (c)	AA	10%, z, 12%, y_b

*Include NIOSH Recommended Exposure Limits and OSHA Permissible Exposure Limits that have been vacated. The values are time-weighted average unless otherwise indicated as follows: c= ceiling value, st= short term

**Rationale for the Recommended High Concentration is as follows:

AA= Based on the concentration of gas required to consume 2 cubic feet of media at 2000 cfm in 8 h

BB= Based on consideration of safety, health, and reactivity with materials of construction

CC= Based on consideration of safety, health, and low odor threshold

DD= Based on NIOSH and OSHA TWAs

EE= Based on considerations of safety and health

***Capacities taken from standard industry sources such as the carbon tables. Media types indicated below:

x= permanganate-impregnated activated alumina

y_a= acid-impregnated activated carbon

y_b= base-impregnated activated carbon

z= virgin activated carbon

3.3. Experimental apparatus and materials

3.3.1. Test Apparatus

The test rig was constructed after the ASHRAE 145.2-2011 Standard [1]. A general schematic of the test rig was shown in Figure 3.1; a photo of the real rig was shown in Figure 3.2. The rig was modified from the ASHRAE 52.2 rig used for particulate air filter tests. Some necessary modifications include the gas generation and injection system, gas detect section, and gas scrubber. Figure 3.3 shows a picture of the gas generation, injection, and dispersing equipment. The modified rig is capable of conducting both particulate and gas phase filter tests.

The test rig was composed of the following segments: (1) blower; (2) Outlet sleeve; (3) upstream expansion; (4) upstream filter; (5) aerosol and dirt inlet; (6) orifice plate; (7) upstream duct; (8) test section; (9) downstream duct; (10) downstream filter (scrubber). Major equipment includes a frequency drive, a challenge gas generator, an aerosol generator (not used in this study), a dirt loader (not used), two pressure transmitters, and a gas analyzer (see Figure 3.4).

The blower (Dayton system) used a 3 horse power Hitachi motor, which was controlled by a Hitachi frequency drive with a range of zero to sixty Hz. The test duct is essentially a square, cross sectional stainless steel duct with a smooth interior finish to minimize the adsorption of contaminants. The duct dimension is 24”×24” (61cm×61 cm), and the total length is 41 ft. (15 m). The test apparatus is capable of testing filters between 500 and 2000 cfm rated airflow.

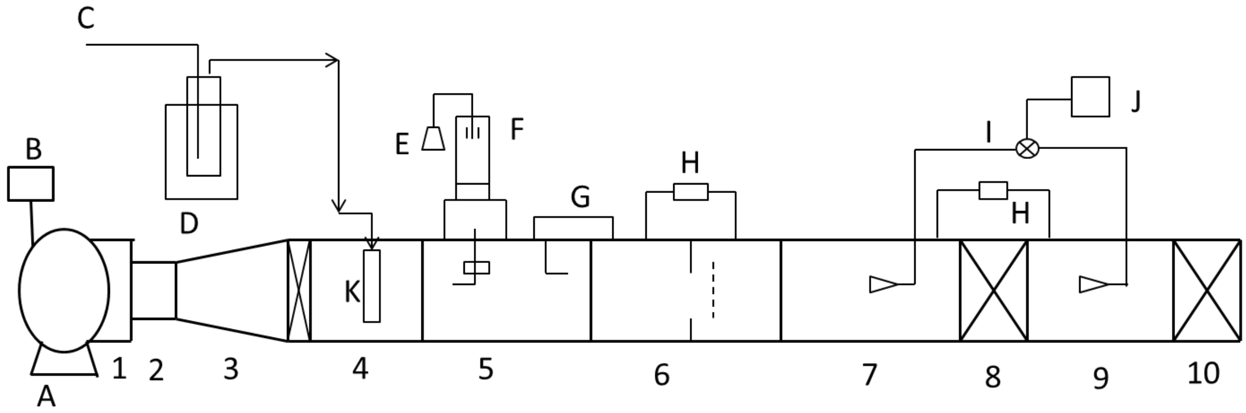

Segments: 1. Outlet sleeve; 2. Connector sleeve; 3. Upstream expansion; 4. Upstream filter; 5. Aerosol and dirt inlet; 6. Orifice plate; 7. Upstream duct 8. Test section; 9. Downstream duct 10. Downstream filter (scrubber)

Equipment: A. Blower; B. Frequency drive; C. Compressed air; D. Gas generator; E. Salt solution; F. Aerosol generator; G. Dirt loader; H. Pressure transmitter; I. Three-way valve; J. Gas detector; K. Gas dispersing tube

Figure 3.1 Schematic of full scale test apparatus

Figure 3.2 Photo of the full-scale test rig

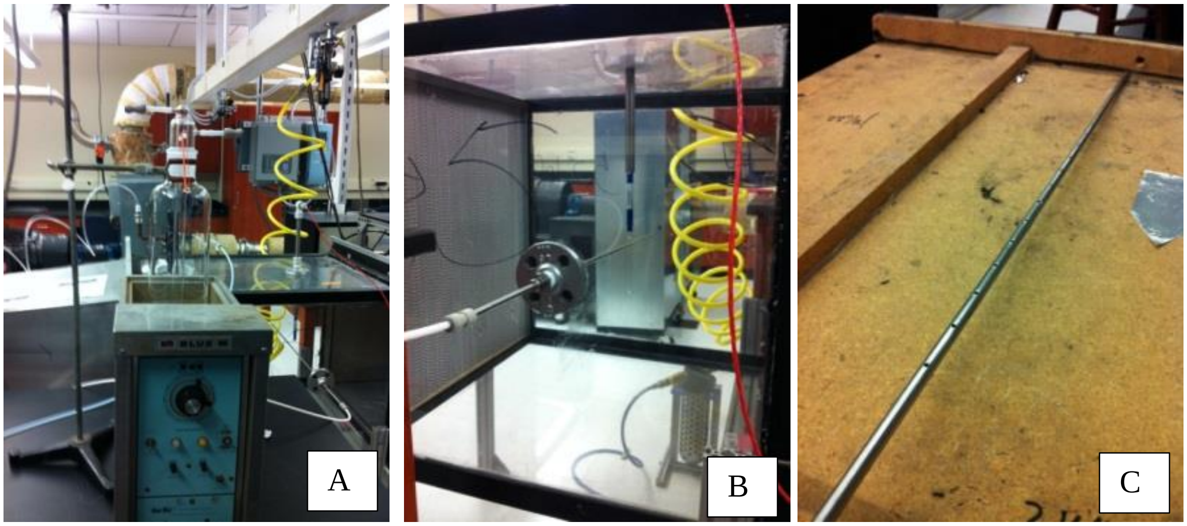

Figure 3.3 (A) Gas generation systems; (B) Gas injection port; (C) Gas dispersing manifold

Figure 3.4 MiniRAE 3000 Handled VOC detector

The pressure drop across the orifice plate and filter section was measured by two Invensys IDP10 differential pressure transmitters. The air flow rate is derived from the pressure drop across the orifice plate. The pressure drop across the orifice plate can be determined by the following equation

$$\Delta P = \frac{1}{2} C_d \rho V^2 \tag{3.1}$$

Where C_d is the friction coefficient of the orifice plate, ρ is the fluid density, and V is the fluid face velocity. The coefficient C_d is determined experimentally.

The laboratory room air was used as the carrier gas for the contaminant. All tests were performed in the conditioned laboratory environment. The room temperature was measured by an Extech 445815 hydrometer, and it was approximately 20 ˚C. The RH was measured by an Omega HH311 humidity meter, and it was 30% (± 5%). Therefore, the air density was assumed as a constant of 1.2 kg/m^3. Since the RH in the room was not controlled, the tests were performed only when the RH was suitable for experiments for the purpose of consistency of test conditions. On most sunny days, the RH is in the required range. The filters were wrapped with plastic bags before testing to prevent the adsorption of water vapor in the air.

Fire hazards and personnel safety are important issues to carefully consider before conducting the gas phase filter test. The lower explosive limit (LEL) and upper explosive limit (UEL) for hexane vapor is 1.2% and 7.4%, respectively. The exposure limits and health effects information for personnel were obtained from the Occupational Safety & Health Administration (OSHA). The OSHA permissible exposure limit (PEL) of hexane is 500ppm or 1800mg/m^3. The National Institute for Occupational Safety and Health (NIOSH) Recommended Exposure Limit (REL) is 50ppm or 180mg/m^3. The hexane-saturated vapor pressure at room temperature is 19kPa (or 19%), which is beyond the UEL, so that the gas mixtures are too rich to burn.

The ASHREA Standard 145.2 introduced six categories of challenge gases: acid gases including SO_2, HCl, and H_2S; aldehydes including formaldehyde, acetaldehyde, and hexanal; basis gases including ammonia and methylpyrrolidone; VOCs including toluene, acetone, benzene, cyclohexane, dichloromethane, ethanol, hexane, iso-butanol, tetrachloroethene, and xylene; and warfare gas such as DMMP. To ensure the test reliability, low diffusivity gas is favorable [2]. VOC gases have relatively low diffusivity. Among the VOC gases, hexane was selected as the challenge gas due to its low toxicity and ease of handling in the laboratory.

Hexane vapor was generated by the flow of the carrier gas (air or N_2) through a bubbler containing liquid n-hexane. To keep the challenge concentration constant, the bubbler was immersed in a constant temperature, stirred water bath (see Figure 3.3) to maintain the isothermal condition during the breakthrough test. The evaporation of hexane is an endothermic process, thus it is important to provide an isothermal environment for the bubbler. The generated mixture gas was injected into the ductwork after the upstream filter and dispersed by a multi-hole gas-dispersing manifold as shown in Figure 3.3 (C). The dispersed gas then mixed with the mainstream of air from the blower. To ensure that the challenge gas is uniformly distributed in the carrier air, a mixing baffle, which consists of a 30 cm diameter orifice plate (Figure 3.5 (A)), and then two 40% perforated plates (Figure 3.5 (B)) were used. In addition, a long upstream duct was also used to enhance the mixing of gas through the turbulent mixing effect. The combination of mixing baffle and long upstream duct ensured that the challenge contaminants were fully mixed with air.

In the gas detection section, a MiniRae 3000 gas detector by Rae System (see Figure 3.4) was used to measure and record the upstream and downstream concentrations of gas. Its photoionization detector (PID) has an extended range of 0 to 15,000 ppm. In the range of 0 to 999.9 ppm, the resolution is 0.1 ppm. The detector is calibrated by a standard 100 ppm isobutylene calibration gas cylinder.

At the outlet of the duct, a high capacity V-bank carbon filter was installed to remove the penetrated gas from the filter section.

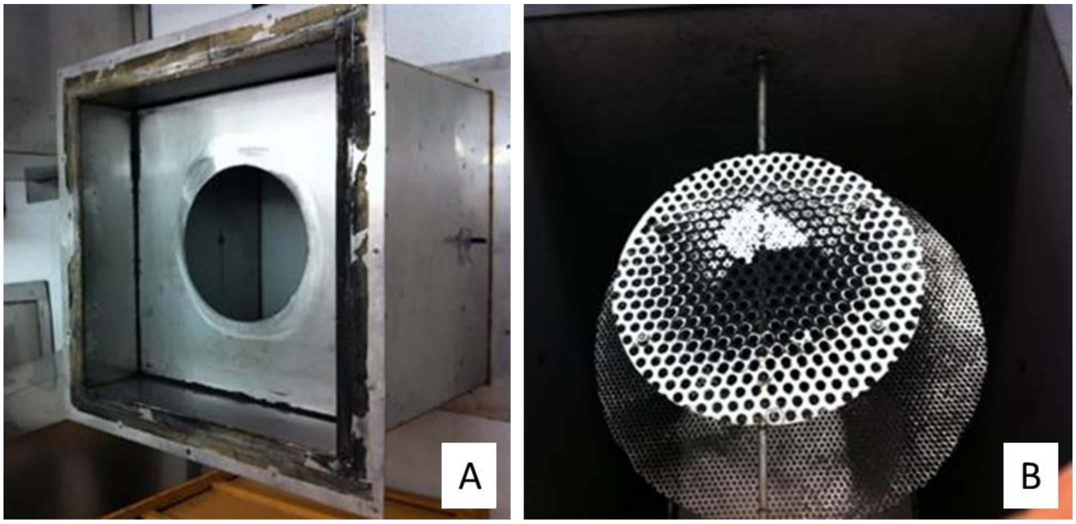

Figure 3.5 (A) Orifice plate, and (B) the following perforated plate

3.3.2. Commercial Carbon Filters

Commercial adsorptive filters are mainly in two forms: granular packed bed and fibrous media.

3.3.2.1. Granular packed bed filter

Packed bed carbon filter is the most common adsorptive filters. The sorbent granules are loosely packed in the packed bed; the particles used are typically in large size (4×12mesh) to reduce the pressure drop. A critical problem for this kind of filter is the bypass and channeling problem. Bypass is the proportion of the challenge gas or vapor that passes around the sorptive media bed without contacting the media; significant bypass is typically because of improper sealing of the rim of the cross-sectional face of the media housing [1]. Channeling is a phenomenon in which the flow of gas through a filter is not uniform, resulting in a variation in residence time over the filter surface and, consequently, variation in efficiency with position. The channeling flow can occur in filters due to nonuniform packing, wall effects, and other media-related causes [1]. The bypass and channeling flow can severely degrade the performance of a filter, and the degree of these two negative effects might be increased with time depending on the operational conditions.

In honeycomb type filters (PBF-1 as shown in Figure 3.6 (A)), the carbon particles are separated by corrugated cardboard cells; this helps reduce the effect of settling but increases the chance of wall channeling due to the low cell diameter to particle diameter ratio. In contrast, the particles in the carbon tray filter (PBF-2 as shown in Figure 3.6 (B)) tend to settle down when subject to vibration in the process of transportation and operation. A void space (gap) will be created in the top of the filter due to the settling effect. The width of gap increases with time and results in severe by-pass flow.

The PBF-1 filter is purchased from grainger.com (the filter brand is Air Handler). The particle size is in 6×12 mesh (3.36-1.68mm), while its cell size (side of triangle) is approximately 1.0 cm (the corresponding hydraulic diameter is 0.58 cm). The ratio of cell diameter to average particle is 2.29, which is much lower than the recommend value [3-5] of 10 to avoid significant wall channeling. To reduce the negative effect of wall channeling, the hydraulic diameter needs to be enlarged by a factor of 4.5 (to 2.52 cm). The corresponding length of side is 4 cm for a triangle cell, and it is 2.6 cm for a square-shaped cell. In order to reduce the wall channeling (but avoid using cells that are too large), a square-shaped cell is favorable.

Figure 3.6 (B) shows a refillable carbon tray filter (PBF-2) made by Air Filters, Inc. The frame of the tray is perforated galvanized steel. The nominal dimension is 24”×24”, and the actual dimension is 23-3/8” × 23-3/8”. The nominal depth of the filter could be 1.0, 2.0, or 4.0 in.

3.3.3.2. Fibrous type filter

Fibrous media is the most popular form in particulate filter due to its high particle removal efficiency and mature process technology (pleater). It is preferred to manufacture the adsorptive media into fibrous form so that one can utilize the existing air filter facilities (especially the pleater that significantly speeds the air filter manufacturing process) and process. Compared to the packed bed filter, the fibrous sorbent media has several important advantages: (a) the media is pleatable; (b) the sorbent is usually boned with fibers so that it won’t settle in transportation and operation; (c) small size sorbent particles can be used to improve the contacting efficiency; (d) the media is more light weight and more economic (less sorbent used). Although fibrous media have many advantages, its biggest disadvantage is its low capacity due to low sorbent load.

Figure 3.6 (C) shows a fibrous filter made by Air Handler. It is denoted as PF-1 in this study. In this filter, sorbent particles (ACP) are sandwiched between two layers of polymer media and thermal boned with polymer fibers. The polymer layers are normal air filtration media (typically MERV 6 as pre-filter) so that the filter is capable of removing both particulate and gas contaminants. The carbon particle size is about 12×40 mesh, and the carbon load is relatively low. The overall performance of this filter is not satisfactory due to its low single pass removal efficiency and low capacity.

Figure 3.6 (D) shows another fibrous filter, which is produced by American Air Filter (AAF). The filter is commercially labeled as AmAir/CE; it is denoted as PF-2 in this study. Table 3.2 gives a summary of physical characteristics of these four filters. Testing of current commercial products provides a performance baseline for the novel MFES filter and composite bed filter.

The appearances of above two filters are fibrous; however, the sorbent is in the form of granules (or particles). In contrast, activated carbon fiber fabrics (ACF felt and ACF cloth) are real fibrous media. Figure 3.7 shows the ACF felt and ACF cloth media, respectively. The diameter of activated carbon fiber is 10-20 μm, which is 1-2 order of magnitude smaller than that of granular sorbent. The difference of ACF felt and ACF cloth is that the former is nonwoven material, while the latter is woven material.

ACF is relatively new sorbent media, characterized by its high surface-to-volume ratio and high removal efficiency. ACF has been used in air and water treatment, and its high performance has been extensively reported [7-10]. The preparation of virgin or chemical modified ACF and characterization has also been reported by many other authors [11-15]. The performance of ACF media was tested in Chapter 2. However, due to the expensive cost of ACF media, full-scale filters made from ACF-media are not found in the market, and they are not tested in the full-scale rig.

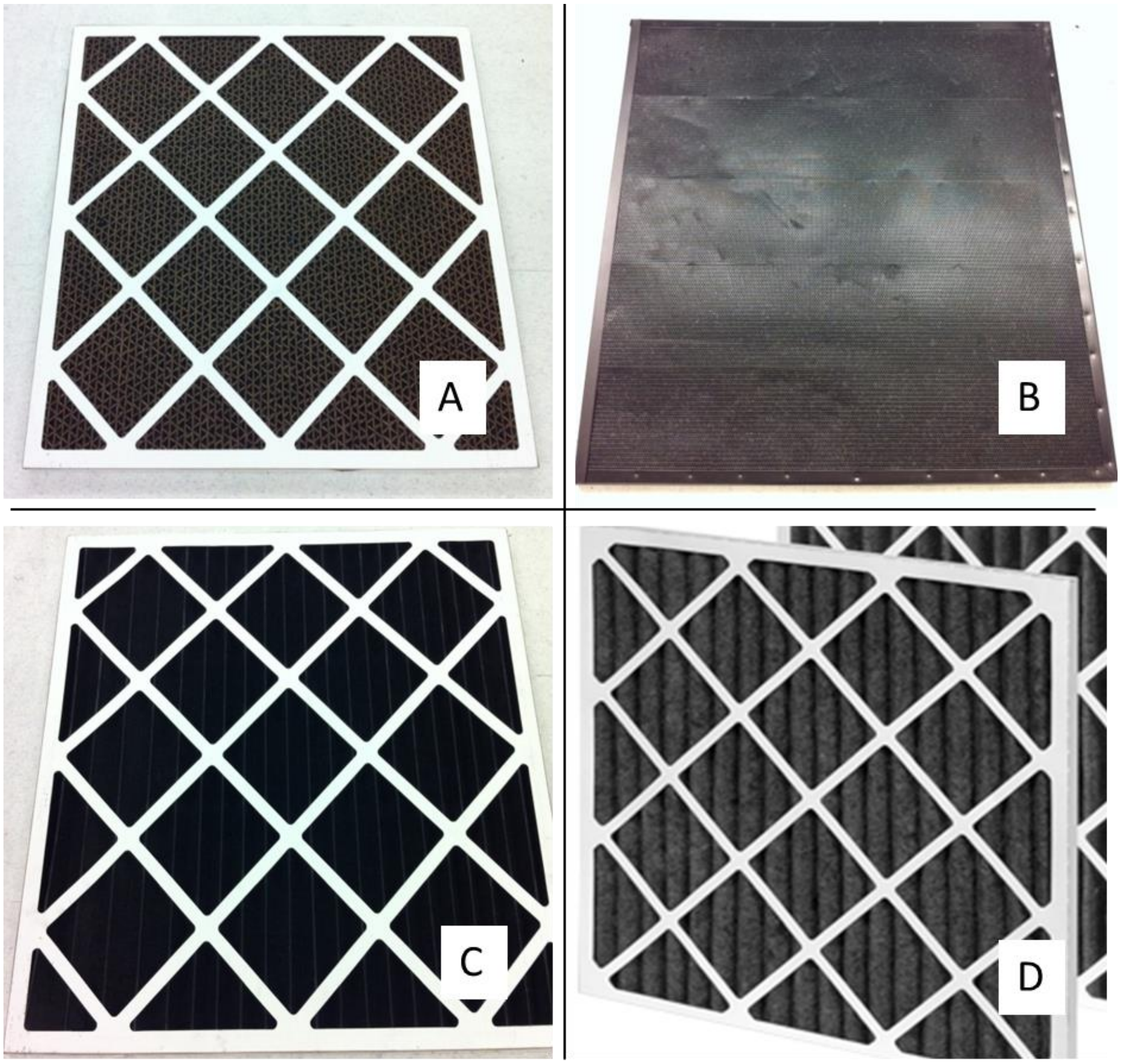

Figure 3.6 (A) honeycomb filter (PBF-1), (B) carbon tray (PBF-2), (C) pleated filter by AirHandler (PF-1), and (D) pleated filter by AAF (PF-2)

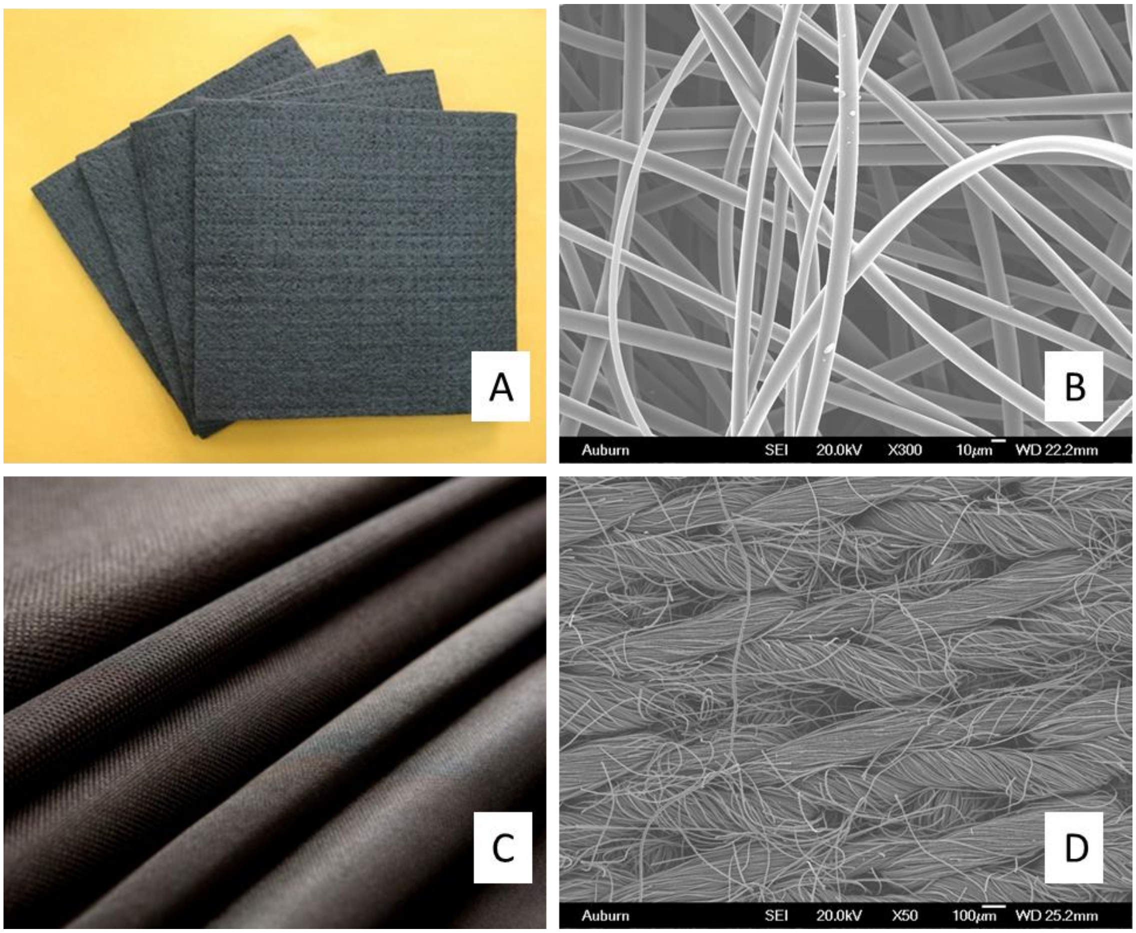

Figure 3.7 Photo (A) and SEM image (B) ACF felt; Photo (C) and SEM image (D) of ACF cloth

Table 3.2 Physical characteristics

Filters	Nominal dimension (inch)	Actual dimension (inch)	Average weight (g)
PBF-1	24×24×1	23-3/8×23-3/8×3/4	1912
PBF-2	24×24×1	23-3/8×23-3/8×1/2	4350
PF-1	24×24×1	23-3/8×23-3/8×3/4	418
PF-2	24×24×1	23-3/8×23-3/8×3/4	428

3.3.3. MFES filters

Figure 3.8 shows the MFES media roll and the pleated MFES filter. The MFES pleated filters were tailor made by Quality Filters, Inc. using MFES media. The MFES media was made via wet lay process by using a continuous papermaking machine. The media is made from LLDPE/PET bicomponent fiber and contains PICA G55C 50x80mesh activated carbon. The basis weight of MFES media is about 217g/m^2; the carbon load is 120g/m^2; and the media thickness is 2.3mm. For the design of the filter, some parameters are important to the performance. Those parameters include the face dimension, the depth of filter (typical options: 1, 2, and 4"), pleat count, the thickness of the media, and the support grating blockage.

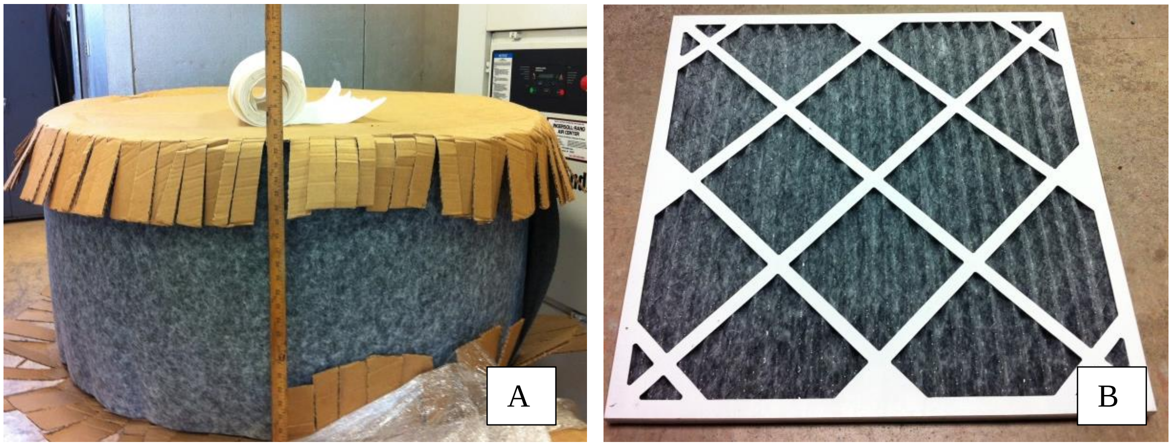

Figure 3.8 (A) 2 ft wide MFES media roll; (B) 24"×24" pleated MFES filter (tailor made by Quality Filter, Inc.)

3.3.4. Multi-Element Structural Array

Multi-Element Structural Array (MESA) is a novel platform that integrates multiple panel filters into a single housing to increase the filtration area and reduce flow resistance. The concept of MESA is inspired by the V-bank filters; but unlike the V-banks, MESA uses off-theshelf filter units. The MESA framework is adapted to the commercial filter, and it can be reused by uninstalling and reinstalling the filter elements. Figure 3.9 shows the photos of “V” and “W” shaped MESA installed with activated carbon honeycomb filters. More details about the construction and benefits of MESA filters can be found in previous work by Ryan Sothern [16].

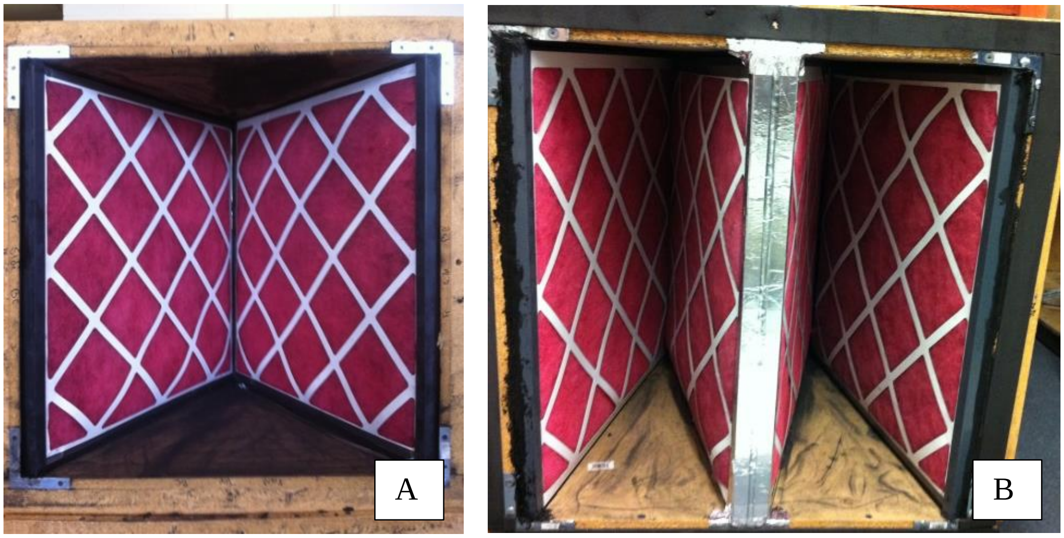

Figure 3.9 (A) “V” shaped MESA with two filter element; (B) “W” shaped MESA with four filter element

3.4. Apparatus pre-qualification test

3.4.1. Test duct velocity uniformity

According to ASHRAE Standard 145.2, the uniformity of the challenge air velocity across the duct cross section should be determined by a nine-point traverse measurement. For each measuring point, 300 samples (with a sampling time interval of 1/6 s) were taken for a one minute period using a hot-wire anemometer (Omega FMA 1000). Each point was repeated three times, and the average value was used. More details about this measurement can be found in the Appendix. The mean value and standard deviation of nine-point measurement were used to compute the coefficient of variation (CV). At an airflow rate of approximately 2000 cfm, the CV was 6.7%, which is lower than 10% as required by Standard 145.2.

3.4.2. Contaminant dispersal in the test duct

According to Standard 145.2, section 5.5, gas contaminant spatial dispersal uniformity needs be established by measuring the concentration at multiple points in the test section. Because the particle diffusion rates are lower than those of gases, a current qualification of test ducts as Standard 52.2 test ducts shall be considered sufficient to provide adequate mixing [1]. In this study, the challenge gas concentration was measured at the same nine points as the velocity uniformity test, and the uniformity of gas concentration was then determined by computing the CV. The traverse measurements were performed at an airflow rate of 500 cfm. For each grid point, a five-minute period sample was taken, with a sampling interval of 6 s. Each point measurement was repeated three times. The CV of the corresponding nine grid point concentrations was 8.7%, which is less than 15% as required by Standard 145.2.

3.4.3. Time variability

The challenge gas concentration time stability is important for a long period performance test. The stability of the gas generation system is the key to maintaining a constant concentration for a long period. According to the ASHRAE Standard 145.2, section 5.5, the variability of challenge with time shall be evaluated by a series of upstream challenge concentration measurements. Figure 3.10 shows the concentration fluctuation during a 200-minute measurement at an air flow rate of 500 cfm. The mean value is 30.11ppm, and the computed CV is 1.6%, which is less than 5% as required by Standard 145.2. The maximum deviation is 5.4%, which is less than 10% as required by the standard.

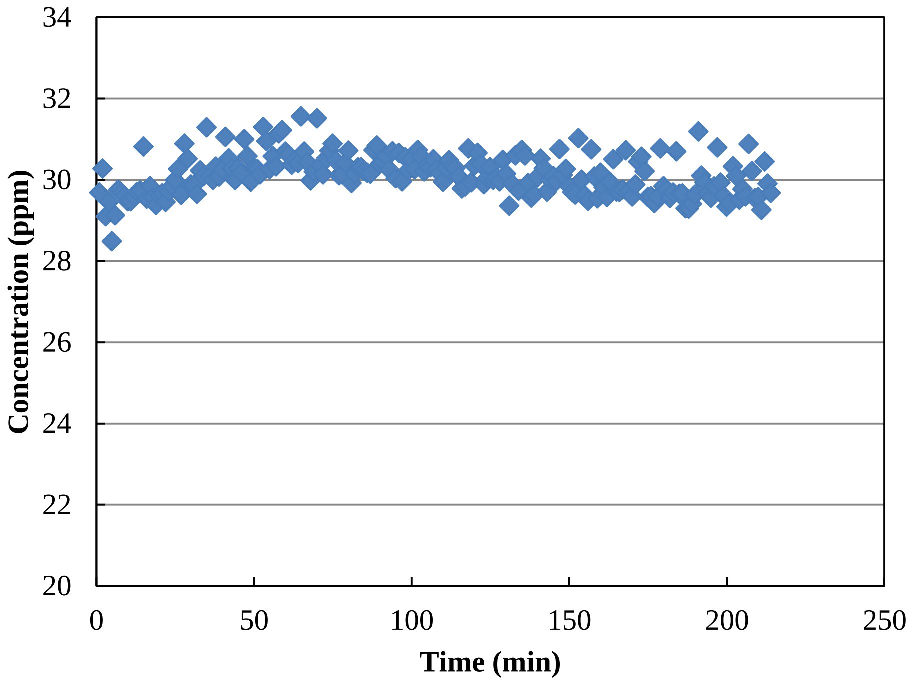

Figure 3.10 Upstream challenge concentration time variability test at airflow rate of 500 cfm

3.4.4. No filter test

The test was conducted following Standard 145.2, section 5.11. An upstream-downstream comparison test was performed without an air-cleaning device in place to check the adequacy of the overall duct. Since no filter was in place, the calculated removal efficiency shows the loss of challenge gas as a result of duct leakage and adsorption on the duct surface [2]. The average no filter removal efficiency is approximately 1%.

3.4.5. Test sequence

The following test sequence is recommended by Standard 145.2 [1].

a. Complete a leak characterization and personal safety evaluation.

b. Visually inspect the air-cleaner sealing surface for defects that might prevent sealing.

c. Install the air cleaner and conduct visual inspection for leaks in the mounting.

d. Equilibrate the test filter at the test condition.

e. Measure the resistance versus the conditioned air flow rate of the clean air cleaner.

f. Start the challenge chemical for the initial efficiency test. Measure upstream and downstream challenge concentration levels.

g. Start the challenge chemical for standard capacity test as soon as is practical after switching generator and analysis equipment. Measure upstream and downstream challenge concentration levels until the desired breakthrough occurs.

h. Periodically monitor downstream of the cleanup scrubbers to determine their effectiveness, if needed.

i. Periodically monitor the operator’s work areas to ensure that any leakage in the room is acceptable, taking steps to ensure that resulting concentrations are less than the applicable PEL, if needed.

3.5. Results and discussion

3.5.1. Pressure drop result

3.5.1.1. Pressure drop of commercial filters

Pressure drop performance is one of the most important technical specifications for filters. Filter manufacturers usually provide a pressure drop curve to rate the permeability of filters. In this study, the pressure drop of the filters was experimentally measured before the breakthrough test. Table 3.3 shows the pressure drop of four commercial filters at rated airflow rates. From Table 3.3, we can see that the pressure drop of packed bed filters is much higher than of fibrous filters. The pressure drop of PBF-1 and PBF-2 is over 250 Pa (1" W.G.), which is the recommended final resistance at rated air flow. Therefore, in practice, packed bed filters are typically used in the form of V-bank. V-bank filters can provide multiple flow areas and hence effectively reduce the pressure drop.

Table 3.3 Pressure drop at rated airflow rate

Filters	Pressure drop (Pa)
PBF-1	277
PBF-2	339
PF-1	72
PF-2	38

Note: the pressure drop was measured at the face velocity of1.25 m/s

3.5.1.2. Effect of MESA on the pressure drop of filters

In the regime of creeping flow (Re<1), the pressure drop of a fibrous media follows Darcy's law.

$$\Delta P = \frac{\mu L}{K_m} u_0 \tag{3.2}$$

Where μ is fluid viscosity, L is thickness of media, K_m is the permeability constant of the media, and u_0 is the superficial velocity.

At higher operating velocities, the pressure drop of media significantly deviates from Darcy's law. To account for the non-Darcian behavior of media, a practical method is to add a second-order term (also known as inertial term). The modified equation is called Forchheimer-extended Darcy's law.

$$\Delta P = Au_0 + Bu_0^2 \tag{3.3}$$

Where constant A is equal to the Darcy's law constant ($\mu L/K_m$), and constant B accounts for the inertial loss.

As we know, the pressure drop of a packed bed can be well described by Ergun's equation. The form of Ergun's equation is the same as Forchheimer's equation, including a liner term (viscous loss) and a second-order term (inertial loss). However, because of the remarkable differences in particle dimensions and void fractions between fibrous media and packed bed, the contribution of second-order loss to the overall pressure drop can be very different under the same operating velocity. These different results indicate that the effect of MESA on packed bed filter and fibrous filter is very different.

Figure 3.11 shows the effect of MESA on the pressure drop of fibrous filters. Figure 3.12 shows the effect of MESA on the pressure drop of packed bed filters. Comparing these two figures, we find that the MESA's effect on packed bed filter is more significant than on fibrous filters. For fibrous filters, W-shaped MESA reduced the pressure drop to 1/4 of that of a single filter. However, for packed bed filters, W-shaped MESA reduced the pressure drop to 1/10 of that of a single filter. This difference primarily resulted from the flow characteristics in fibrous media and packed bed as described above.

The relation of pressure drop and face velocity is almost linear for fibrous filter, while it is more close to quadratic (2^{nd} order) for packed bed filter. The different relationships between pressure drop and face velocity can be explained by the Reynolds number.

For fibrous media, the Reynolds number is smaller than 10 under the operating velocity, and thus viscous loss is the dominant loss due to the laminar flow. The viscous loss is linear to the velocity. However, for the packed bed filter, the Reynolds number is much higher (ca. 500 at 2.5 m/s), and second-order inertial loss becomes significant due to the turbulent flow. Therefore, the packed bed filter's resistance is more sensitive to face velocity due to the higher order dependence on velocity compared to fibrous filter. Consequently, the effect of MESA on packed bed is also more significant.

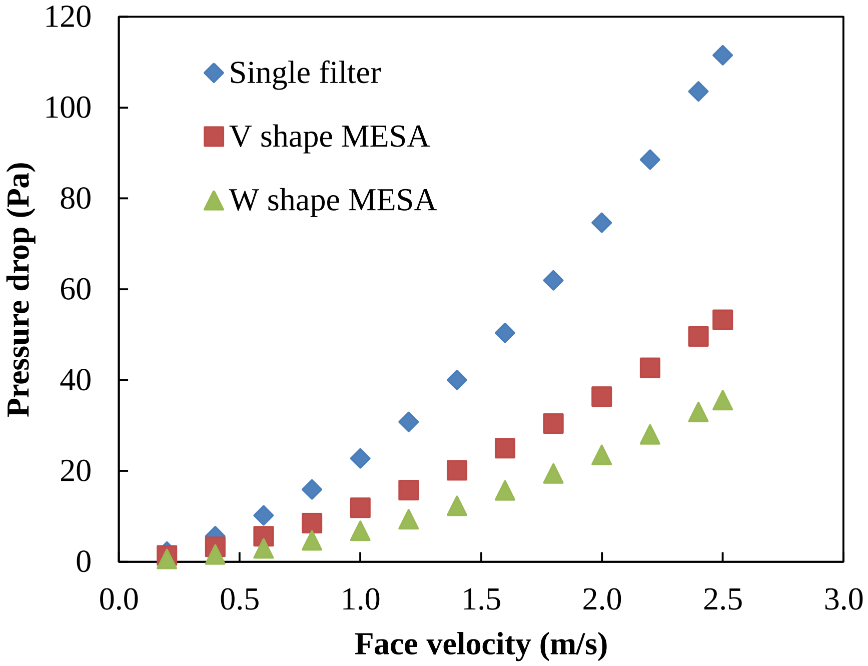

Figure 3.11 The effect of MESA on the pressure drop of fibrous filters

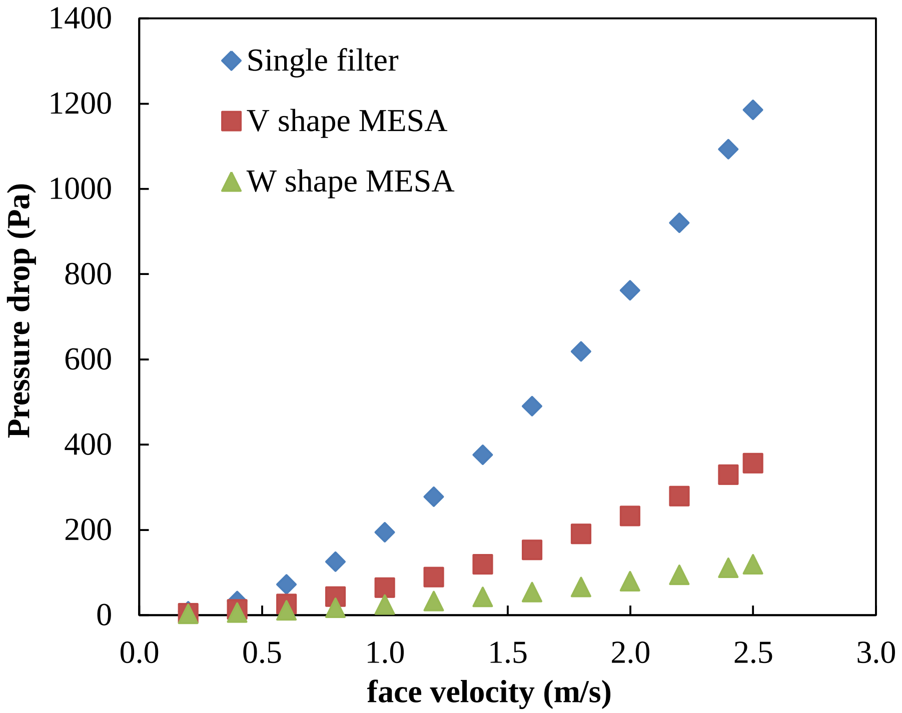

Figure 3.12 The effect of MFSA on pressure drop of packed bed filters

3.5.2. Breakthrough results

3.5.2.1. Determination of performance

Initial removal efficiency, E_0

$$E_0 = \left(1 - \frac{C}{C_0}\right) \times 100\% \tag{3.4}$$

Where C and C_0 are outlet and inlet challenge concentrations, respectively.

Breakthrough time (t_b) is defined as the elapsed time that desired breakthrough percentage is reached. For a normal HVAC filter performance test, the 50% breakthrough time (t_{b50}), and 5% breakthrough time (t_{b5}) have been reported as useful indicators of performance.

The 95% breakthrough time (t_{b95}) and 100% breakthrough time (t_{b100}) are less commonly reported due to the experimental time required to make the determination [1].

The capacity for removal (C_R) of filter is calculated by equation 3.5.

$$C_R = C_0 t_{b100} - \int_0^{t_{b100}} C\,dt \tag{3.5}$$

Where C_0 is inlet challenge concentration in ppm, t_{b100} is the required time when 100% breakthrough occurs, and $\int_0^{t_{b100}} C\,dt$ is the integrated area under the breakthrough curve in ppm·min. The integration of area is completed by using a trapezoidal numerical integration function called “trapz” in Matlab. The value of C_R is dependent on the super facial velocity, thus any performance comparison must be made under the same face velocity.

The sorbent utilization (SU) can be estimated by following equation:

$$SU = \frac{\int_0^{t_b}\left(1-\frac{C}{C_0}\right)dt}{\int_0^{\infty}\left(1-\frac{C}{C_0}\right)dt} \times 100\% \tag{3.6}$$

For low breakthrough (<5%), the sorbent utilization can be estimated by the following equation without significant deviation.

$$SU = \frac{t_b C_0}{C_R} \tag{3.7}$$

The adsorption rate constant K’ can be determined via the method described in Chapter 2 (section 2.3.3). The breakthrough data was first plotted with $\log\left(\frac{C}{C_0-C}\right)$ versus time and then analyzed by linear regression method. The slope of the fitted linear line is equal to 0.43K’.

3.5.2.2. Tests of commercial filters

Tests were performed at 480 CFM (0.6 m/s face velocity) airflow and 30 ppm hexane challenge concentration. The activated carbon honeycomb filter (PBF-1) was first tested in the full scale rig. The average weight of the filter is 1912 g, including the pre-filter and frame; the load of activated carbon is approximately 1500 g. This filter has a honeycomb like structure. The honeycomb structure provides the benefit that the particles in cells are not significantly affected by the settling effect caused by gravity and shake. However, this structure reduces the packing density of sorbents in the filter. Comparing the PBF-1 and PBF-2, we can find that the sorbent load in the honeycomb structure is much less than in the simple packed bed filter.

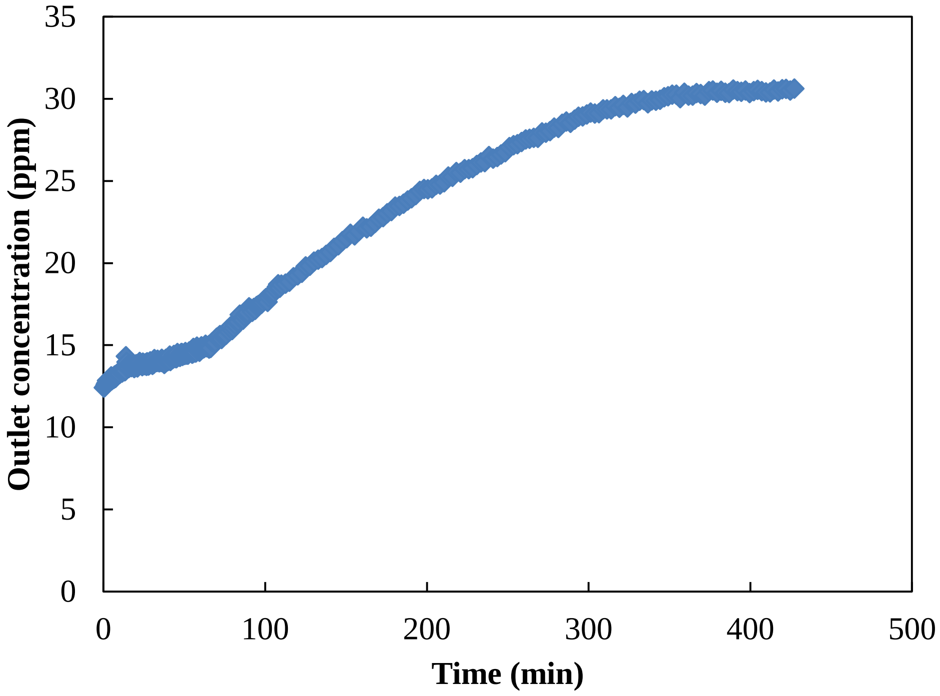

Figure 3.13 Experimental breakthrough curve of PBF-1

Figure 3.13 shows the experimental breakthrough curves for PBF-1. The nominal dimension of the filter is 24×24×1. The experimental conditions are: C_0=30 ppm, T= 21 °C, u_0=0.6 m/s. If not specified, the experimental condition is the same for other filter tests. The performances of four commercial filters are given in Table 3.4. This initial removal efficiency is only 59%, which is much lower than the result from media tests in bench scale, indicating that the particle packing in the full scale filter is far from ideal packing. Channeling flow and non-uniform packing have significant effects on the performance of a full-scale filter.

Table 3.4 Performance summary of four tested filters

Filter	Average weight (g)	C_R (ppm·min)	K' (min^{-1})	E_0 (%)	t_{b5} (min)	t_{b50} (min)
PBF-1	1912	2905	0.012	59	0	21
PBF-2	4350	6474	0.0084	83	0	216
PF-1	418	51.3	0.35	46	0	0
PF-2	428	77.6	0.18	43	0	0

PBF-2 is a simple, refillable carbon tray filter. Figure 3.14 shows the experimental breakthrough curve of PBF-2. From Table 3.4, we can see that the capacity of PBF-2 is much higher than PBF-1 due to its higher carbon loading (weight). The initial removal efficiency is also improved with respect to PBF-1.

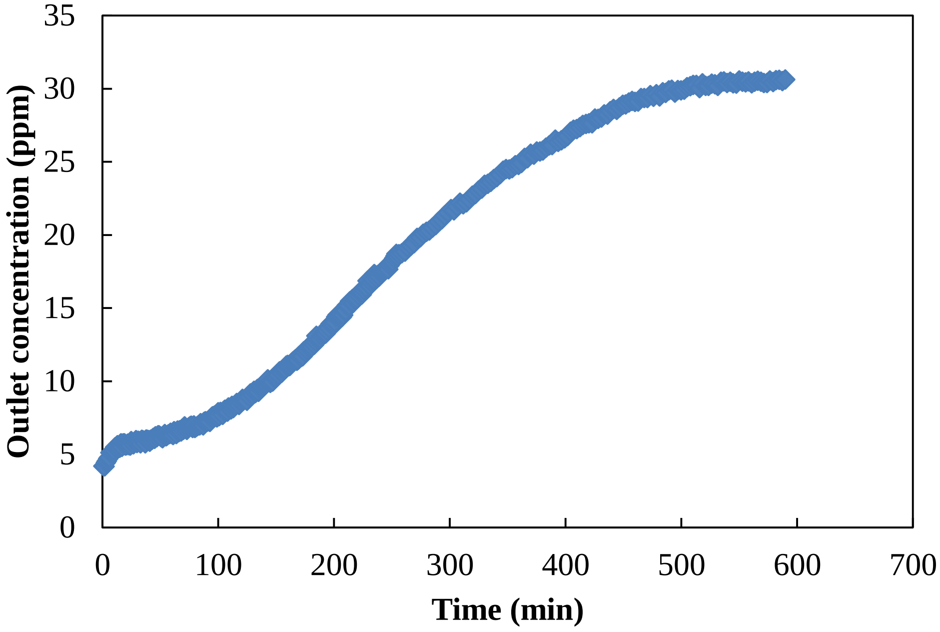

Figure 3.14 Experimental breakthrough curve of PBF-2

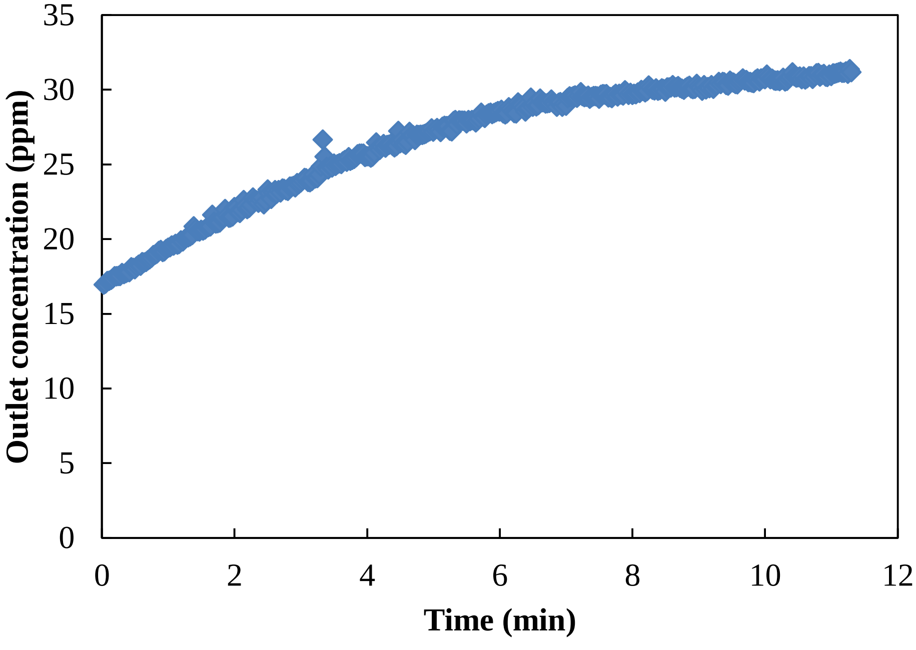

Figure 3.15 Experimental breakthrough curve of PF-1

Figure 3.15 shows the experimental breakthrough curve of the PF-1 filter. The initial removal efficiency is only 46%. This type of filter is designed for odor control in HVAC systems, where high removal efficiency is not required.

AmAir CE carbon pleated filter (PF-2) is designed to provide odor and particulate control. The filter combines non-woven polyester fibers with CTC 60 granular activated carbon. The carbon particles are relatively large (ca. 12×40 mesh), and are bonded with fiber via thermal bonding method. The nominal dimension is 24×24×1, and the total weight (including the frame) is 428 g. Figure 3. **16** shows the experimental breakthrough curve. The filter exhibited very little chemical capacity and low removal efficiency. The initial removal efficiency is below 50% in this testing condition, meaning that this type of filter is not suitable for applications requiring high removal efficiency, such as fuel cells, protective gas masks, etc. Another phenomenon observed is that the shape of breakthrough curve is more likely a linear line rather than an S-shaped curve, indicating that the channeling flow in this filter is severe.

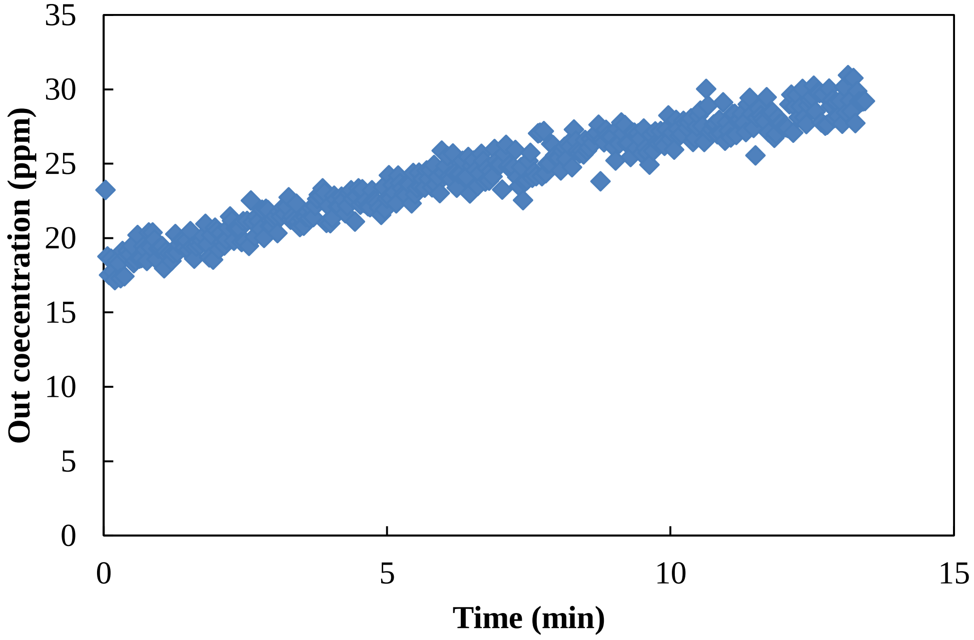

Figure 3. 16 Experimental breakthrough curve of PF-2

From the test results of full-scale filters, some conclusions are drawn. First, the packed bed filter has a much higher chemical capacity than fibrous filters. However, the biggest challenge for packed bed filters is the channeling flow (or by-pass flow) and settling issues. Honeycomb structure can reduce the effect of settling, but it causes severe channeling flow. In carbon tray filters, particle settling with time is inevitable as long as the filters are placed in a vertical direction and the flow is in a horizontal direction. Secondly, both packed bed filters and fibrous filters exhibited low removal efficiency. Increasing the thickness of bed can effectively improve the removal efficiency, but it makes the filters very heavy. Within a 1” bed depth, composite bed filter provides another technique to improve the removal efficiency. The benefits of composite bed filter include compact design (less than 1.0 inch), high removal efficiency, and high bed utilization. In addition, since the composite bed filter is compact, it can be easily constructed into a MESA filter (V-bank filter). For example, for a 1” nominal depth composite bed filter, 12 elements (WWW shaped MESA) can be assembled into a filter box with more than 50% open area for flow.

3.5.2.3. Tests of MFES filters

Figure 3.17 shows the experimental breakthrough curves of flat MFES media and pleated MFES filters (1” and 2” depth). The double layer filter was obtained by laminating two layers of media into one layer, as shown in Figure 3.18. The wire mesh was sandwiched by two layers of media and bonded with the media by adhesive. The operational airflow is 480 CFM; the corresponding face velocity is 0.6 m/s. The inlet hexane challenge concentration is 30 ppm. The adsorption performances are given in Table 3.5.

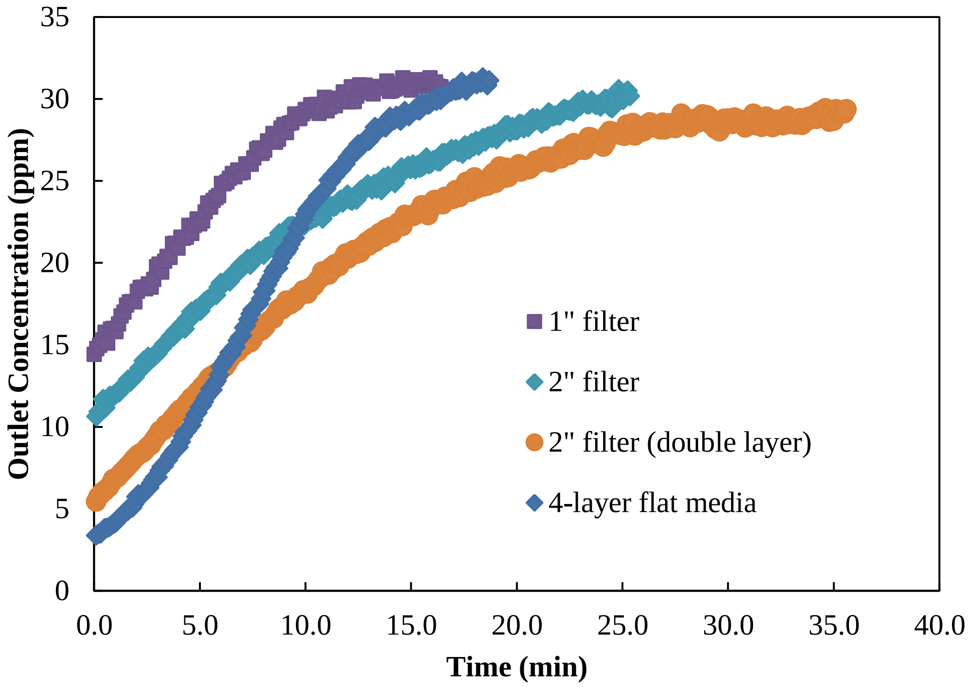

Figure 3.17 Experimental Breakthrough results of MFES media and MFES filter

Table 3.5 Performance summary of MFES media and MFES filters

Filter/media	PF	Wt. of filter (g)	Est. Wt. of media (g)	C_R (ppm·min)	K' (min^{-1})	E_0 (%)	t_{b50} (min)
Flat media (4 layers)	1	322	322	218	0.33	89	6.8
1” depth filter	1.5	385	120	84	0.24	52	0.4
2” depth filter	3.5	695	280	181	0.17	65	3.1
2” filter (double layer)	3.5	1020	560	340	0.18	82	7.2

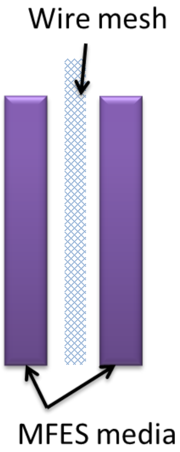

Figure 3.18 Illustration of media lamination using wire mesh and adhesive

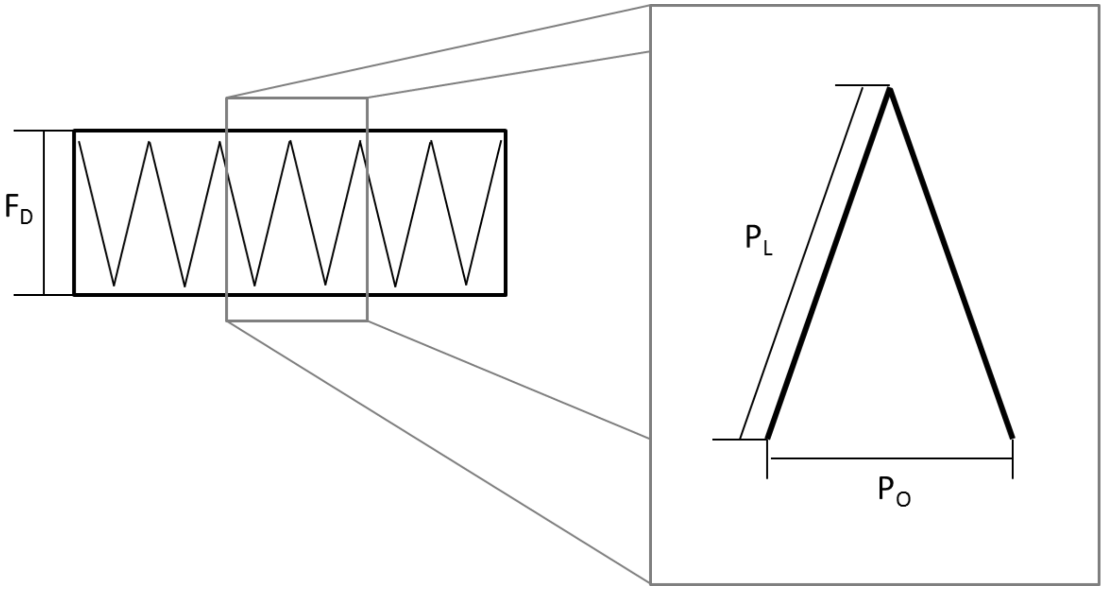

Figure 3.19 Illustration of pleat in filter. FD: Filter depth; PL: Pleat length; PO: Pleat opening

The effect of filter depth was first investigated by comparing the breakthrough results of 1” and 2” filters. It is evident that a 2” depth filter has higher initial removal efficiency and total capacity than a 1” depth filter. The improvement in removal efficiency can be explained by the fact that the reduction of media velocity in the 2” filter increases the residence time of gas in the media. However, this effect can be partially offset by the decrease of the external mass transfer coefficient due to the decrease of media velocity. The factors of filter depth and pleat count can be lumped into one factor – pleat factor. The pleat factor (PF) is defined as the total face area of media over cross section area of the duct.

Because of the technique (pleater) used to construct the pleated filter, the pleat length (P_L) is equal to the filter depth (F_D), as shown in Figure 3.19 [17]. The total media area for a pleated filter is as follows:

$$A_T = 2 \times F_D \times P_C \times F_W \tag{3.8}$$

Where A_T is the total available media area, F_C is the pleat count, and F_W is the filter width.

Since the media area for a flat media is equal to $F_W \times F_L$, the pleat factor for a single filter can be derived as:

$$PF = 2 \times F_D \times P_C / F_L \tag{3.9}$$

From equation 3.9, we can find that the pleat factor is proportional to the filter depth and pleat count. In this study, all tested filters' face dimension is 24"×24", and the pleat count is 24. Table 3.6 gives the MFES filter's dimensions and pleat factors.

Table 3.6 Summary of MFES filter's dimensions and pleat factors

Nominal depth (inch)	Actual depth (inch)	P_C	PF
1	0.75	24	1.5
2	1.75	24	3.5
4	3.75	24	7.5

For the pleated filter, the media velocity (u_m) is defined as:

$$u_m = \frac{u_0}{PF} \tag{3.10}$$

The media velocity is the actual face velocity when the fluid flows through the media. Both the resistance of media and the mass transport between fluid and media are associated with media velocity rather than with the system's face velocity.

When the external mass transfer is the control step of the overall adsorption rate, the initial removal efficiency of the bed can be calculated by the following equation [18]:

$$-log(1 - E_0) = 0.43 \cdot k_f \cdot \alpha \cdot \frac{L}{u_m} \tag{3.11}$$

Where E_0 is the initial removal efficiency, k_f is the mass transfer coefficient, α is the surface area to volume ratio, and L is the thickness of media or bed.

According to most of the mass transfer coefficient correlations, the relationship between k_f and media velocity is as follows:

$$k_f \propto \sqrt{u_m} \tag{3.12}$$

Combining equations 3.11 and 3.12, we can derive the following relationship between removal efficiency and pleat factor:

$$-log(1 - E_0) \propto \frac{L}{\sqrt{u_m}} \propto L \cdot \sqrt{PF} \tag{3.13}$$

Equation 3.13 can be converted to ratio form (equation 3.14) if a reference filter's removal efficiency was known.

$$\frac{log(1-E_0)}{log\left(1-E_0^{ref}\right)} = \frac{L}{L^{ref}} \cdot \sqrt{\frac{PF}{PF^{ref}}} \tag{3.14}$$

Where E_0^{ref} is the reference filter's initial removal efficiency, L^{ref} is the reference filter's media thickness, and PF^{ref} is the reference filter's pleat factor. Equation 3.14 is useful to predict various filters' removal efficiencies as long as the media's removal efficiency is known. In this study, the flat media's removal efficiency is first measured. As shown in Table 3.7, 4-layer flat media's initial removal efficiency is 89%, which is used as the reference value to compute other filter's removal efficiency. According to equation 3.6, the initial removal efficiency for a single layer media is 42%. The predicted values of E_0 for 1" and 2" filters are given in the table. The predicted values agree with the experimentally observed value with small deviation, indicating that equation 3.14 is valid to predict the removal efficiency of filters with various media thickness and pleat factors. It should be noted that the derivation of equation 3.14 ignores the effect of channeling or bypass flow. When significant channeling flow exists in the filter's bed, the predicted value of E_0 might have remarkable deviation from the experimental value.

Table 3.7 Experimentally observed removal efficiency and predicted removal efficiency

Filter/media	PF	E_0 (%)	Predicted E_0 (%)
Flat media (4 layers)	1	89	As ref.
1" depth filter	1.5	52	49
2" depth filter	3.5	65	64
2" depth filter (double layers)	3.5	82	87

3.6. Conclusion

A full-scale test rig was designed and constructed based on ASHREA Standard 52.2 and 152.2 to systematically assess the performance of the filters in terms of pressure drop, gas life, single pass removal efficiency, etc. Pre-qualification exams, including air leakage, face velocity uniformity, and challenge gas uniformity, were conducted to verify the reliability of the test rig. The filters were tested at 0.6 m/s face velocity with 30 ppm hexane in the air as the challenge gas. Experimental results show that the commercial packed bed type filter and fibrous filter have very low initial removal efficiency. The filters were immediately broken through under the above mentioned experimental conditions. The slow mass transport of large particle size and the severe channeling and bypass flow in the bed were considered the main reasons for the low efficiency of filters. To improve the performance of the filters, a novel multi-element structured array (MESA) and composite bed design were developed. The MESA can significantly increase the carbon load and available media area. The composite bed takes advantage of the high capacity of packed bed and the high contacting efficiency of MFES media; it can significantly improve the overall performance of the filter in terms of single pass removal efficiency, breakthrough time, bed utilization, and pressure drop. The combination of MESA and composite bed technologies provides a novel filter design, capable of providing long term protection and high removal efficiency with a much lower pressure drop penalty. This novel filter has great promise in application scenarios where high purity air is required.

Reference

[1] American Society of Heating RaA-CE. Standard 145.2-2011 -- Laboratory Test Method for Assessing the Performance of Gas-Phase Air Cleaning Systems: Air Cleaning Devices (ANSI approved). 2011.

[2] Bastani A, Lee C-S, Haghighat F, Flaherty C, Lakdawala N. Assessing the performance of air cleaning devices – A full-scale test method. Building and Environment. 2010;45(1):143-9.

[3] de Klerk A. Voidage variation in packed beds at small column to particle diameter ratio. AIChE Journal. 2003;49(8):2022-9.

[4] Winterberg M, Tsotsas E. Impact of tube-to-particle-diameter ratio on pressure drop in packed beds. AIChE Journal. 2000;46(5):1084-8.

[5] Subagyo, Standish N, Brooks GA. A new model of velocity distribution of a single-phase fluid flowing in packed beds. Chemical Engineering Science. 1998;53(7):1375-85.

[6] Karwa AN, Tatarchuk BJ. Aerosol filtration enhancement using carbon nanostructures synthesized within a sintered nickel microfibrous matrix. Separation and Purification Technology. 2012;87(0):84-94.

[7] Suzuki M. Activated carbon fiber: Fundamentals and applications. Carbon. 1994;32(4):577-86.

[8] Brasquet C, Le Cloirec P. Adsorption onto activated carbon fibers: Application to water and air treatments. Carbon. 1997;35(9):1307-13.

[9] Lorimier C, Subrenat A, Le Coq L, Le Cloirec P. Adsorption of Toluene onto Activated Carbon Fibre Cloths and Felts: Application to Indoor Air Treatment. Environmental Technology. 2005;26(11):1217-30.

[10] Mangun CL, DeBarr JA, Economy J. Adsorption of sulfur dioxide on ammonia-treated activated carbon fibers. Carbon. 2001;39(11):1689-96.

[11] Carrott PJM, Nabais JMV, Ribeiro Carrott MML, Pajares JA. Preparation of activated carbon fibres from acrylic textile fibres. Carbon. 2001;39(10):1543-55.

[12] Ko YG, Choi US, Kim JS, Park YS. Novel synthesis and characterization of activated carbon fiber and dye adsorption modeling. Carbon. 2002;40(14):2661-72.

[13] Ko T-H, chiranairadul P, Lu C-K, Lin C-H. The effects of activation by carbon dioxide on the mechanical properties and structure of PAN-based activated carbon fibers. Carbon. 1992;30(4):647-55.

[14] Wang J, Zhao F, Hu Y, Zhao R, Liu R. Modification of Activated Carbon Fiber by Loading Metals and Their Performance on SO2 Removal. Chinese Journal of Chemical Engineering. 2006;14(4):478-85.

[15] Valente Nabais JM, Carrott PJM, Ribeiro Carrott MML, Menéndez JA. Preparation and modification of activated carbon fibres by microwave heating. Carbon. 2004;42(7):1315-20.

[16] Sothen RA, Tatarchuk BJ. A Semi-Empirical Pressure Drop Model: Part II—Multi-Element Pleated Filter Banks. HVAC&R Research. 2009;15(2):269-86.

[17] Sothen RA, Tatarchuk BJ. A Semi-Empirical Pressure Drop Model: Part I—Pleated Filters. HVAC&R Research. 2008;14(6):841-60.

[18] Fogler HS. Elements of Chemical Reaction Engineering (4th Edition): Prentice Hall; 2005.

Chapter 4

Adsorption Model

An adsorption breakthrough model was developed based on the transient mass balance, equilibrium isotherm, linear driving force approximation, and constant pattern transition assumption. Because physisorption is a fast process, the adsorption of hexane onto activated carbon is considered in mass transfer control. However, the mass transport involved in the adsorption process is complicated. Four different mass transfer mechanisms including external mass transfer (or film diffusion), surface diffusion in the adsorbed phase, gas phase molecular, and Knudsen diffusion in the pore, are significant to the overall adsorption rate. In this study, by analogy with the electrical resistance model, these four mass transfer resistances were combined into one overall mass transfer coefficient. The axial dispersion is another important factor that influences the adsorption performance, thus the dispersion term usually appears in the mass balance equation in a dispersed plug flow model. In order to produce an analytical solution for the model, the axial dispersion was considered as an additional mass transfer resistance, and was also grouped within the overall mass transfer coefficient. This simplification greatly reduces the complexity of the equations, and is a good approximation in most cases. Some important assumptions used in this model are summarized as follows:

(1) Local equilibrium exists between the gas phase and adsorbed phase

(2) Plug flow conditions

(3) Constant pattern mass transfer zone

(4) Linear driving force for intraparticle mass transfer.

4.1. Mass balance

For plug flow without axial dispersion, the differential mass balance for the adsorbate around a thin layer in the fixed bed can be described by the following equation [1, 2]:

$$(1-\varepsilon_b)\frac{\partial \bar{q}}{\partial t} = -u_0\frac{\partial c}{\partial z} - \varepsilon_b\frac{\partial c}{\partial t} \qquad (4.1)$$

The term on the left-hand side of equation represents the local adsorbate uptake rate; the two terms on the right-hand side represent the convective and transient terms, respectively.

4.2. Isotherm

If the adsorption sites have equal energies and there is no interaction between adsorbed molecules, the isotherm follows Henry's law (Equation 4.2) at very low concentrations, and the Langmiur equation (Equation 4.3) at moderate concentrations:

$$q^* = Hc \qquad (4.2)$$

Where H is the equilibrium constant analogous to Henry's constant.

$$q^* = q_m\frac{k_L c}{1+k_L c} \qquad (4.3)$$

Where q_m is the limiting adsorptive capacity of the solid with monolayer coverage; k_L is Langmuir's equilibrium constant.

If the adsorption sites do not have identical energies and the energy distribution complies with exponential law, the isotherm follows the Freundlich equation:

$$q^* = K_f c^{1/n} \tag{4.4}$$

Where K_f and n are Freundlich constants.

Both Langmuir and Freundlich isotherm are based on flat surface adsorption theory. Some other isotherm equations based on this theory include BET isotherm, Toth isotherm, Radke-Prausnitz isotherm, Sips isotherm, UNILAN equation, etc. [3]. Another category of isotherm equations is based on the pore filling theory, which is grounded in the Polanyi potential theory. The most popular isotherms in this category are two-parameter Dubinin-Radushkevich (DR) and three-parameter Dubinin-Astakhov (DA) equations.

$$\frac{W}{W_0} = \exp\left(-k\left(\frac{\varepsilon}{\beta}\right)^2\right) \tag{4.5}$$

$$\frac{W}{W_0} = \exp\left(-k\left(\frac{\varepsilon}{\beta}\right)^m\right) \tag{4.6}$$

Where,

$$\varepsilon = RTln\left(\frac{P_i^s}{p_i}\right) \tag{4.7}$$

Where ε (J/mol) is called the adsorption potential, which is the work required to compress the solute from its partial pressure to its saturation pressure; W (m^3/kg) is the adsorbate volume adsorbed by sorbent as saturated liquid; W_0 is the micropore volume of the adsorbent; β is the affinity coefficient; m is a parameter related to the pore size distribution. [4]

According to the IUPAC system, the adsorption equilibrium isotherms can be classified into six types as shown in Figure 4.1. Type I isotherms, those that have a limiting value (saturation capacity) are the most common. The majority of adsorption onto microporous adsorbents exhibits this type of isotherm. The classical Langmiur and Freundlich isotherms belong to this category. One of the characteristics of type I isotherms is their increased equilibrium adsorption capacity in the low relative pressure region, when compared to linear or Type III isotherms. Because this attribute is beneficial to the adsorption step, this is considered the "favorable" isotherm. The favorable isotherm is necessary to approach a constant pattern transition profile in the uptake step, and it has a compact wave shape. In contrast, type III isotherms are classicaly unfavorable isotherms. Type II isotherms represent adsorption on macroporous adsorbents with strong adsorbate-adsorbent interactions, while type III represents the adsorption with weak interaction. Type IV and V isotherms describe mono-and multilayer adsorption, along with capillary condensation in the micropore. Type VI isotherms represent multi-step adsorption isotherms [5]. In this study, hexane adsorption onto activated carbon belongs to the type I isotherm category.

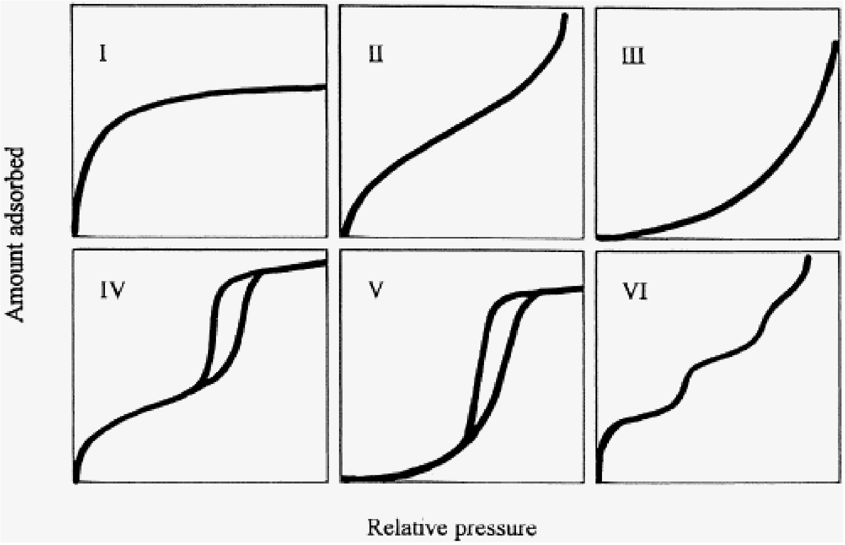

Figure 4.1 The Brunauer and the IUPAC classifications of gas-solid adsorption isotherms [5]

4.3. Separation factor

The concept of separation factor is analogous to the relative volatility in distillation processes. The separation factor in an adsorption process is defined by equation 4.8. The separation factor is useful for characterizing isotherm types. The favorable, linear, and unfavorable isotherms correspond to R<1, R=1, and R>1, respectively.

$$R = \frac{c}{c_0 - c}\left(\frac{q_0 - q^*}{q^*}\right) \tag{4.8}$$

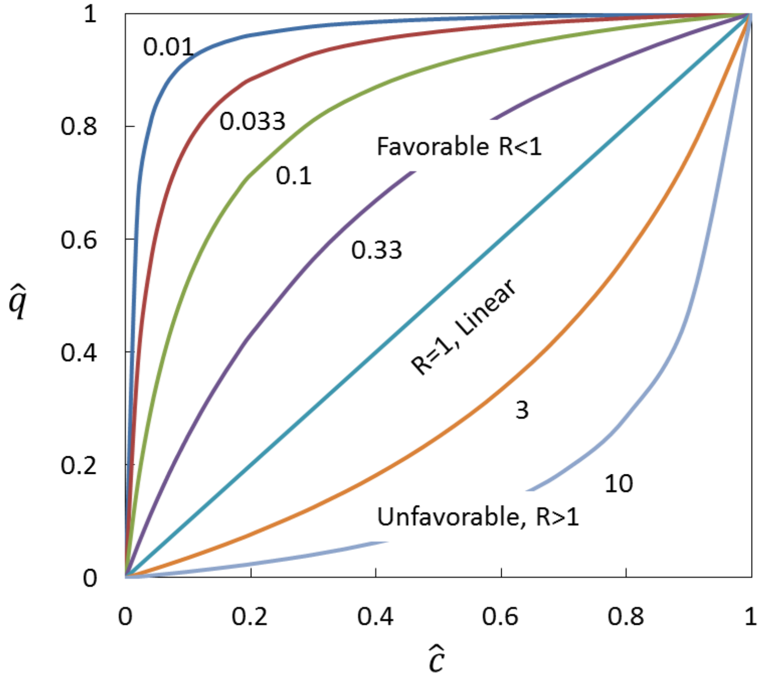

Figure 4.2 Relationship between separation factor and type of isotherm

The separation factor R is generally a function of concentration c. However, for the Langmiur isotherm, R is constant and depends only on the initial feed concentration c_0. This "constant separation factor" characteristic is one great advantage of the Langmiur equation [6]. The constant separation factor for Langmiur equation is:

$$R = \frac{1}{1 + k_L c_0} \tag{4.9}$$

Using the separation factor, the Langmiur equation can be rewritten:

$$\hat{q} = \frac{\hat{c}}{R + (1 - R)\hat{c}} \tag{4.10}$$

Where $\hat{q}$ and $\hat{c}$ are dimensionless concentrations defined as $\hat{q} = \frac{q}{q_0}$ and $\hat{c} = \frac{c}{c_0}$.

4.4. Constant pattern behavior

When the equilibrium isotherm is linear or unfavorable, the mass transfer zone (MTZ) broadens continuously as the front progresses through the sorbent bed. However, if the isotherm is favorable, the width of the MTZ approaches a constant, and the concentration profile in the mass transfer zone approaches a constant-pattern form. The formation of a constant pattern profile can be explained by the following argument.

In the mass transfer zone, the velocity u_c of concentration front is determined by equation 4.11[7] [8].

$$u_c = \frac{u_0}{(1 - \varepsilon_b)\frac{\partial q^*}{\partial c} + \varepsilon_b} \tag{4.11}$$

Equation 4.11 shows that the local velocity of concentration front is a function of $\frac{\partial q^*}{\partial c}$. For a favorable isotherm, $\frac{\partial q^*}{\partial c}$ is a decreasing function of c. As shown in Figure 4. **4** (a), the c at the leading front of the MTZ is small, while the c at rear part of the MTZ is close to c_0, therefore $(\frac{\partial q*}{\partial c})_{front} > (\frac{\partial q*}{\partial c})_{rear}$. According equation 4.11, a greater value of $\frac{\partial q^*}{\partial c}$ leads to a smaller value of u_c; this means that the trailing part of the MTZ will propagate faster than the leading part. As a result, the MTZ is compressive or “self-sharpening” as it progresses through the bed [9, 10]. This compressive effect is counterbalanced by the dispersive effect that results from axial dispersion and mass transfer resistance, and the concentration profile will eventually converge to the limiting “constant pattern” form. The combination of the constant pattern approximation and the mass balance equation leads to an important relationship between $\bar{q}$ and c [2, 6], which is referred to as the constant pattern condition:

$$\frac{c}{c_0} = \frac{\bar{q}}{q_0} \tag{4.12}$$

This can be rewritten as:

$$\bar{q} = K_0 c \tag{4.13}$$

Where the equilibrium constant K_0 is defined as $K_0 = \frac{q_0}{c_0}$ and q_0 is the solid phase concentration in equilibrium with c_0. As determined by analogy with absorption operation, the relationship between mass transfer driving force and equilibrium curve is shown in Figure 4.3. It is evident that the more favorable isotherm (curve II) has a greater driving force than the less favorable one (curve I). As shown in Figure 4.3, for a local fluid phase concentration c in the MTZ, the corresponding solid phase concentrations on the operating line and isotherm are $\bar{q}$ and q^*, respectively. Therefore, the local driving force at an arbitrary fluid phase concentration (c) can be represented as $(q^* - \bar{q})$ or $(c-c^*)$.

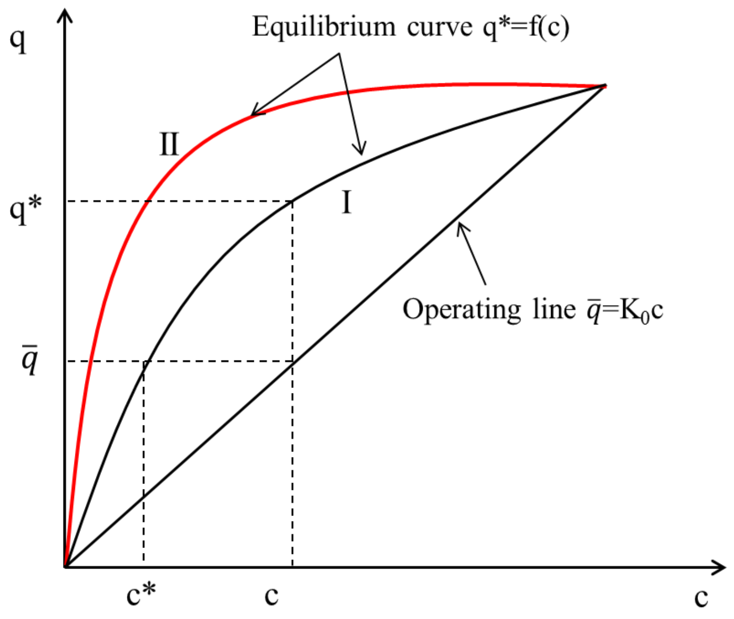

Figure 4.3 Adsorption operating line and equilibrium curve

4.5. Mass transfer zone and breakthrough curve

As shown in Figure 4. **4** (a), the mass transfer zone is the region where the fluid phase concentration drops from near feed value ($0.99c_0$) to near zero ($0.01c_0$). Upstream of the MTZ, the adsorbent is saturated, while downstream of the MTZ, the bed is free of gas. In the MTZ, if the transition profile is symmetric, only half of the adsorbent capacity is used. In other words, the length of unused bed (LUB) is equal to half of the length of the MTZ (Z_c).

The breakthrough curve, as shown in Figure 4. **4** (b), is the direct reflection of the adsorption wave at the outlet of the adsorbent bed. The shapes of transition profile and the breakthrough curve are in mirror symmetry. Typically, the breakthrough concentration c_b is defined as 1% (or 5%) of c_0, the saturation concentration c_s is defined as 99% (or 95%) of c_0, t_b is the break time associated with the c_b, and $t_{1/2}$ is the half break time (i.e., the time when outlet concentration reaches $0.5c_0$), which is equal to the stoichiometric time (or capacity) τ for a symmetrical breakthrough curve. In most cases, $t_{1/2}$ is a good approximation of τ without significant deviation.

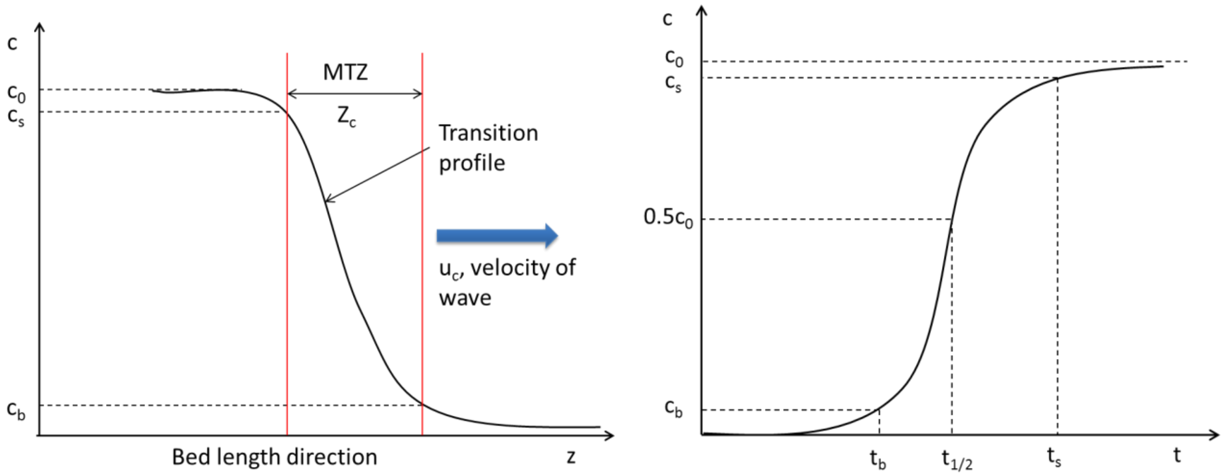

Figure 4. 4 (a) MTZ and concentration profile (b) breakthrough curve of adsorption

The local uptake rate in the mass transfer zone (MTZ) depends on the driving force (c-c*), along with the mass transfer coefficient. As shown in Figure 4.3, the magnitude of the driving force depends on the shape of the equilibrium curve. For instance, the more favorable isotherm (curve II) has a greater driving force than the less favorable isotherm (curve I). On the other hand, the mass transfer coefficient depends on many factors, such as particle size, flow rate, pore structure, etc. It can be concluded that both the isotherm and mass transfer rate have significant influence on the rate of uptake in the MTZ, and together they determine the width of the MTZ and the shape of the concentration profile. In practice, to decrease the length of unused bed

(LUB) or increase the percent utilization of the bed, a compact MTZ is desired. It is evident that both a highly favorable isotherm and a high mass transfer coefficient will lead to a short MTZ.

4.6. External and Internal Mass transport

As shown in the Figure 4.5, the adsorption of gas from the air to adsorbent may involve one or more of the following steps: (a) the external mass transfer of adsorbate from bulk fluid to the exterior surface of the sorbent through a gas film (boundary layer); (b) internal diffusion by means of molecular diffusion, Knudsen diffusion, and surface diffusion; (c) adsorption of the molecules on the active site of adsorbent. Generally, the physisorption process is adequately fast so that the overall rate of adsorption is controlled by the mass transfer steps, i.e., steps (a) and (b). It is of interest to note that intracrystalline pore diffusion is not involved for hexane adsorption onto activated carbon, because hexane molecules are only adsorbed on the surface of the crystalline rather than inside the crystalline.

The following discussion attempts to combine all of the four mass transfer resistances into one overall mass transfer resistance, and to apply this overall resistance in the rate law equation.

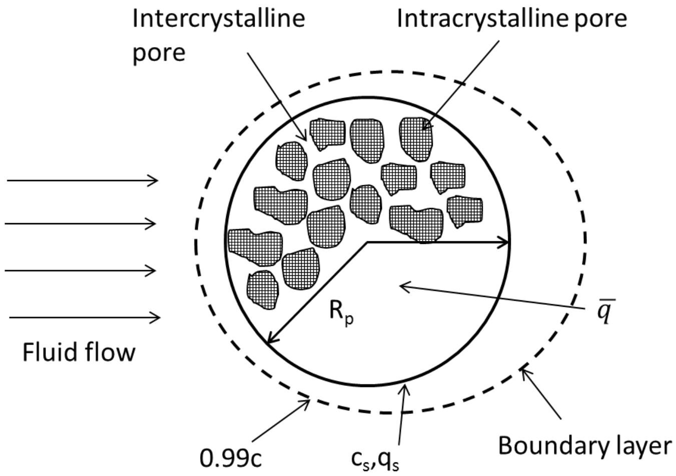

Figure 4.5 Diagram of adsorbent pellet.

Where c is the adsorbate concentration in bulk fluid; q_s, c_s is the respective exterior surface concentration in solid phase and gas phase; $\bar{q}$ is the average solid phase concentration.

4.6.1. External mass transfer

When the adsorbate flows through the packed bed, the local adsorption rate through external film diffusion can be described by equation 4.14. The term $\frac{\partial \bar{q}}{\partial t}$ represents the local uptake rate from the bulk fluid phase to the adsorbent phase. The adsorbate concentration gradient between the bulk fluid and the external surface of adsorbent ($c-c_s$) acts as the mass transfer driving force, while k_f is the external mass transfer coefficient, and α is the bed's external surface area to volume ratio.

$$(1-\varepsilon_b)\frac{\partial \bar{q}}{\partial t} = k_f \alpha (c - c_s) \tag{4.14}$$

According to the boundary layer theory, the solid-to-fluid mass transfer coefficient is

$$k_f = \frac{D_m}{\delta} \tag{4.15}$$

Where, δ is the average thickness of boundary layer.

The external mass transfer coefficient is the greatest concern for MFES, because it is the primary reason for an enhanced adsorption rate. In this respect, a detailed analysis was conducted, with particular attention paid to the effect of fibers on the formation of plug flow conditions, and the thickness of boundary layer surrounding the particles.

The boundary layer theory was first introduced by Ludwig Prandtl in 1904. He divided the flow field surrounding the submersed object into two regions: one within the boundary layer (close to the solid surface) where viscosity is significant, and one outside the boundary layer where the effect of viscosity is negligible, and the fluid can be treated as inviscid. The flow inside the boundary layer can be laminar or turbulent. For the turbulent boundary layer, a very thin laminar (viscous) sublayer adjacent to the solid surface exists. Nearly all resistance to heat and mass transfer is found in this relatively stagnant laminar layer (for the laminar boundary layer) or in the viscous sublayer (for turbulent boundary layer).

In chemical engineering, this boundary layer is also known as the stagnant gas film. Like the hydrodynamic boundary layer, the mass transfer boundary layer thickness, δ, is defined as the distance from the solid surface to where the concentration reaches 99% of the bulk concentration. In turbulent fluid, the mass transfer process is enhanced by additional transverse motion (fluctuation) and eddies, whereas in the laminar fluid, the mass transfer can only occur through molecular diffusion. Typically, molecular diffusion is much slower than direct mass exchange by bulk motion. Based on the above analysis, it was determined that the thin boundary layer is ideal for reducing the mass transfer resistance.

Generally, the viscous sublayer (in a turbulent boundary layer) is much thinner than the laminar boundary layer. This is the underlying reason for turbulent flow’s significant enhancement of the momentum, heat and mass transport. However, in common operation conditions, the flow in packed beds or MFES media is in the regime of laminar flow, or is in a transition region where the turbulent effect on the thickness of the boundary layer is not significant. Nevertheless, it is still possible to decrease the thickness of the boundary by hindering the development of the boundary layer.

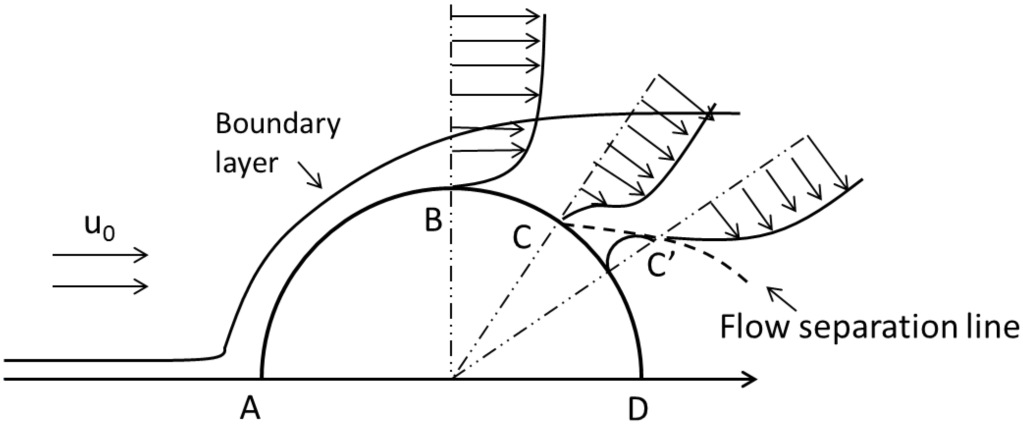

A is the stagnant point, from where the thickness of boundary layer increases; C is the flow separation point where the flow becomes detached from the surface of the object; C', back flow, eddies and vortices occur behind point C'.

Figure 4.6 Boundary layer development and flow separation

As shown in Figure 4.6, from the stagnant point A, the boundary layer thickness increases as the fluid flows around the object, thereby increasing the resistance to heat and mass transfer. However, after point C, flow separation occurs, causing the reverse pressure gradient to produce back flow; eddies and vortices are formed in this region as well. The flow separation and eddies cause substantial mechanical energy loss due to the enhanced momentum exchange (increased friction), but they also enhance the mass and heat exchange. The development of the boundary layer in a packed bed is very complicated. The surface roughness of the particles, the interference between particles, and many other factors have an impact on the development of the boundary layer. Any additional interference that causes turbulence and hinders the development of boundary layer is beneficial to enhancement of heat and mass transport. This effect has been observed in heat exchangers [11]. When the fluid flows through the staggered tube rows, the heat exchange rate is enhanced due to the additional turbulence caused by the staggered configuration as shown in Figure 4.7 (a) and (b).

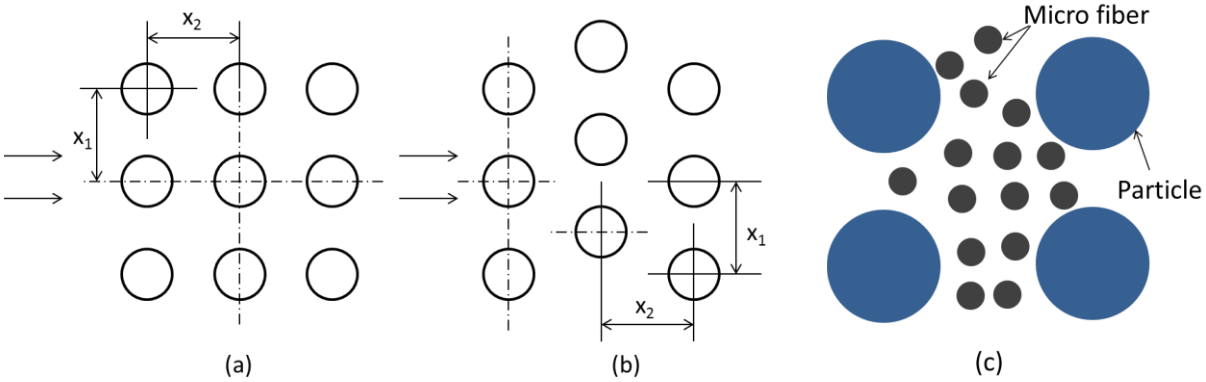

Figure 4.7 (a) Aligned tube rows; (b) Staggered tube rows; (c) Particles surrounded by microfibers in MFES

The Nusselt number in these two different configurations can be correlated using Re and Pr by the following equations [11]:

Aligned rows:

$$Nu = 0.52Re^{0.5}Pr^{0.36} \tag{4.16}$$

Staggered rows:

$$Nu = 0.71Re^{0.5}Pr^{0.36} \tag{4.17}$$

By comparing equations 4.16 and 4.17, we find that the Nu in staggered rows is increased by 36.5% compared to that in aligned rows. The heat transfer enhancement is mainly due to the additional turbulence caused by the fluid block and the separation effect of staggered tubes. The additional turbulence hinders the development of boundary layer, and hence decreases the average thickness of boundary layer. The mass transfer process is analogous to heat transfer, thus similar enhancement can be anticipated due to the decrease of boundary layer thickness.

As shown in Figure 4.7(c), some proposed effects as a result of fibers surrounding the particles are summarized as follows: (1) they will act as the obstacles on the pathway of fluid flow and hinder the development of the laminar boundary layer; (2) they will increase the roughness of particles, and hence increase the turbulence of flow; (3) they will increase the static mixing effect. All of the above mentioned effects have a positive impact on decreasing the thickness of the boundary layer surrounding the particles, therefore increasing the mass transfer coefficient.

4.6.2. Internal mass transport

The linear driving force approximation for intraparticle diffusion was first used by Glueckauf et al [12]. More recently, Rice [13] provided a simpler derivation based on the assumption that the solid phase concentration distribution inside the pellet is parabolic, i.e.,

$$q = a_0 + a_2 r^2 \tag{4.18}$$

Using the linear driving force approximation, the intraparticle diffusion rate can be expressed as:

$$\frac{\partial \bar{q}}{\partial t} = k_p (q_s - \bar{q}) \tag{4.19}$$

Where k_p is the so-called intraparticle mass transfer coefficient; q_s is the solid phase concentration of adsorbate at the exterior surface of pellet; $\bar{q}$ is the average solid phase concentration of adsorbate in the pellet.

The complexity of the external mass transfer problem arises from the calculation of the thickness of the boundary layer, which is influenced by many factors. Conversely, the complexity of the internal mass transfer problem arises from the multiple mechanisms involved. Generally, when a gas species diffuses into porous particles, five different diffusion mechanisms may be involved. These five mechanisms include molecular diffusion, Knudsen diffusion, surface diffusion, intracrystalline diffusion, and pressure flow. The pressure flow is caused by the pressure gradient across the particles. This effect is usually negligible in a packed bed [6]. In this study, the effects of pressure flow and intracrystalline diffusion were neglected.

In a complicated heat transfer problem, such as conduction with resistances in series and parallel, the total thermal resistance is usually analyzed by using a thermal circuit, which is analogous with electrical circuit. The addition rule for electrical circuits also applies for thermal circuits.

Addition rule 1 (resistances in series):

$$R = R_1 + R_2$$

Addition rule 2 (resistance in parallel):

$$\frac{1}{R} = \frac{1}{R_1} + \frac{1}{R_2}$$

This circuit analysis method was also useful for analysis of the mass transport resistance when multiple mass transfer processes were involved. Based on the existing adsorption theory (neglecting the pressure flow and intracrystalline diffusion), a mass transfer circuit is depicted as in Figure 4. 8.

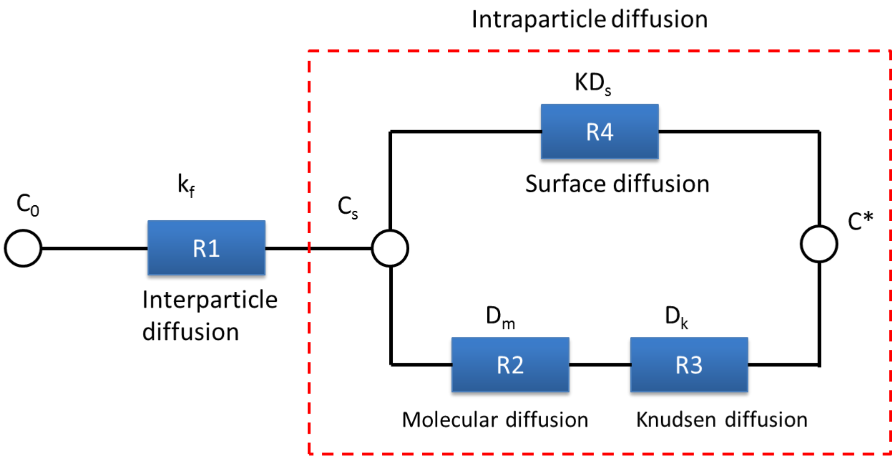

Figure 4. 8 Schematic diagram of equivalent mass transfer circuit (EMTC) for adsorption process.

It is evident that the external mass transfer resistance is in series with the internal mass transfer resistance. For internal mass transport, two different mechanisms exist, each of which will happen in different phase. Pore diffusion will occcur in gas phase and surface diffusion will occur in solid phase. Pore diffusion and Surface diffusion will carried out parallel to one another, because since these two processes are independent of each other. For pore diffusion, two different resistances exist: molecular diffusion resistance and Knudsen diffusion resistance. Molecular diffusion resistance arises from the collision between molecules, while Knudsen diffusion resistance arises from the collision between molecules and pore's wall. It is obvious that these two resistances are in series. When the pore is relatively large (compared to the mean free path of molecules), Knudsen diffusion effect is negligible. However, when the pore size is comparable to the mean free path, Knudsen diffusion resistance becomes important.

When it is necessary to determine the dominating mass transport resistance, it is important to know the following principle: when the resistances are in series, the greater resistance (i.e., the slower step for mass transport) controls the overall rate, whereas when the resistances are in parallel, the smaller resistance (i.e., the faster step) will dominate the overall rate. For instance, surface diffusion and pore diffusion work in parallel, so the faster process is the dominating process. However, molecular diffusion and Knudsen diffusion are in series, so the slow process is the dominating one.

Now we are going to lump these three internal mass transfer resistances using the simple addition rule of circuits.

The molecular and Kundsen diffusion are in series, so the total resistance of pore diffusion is:

$$R_p = R_m + R_K = \frac{\tau_p}{D_m} + \frac{\tau_p}{D_K} \tag{4.20}$$

Where R_p is the total resistance of pore diffusion; R_m and R_K are the resistances of molecular diffusion and Knudsen diffusion, respectively; τ_p is the tortuosity factor; D_m is the molecular diffusivity; D_K is the Knudsen diffusivity. Here the resistance is represented as the reciprocal of diffusivity.

The surface diffusion is in parallel with the pore diffusion so Addition rule 2 applies. The diffusivity is equal to the reciprocal of diffusion resistance (a similar relationship to electrical resistance and conductance). The overall intraparticle diffusion resistance (and the effective intraparticle diffusivity) can be calculated by the following equation [14]:

$$\frac{1}{R_e} = \frac{1}{R_p} + \frac{1}{R_s} = \frac{1}{\frac{\tau_p}{D_m} + \frac{\tau_p}{D_K}} + \frac{1-\varepsilon_p}{\varepsilon_p}\frac{KD_s}{\tau_s} = D_e \tag{4.21}$$

Where D_e and R_e are the effective intraparticle diffusivity and the effective intraparticle mass transfer resistance, respectively; D_s is the surface diffusivity; τ_s is the surface diffusion tortuosity factor. Experimental tortuosity factors generally fall with the range of 2-6 [6], in this study, assuming $\tau_p = \tau_s = 4$. Provided that the formula to calculate the effective intraparticle diffusivity (D_e) can be obtained, we can now calculate the intraparticle mass transfer coefficient (k_p) using the existing expression. Glueckauf and Rice [12, 13] gave an expression to correlate k_p and D_e.

$$k_p = \frac{60\varepsilon_p D_e}{d_p^2 K} \tag{4.22}$$

4.6.3. Combination of external and internal mass transfer rate equations

In the external and internal mass transfer equations, the variables c_s and q_s are unknown, so they need to be eliminated. By combining the external rate equation (equation 4.14) and the internal rate equation (equation 4.19), we can obtain the overall mass transfer rate equation:

$$(1 - \varepsilon_b)\frac{\partial \bar{q}}{\partial t} = k_G \alpha (c - c^*) \tag{4.23}$$

Where c* is the fluid phase concentration in equilibrium with the average solid phase concentration $\bar{q}$. $k_G \alpha$ is the overall volumetric mass transfer coefficient. The relationship between $k_G \alpha$ and the external and internal mass transfer coefficient is given by:

$$\frac{1}{k_G \alpha} = \frac{1}{k_f \alpha} + \frac{1}{(1 - \varepsilon_b) k_p K_0} \tag{4.24}$$

Assuming the general isotherm equation is:

$$q^* = f(c) \tag{4.25}$$

Then the relation between c* and $\bar{q}$ can be expressed as:

$$c^* = f^{-1}(\bar{q}) \tag{4.26}$$

Applying the constant conditions:

$\bar{q} = K_0 c$

The adsorption rate equation (equation 4.23) can be expressed as:

$$(1-\varepsilon_b)K_0\frac{\partial c}{\partial t} = k_G\alpha\big(c - f^{-1}(K_0 c)\big) \tag{4.27}$$

Appling the boundary conditions

$c = 0.5c_0\ at\ t = t_{1/2}$

Equation 4.27 can be rearranged and integrated as:

$$t = t_{1/2} + \frac{(1-\varepsilon_b)K_0}{k_G\alpha}\int_{\frac{c_0}{2}}^{c}\frac{dc}{c - f^{-1}(K_0 c)} \tag{4.28}$$

For Langmiur isotherms, the analytical solution for equation 4.28 is [2]:

$$\left[\ln(2P) - \frac{1}{1+k_L c_0}\ln 2(1-P)\right] = \frac{1}{(1-\varepsilon_b)K_0}k_G\alpha\left(t - t_{\frac{1}{2}}\right) \tag{4.29}$$

Where the dimensionless concentration $P = c/c_0$.

If axial dispersion is significant, the effect of axial dispersion can be considered as a mass transfer resistance, and may be lumped into the overall mass transfer coefficient[15].

$$\frac{1}{k_G\alpha} = \frac{1}{k_f\alpha} + \frac{1}{(1-\varepsilon_b)k_p K_0} + \varepsilon_b\frac{D_z}{u_0^2} \tag{4.30}$$

Where the term $\varepsilon_b\frac{D_z}{u_0^2}$ represents the additional mass transfer resistance caused by axial dispersion.

4.6.4. Parameters estimation

The molecular diffusivity D_m is estimated by Fuller's equation [3].

$$D_m = \frac{10^{-3}T^{1.75}(\frac{1}{M_A}+\frac{1}{M_B})^{\frac{1}{2}}}{P[(V_A)^{\frac{1}{3}}+(V_B)^{\frac{1}{3}}]^2} \tag{4.31}$$

Where D_m is the molecular diffusivity in cm^2/s; the molecular weight of air M_A=28.97 g/mol; the molecular weight of hexane M_B=86.18 g/mol; the total pressure P=1.0 atm; the temperature T=294K; the diffusion volume of air V_A=20.1 cm^3/mol; the diffusion volume of hexane V_B=126.721 cm^3/mol. The calculated molecular diffusivity is 0.075 cm^2/s or 7.5×10^{-6} m^2/s.

When the system's pressure is low, or the pore is small, the mean free path of the gas molecule might be greater than pore diameter. In this case, the resistance due to Knudsen diffusion becomes relevant. The significance of Knudsen diffusion can be determined by Knudsen number.

The mean free path can be estimated by equation 4.32. Its magnitude may be estimated by the following equation [Perry book, 5-54]

$$\lambda = \frac{3.2\mu}{P}(\frac{RT}{2\pi M})^{\frac{1}{2}} \tag{4.32}$$

Where λ is the mean free path in m, the viscosity of air $\mu=1.83\times10^{-5}$ kg/(m·s) at 294 K; the pressure $P=1.01\times10^{-5}$ Pa; the gas constant R=8.314 J/(mol·K); the molecular weight of hexane M=0.08618 kg/mol. The calculated mean free path is 3.9×10^{-8} m.

The Knudsen number (Kn) is defined as the ratio of the molecular mean free path to the average pore diameter. When Kn<<1, Knudsen diffusion resistance is negligible; when Kn>>1, the Knudsen diffusion become the dominant resistance.

$$Kn = \frac{\lambda}{d_{pore}} \tag{4.33}$$

In this study, the average pore diameter (d_{pore}) for activated carbon is 1.92×10^{-9} m. The corresponding Knudsen number is 20.3, which is higher than one, so the continuum assumption of fluid is no longer valid, and the Knudsen diffusion becomes the rate control mechanism in the pore diffusion.

The Kundsen diffusivity D_K can be estimated by [16]

$$D_K = 4850 d_{pore} (\frac{T}{M})^{1/2} \tag{4.34}$$

D_K is the Knudsen diffusivity in cm^2/s; the average pore diameter $d_{pore}=1.92\times10^{-7}$ cm; the temperature T=294K; the molecular weight of hexane M=86.18g/mol. The calculated value of $D_K=1.72\times10^{-3}$ cm^2/s.

Surface diffusion is present in parallel with the pore diffusion in the intraparticle diffusion process. Although the mobility of the adsorbed phase adsorbate is generally much smaller than that of gas phase, the concentration, which is close to the condensed phase, is much higher, so the contribution of surface diffusion might be significant [6]. It is of interest to note that the significance of surface diffusion depends on the product K_0D_s rather than on D_s alone [14]. However, the measurement of D_s is still a big challenge for current technology.

4.7. Conclusion

An analytical adsorption model based on the Langmuir isotherm, linear driving force approximation, and constant pattern wave theory was developed. The physisorption process is controlled by the mass transport; however, multiple mass transfer steps are involved in the adsorption process. The relationship between all present mass transfer steps is not straightforward. Therefore, in this study, a mass transfer circuit (which is analogous with electrical circuit) was developed to understand the relationship between multiple mass transfer steps, and to analyze the overall mass transfer resistance. Through the mass transfer circuit, we can clearly see that the external and internal mass transfers are in series, and therefore their transport resistances are additive. For the internal mass transport, the pore diffusion and surface diffusion are two parallel processes, and therefore their diffusivities (reciprocal of resistance) are additive. Meanwhile, molecular diffusion and Knudsen diffusion are two different mechanisms for pore diffusion, and their resistances are in series. The overall resistance is calculated by adding all four mass transfer resistances based on the circuit.

Reference

[1] Klotz IM. The Adsorption Wave. Chemical Reviews. 1946;39(2):241-68.

[2] Zhang X, Chen S, Bi HT. Application of wave propagation theory to adsorption breakthrough studies of toluene on activated carbon fiber beds. Carbon. 2010;48(8):2317-26.

[3] Perry R. Perry's Chemical Engineers' Handbook: McGraw-Hill Professional; 2007.

[4] Kapoor A, Ritter JA, Yang RT. On the Dubinin-Radushkevich equation for adsorption in microporous solids in the Henry's law region. Langmuir. 1989;5(4):1118-21.

[5] Donohue MD, Aranovich GL. Classification of Gibbs adsorption isotherms. Advances in Colloid and Interface Science. 1998;76–77(0):137-52.

[6] Ruthven DM. Principles of Adsorption and Adsorption Processes: Wiley-Interscience; 1984.

[7] Hwang Y-L. Wave Propagation in Mass-Transfer Processes: From Chromatography to Distillation. Industrial & Engineering Chemistry Research. 1995;34(8):2849-64.

[8] DeVault D. The Theory of Chromatography. Journal of the American Chemical Society. 1943;65(4):532-40.

[9] Sabio E, Zamora F, Gañan J, González-García CM, González JF. Adsorption of p-nitrophenol on activated carbon fixed-bed. Water Research. 2006;40(16):3053-60.

[10] Lua AC, Jia Q. Adsorption of phenol by oil–palm-shell activated carbons in a fixed bed. Chemical Engineering Journal. 2009;150(2–3):455-61.

[11] V JHL, IV JHL. A Heat Transfer Textbook: Dover Publications; 2011.

[12] Glueckauf E. Theory of chromatography. Part 10.-Formulae for diffusion into spheres and their application to chromatography. Transactions of the Faraday Society. 1955;51(0):1540-51.

[13] Rice RG. Approximate solutions for batch, packed tube and radial flow adsorbers—comparison with experiment. Chemical Engineering Science. 1982;37(1):83-91.

[14] Schneider P, Smith JM. Adsorption rate constants from chromatography. AIChE Journal. 1968;14(5):762-71.

[15] Suzuki M. Activated carbon fiber: Fundamentals and applications. Carbon. 1994;32(4):577-86.

[16] Tien C. Adsorption Calculations and Modeling: Butterworth-Heinemann; 1995.

Chapter 5

Introduction to PEM Fuel Cell Contamination

5.1. Introduction to PEM fuel cells

Fuel cells, which differ from batteries, are electrochemical devices that convert chemical energy in fuels into electrical energy directly via electrode reactions [1]. Compared to a thermal engine, the fuel cells are not limited by Carnot efficiency. One of the main drivers for fuel cell development is the increasing concern about environmental protection and the energy crisis [2].

The advantages of fuel cells include:

(1) High efficiency and high power density. The cell efficiency can typically reach up to 40-60%. The efficiency can be further improved by using combined heat and power (CHP) systems [3].

(2) Zero emission. When hydrogen is used as fuel, the production of fuel cells is just H_2O; it is CO_2 emission free. This is the biggest advantage of fuel cells over internal combustion engines in automobile applications.

(3) Quiet operation and high stability. There are no moving parts for fuel cells, so it is very quiet and stable in operation.

(4) Modular structure. The fuel cell stack is comprised of standard fuel cell modules. It is easy to scale up and convenient for design and packing.

The potential commercial use of fuel cells is in three main applications: transportation, stationary power generation, and portable applications. The high efficiency and zero emission characteristics make fuel cells a competitive alternative to internal combustion engines (ICEs) in vehicles.

According to the type of electrolyte used, fuel cells can be classified into five types: 1) proton exchange membrane fuel cell (PEMFC), 2) alkaline fuel cell (AFC), 3) phosphoric acid fuel cell (PAFC), 4) molten carbonate fuel cell (MCFC), and 5) solid oxide fuel cell (SOFC). The major differences of various types of fuel cells are summarized in Table 5.1. Among these fuel cells, the PEMFC operates at the lowest temperature, and the sluggish reaction rate must be addressed by catalysts (typically Pt catalysts). This characteristic of PEMFC also makes it the fuel cell most vulnerable to contaminants. This study focuses on the contamination issue of PEMFC. The contamination issues for other types of fuel cells are quite different, and will not be discussed here.

Table 5.1 Summary of Major Differences of the Fuel Cell Types [1]

	PEMFC	AFC	PAFC	MCFC	SOFC
Electrolyte	Hydrated polymer ion exchange membranes	Potassium hydroxide in asbestos matrix	Immobilized liquid phosphoric acid in SiC	Immobilized liquid molten carbonate in $LiAlO_2$	Perovskites (ceramics)
Electrodes	Carbon	Transition metals	Carbon	Nickel and Nickel oxide	Perovskites
Operating temperature	40 - 80 ˚C	65 - 220 ˚C	205 ˚C	650 ˚C	600 – 1000 ˚C
Charge carrier	H^+	OH^-	H^+	CO_3^{2-}	O_2^-

External reformer for hydrocarbon fuels	Yes	Yes	Yes	No, for some fuels	No, for some fuels and cell designs
Product water management	Evaporative	Evaporative	Evaporative	Gaseous product	Gaseous product
Product heat management	Process gas + liquid cooling medium	Process gas + electrolyte circulation	Process gas + liquid cooling media	Internal reforming + process gas	Internal reforming + process gas

PEMFC uses a solid polymer membrane as the electrolyte. The development of Nafion (a fluorinated sulfonic acid polymer material) in the 1960s by DuPont was a milestone for PEMFC. Nafion is a good proton conductor with excellent thermal and mechanical stability and hence can be manufactured in very small thickness. DuPont now can produce a membrane of 2 mils or less. The reduction of membrane thickness is important to reduce electrical resistance and mass transfer resistance. The membrane must be hydrated to work well, so water management is critical for PEMFC. The low operating temperature (<100 ˚C) enables the PEMFC rapid start-up and allows use of a wide range of materials. However, the low temperature causes a sluggish anode and cathode reaction; this problem needs to be addressed by using highly active but expensive platinum (Pt) catalyst. In the early stage, the Pt loading is large and makes a significant portion of the entire cost of the fuel cell. The current technology has substantially improved catalyst performance, allowing the low Pt loading (less than 1.0 mg Pt/cm^2) electrolyte. Even though common PEMFC usually operates at temperatures less than 100 ˚C, the so-called high temperature PEM fuel cells (HT-PEMFCs) operate at temperatures above 100 ˚C. There are several technological reasons for operating at a higher temperature. Reaction rates at electrodes are increased, water management and cooling are simplified, and low purity hydrogen rich reformed stream can be used as fuel [4]. In addition, since the adsorption of CO on Pt is exothermic, the adsorption is disfavored at a high temperature [5]. At 130 ˚C, Pt based catalyst can tolerate up to 1000 ppm CO [6]. The major challenge for HT-PEMFCs is the development of high quality membrane.

The fuel used in PEMFC can either be pure hydrogen or reformer gas. Challenges for PEMFC include water and heat management, reduction of the amount of platinum on the catalyst, and improvement of the stack’s stability and life. When the fuel cells are operated in a polluted air environment, the fuel cell contamination is a big issue.

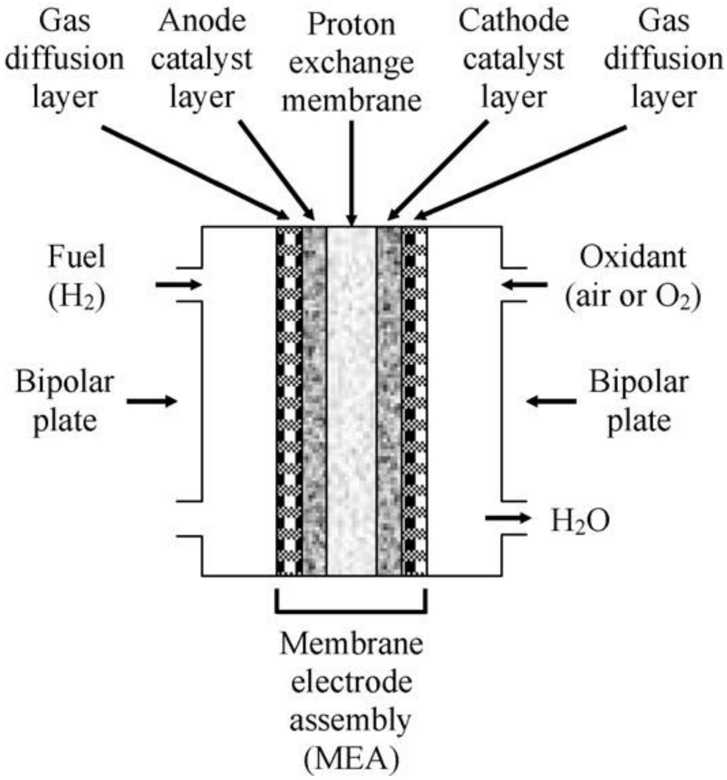

Figure 5.1 Structure of a PEM fuel cell

5.2. Fuel cell contamination issues

Impurities in hydrogen fuel and air will cause performance degradation and sometimes permanent damage to the membrane electrode assembly (MEA). MEA is the key component of PEM fuel cells, and it consists of anode and cathode catalyst layers (CLs), gas diffusion layers (GDLs), and a proton exchange membrane. The CL is typically several micrometers thick, and the most common catalyst is Pt supported on carbon. The CL is where electrochemical reactions take place. The reaction rate related processes involved in the CL include mass transport of reactants, surface reaction on the Pt surface (i.e., HOR at anode and ORR at cathode), proton transport, and electron conduction. When impurities are present in the reactants stream, one or more of the above processes can be negatively affected and thereby reduce the kinetics of reactions [7]. For PEM fuel cells, the CLs are considered the most vulnerable and sensitive to contamination issues [8].

The three major research areas on fuel cell contamination are:

1) Theoretical model to provide a fundamental understanding of the contamination mechanisms
2) Experimental observation of degradation and polarization curve
3) Developing Mitigation strategies

The MEA has been proven to be the component most affected by fuel cell contaminants. There exist three major poisoning effects: kinetic effect, conductivity effect, and mass transfer effect. Some major contaminants identified in PEM fuel cell operation are summarized in Table 5.2.

Table 5.2 Major contaminants encountered in the PEM fuel cell operation [8]

Contaminants source	Contaminants
Air	N2, NO_x, SO_x, NH_3, O_3
Hydrogen-rich reformate	CO, CO_2, H_2S, NH_3, CH_4
Bipolar metal plates	Fe^{3+}, Ni^{2+}, Cu^{2+}, Cr^{3+}
Polymer membrane	Na^+, Ca^{2+}
Sealing materials	Si
Coolant	Si, Al, S, K, Fe, Cu, Cl, V, Cr
Battlefield chemicals	SO2, NO2, CO, propane, benzene
Compressor	Oils vapor

5.2.1. Anode contamination

The anode contaminants are mainly from the fuel process, i.e., the reforming process. Currently, hydrogen is produced primarily through reformation of hydrocarbon, such as natural gases and methanol from biomass [9, 10]. Some other hydrogen production methods include partial oxidation [11, 12], electrolysis, and hydrolysis of sodium borohydride [13]. The gas produced from the reformation process is called “reformate,” a hydrogen-rich gas with a variety of undesired impurities such as CO, CO_2, and H_2S. A typical reformate gas contains 40-70% H_2, 15-25% CO_2, 1-2% CO and trace of sulfur compound [8].

5.2.1.1 CO contamination

10 ppm CO will significantly reduce the cell performance [1]. The reformate stream needs to pass through a separation unit, which is comprised of a thermal swing or pressure swing adsorption (PSA) system [14]. The benefit of a PSA system is that the process is fast, and it can operate continuously without disrupting the regeneration process.

A thermodynamics analysis was conducted by Yang et al. to analyze the temperature effect on catalyst tolerance. They found that catalyst tolerance is related to the thermodynamics of adsorption of CO and H_2 on Pt. CO adsorbs associatively, while the H_2 adsorbs dissociatively on Pt surface. The bond between Pt and CO is much stronger than between Pt and H, hence the active sites on the Pt surface are preferably occupied by CO. This preferential adsorption of CO will significantly reduce the activity of the Pt catalyst. The CO adsorption is favored at low temperatures since it is a highly exothermic process [15]. Dhar et al. [5] stated that the CO adsorption on Pt surface follows the Temkin isotherm at 298 K. Coverage of CO is dependent on the catalyst surface properties such as surface roughness [16, 17]. Electro-oxidation of CO is one of the approaches to mitigating the CO poisoning effect. The effect of electro-oxidation is dependent on the adsorption potential [18] and operating temperature [19].

$$CO(g) + Pt \rightarrow Pt\text{–}CO \tag{5.1}$$

$$H_2 + 2Pt \rightarrow 2Pt\text{–}H \tag{5.2}$$

Although the acidic membrane in PEMFCs has good tolerance to CO_2, the in situ production of CO from CO_2 makes CO_2 a harmful poisoning impurity [20]. The formation of CO is via the reverse water-gas shift reaction on platinum sites. Further thermodynamic calculation shows that the equilibrium concentration of CO can reach up to 20-100 ppm [20, 21].

In addition, the presence of CO together with CO_2 has a synergetic effect that further enhances the poisoning effect on the fuel cell performance [22].

To remove the CO and CO_2, Majlan et al. [23] developed a compact pressure swing adsorption (CPSA) system using activated carbon as the adsorbent. The adsorption pressure is 5.0 atm, while the desorption pressure is 1.0 atm. 99.999% H_2 purity can be achieved using this adsorption system.

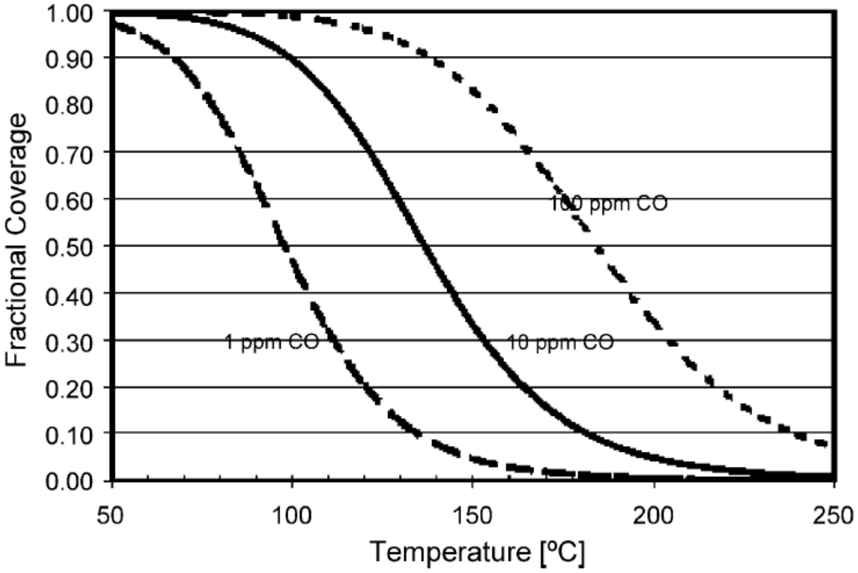

Figure 5.2 The CO coverage on Pt surface at various CO concentrations (1 to 100 ppm).

5.2.1.2 NH_3 contamination

A trace amount of NH_3 will result from significant fuel cell performance degradation [24-26]. Ammonia is mainly from the process of hydrogen production due to several causes, such as the reaction of N_2 and air in the reforming process and used as tracer gas in natural gas. Ammonia tends to form ammonium (NH4+) in the acidic polymer membrane (e.g., Nafion) because it is basic. The exchange effect of NH_4^+ and H^+ will reduce the membrane's proton conductivity. Ammonia in the fuel side can also contaminate the cathode side because it can cross the membrane via diffusion. It was reported that cathode contamination by NH_3 is caused by affecting the ORR at the cathode [27].

5.2.2. Cathode contamination

The kinetics of ORR at the cathode are typically much slower than that of HOR at anode, and, thereby, the cathode contamination issues have a more adverse effect on the fuel cell performance [28]. However, previous research has been so focused on anode contamination that cathode issues had been largely overlooked. This is mainly because the hydrogen-rich reformate, which contains many impurities such as CO, NH_3, and H_2S, is the most popular fuel for PEM fuel cells.

The air is the most economical oxidant to feed the fuel cells. The air contaminants are mainly from the industrial process and automobile emission. Common air impurities include SOx (SO_2 and SO_3), H_2S, NOx (NO and NO_2), ozone, and hydrocarbon such as propane, propylene.

5.2.2.1 SOx contamination

SOx, including the SO_2 and SO_3, are common contaminants in the cathode air stream. SO_2 is mainly from the combustion of coal and petroleum. SO_2 is a major air pollutant and is the major cause of acid rain. Typically, in urban areas with heavy traffic and in some developing countries where the coal is an important energy source, the SO_2 concentration is relatively high. SO_2 in the cathode air degrades the fuel cell performance mainly due to the adsorption of SO_2 on the Pt surface [29]. In addition, SO_2 is an acidic compound; it can change the PH value inside the MEA, resulting in performance degradation of the MEA.

Tests of the cumulative effect of contaminants at the EPA level are not practical. Therefore, accelerated durability tests are needed to aid the development of new material and filtration devices. The EPA levels of impurities in air can be found on the official website of the EPA. The allowable concentration for NO_2 and SO_2, are 100 ppb and 75 ppb, respectively [30].

Mohtadi et al. [31] tested some common air impurities, including NO_2, SO_2, and H_2S. They found that the poisoning rate of NO_2 doesn't strongly depend on the NO_2 concentration, and the cell performance can be totally recovered in neat air. However, the poisoning rate of SO_2 appears to be strongly dependent on the concentration of SO_2, and the cell performance can only be partially recovered after exposure to SO_2. They also compared the effects of SO_2 concentration and dosage on the performance of fuel cells. The experimental results in Figure 5.3 show that the fuel cell performance is more sensitive to the SO_2 concentration than to the total dosage. With the same total SO_2 dosage, 5 ppm SO_2/air exposure degrades the cell's performance by 78%, as compared to 53% degradation caused by 2.5 ppm SO2/air exposure.

In addition, the polarization curve (

Figure 5.4) shows that the SO_2 poison effect causes significant overpotential under steady state operation. The performance recovery from re-introducing neat air is small. However, the cell performance can be recovered by applying CV on the poisoned cathode.

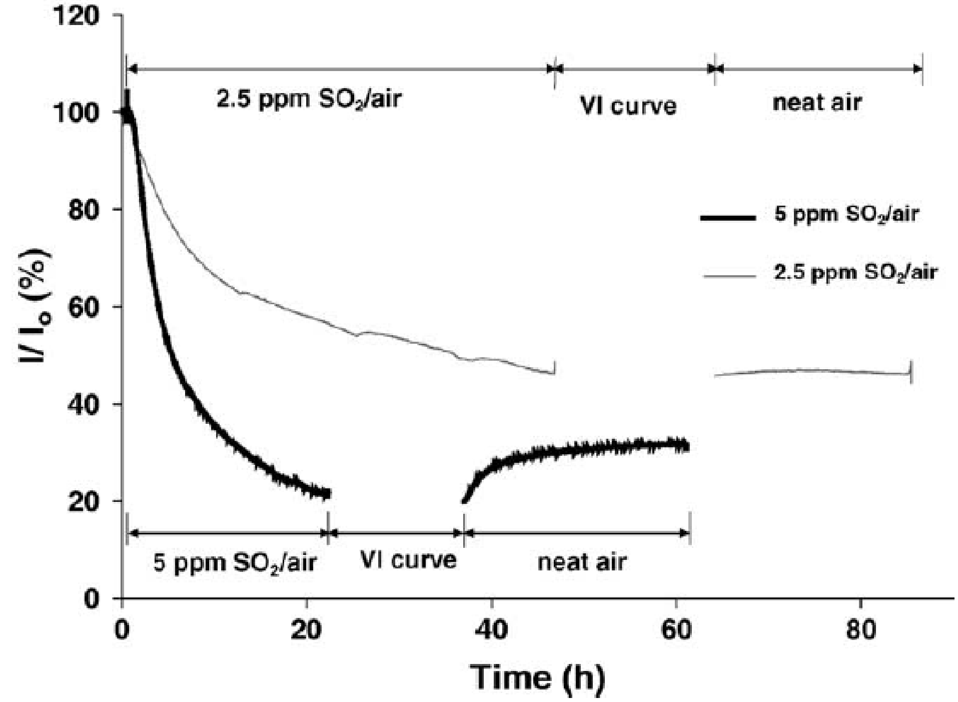

Figure 5.3 Current vs. time curve after exposure to 2.5 and 5 ppm SO2/air [31]

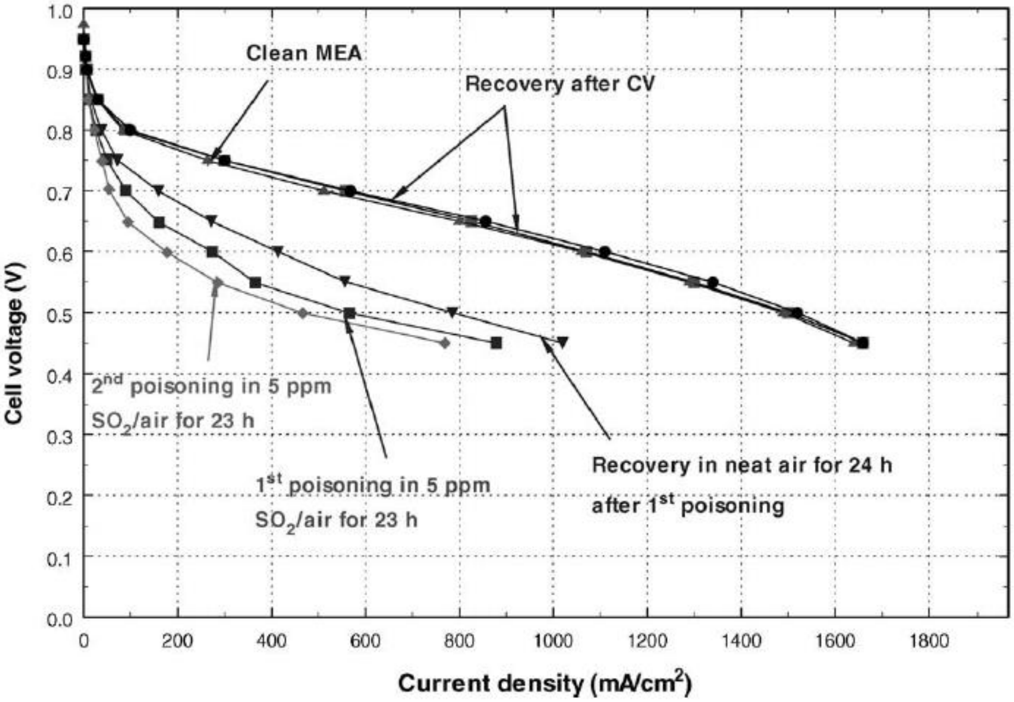

Figure 5.4 Polarization curve for steady state performance [31]

It was reported that the effect of SO_2 on the performance of the fuel cell varies with the operating voltage. Baturina et al. [32] studied the effect of 1 ppm SO_2 in air on the performance of fuel cells at operating voltages of 0.5, 0.6, and 0.7 V. As shown in Figure 5.5, the current density gradually decreases with time when the cathode was exposed to SO_2. They also found that the sulfur coverage on the catalyst decreases as the cathode potential increases after exposure to SO_2. The sulfur coverage approaches zero when the cells operate at 0.9 V. However, the sulfur coverage is not the only indicator of poison effect; sulfate/bisulfate ions are identified as the product of SO_2 adsorption at high voltage. The existence of sulfate/bisulfate on the Pt surface also impedes the ORR. They found that the cells operated at 0.6 V exhibited the highest tolerance to poisoning.

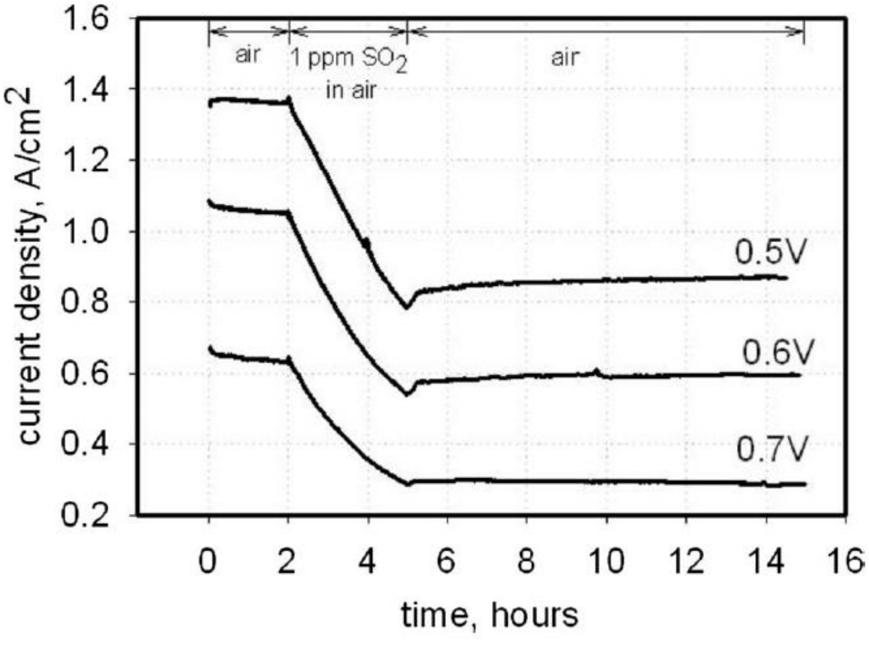

Figure 5.5 Current density with time at various operating voltage (0.5-0.7 V) after exposure to 1 ppm SO_2, 80 ˚C, and 100% RH [32]

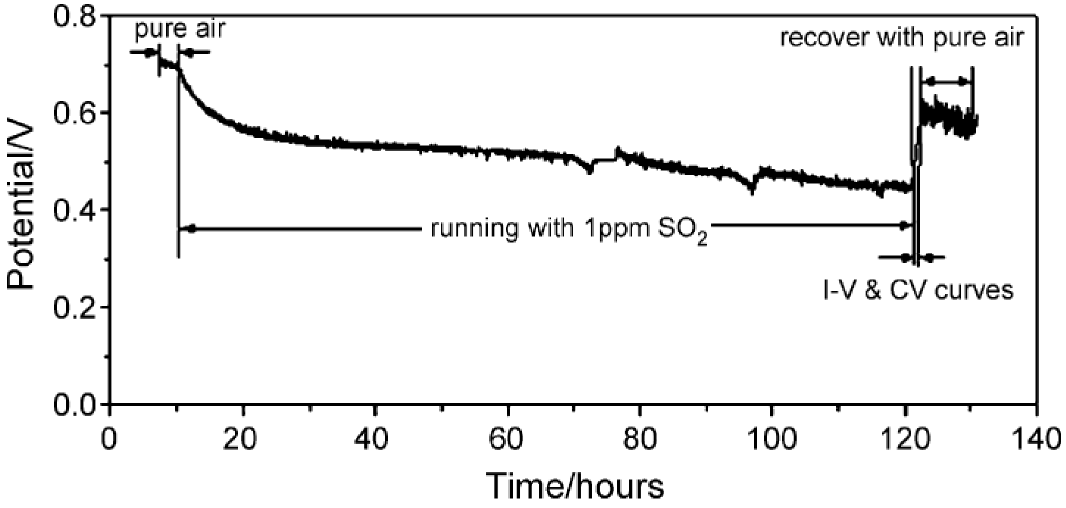

Figure 5.6 Potential vs. time curve after exposure to 1 ppm SO2/air, current density: 500 mA/cm2 [33]

Jing et al. [33] studied the cumulative effect of low concentration SO_2 (1 ppm) on the performance of fuel cells in a long term run. As shown in Figure 5.6, the cell voltage gradually decreases with time. After a 100 h run, the performance degraded by 35%, from 0.68 V to 0.44 V. The performance can be partially recovered by using CV scanning.

5.2.2.2 H_2S contamination

H_2S are usually present in the anode fuel feed; however, the H_2S poisoning effect can extend to the cathode because it can cross over the MEA from the anode side. Mohtadi et al.[31] used 200 ppm H_2S to test the cell performance degradation. The high concentration of H_2S almost completely deteriorated the cell after several hours of exposure. They found that the cell performance can be significantly recovered after CV scanning. Mathieu and Primet [35] proposed a poising mechanism as shown in equation 5.3. The H_2S strongly adsorbs on Pt and occupies the active sites that otherwise are available for ORR.

$$H_2S - Pt \rightarrow Pt - S + H_2 \tag{5.3}$$

The cell performance recovery by CV scanning can be explained by the following reactions:

$$Pt - S + 3H_2O \leftrightarrow SO_3 + 6H^+ + 6e^- + Pt \tag{5.4}$$

$$Pt - S + 4H_2O \leftrightarrow SO_4^{2-} + 8H^+ + 6e^- + Pt \tag{5.5}$$

Nagahara et al. [36] further pointed out that it was possible to completely recover cell performance by using high RH gas to flush the cathode and remove the adsorbed sulfate ions.

5.2.2.3 VOCs contamination

According to the U.S. Environmental Protection Agency, the “Volatile organic compounds (VOCs)” means any compound of carbon, excluding carbon monoxide, carbon dioxide, carbonic acid, metallic carbides or carbonates, and ammonium carbonate, which participates in atmospheric photochemical reactions. VOCs have a high vapor pressure at ordinary room temperature because of their low boiling point. The major sources of VOCs include solvents, paints and coatings, inks, glues, monomers, etc. In the battlefield, VOC concentrations are much higher. Moore et al. [38] studied the effect of VOC contaminants, including propane, benzene, sarin, sulfur mustard, and cyanogen chloride (CNCl), on the performance of PEM fuel cells. They found that the chemical warfare agent seriously degraded the performance of fuel cells.

Figure 5.7 shows the effect of benzene (50 ppm) in air on the performance of a PEM fuel cell. The cell potential decreased immediately as long as the benzene was introduced to the air stream. Withdrawal of benzene did stop the performance’s further degradation, but the cell performance was not recovered. However, after an excursion to open circuit potentials for 1 min, the cell performance was almost completely recovered. Figure 5.8 shows the effect of high concentration chemical warfare agents on the performance of the PEM fuel cell. The cell potential dramatically dropped to lower than 0.1 V after exposure to high concentration contaminants and then leveled off. The recovery was very limited when the contaminants were ended, indicating that the contamination effect was permanent.

Moore et al. also discussed the possible poisoning mechanisms of those contaminants. They proposed that the benzene contaminates the cell because it preferentially adsorbs onto the active site of catalyst and hence decreases the ORR. The contamination effect appears to be related to the cell's potential. The contamination effect is more significant at higher current densities corresponding to lower oxidizing potential [38]. The poisoning mechanism of HCN and CNCl is similar to benzene.

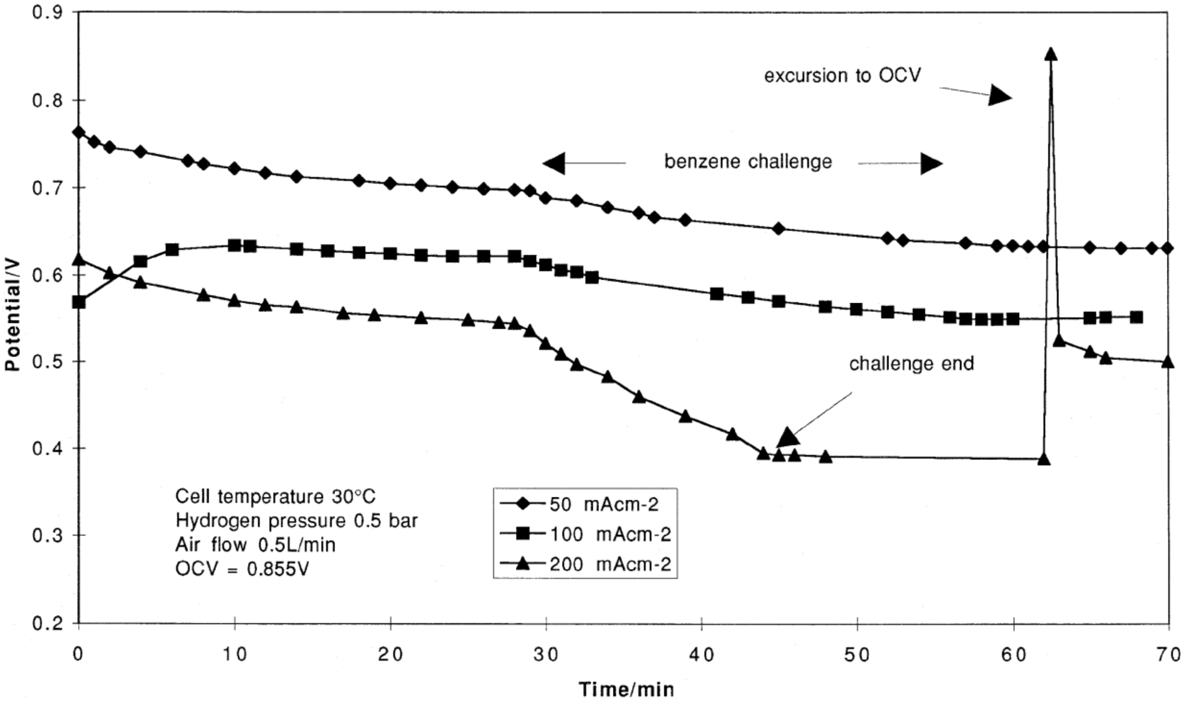

Figure 5.7 Effect of benzene (50 ppm) in air on the performance of PEM fuel cell [38]

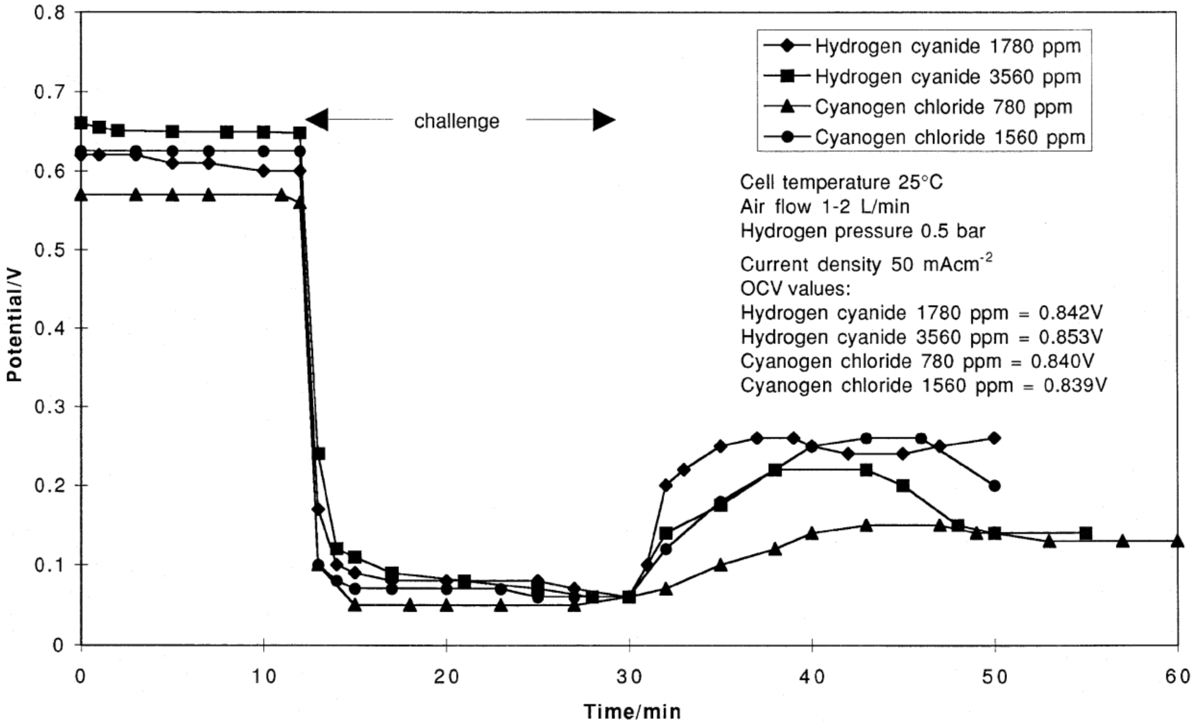

Figure 5.8, Effect of HCN and CNCl on the performance of PEM fuel cell [38]

Hui et al. [39-41] studied the effect of toluene on the performance of PEM fuel cells at different toluene concentrations and different operating conditions. Figure 5.9 shows the influence of toluene concentration at constant current density. The potential drops immediately after exposure to toluene gas and then reaches a steady state. The steady state potential appears to be a function of toluene concentration. Higher toluene concentration resulted in greater potential drops. The effect of toluene contamination was also impacted by the operating current density. When exposed to 50 ppm toluene, the power output dropped 5% at 50 mA/cm^2, compared to 28% at 200 mA/cm^2 [40]. In addition, they also studied the effects of other operating conditions such as RH, operating pressure, and air stoichiometric ratio. They found that increasing the RH and operating pressure reduced the contamination effect, while increasing the air stoichiometric ratio resulted in more severe poisoning. They also used alternating current (AC) impedance and CV techniques to investigate the toluene poisoning mechanism. They found that toluene poisoned the fuel cells by influencing either the ORR kinetics or the mass transfer process, but the former is the primary one. Further study on toluene adsorption and electrochemical reaction on the Pt electrode was conducted by Zheng et al. [39].

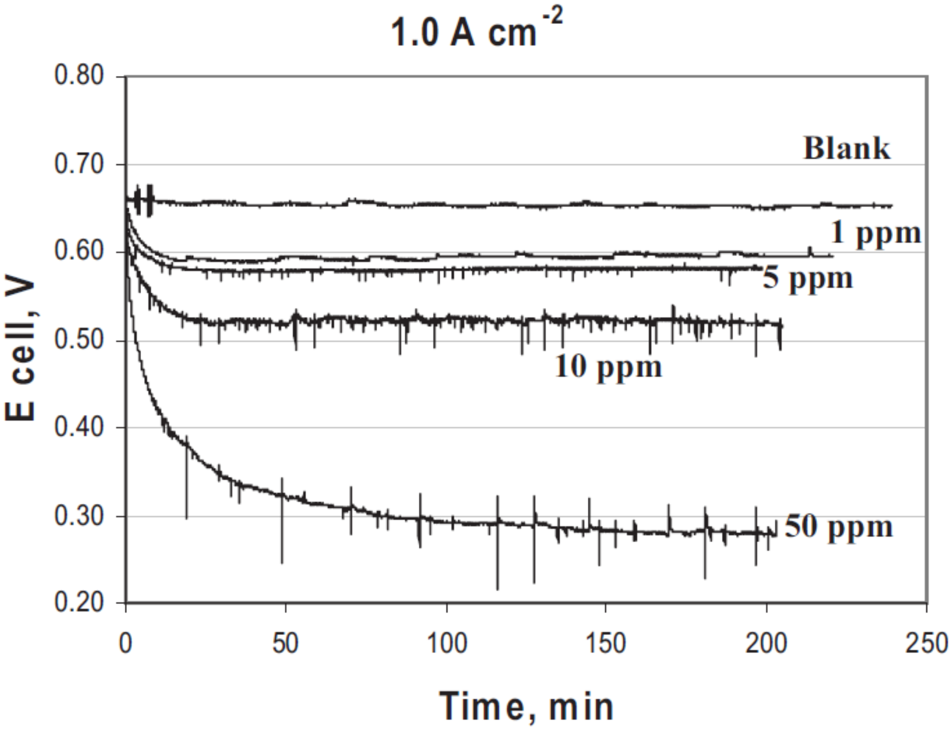

Figure 5.9, Effect of toluene concentration on the performance of PEM fuel cell [40]

5.2.2.4. Other contaminations

Some cations can enter the polymer membrane and compete with the proton for the SO^{3-} site (Nafion membrane) and hence decrease the proton conductivity of membrane. Collier et al. [64] stated that most cations, such as Cu^{2+}, Na^{+}, K^{+}, and Mg^{2+}, excluding Li^{+}, have a higher affinity to sulfonic acid, hence the membrane is quite vulnerable to foreign cations. The exchange between foreign cations and proton also changes the water content in the membrane. The reduction of water content will accelerate the mechanical degradation of the membrane.

Okada [65] reported that the ion contaminants also influence the oxygen reduction reaction at the cathode. Small amounts of ions will significantly slow down the ORR kinetics because the ions tend to adsorb onto the Pt surface and cover the active sites. Besides the cations, it was reported that the anion Cl^- will also significantly degrade the MEA performance [66]. In addition, metal ions such as Fe^{3+} can degrade the membrane because of the formation of peroxide. Typically, the membrane's conductivity decreases proportionately to the cation charge.

The formation of peroxy and hydroperoxy radicals during fuel cell operation will also degrade the polymer membrane. There are two proposed mechanisms to explain the formation of radicals. One mechanism is proposed by General Electric [65, 67], and another is proposed by Pazio et al. [68]. Pozio's proposal suggested that the formation of peroxide is from the incomplete reduction of oxygen on the Pt surface.

The metal impurities have a significant effect on the performance of MEA. St Pierre at Ballard Power Systems found that if the H^+ is replaced by Fe^{3+}, the open circuit voltage drops to near zero. But, this type of ion exchange effect is partially reversible. In addition, the MEA's tolerance to CO is substantially reduced due to metal contamination [8]. The operating conditions also affect the metal contamination effects. The speed of membrane degradation is dependent on the operating cell potential and the operating status; typically, the membrane degradation in transient operation proceeds much faster than that in steady state operation.

Due to the wide variety of possible contaminants in air, it is difficult to develop suitable, highly tolerant catalysts. Using a filtration system to filter the gas is the most practical approach to mitigate the cathode contamination effect.

5.3. VOCs treatment methods

5.3.1. Catalytic oxidation

In industrial processes, the VOCs and hydrocarbon fumes in the off-gas are typically removed in an afterburner or post-combustor. Thermal oxidation of VOCs requires a very high temperature, typically 800-900 ˚C. The high temperature will consume a lot of energy and produce undesired by-products, such as nitrogen oxides and CO.

Compared to thermal combustion, catalytic oxidation/combustion is an improved method to treat VOCs. It is widely used industrially to treat flammable solvent vapors, odors, and some other VOCs in the air. By means of oxidation catalysts, the required combustion temperature can be lowered to 200-400 ˚C. At the same time, the catalytic oxidation can also minimize the formation of undesired by-products. Precious metals such as Pt and Pd are well-established as efficient catalysts for oxidation of VOCs [42-44]. The catalytic oxidation process can typically provide very high conversion, up to 99.9%. Figure 5.10 shows a Topsoe catalytic combustion unit, which is suitable for air with medium or high concentrations of VOCs.

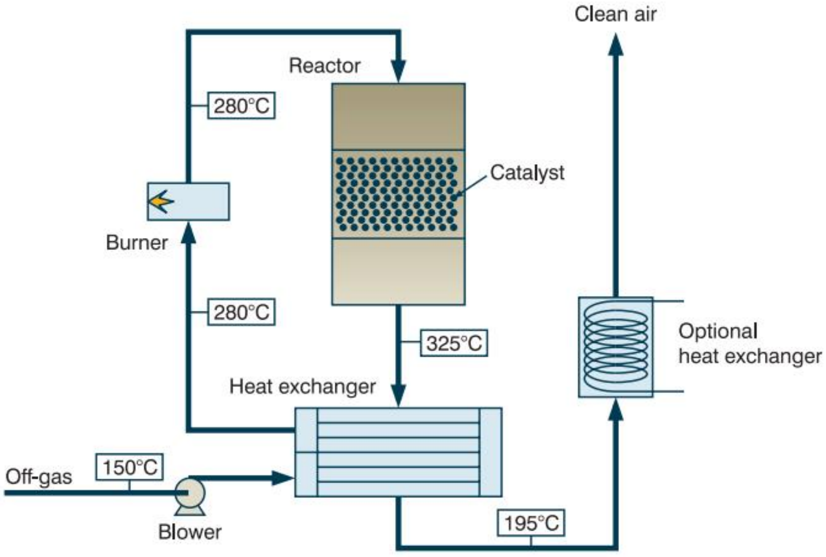

Figure 5.10 Illustration for a Topsoe catalytic combustion unit (CATOX) [45]

A novel Pt-structured catalyst using anodic aluminum as support was reported by Wang et al. [46]. Figure 5.11 shows photographs of four different shapes of structured catalysts. Figure 5.12 shows the cross-sectional SEM photo of anodic alumina support. The alumina support was synthesized through anodization technology followed by a hot water treatment [47]. The BET surface area of anodic alumina can reach up to 204.6 g/m^2, which is close to commercial powder alumina support. Compared to the traditional packed bed, this structured catalyst has a high surface area and low pressure drop. The conventional ceramic monolithic catalysts have poor heat transport ability and result in a significant adiabatic temperature rise (over 100 ˚C) for catalytic oxidation, which is a strong exothermic reaction. In contrast, the aluminum substrate has excellent thermal conductivity, and the heat can be effectively removed. In addition, compared to the typical straight and long channels in monolithic reactors, the anodic aluminum structured reactor has short channels with shifted arrangement bent, as shown in Figure 5.11 (b). This design can significantly improve the external mass transfer between the flowing fluid and catalyst. When this novel structured catalyst is used in the application of catalytic oxidation of VOCs, the performance of the reactor can be significantly improved in terms of conversion and stability.

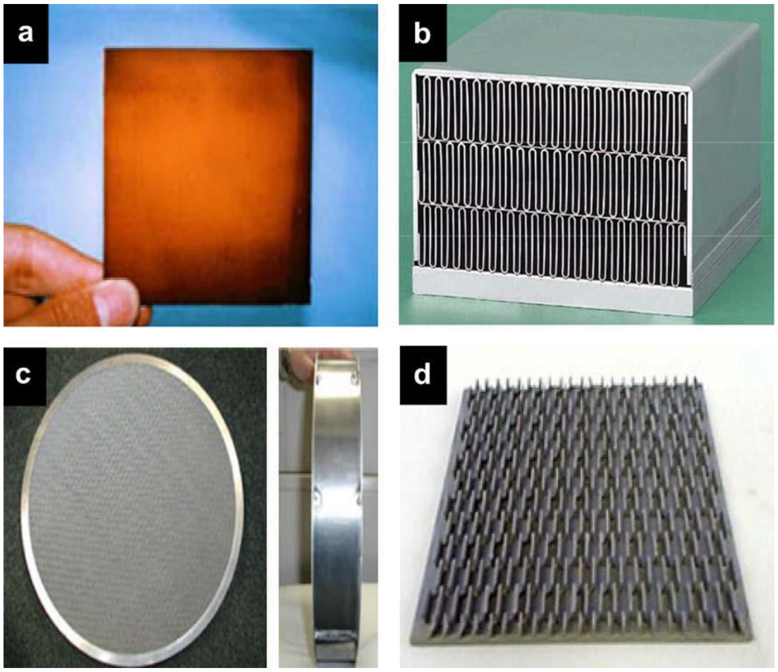

Figure 5.11 Structured catalysts with porous anodic alumina plate-type supports. (a) plate-type catalysts; (b) corrugated reactor; (c) mesh-type reactor; and (d) fin-type reactor.

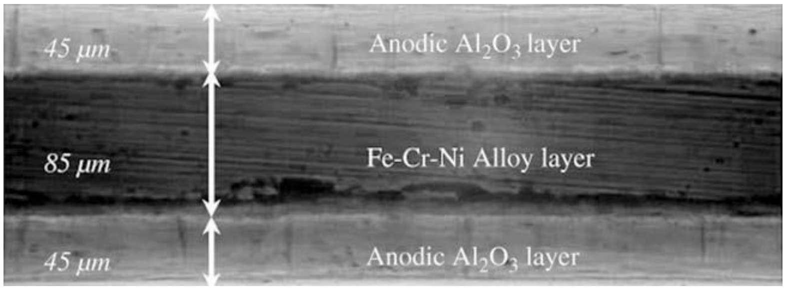

Figure 5.12 Cross-sectional photograph of anodic alumina support plate. The anodic Al2O3 layer is produced via anodization of aluminum layer. The Fe-Cr-Ni interlayer alloy layer is applied to provide higher electrical resistance for the purpose of fast electrical heating.

5.3.2. Photocatalytic degradation

Photocatalytic degradation, in particular, has become a popular alternative treatment of VOCs [48] due to the possible use of solar energy. A large variety of VOCs can be oxidized by

O_2 over the TiO_2 catalyst [49, 50]. The general mechanism of Photocatalytic oxidation can be described as Figure 5.13.

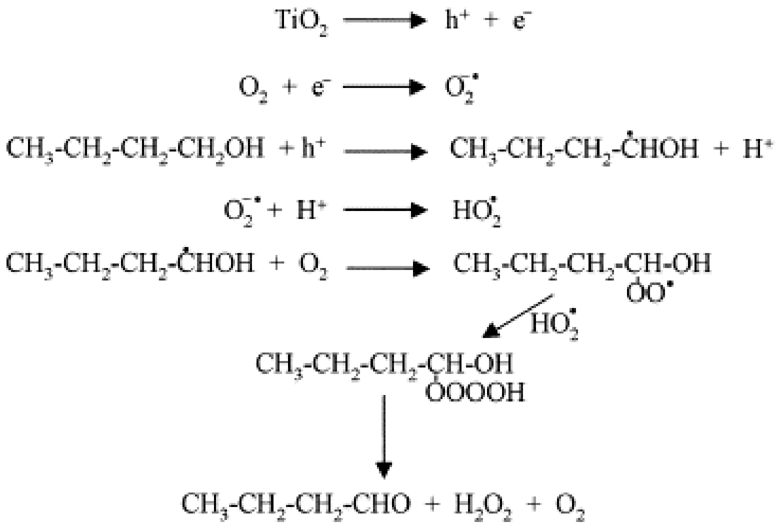

Figure 5.13, Mechanism of Photocatalytic oxidation, butanol as a representative of VOCs[51].

Under irradiation (typically UV light), hole-electron pairs (h^+-e^-) are formed on the surface of the TiO_2. The holes act as strong oxidizers; they can directly oxidize the adsorbed VOCs. More detailed discussions about the mechanism of photocatalysis can be found somewhere else [52]. Bianchi et al. [53] compared four commercial TiO_2 powders, two nano particles and two micro-sized particles. They found that both micro-sized and nano-sized particles had almost the same photocatalytic performance.

5.3.3. Adsorption

Adsorption on porous sorbents, such as activated carbon, is considered the best method for removal of relatively low concentration (from tens to thousands of ppmv) VOCs [54]. For PEM fuel cell application, the required purification is very high, typically in ppm level. Some other purification technologies, such as incineration, membrane separation, catalytic combustion, and condensation, are difficult or uneconomical to reach such low concentration. Common sorbents include activated carbon, zeolite, and polymer adsorbents [55, 56]. The zeolite has uniformly sized pores; hence it can selectively adsorb some species of VOCs. In contrast, activated carbon and polymer adsorbents have a broad range of pore sizes (from macro to micro pore), and the pores are not highly selective as to which VOC they will adsorb. The regeneration of adsorbents is typically accomplished by temperature swing or pressure swing method [57].

Activated carbon is characterized by its large surface area, typically more than 1000 m^2/g, and hydrophobic properties. Activated carbon is useful for adsorbing most organic pollutants with molecular weights between 45 and 130 [58, 59].

According to the particle size, the activated carbon can be classified as: granular activated carbon (GAC), powdered activated carbon (PAC), or activated carbon fiber (ACF). GAC is the most common form of carbon; typically, the pellet size of GAC is greater than 1 mm. GAC is mainly used in air/gas purification applications, such as flue gas emissions and gas process streams, because of its low pressure drop at high flow rate. Common particle sizes of commercial GAC are 4×6 mesh, 6×12 mesh, and 12×20 mesh. In contrast, PAC is primarily used in water treatment or other liquid purification. The flow rate in liquid phase purification is typically much lower than in gas phase application, so the flow resistance of sorbent bed is not a big concern. Common particle sizes of commercial PAC are 12×40, 20×50 mesh, etc. The average size of particles is typically smaller than 1 mm. ACF is a relatively new form of carbon adsorbent. However, because of its unique advantages in adsorption kinetics and form flexibility, it has been used in many industrial processes [60].

Chiang et al. [61] studied the effect of pore structure and temperature on VOC adsorption onto activated carbon. They found that the pores' shapes are dependent on the raw material. The shape of the pores on bituminous coal derived carbon is different from that on coconut shell and peat derived carbon. The heat of adsorption and entropy change is influenced by the pore structures. The heat of adsorption varies between 32.84 and 68.41 kJ/mol for benzene adsorption onto three types of activated carbon. Physical adsorption is the predominant mechanism for VOC adsorption onto activated carbon.

The breakthrough behavior of VOCs in GAC filled packed bed adsorber has been extensively studied by many authors [59]. The effects of various parameters such as bed length, gas concentration, and flow rate on the breakthrough performance were also widely studied. Since activated carbon is the most popular adsorbent, and because of its ability to remove a broad range of VOCs species, it was selected as the adsorbent for PEMFC filtration in this study.

5.3.4. Advantages of microfibrous entrapped sorbent

The major advantage of MFES is that it has both high contacting efficiency and low pressure drop. The use of micro-sized sorbent makes MFES's contacting efficiency close to the ACF bed or packed bed with same particle size, but the pressure drop is lower than the ACF bed and much lower (about one order of magnitude) than in packed bed. Compared to the traditional packed bed adsorber, which typically uses large particles, MFES's contacting efficiency is about 10 times greater.

The performance of GAC adsorber is mainly limited by its slow adsorption kinetics, which is caused by its relatively high external and internal mass transfer resistances. The low adsorption kinetics of GAC bed results in greater volume of device, lower throughput, and lower bed utilization (thicker mass transfer zone). PAC, whose size is smaller than GAC, has faster adsorption kinetics, but its utilization in gas phase separation is limited by its high flow resistance [62]. When GAC and PAC are used in the form of packed bed, the particles are loosely packed. The packed bed's void fraction is not adjustable, typically about 0.4. In contrast, MFES's void fraction is very flexible because the space between the fibers is independent of the fiber diameter, as shown in Figure 5.14. The void fraction of MFES can reach up to 99%. Another drawback of packed bed (of GAC or PAC) is its nonuniformity of structure, which results in bypass or channeling flow. The bypass or channeling flow will significantly reduce the performance of a contacting system. In contrast, the MFES media has a very uniform structure due to the wet laid process, and it is free from channeling flow.

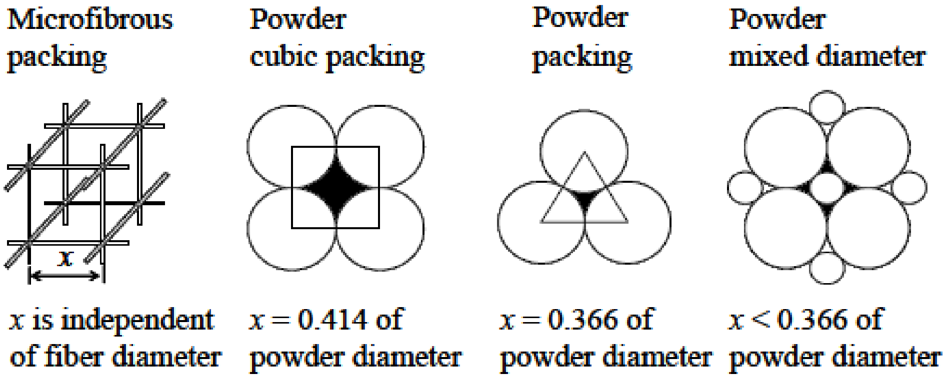

Figure 5.14 Packing structure of the micro-fiber and powder-based porous material [63]

Reference

[1] Laboratory NET, Energy USDo. Fuel Cell Handbook: University Press of the Pacific; 2005.

[2] St-Pierre J, Wilkinson DP. Fuel cells: A new, efficient and cleaner power source. AIChE Journal. 2001;47(7):1482-6.

[3] Larminie J, Dicks A. Fuel Cell Systems Explained (Second Edition): Wiley; 2003.

[4] Zhang J, Xie Z, Zhang J, Tang Y, Song C, Navessin T, et al. High temperature PEM fuel cells. Journal of Power Sources. 2006;160(2):872-91.

[5] Dhar HP, Christner LG, Kush AK. Nature of CO Adsorption during H 2 Oxidation in Relation to Modeling for CO Poisoning of a Fuel Cell Anode. Journal of The Electrochemical Society. 1987;134(12):3021-6.

[6] Gang X, Qingfeng L, Hjuler HA, Bjerrum NJ. Hydrogen Oxidation on Gas Diffusion Electrodes for Phosphoric Acid Fuel Cells in the Presence of Carbon Monoxide and Oxygen. Journal of The Electrochemical Society. 1995;142(9):2890-3.

[7] Proton Exchange Membrane Fuel Cells: Contamination and Mitigation Strategies (Green Chemistry and Chemical Engineering): CRC Press; 2010.

[8] Cheng X, Shi Z, Glass N, Zhang L, Zhang J, Song D, et al. A review of PEM hydrogen fuel cell contamination: Impacts, mechanisms, and mitigation. Journal of Power Sources. 2007;165(2):739-56.

[9] Dicks AL. Hydrogen generation from natural gas for the fuel cell systems of tomorrow. Journal of Power Sources. 1996;61(1–2):113-24.

[10] Höhlein B, Boe M, Bøgild-Hansen J, Bröckerhoff P, Colsman G, Emonts B, et al. Hydrogen from methanol for fuel cells in mobile systems: development of a compact reformer. Journal of Power Sources. 1996;61(1–2):143-7.

[11] Welaya YMA, El Gohary MM, Ammar NR. Steam and partial oxidation reforming options for hydrogen production from fossil fuels for PEM fuel cells. Alexandria Engineering Journal. 2012;51(2):69-75.

[12] Iulianelli A, Liguori S, Calabrò V, Pinacci P, Basile A. Partial oxidation of ethanol in a membrane reactor for high purity hydrogen production. International Journal of Hydrogen Energy. 2010;35(22):12626-34.

[13] Wee J-H, Lee K-Y, Kim SH. Sodium borohydride as the hydrogen supplier for proton exchange membrane fuel cell systems. Fuel Processing Technology. 2006;87(9):811-9.

[14] Vasiliev LL, Kanonchik LE, Kulakov AG, Mishkinis DA, Safonova AM, Luneva NK. New sorbent materials for the hydrogen storage and transportation. International Journal of Hydrogen Energy. 2007;32(18):5015-25.

[15] Li Q, He R, Gao J-A, Jensen JO, Bjerrum NJ. The CO Poisoning Effect in PEMFCs Operational at Temperatures up to 200°C. Journal of The Electrochemical Society. 2003;150(12):A1599-A605.

[16] Davies JC, Nielsen RM, Thomsen LB, Chorkendorff I, Logadóttir Á, Lodziana Z, et al. CO Desorption Rate Dependence on CO Partial Pressure over Platinum Fuel Cell Catalysts. Fuel Cells. 2004;4(4):309-19.

[17] Kim J-D, Park Y-I, Kobayashi K, Nagai M, Kunimatsu M. Characterization of CO tolerance of PEMFC by ac impedance spectroscopy. Solid State Ionics. 2001;140(3–4):313-25.

[18] Kita H, Shimazu K, Kunimatsu K. Electrochemical oxidation of CO on Pt in acidic and alkaline solutions: Part I. voltammetric study on the adsorbed species and effects of aging and Sn(IV) pretreatment. Journal of Electroanalytical Chemistry and Interfacial Electrochemistry. 1988;241(1–2):163-79.

[19] Dhar HP, Christner LG, Kush AK, Maru HC. Performance Study of a Fuel Cell Pt-on-C Anode in Presence of CO and CO 2, and Calculation of Adsorption Parameters for CO Poisoning. Journal of The Electrochemical Society. 1986;133(8):1574-82.

[20] de Bruijn FA, Papageorgopoulos DC, Sitters EF, Janssen GJM. The influence of carbon dioxide on PEM fuel cell anodes. Journal of Power Sources. 2002;110(1):117-24.

[21] Janssen GJM. Modelling study of CO2 poisoning on PEMFC anodes. Journal of Power Sources. 2004;136(1):45-54.

[22] Smolinka T, Heinen M, Chen YX, Jusys Z, Lehnert W, Behm RJ. CO2 reduction on Pt electrocatalysts and its impact on H2 oxidation in CO2 containing fuel cell feed gas – A combined in situ infrared spectroscopy, mass spectrometry and fuel cell performance study. Electrochimica Acta. 2005;50(25–26):5189-99.

[23] Majlan EH, Wan Daud WR, Iyuke SE, Mohamad AB, Kadhum AAH, Mohammad AW, et al. Hydrogen purification using compact pressure swing adsorption system for fuel cell. International Journal of Hydrogen Energy. 2009;34(6):2771-7.

[24] Rajalakshmi N, Jayanth TT, Dhathathreyan KS. Effect of Carbon Dioxide and Ammonia on Polymer Electrolyte Membrane Fuel Cell Stack Performance. Fuel Cells. 2003;3(4):177-80.

[25] Uribe FA, Gottesfeld S, Zawodzinski TA. Effect of Ammonia as Potential Fuel Impurity on Proton Exchange Membrane Fuel Cell Performance. Journal of The Electrochemical Society. 2002;149(3):A293-A6.

[26] Halseid R, Vie PJS, Tunold R. Effect of ammonia on the performance of polymer electrolyte membrane fuel cells. Journal of Power Sources. 2006;154(2):343-50.

[27] Halseid R, Heinen M, Jusys Z, Jürgen Behm R. The effect of ammonium ions on oxygen reduction and hydrogen peroxide formation on polycrystalline Pt electrodes. Journal of Power Sources. 2008;176(2):435-43.

[28] Song C, Tang Y, Zhang JL, Zhang J, Wang H, Shen J, et al. PEM fuel cell reaction kinetics in the temperature range of 23–120 °C. Electrochimica Acta. 2007;52(7):2552-61.

[29] Garsany Y, Baturina OA, Swider-Lyons KE. Impact of Sulfur Dioxide on the Oxygen Reduction Reaction at Pt/Vulcan Carbon Electrocatalysts. Journal of The Electrochemical Society. 2007;154(7):B670-B5.

[30] EPA. [cited; Available from: http://www.epa.gov/air/criteria.html

[31] Mohtadi R, Lee Wk, Van Zee JW. Assessing durability of cathodes exposed to common air impurities. Journal of Power Sources. 2004;138(1–2):216-25.

[32] Baturina OA, Swider-Lyons KE. Effect of SO2 on the Performance of the Cathode of a PEM Fuel Cell at 0.5–0.7 V. Journal of The Electrochemical Society. 2009;156(12):B1423-B30.

[33] Jing F, Hou M, Shi W, Fu J, Yu H, Ming P, et al. The effect of ambient contamination on PEMFC performance. Journal of Power Sources. 2007;166(1):172-6.

[34] Contractor AQ, Lal H. Two forms of chemisorbed sulfur on platinum and related studies. Journal of Electroanalytical Chemistry and Interfacial Electrochemistry. 1979;96(2):175-81.

[35] Mathieu M-V, Primet M. Sulfurization and regeneration of platinum. Applied Catalysis. 1984;9(3):361-70.

[36] Nagahara Y, Sugawara S, Shinohara K. The impact of air contaminants on PEMFC performance and durability. Journal of Power Sources. 2008;182(2):422-8.

[37] Zhai J, Hou M, Zhang H, Zhou Z, Fu J, Shao Z, et al. Study of sulfur dioxide crossover in proton exchange membrane fuel cells. Journal of Power Sources. 2011;196(6):3172-7.

[38] Moore JM, Adcock PL, Lakeman JB, Mepsted GO. The effects of battlefield contaminants on PEMFC performance. Journal of Power Sources. 2000;85(2):254-60.

[39] Shi Z, Song D, Li H, Fatih K, Tang Y, Zhang J, et al. A general model for air-side proton exchange membrane fuel cell contamination. Journal of Power Sources. 2009;186(2):435-45.

[40] Li H, Zhang J, Shi Z, Song D, Fatih K, Wu S, et al. PEM Fuel Cell Contamination: Effects of Operating Conditions on Toluene-Induced Cathode Degradation. Journal of The Electrochemical Society. 2009;156(2):B252-B7.

[41] Li H, Zhang J, Fatih K, Wang Z, Tang Y, Shi Z, et al. Polymer electrolyte membrane fuel cell contamination: Testing and diagnosis of toluene-induced cathode degradation. Journal of Power Sources. 2008;185(1):272-9.

[42] van den Brink RW, Louw R, Mulder P. Formation of polychlorinated benzenes during the catalytic combustion of chlorobenzene using a Pt/γ-Al2O3 catalyst. Applied Catalysis B: Environmental. 1998;16(3):219-26.

[43] Okumura K, Kobayashi T, Tanaka H, Niwa M. Toluene combustion over palladium supported on various metal oxide supports. Applied Catalysis B: Environmental. 2003;44(4):325-31.

[44] Scirè S, Minicò S, Crisafulli C. Pt catalysts supported on H-type zeolites for the catalytic combustion of chlorobenzene. Applied Catalysis B: Environmental. 2003;45(2):117-25.

[45] CATOX.ashx. 2014 [cited; Available from: http://www.topsoe.com/business_areas/air_pollution_control/processes/~/media/PDF%20files/CATOX/CATOX.ashx

[46] Wang L, Tran TP, Vo DV, Sakurai M, Kameyama H. Design of novel Pt-structured catalyst on anodic aluminum support for VOC's catalytic combustion. Applied Catalysis A: General. 2008;350(2):150-6.

[47] Zhou L, Guo Y, Yagi M, Sakurai M, Kameyama H. Investigation of a novel porous anodic alumina plate for methane steam reforming: Hydrothermal stability, electrical heating possibility and reforming reactivity. International Journal of Hydrogen Energy. 2009;34(2):844-58.

[48] Legrini O, Oliveros E, Braun AM. Photochemical processes for water treatment. Chemical Reviews. 1993;93(2):671-98.

[49] Peral J, Ollis DF. Heterogeneous photocatalytic oxidation of gas-phase organics for air purification: Acetone, 1-butanol, butyraldehyde, formaldehyde, and m-xylene oxidation. Journal of Catalysis. 1992;136(2):554-65.

[50] Photocatalysis and Water Purification: From Fundamentals to Recent Applications: Wiley-VCH; 2013.

[51] Benoit-Marquié F, Wilkenhöner U, Simon V, Braun AM, Oliveros E, Maurette M-T. VOC photodegradation at the gas–solid interface of a TiO2 photocatalyst: Part I: 1-butanol and 1-butylamine. Journal of Photochemistry and Photobiology A: Chemistry. 2000;132(3):225-32.

[52] Zhao C, Pelaez M, Dionysiou DD, Pillai SC, Byrne JA, O'Shea KE. UV and visible light activated TiO2 photocatalysis of 6-hydroxymethyl uracil, a model compound for the potent cyanotoxin cylindrospermopsin. Catalysis Today. 2014;224(0):70-6.

[53] Bianchi CL, Gatto S, Pirola C, Naldoni A, Di Michele A, Cerrato G, et al. Photocatalytic degradation of acetone, acetaldehyde and toluene in gas-phase: Comparison between nano and micro-sized TiO2. Applied Catalysis B: Environmental. 2014;146(0):123-30.

[54] Clark RM, Jr. BWL. Granular Activated Carbon: Design, Operation and Cost: Lewis Publishers; 1989.

[55] Zheng K, Pan B, Zhang Q, Han Y, Zhang W, Pan B, et al. Enhanced removal of p-chloroaniline from aqueous solution by a carboxylated polymeric sorbent. Journal of Hazardous Materials. 2007;143(1–2):462-8.

[56] Qiu W, Zhang K, Liu J, Koros WJ, Sun Q, Deng Y. Macroporous polymeric sorbents with high selectivity for separation of phenols. Polymer. 2010;51(16):3793-800.

[57] Nastaj JF, Ambrożek B, Rudnicka J. Simulation studies of a vacuum and temperature swing adsorption process for the removal of VOC from waste air streams. International Communications in Heat and Mass Transfer. 2006;33(1):80-6.

[58] Foster KL, Fuerman RG, Economy J, Larson SM, Rood MJ. Adsorption characteristics of trace volatile organic compounds in gas streams onto activated carbon fibers. Chemistry of Materials. 1992;4(5):1068-73.

[59] Mohan N, Kannan GK, Upendra S, Subha R, Kumar NS. Breakthrough of toluene vapours in granular activated carbon filled packed bed reactor. Journal of Hazardous Materials. 2009;168(2–3):777-81.

[60] Suzuki M. Activated carbon fiber: Fundamentals and applications. Carbon. 1994;32(4):577-86.

[61] Chiang Y-C, Chiang P-C, Huang C-P. Effects of pore structure and temperature on VOC adsorption on activated carbon. Carbon. 2001;39(4):523-34.

[62] Shmidt JL, Pimenov AV, Lieberman AI, Cheh HY. Kinetics of Adsorption with Granular, Powdered, and Fibrous Activated Carbon. Separation Science and Technology. 1997;32(13):2105-14.

[63] Harris DK, Cahela DR, Tatarchuk BJ. Wet layup and sintering of metal-containing microfibrous composites for chemical processing opportunities. Composites Part a-Applied Science and Manufacturing. 2001;32(8):1117-26.

[64] Collier A, Wang H, Zi Yuan X, Zhang J, Wilkinson DP. Degradation of polymer electrolyte membranes. International Journal of Hydrogen Energy. 2006;31(13):1838-54.

[65] Handbook of Fuel Cells: Fundamentals, Technology, Applications: Wiley; 2003.

[66] Schmidt TJ, Paulus UA, Gasteiger HA, Behm RJ. The oxygen reduction reaction on a Pt/carbon fuel cell catalyst in the presence of chloride anions. Journal of Electroanalytical Chemistry. 2001;508(1–2):41-7.

[67] Xie J, Wood DL, Wayne DM, Zawodzinski TA, Atanassov P, Borup RL. Durability of PEFCs at High Humidity Conditions. Journal of The Electrochemical Society. 2005;152(1):A104-A13.

[68] Pozio A, Silva RF, De Francesco M, Giorgi L. Nafion degradation in PEFCs from end plate iron contamination. Electrochimica Acta. 2003;48(11):1543-9.

Chapter 6

Cathode Filtration System Design and Optimization for PEM Fuel Cells

Introduction

The proton exchange membrane fuel cell (PEMFC) has a great potential of providing clean energy in many applications such as automobiles, portable power sources, stationary power plants, etc. A practical challenge for PEMFC is that its performance is significantly impacted by the air quality. Cathode contamination causes significant performance degradation, primarily resulting from the poisoning of the membrane electrode assembly (MEA). Given the variety of contaminant species in the air, the simplest solution to mitigate the contamination effect is using cathode filtration. However, cathode filtration increases the parasitic power loss and hence reduces the net power output of fuel cells. Typically, total system parasitic losses can reach up to 10-20% of net power output, depending on the system design and optimization. 'Sankey diagram' (as shown in Figure 6.1) is a useful way to illustrate the various energy flows and power losses in a fuel cell system. Although the reactant airflow is less than the cooling airflow, it needs to overcome additional pressure drop from the filtration devices – the humidifier and the narrow and long stack channels – and much more electric power is consumed by the reactant air blower/compressor than by the cooling air.

Although small scale PEM fuel cells are operated at atmospheric air pressure, larger scale fuel cells are typically operated at higher pressure (2-3 atm). The higher pressure will significantly increase the power consumption of the compressor. For example, when the fuel cells are operated at a pressure of 3 bar, the power consumption by the compressor will be approximately 20% of generated power for a 100 kW fuel cell system [1]. Compared to a small-scale fuel cell system, the larger scale system is much more complex, and the parasitic power loss is much more significant. System optimization is very important to improve the total efficiency of larger scale fuel cells.

This study aims to maximize the net power output and life-time of fuel cells in a polluted air environment by using novel filter media and optimizing the filtration design. A novel adsorptive sorbent media, activated carbon fiber enhanced microfibrous entrapped sorbent, was developed and used as a polishing layer to improve the performance of traditional packed bed filter. The full size activated carbon filter (24×24”) was tested in a full scale test rig. The resulting breakthrough data was applied to determine the adsorptive filter parameters, including the saturation capacity and adsorption rate constant. At last, a filter design methodology was developed through carefully considering the attributes of the fuel cell operating conditions (air flow rate, stoichiometric ratio, operating temperature and pressure, current density, etc.) and polluted air properties (contaminants types and concentration). The optimization process is based on the trade-off between the power reduction due to contamination and the parasitic power loss caused by additional contaminant filtration. The design methodology was successfully applied to a 60 kW fuel cell to simulate the relationships between net output and filtration with time. The simulation results show that the optimization of filtration design can significantly reduce the power consumption of the compressor and hence improve the total efficiency of the fuel cell system.

This paper focuses on the optimization of system rather than on stack performance. Later in this paper, the concepts of stack efficiency and system efficiency will be discussed. It is important to distinguish the gross stack output and net system output. The overall fuel cell system simulation is divided into two stages. The first stage is to model key components such as the compressor and the cooling system, and the second stage is to develop an optimization algorithm by studying the trade-off between stack performance and other system components.

The two components simulated and optimized are the fuel cell stack and the air supply system, which includes the filtration devices. A general idea of the fuel cell system optimization is illustrated in Figure 6.6. This figure reveals that the nature of fuel cell system optimization is the balance between gross output and parasitic loss, while the optimization objective function is the net power output. The details of all involved components in full cell systems will be discussed. Some simplifications must be made to make the optimization scheme practical based on the importance analysis of various components and parameters.

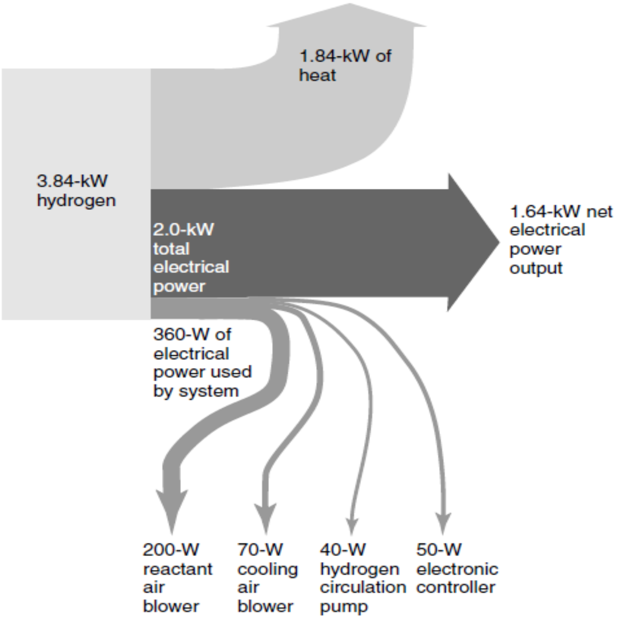

Figure 6.1 Sankey diagram for the 2.0 kW fuel cell systems, reproduce from [1]

6.1. Fundamentals of Fuel cells

6.1.1. Cell model

The voltage of the fuel cell can be modeled as

$$V_{cell} = E_{Nernst} - \Delta V_{act} - \Delta V_{ohm} - \Delta V_{conc} \tag{6.1}$$

Where E_{Nernst} is the Nernst potential determined by Nernst equation [1]

$$E_{Nernst} = E^0 + \frac{RT}{2F} \ln\left(\frac{P_{H_2} P_{O_2}^{0.5}}{P_{H_2O}}\right) \tag{6.2}$$

Where ΔV_{act} , ΔV_{ohm} , and ΔV_{conc} are activation overvoltage, Ohmic overvoltage, and concentration overvoltage, respectively.

The activation overvoltage can be described by Tafel equation, which is an empirical equation

$$\Delta V_{act} = a \ln\left(\frac{i}{i_0}\right) \tag{6.3}$$

Where i_0 is so called “exchange current density,” and constant a is called “Tafel slope.” For a low temperature hydrogen fuel cell, a typical value for i_0 is about 0.1 mA/cm^2 at the cathode and about 200 mA/cm^2 at the anode. Since the value of i_0 at cathode is much smaller than that at anode, the overpotential at cathode is much greater than that at anode. Typically, the constants in Tafel equations need be determined by experiments. Additionally, activation overvoltage can also be modeled by semi-empirical equations. An example of such an equation can be found in reference [2].

The Ohmic overvoltage follows Ohm's law

$$\Delta V_{ohm} = i \cdot r = i(r^{elec} + r^{prot}) \tag{6.4}$$

Where r is the area-specific resistance in kΩ cm^2; r^{elec} and r^{prot} represent electrical resistance between the electrodes and flow resistance of proton in the electrolyte, respectively. In most fuel cells, r^{prot} is the major resistance.

The concentration overvoltage, also known as mass transport overvoltage, can be modeled in the following equation [3]

$$\Delta V_{conc} = -\frac{RT}{2F}\ln\left(1 - \frac{i}{i_L}\right) \tag{6.5}$$

Where R is gas constant, T the cell temperature in K, F the Faraday's constant, and i_L is the limiting current density when the hydrogen is completely used. The concentration overvoltage is the dominant loss when the fuel cell operates at high current density.

The fuel cell contamination models are based on the fundamentals of fuel cell models, i.e., by studying the effects of contamination on each term in equation 6.1.

6.1.2. Cell efficiency and system efficiency

6.1.2.1 Cell efficiency

For the fuel cells, if all the energy from the hydrogen fuel were transformed into electrical energy, then the electromotive force (EMF) would be given by

$$E = \frac{-\Delta \overline{h_f}}{2F} = 1.25\ V \text{ if using the lower heating value (LHV)} \tag{6.6}$$

This is the maximum voltage that would be obtained from a 100% efficiency system. The actual cell voltage is always smaller than the ideal EMF, and the cell efficiency can be expressed as

$$Cell\ efficiency = \frac{V_c}{1.25} \times 100\% \quad \text{(with reference to LHV)} \tag{6.7}$$

The energy transformation in fuel cells is limited by both thermodynamics and kinetics.

The maximum electrical energy available is equal to the change in Gibbs free energy rather than enthalpy, so

$$Maximum\ efficiency\ possible = \frac{\Delta\overline{g_f}}{\Delta\overline{h_f}} \times 100\% \tag{6.8}$$

This maximum efficiency is also known as ‘thermodynamic efficiency,’ which is approximately 80% under normal fuel cell operating conditions.

In practice, fuel cell efficiency is more limited by the kinetic factors. This limitation is known as activation losses. These losses are caused by the sluggish electrochemical reactions that take place on the surface of the electrodes. Besides the surface reaction rate limitation, the overall reaction rate might also be limited by the mass transport process. The voltage losses caused by mass transfer limitation are called mass transport or concentration losses. Fuel cell efficiency might also be reduced due to fuel crossover, internal currents, and ohmic losses.

6.1.2.2 System efficiency

In addition to the stacks, practical fuel cell systems also require some auxiliary sub-systems or components. Those auxiliary components are the so-called balance of plant (BoP). Generally, the BoP contains fuel processor, air supply system, thermal management (cooling system), water management, electric power conditioning, and control systems. The BoP will consume significant amounts of power from the stack and hence decrease the overall efficiency of the fuel cell system. Among the BoP components, the compressor is the largest parasitic load, especially in a pressurized system. Based on the above discussion, the overall fuel cell system efficiency can be defined as the net power output divided by the thermal input of fuels.

$$E_{sys} = E_{FC} \times \eta_{H_2} \times \left(1 - \frac{P_{BoP}}{P_{FC}}\right) \tag{6.9}$$

Where, E_{sys} is the overall system efficiency, E_{FC} is the efficiency of the fuel cell stack, a typical value of E_{FC} is 0.6 [4], η_{H_2} is the utilization of the hydrogen, P_{BOP} is the power consumed by the balance of plant, and the P_{FC} is the gross power of the stack.

To improve the system efficiency, some efforts can be made

(a) Maximizing the utilization of hydrogen. For open systems, lowering the hydrogen stoichiometry and for closed systems, lowering the purging frequencies can decrease the waste of hydrogen.
(b) Minimizing the flow of air. Since the flow of air is generally 4 times greater than the flow of hydrogen, the air supply system poses a significant parasitic loss.
(c) Minimizing the pressure drop at anode and cathode. The pressure drop of the flow field inside the stack, the filters, and manifolds requires an increase of the reactant pressure at the inlet that increases the energy consumption of the compressor.

Since the BoP consumes a significant amount of power, optimization of BoP design is essential to improve the system efficiency of fuel cells. Extensive efforts have been made in various aspects of fuel cell systems. One effort is to optimize the flow channels inside the stack to improve the reactant gas transport and pressure drop [6-8]. Cunningham et al studied the air supply system optimization for fuel cells, including the selection of compressors, using air supply model [9] to optimize the operation parameters, etc.

The air supply system is the most important parasitic load for the fuel cell system. In a pressurized system, the power requirement from the air compressor can reach up to 20% of the fuel cell power output. In most practical fuel cell systems, the air supply system includes an air compressor and the filtration system. The filtration system is used to purify the air to ensure that the air supply system can deliver qualified (clean) air to the fuel cell stacks. The focus of the present work is improving the efficiency of air supply systems, i.e., reducing the power consumption of air supply systems while maintaining the ability to provide adequate and clean air.

6.2. Balance of Plant

To support the operation of PEMFC, some auxiliary sub-systems or components are required. Those auxiliary components are the so-called balance of plant (BoP). Together with the stack, the BoP forms the fuel cell system [5]. Figure 6.2 shows a 1.2 kW Ballard Nexa fuel cell module in our laboratory. Some important components in this module are illustrated in the figure. Figure 6.4 presents a simplified block diagram of the major components required within a PEMFC system. Those components can typically be classified into five major subsystems: fuel supply subsystem (including the fuel processor), air supply subsystem, water and thermal management subsystem, power conditioning subsystem, and control electronics. A brief description of those subsystems is presented in the following discussion.

6.2.1. Fuel supply subsystem

For a direct-hydrogen fuel cell system, a high-pressure compressed hydrogen gas (CHG) tank is used to feed the stack, and no further fuel processing is required. The CHG is the simplest way to provide fuel for PEMFC. A simple pressure regulating system and mass flow control are adequate to ensure that the stack receives hydrogen at the required pressure and flow rates. There is no need for optimization between the stack and the CHG tank. If other fuels such as natural gas, methanol, and gasoline are used, a fuel processor is required to convert a fuel to H_2. Generally, the fuel conversion efficiency is ca. 90% for common fuels [5]. Fuel processing includes the fuel cleaning, fuel conversion, and reformate gas alteration. Fuel processing is a very complicated process, and it has a lot of interaction with the stack. Typically, design optimization is required for processors to improve the overall performance of fuel cell systems. More information about fuel processing can be found in reference [5].

6.2.2. Air supply subsystem

Both reactant air and cooling air have to be moved around the fuel cell system. Depending on the required pressure, there are two main choices: blowers and compressors. The blowers can only provide near ambient pressure air but can vary the mass flow rate to achieve variable air stoichiometric ratios (SRa). In contrast, the compressors can provide relatively higher-pressure air with varying mass flow rates.

The different operating conditions such as pressure ratio and stoichiometric ratio for air supply systems have significant impact on the gross output of the fuel cell stack. Therefore, studying and understanding the interaction between the air supply system and the fuel cell stack is the key for system optimization.

6.2.3. Water and thermal management

Humidity control is critical to PEM fuel cells since either flooding or dehydration of the stack will severely degrade or even damage the stack components. A proton exchange membrane must be humidified (with a certain amount of water content) to conduct proton. Drying out of the membrane will significantly increase the membrane resistance and reduce the membrane durability. On the other hand, flooding hinders the diffusion of oxygen through the gas diffusion layers to the cathode catalyst layer, resulting in significant cathode potential. A water management system functions to humidify the feed stream and remove the excess water from the exhaust gases.

PEM fuel cell stacks are very sensitive to temperature. Typically, high efficiency can only be achieved when the stacks are operated in a narrow range of temperatures near the optimal point. In converting the hydrogen energy into electricity, the efficiency of the fuel cell is approximately 50%. This means that the heat-generating rate is nearly equal to the gross output of the stacks. Since only a small amount of heat can be carried by the gas product streams, the heat must be removed effectively by a cooling system. In addition, the thermal management system is also necessary for the start-up and shut-down operation.

6.2.4. Power conditioning subsystem

The power conditioner's function is to convert DC power from the stack to usable AC power. DC-DC converters and DC-AC inverters are employed in power conditioners. A DC-DC converter is used to increase the voltage of output to a regulated voltage (typically 400 V for 120/240 V AC output). A DC-AC inverter is to convert the DC to useful AC power at 60 or 50 Hz. Generally, the power conversion efficiency of conditioners is in the range of 0.9-0.95.

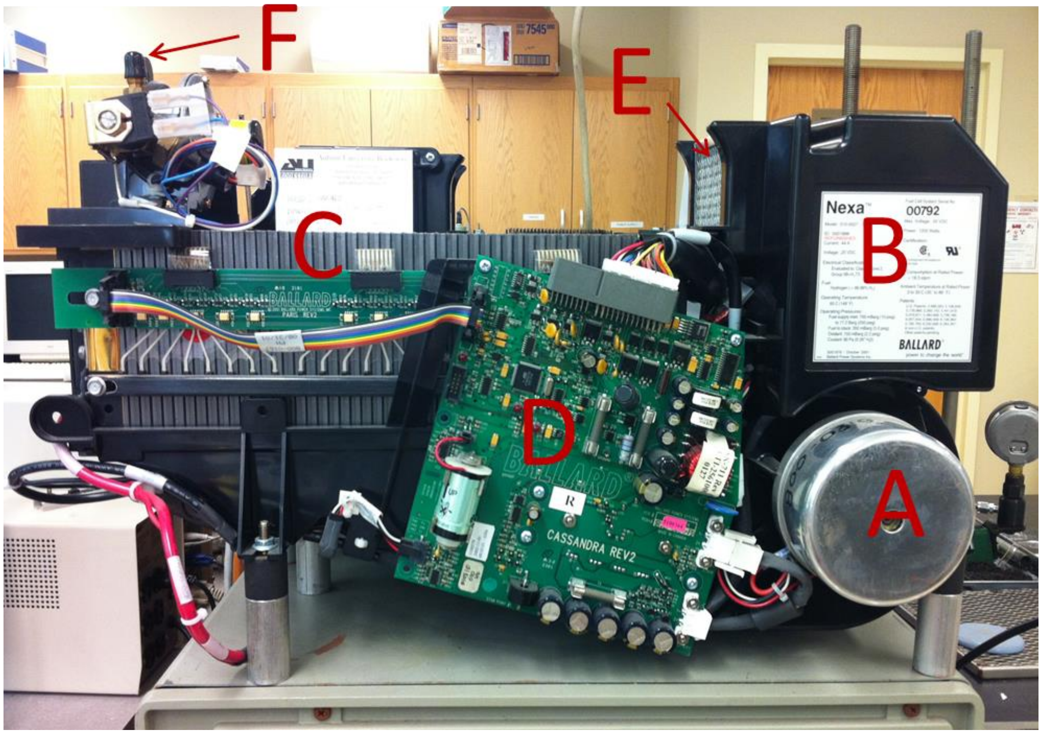

Figure 6.2 Photo of a 1.2 kW Ballard NexaTM fuel cell model. The cooling air is blown up by blower A; the reactant air is pumped by compressor B to the stack. The air intakes through filter F, and the hydrogen fuel enters through port F.

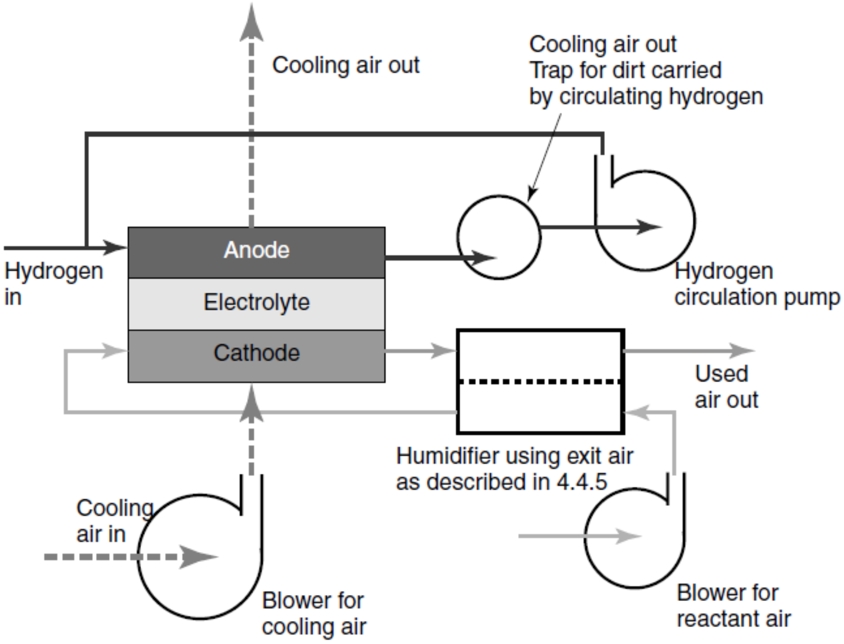

Figure 6.3 Flow chart of the PEM fuel cell system, reproduced from [1]

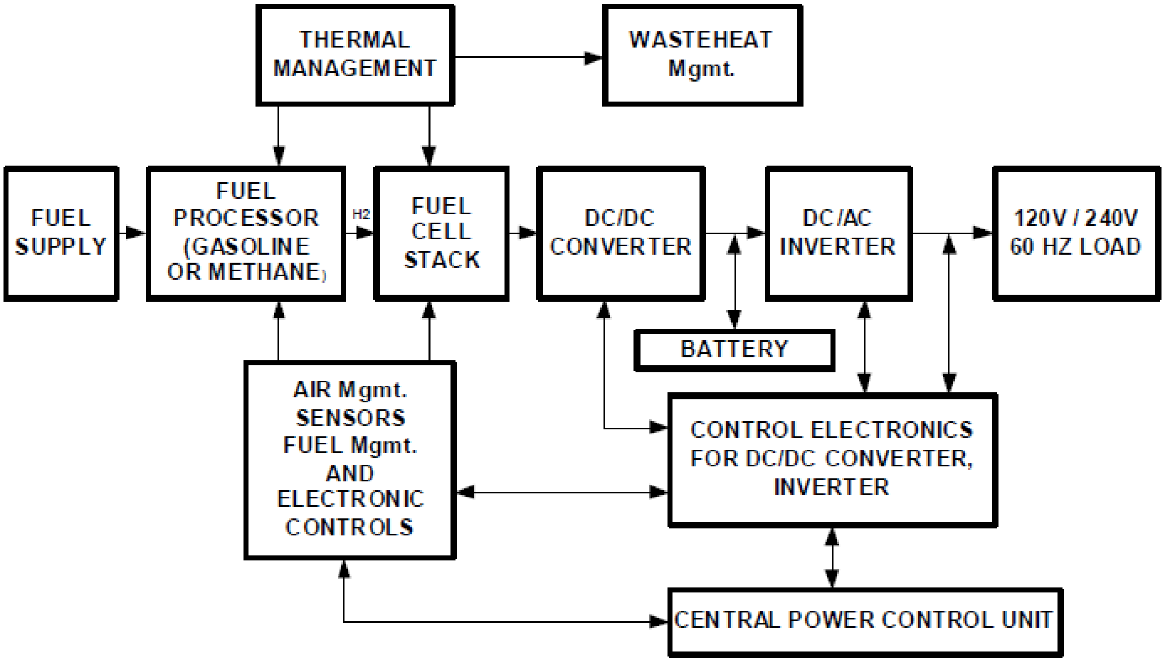

Figure 6.4, Block diagram of a typical PEM fuel cell system, reproduced from [5]

6.3. Design equations and models for components

6.3.1. Air flow requirement

The required mass flow rate of air can be described as

$$\text{Air mass flow rate} = 1.28 \times 10^{-3} \lambda \cdot \frac{P_e}{V_c} \,(\text{kg/h}) \tag{6.10}$$

Where λ is the air stoichiometric ratio defined as the ratio of total amount of air to consumed air, P_e is the power in watts, and V_c is average voltage of each cell in V. V_c is typically between 0.6 and 0.7 V, so 0.65 V is a good approximation for most fuel cells. In practice, λ is at least 2, and typically between 2 and 3. The excess air flow can avoid the depletion of oxygen upon exit and keep high concentrations of oxygen in the stack. In addition, the excess air is also important to remove the product water and generated heat during the electrochemical process.

6.3.2. Compressor power

Both air (reactant air and cooling air) and fuel have to be moved around in fuel cell systems. Depending on the required pressure, different devices including pumps, fans, compressors, and blowers can be used to move the gas. Typically, the compressors can provide relatively higher pressure, while other devices can only provide lower pressure.

The power consumption of a blower can be expressed as

$$P = \frac{Q \cdot \Delta P}{\eta_f \cdot \eta_m} \tag{6.11}$$

Where P is power consumption in W, Q is air flow rate in m^3/s, ΔP is pressure increase in Pa, η_f is fan's mechanical efficiency, and η_m is motor's mechanical efficiency. A typical value of η_f is 0.69, while η_m is 0.87.

There are four main types of compressors: roots compressor, screw compressor, centrifugal compressor, and axial flow compressor. Among these, the centrifugal compressor is the most common type.

The required shaft work to run a compressor can be described by the following equation

$$Compressor\ power\ = \dot{m} \cdot c_p \frac{T_1}{\eta_c \cdot \eta_m}\left(\left(\frac{P_2}{P_1}\right)^{\frac{\gamma-1}{\gamma}} - 1\right) \tag{6.12}$$

Where $\dot{m}$ is the mass flow rate of gas in kg s^{-1}, η_c is the isentropic efficiency, which is the ratio of isentropic work to real work; it can be estimated from the compressor performance charts. A typical value of η_c is 0.6 [10]. c_p is specific heat capacity in J $kg^{-1}K^{-1}$, the value of c_p for air is 1004 J $kg^{-1}K^{-1}$. T_1 is the inlet temperature. γ ($=c_p/c_v$) is the ratio of the specific heat capacities of the gas; γ is 1.4 for adiabatic process. P_2/P_1 is the pressure ratio. η_m represents the mechanical efficiency of motor and compressor. η_m is the product of mechanical efficiency of motor and mechanical efficiency of compressor. A typical value of a motor's mechanical efficiency is 0.9. The compressor's mechanical losses include the losses in the bearings and drive shaft; a typical value for compressor's mechanical efficiency is 0.8. Therefore, η_m is approximately 0.72.

6.3.3. Compressor performance charts

The efficiency and performance of a compressor depend on many factors including inlet and out pressure, gas flow rate, inlet temperature, compressor rotor speed, gas density, and gas viscosity. Using the compressor performance charts (Figure 6.5 shows an example), we can find the rotor speed and the efficiency of a compressor as long as we know the required gas flow rate and pressure ratio. From Figure 6.5, we can see that there exist high efficiency regions, but they are very narrow. The best efficiency is about 0.7 for centrifugal compressors. In this study, a value of 0.6 is used for the compressor.

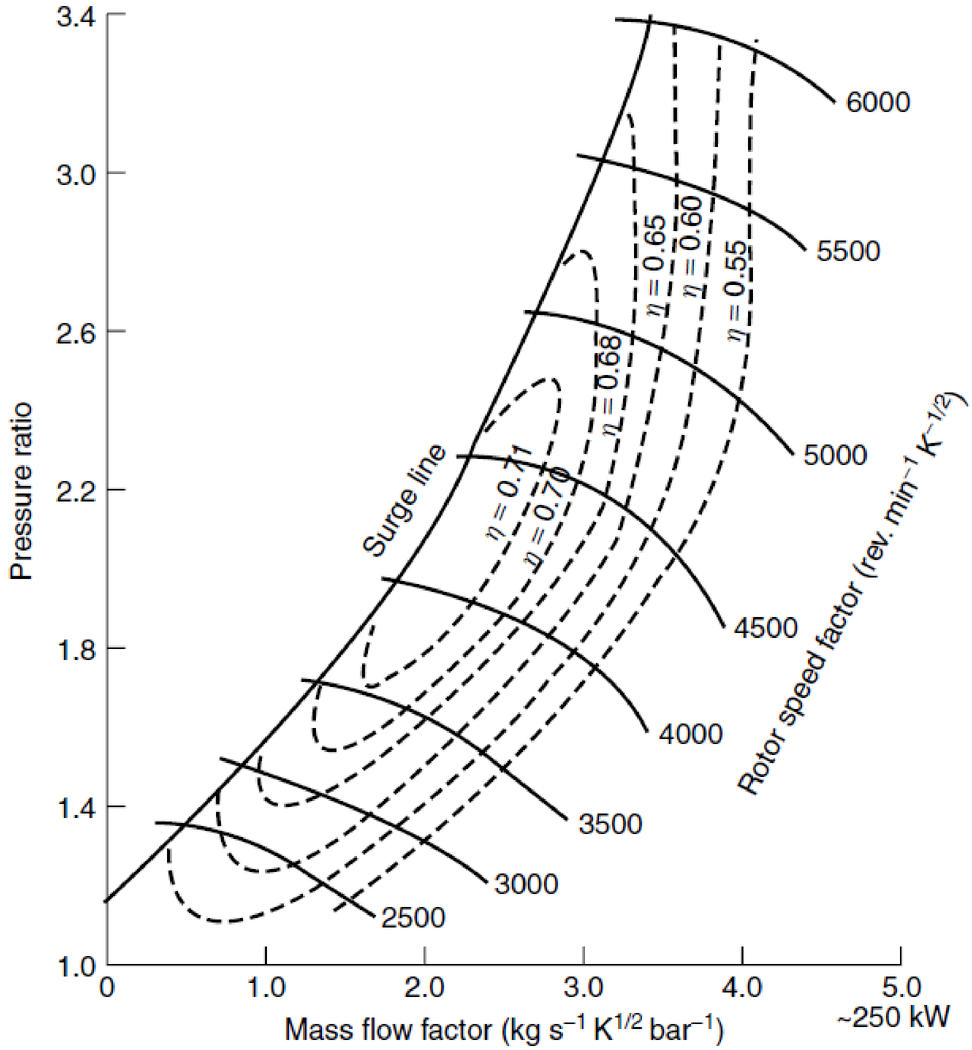

Figure 6.5 Performance chart for a centrifugal compressor

6.3.4. Design equation for cooling system

Heat is produced in the stack and needs be removed to maintain the operating temperature of fuel cells. Thermodynamics theory shows that if all the enthalpy of a reaction is converted into electrical energy, then the output voltage is 1.25 V (water product in vapor phase).

The difference between the actual voltage and the maximum voltage is the energy that is converted into heat.

The heat generated by a fuel cell stack can be described as

$$Heat\ gereration\ rate = P_e\left(\frac{1.25}{V_c} - 1\right) \tag{6.13}$$

To maintain the steady-state operation, the heat removal rate must be equal to the heat generation rate. Cooling is critical for safe and efficient operation of PEM fuel cells. Zhang et al. [11] reviewed the current cooling technologies in PEM fuel cell stacks and discussed the advantages, challenges, and progress of various techniques. Zhang et al classified the cooling techniques into four categories: 1) cooling with heat spreaders, 2) cooling with separate air flow, 3) cooling with liquid, and 4) cooling with phase change [12].

For large-scale fuel cell stacks (>100 kW), the waste heat is huge. Since the temperature difference between the PEM fuel cell and the ambient is small, the heat exchanger must have a large heat transfer area to effectively remove the heat.

Increasing the cathode air supply can remove more heat but can cause dry out of the membrane, so separate channels for cooling air are used in practice. Separate air cooling is suitable for small scale PEM fuel cell stacks in the range of 100 W to 2 kW. The Nexa^{TM} module used in our lab is a representative of PEM fuel cell stack using separate air flow cooling. For larger scale stacks, air cooling is not sufficient, and liquid cooling is used instead. The blower used to provide separate cooling air flow typically consumes 2-3% of the stack power [13]. The power required by the pump using water as coolant is given as [14]

$$P_{cool,pump} = \frac{\dot{m}_{H_2O}}{\rho_{H_2O}} \Delta P_{loop} \frac{S_F}{\eta_{pump} \cdot \eta_{motor}} \tag{6.14}$$

Where S_F is safety factor (assigned a value of 1.5) to account for any pressure losses that are not considered, ΔP_{loop} is the pressure drop through the coolant loop, and η_{pump} and η_{motor} are the efficiencies of pump and motor, respectively. The mass flow rate of water required to remove the heat is given as [10]

$$\dot{m}_{H_2O} = \frac{Q_{total} - Q_{gas}}{c_{p,H_2O}(T_{stack} - T_{H_2O,in})} \tag{6.15}$$

Where Q_{total} and Q_{air} are the total heat produced by the stack and total heat taken by gas stream, respectively, c_{p,H_2O} is the specific heat of water.

The power consumption of the humidifier pump can be described by an equation similar to equation 6.14. However, the water balance for humidifiers is more complicated. A detailed method to calculate the required amount of water can be found in reference [10].

The heat transfer coefficients with liquid flow are much higher than with air flow. In addition, the specific heat capacity of a liquid (such as water) is also much higher than air [15]. Therefore, liquid cooling is the most widely used technique for large scale stacks. The advantages and disadvantages of currently available cooling techniques are summarized in Table 6.1.

Table 6.1 Summary of various cooling strategies for PEM fuel cell stacks, reproduced from [11]

Cooling strategy	Techniques	Advantages	Disadvantages

Heat spreaders/edge cooling	Using highly thermal conductive materials	Simple system No internal coolant Small parasitic power	Limited heat transfer length Expensive material
	Using heat pipes as heat	Simple system Small parasitic power	Development of heat pipes with small thickness and low weight
Cooling with separate air flow	Separate air channels for cooling	Simple system Small parasitic power	Trade-off between cooling performance and parasitic power
Liquid cooling	Channels integrated in BPPs (DI water/ antifreeze coolant)	Strong cooling capability Flexible control of cooling capability	Radiator size Coolant degradation Large parasitic power
Phase change cooling	Evaporative cooling (Direct water injection, porous WTPs, wicking lands/channels)	Simultaneous cooling and internal humidification Simplified system	Dynamic control of water evaporation rate Thermal mass of liquid water on cold startup
	Cooling through boiling	Elimination of coolant pump Simplified system	Development of suitable working media Tw-phase flow instability

6.3.5. Filter breakthrough equation

An adsorptive filter's performance can be predicted by an empirical or theoretical equation. Numerous models such as Amundson equation [16], Yoon and Nelson equation [17], and Wheeler's equation [18] have been published. A modification of Wheeler's equation (equation 2.4) was used in this study. The model parameters (K' and τ) are obtained by a regression analysis of experimental data from full-scale filter tests. Filter attributes include the face area (A), thickness (L), weight of sorbent (m), and voidage of sorbent bed (ε_b). The concerned air properties include the face velocity (u_0) and inlet contaminant concentration (C_0).

6.3.6. Pressure drop of filter

The pressure drop of packed bed filter can be described by the Ergun equation.

$$\frac{\Delta P}{L} = 150\left(\frac{\mu u_0}{d_p^2}\right)\frac{(1-\varepsilon)^2}{\varepsilon^3} + 1.75\left(\frac{\rho u_0^2}{d_p}\right)\frac{1-\varepsilon}{\varepsilon^3} \tag{6.16}$$

For microfibrous media, the Ergun equation is not applicable since the void fraction of this media is too high (typically greater than 0.8). To estimate the pressure drop across microfibrous media, Cahela et al [19] developed a porous media permeability model, or PMP model, in 2001. This model considered the form drag losses neglected in the Ergun equation. Many experiments' results prove that the PMP model has good accuracy for predicting the pressure drop of microfibrous media.

In practice, the pressure drop of the filter can also be predicted by the Forchheimer equation.

$$\Delta P = Au_0 + Bu_0^2 \tag{6.17}$$

Constant A and B for a specific media can be simply determined by experimental pressure drop data. This method is straightforward and more accurate; however, pressure drop tests must be conducted to find out the parameters.

6.3.7. Contamination models

Contamination model is a useful tool to predict the effect of a contaminant on the performance of a fuel cell. Therefore, it is useful to determine the operating conditions and filtration requirements. Currently, numerous models for anode contamination have been established, mainly for CO [20-25] and H_2S [26, 27]. Models for cathode contamination are relatively few. The methodology to develop a cathode contamination model will be briefly discussed below.

Cathode contaminants degrade the fuel cell performance by affecting the fuel cell’s kinetics (ORR), conductivity, mass transport properties, and water management. Because the kinetics’ influence is the major reason for ?, most cathode contamination models are developed based on the effects of contaminants on ORR kinetics. Several ORR mechanisms have been proposed based on either associative or dissociative models [28-30]. The associative model proposed that the adsorption of oxygen on a catalyst surface is associative, while the dissociative model assumed that the oxygen is dissociative. Based on the associative mechanism, a general cathode contamination model was developed by Shi et al. [31]. They assumed that the toluene (contaminant) adsorption is the dominant mechanism for cathode contamination. By using this model and ORR parameters obtained from experimental results, they can predict the degree of cell performance degradation at different contaminant levels and current density. If know the performance requirement and current density, the model can be used to predict the maximum allowable contaminant concentration. For example, to limit the voltage drop caused by contamination less than 10 mV at current density of 1.0 A/cm^2, toluene concentration needs to be less than 0.1 ppm.

Li et al [32] developed a contamination model based on the Langmuir adsorption model. This model assumes that anode polarization is negligible, and cathode polarization is in the Tafel region.

$$\mathrm{V_c = E^{OCV} + b\left[\ln[(1 - \theta_T)\left(i^0_{O_2}\right)] - \ln\left(\frac{I_c I_d}{I_d - I_c}\right)\right] - I_c R_m} \tag{6.18}$$

$$\frac{1}{\theta_T} = \frac{1}{C_T B_{ads}} + 1 \tag{6.19}$$

Where V_c, I_c are cell voltage and current, respectively, E^{OCV} is open circuit voltage, b is Tafel slope, $i_{O_2}^0$ is apparent exchange current density for ORR, I_d is diffusion limiting current density, and R_m is cell electrical resistance. Equation 6.19 represents the Langmuir equation for toluene adsorption on the Pt surface. Where θ_T is the surface coverage of toluene on Pt, C_T is bulk concentration of toluene, and B_{ads} is a constant reflecting the affinity between toluene and Pt surface. The adsorption of toluene on Pt reduces the apparent exchange density of the ORR from $i_{O_2}^0$ to $[(1-\theta_T)(i_{O_2}^0)$.

Besides the kinetic models discussed above, empirical models for cathode contamination are also available. Equation 6.20 [33] is an empirical model for SO_2 and NO_2 contamination at cathode.

$$E_c = E_0 - \left(b_1 + K_{cK}C_p\right)\log(i) - R_0 i + K_{cK}C_p \log(i)\exp(-K_3 t) \tag{6.20}$$

$$E_0 = E_r + blog(i_0) \tag{6.21}$$

Where E_r is the reversible voltage, b and i_0 are the Tafel parameters, R_0 is the ohmic resistance, K_{cK}, K_3 are constants that relate to the contaminants, C_p is the concentration of contaminant, and t is contamination time.

6.4. System optimization and cathode filtration optimization

The fuel cell system optimization involves the complicated interaction between the stack and multiple BoP components. A comprehensive analysis of the interactions between stack and BoP is beyond the scope of this study. Since the air supply subsystem is the major parasitic load in the whole system (for direct-hydrogen fuel cells), this study focuses on the interaction of the stack with the air supply subsystem. Power consumption from other BoP components is considered as constant, i.e., not varying with the stack operating condition. Figure 6.6 shows the general interactions between the stack and the BoP as well as the energy balance between the stack's gross output and parasitic losses. The optimization of stack and air supply can be divided into two stages. In the first stage, assuming the air is clean and no filtration is required, the major optimization problem is the selection of operating pressure and SRa for a desired power output and current density. In the second stage, when the air is contaminated and filtration devices are involved, the optimization problem is mainly the balance between the gross output loss due to cathode contamination and an increase in parasitic power of the compressor (due to the additional pressure drop from filters).

Figure 6.7 shows the proposed relationship between the filtration and the net power output of the stack. It clearly illustrates the effect of filtration on cathode contamination and on the compressor's parasitic power. When there is no filtration (or inadequate filtration), the net power output decreases primarily due to the contamination effect. This region is indicated as the contamination loss zone, as shown in the figure. In contrast, when the filtration is excessive (filter is too thick), the parasitic loss caused by the filtration devices becomes significant. This region is called the parasitic loss zone. Between the contamination loss and parasitic loss zones, there exists an optimum filtration point for net power output. To find this optimal point, it is important to know the fuel cell stack characteristics, key operating parameters, and air properties.

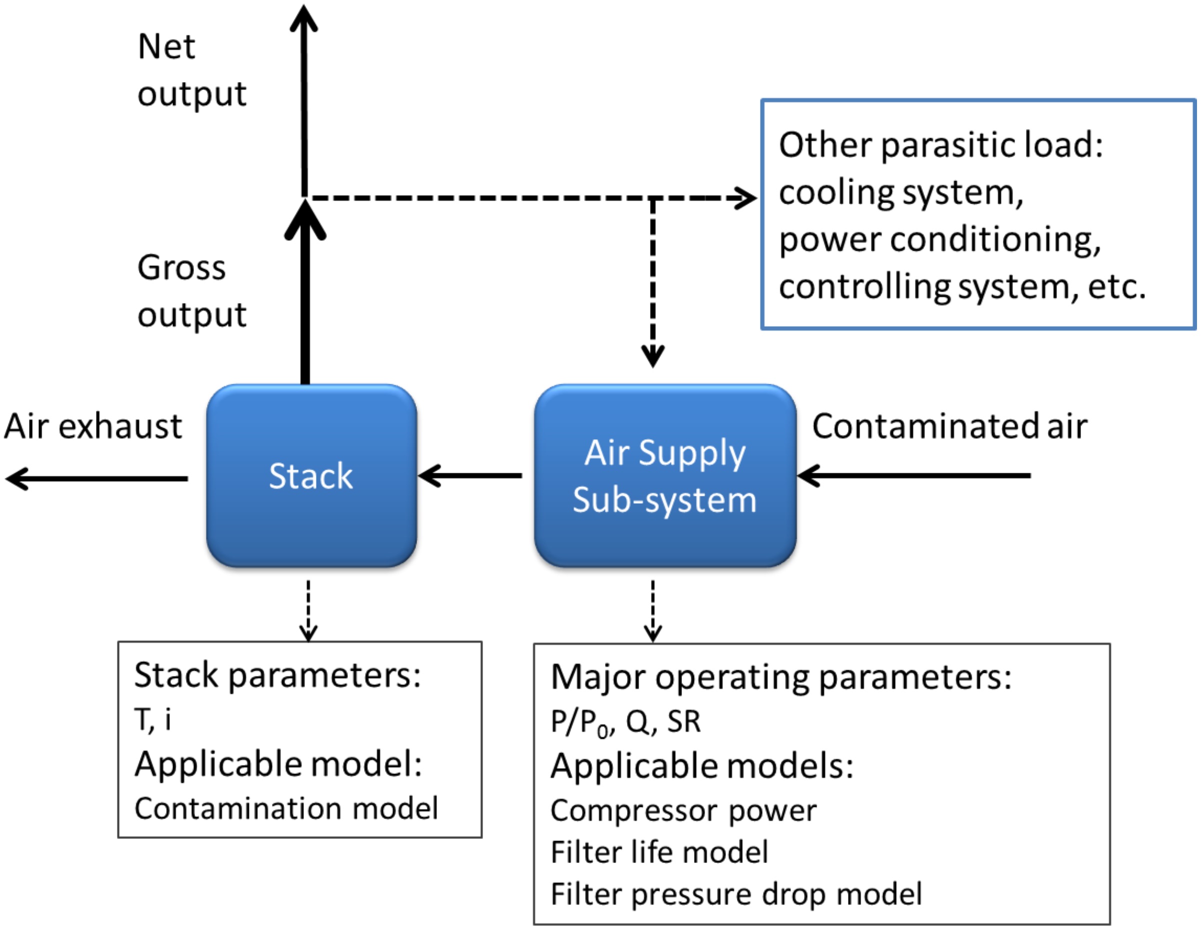

Figure 6.6 Schematic description of fuel cell system optimization: energy balance between gross output and parasitic losses

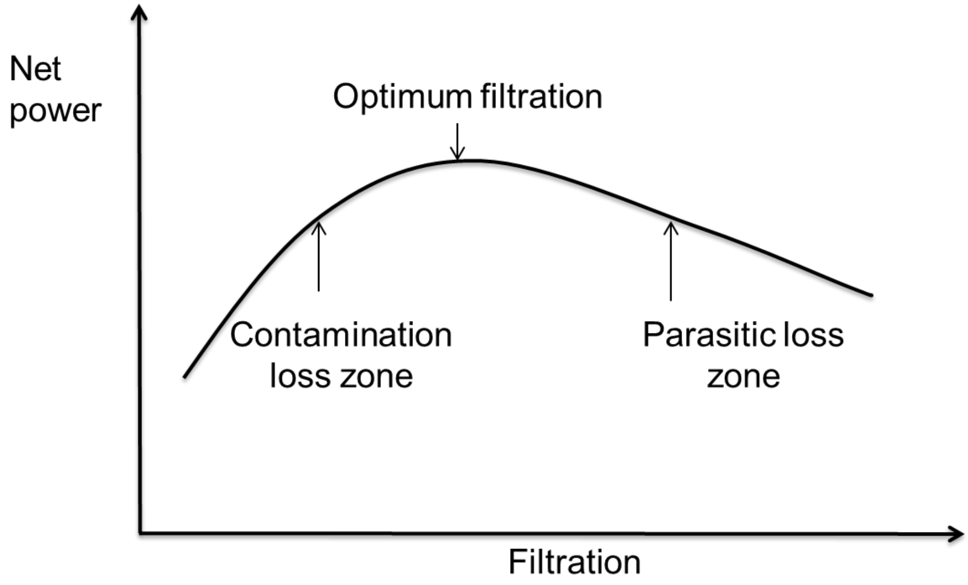

Figure 6.7 Proposed relationship between filtration and net power output of stack

6.4.1. Effect of operating conditions

The cathode contamination effects on fuel cell performance are impacted by the operating conditions. The fuel cell's tolerance to cathode contaminants is very dependent on the operating conditions; therefore, the fuel cell's filtration demand or air purity requirement is also dependent on the operating conditions. The effects of multiple operating parameters on the fuel cell's contamination effects will be discussed below. When designing a cathode filter for specific fuel cell applications, those effects should be taken into account to reach the optimization of filtration.

6.4.1.1 Effect of current density

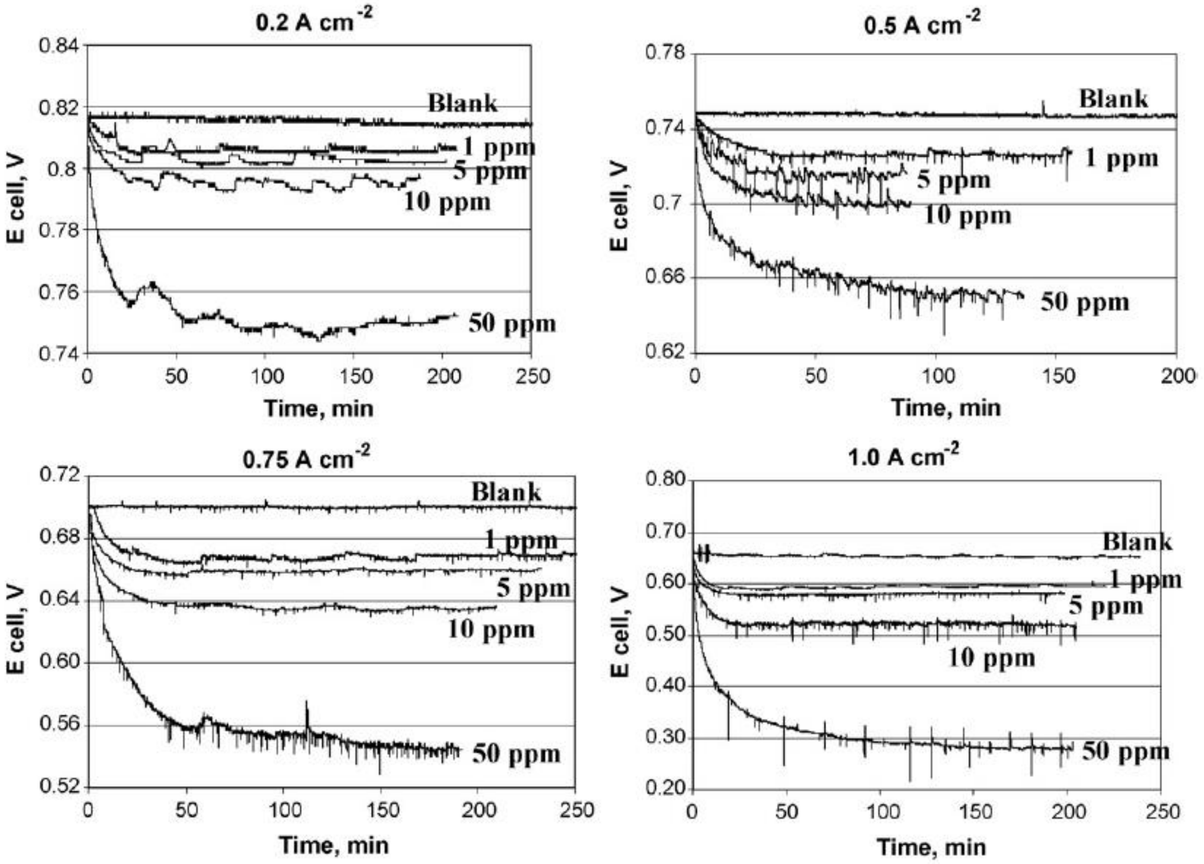

Figure 6.8 Toluene contamination effect at various current densities. Operating conditions: SRa= 3.0, RH=80%, cell temperature 80 ˚C, pressure 30 psig. Reproduced from [32]

Figure 6.8 shows the cell voltages declining when the toluene is introduced into the air stream, and then leveling off. The plateau voltage represents the final effect of a specific concentration of contaminant. This set of experimental results indicates that the current density is an important consideration for the filtration requirement because of the effect of current density on the fuel cell's contamination tolerance. As shown in Figure 6.8, under the same concentration of toluene of 50ppm, the cell voltage drop is ca. 100 mV at 0.5 A/cm^2, but it increases to 370 mV at 1.0 A/cm^2. In addition, at a higher current density, the initial cell voltage (without contamination) is also lower; hence further voltage drop is undesired in this case.

Typically, the contamination effect is more severe at a higher current density. When the fuel cell is operated at a higher current density, more filtration is required.

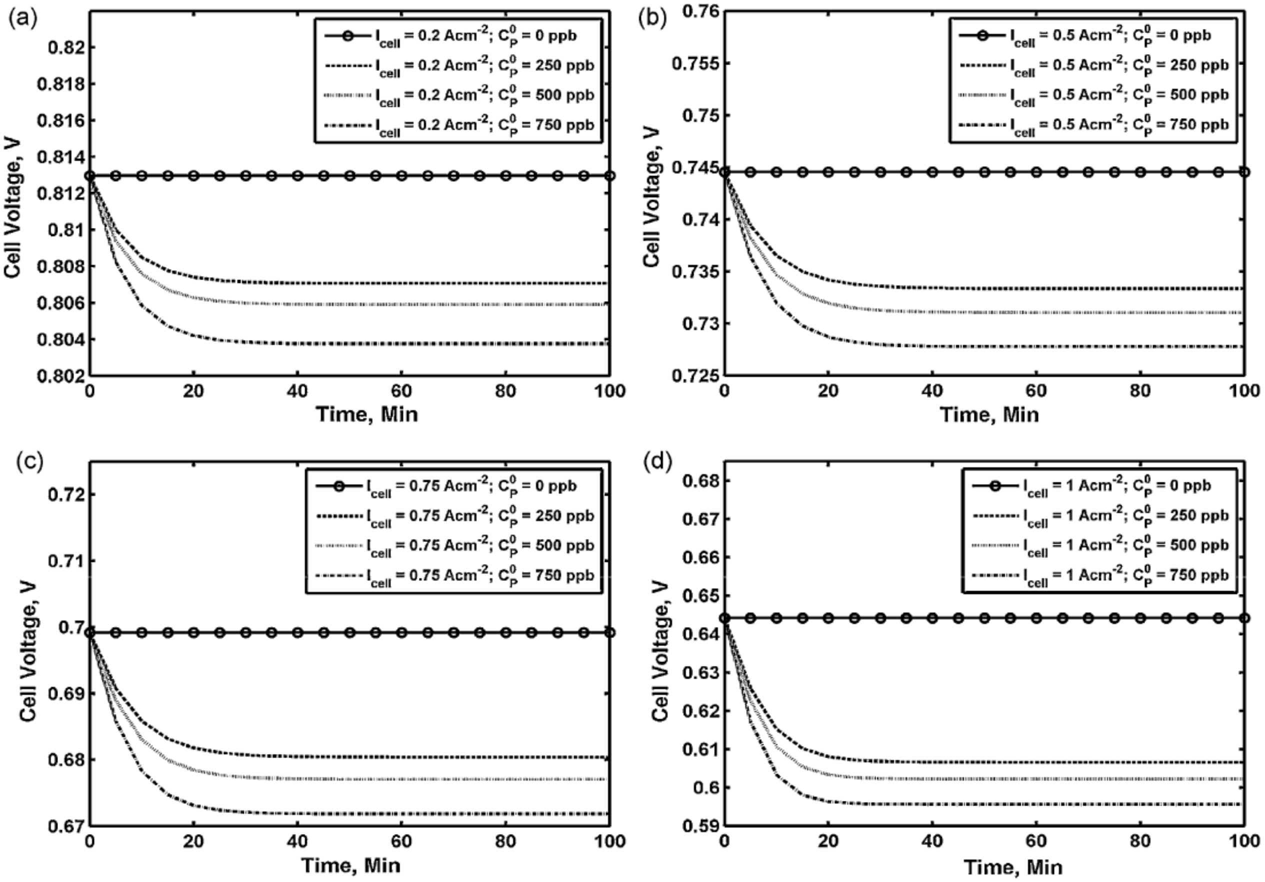

Figure 6.9, Simulated fuel cell performance degradation at various toluene concentrations and current densities. Reproduced from [31]

Figure 6.9 shows the predicted fuel cell performance degradation at various toluene concentrations and current densities. From these simulated results, we can see that the current density has a significant effect on the fuel cell's contamination tolerance.

6.4.1.2. Effect of operating pressure

The system pressure influences the stack performance by affecting the reactant gas partial pressure. Figure 6.10 shows the impact of pressure on the net efficiency in a wide range of net power outputs. The peak net power of this stack is ca. 30 kW with a small difference at different pressure. In the low power region, lower pressure outperforms higher pressure, where the compressor power consumption is low and very little performance benefit can be achieved from increased pressure. In the high power region, increasing the pressure is beneficial to improve the net efficiency and net power output. The optimal pressure ratio for high power output is located near 2.5. Beyond this value, the benefit of higher operating pressure is quickly offset by the increased power requirement from the compressor.

The effect of pressure on contamination in the air stream was investigated by Li et al.[34]. Figure 6.11 shows the experimental results of contamination effects of toluene at various back pressures. As observed in Figure 6.11, increasing the pressure is beneficial to enhancing the baseline performance and reducing the cell voltage loss caused by contamination. The increased baseline voltage at higher pressure is contributed to the higher partial pressure of oxygen, which increases the open circuit voltage according to the Nernst equation. However, the positive effect of higher pressure on the contamination effect is not well understood.

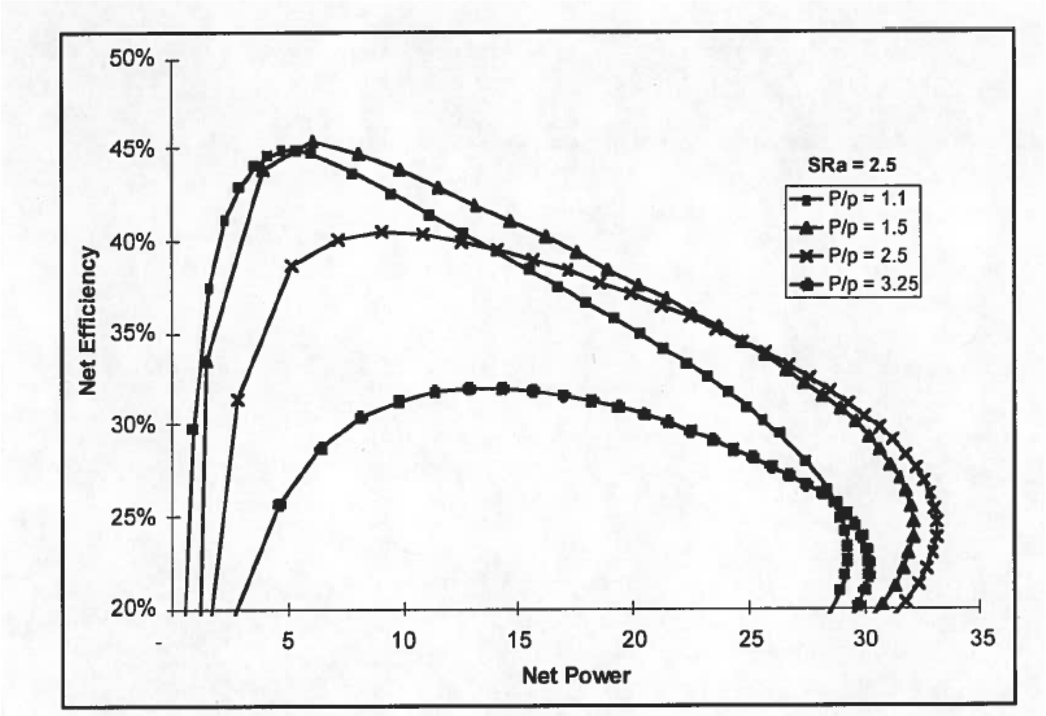

Figure 6.10, Net efficiency versus net power output at various pressure ratios [35]

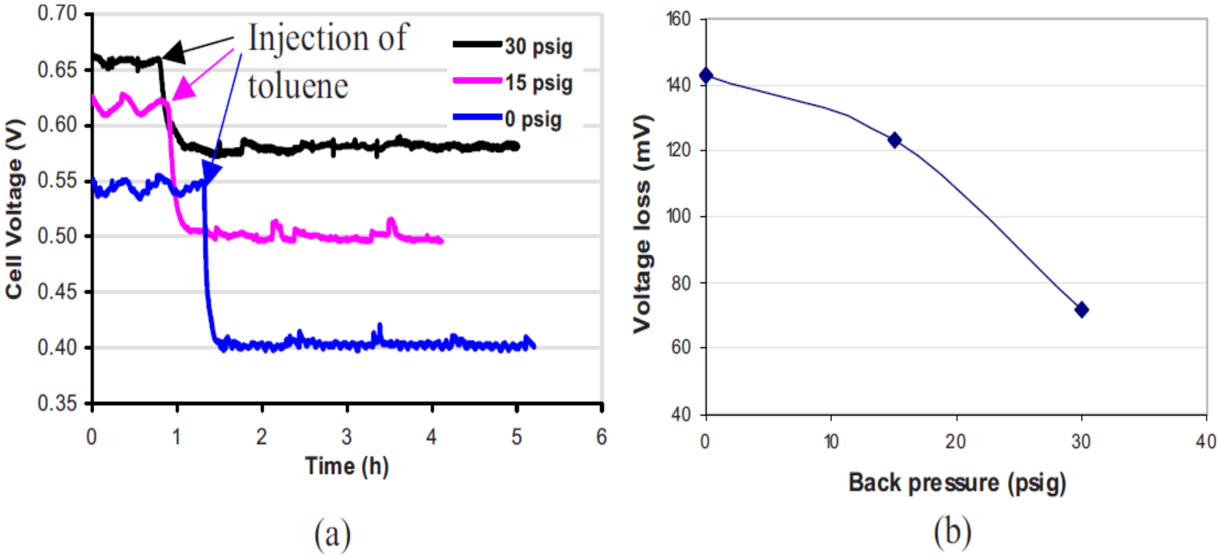

Figure 6.11, (a) Contamination effect at various pressures; (b) steady-state cell voltage losses versus operating pressure. Operating conditions: toluene 5 ppm; current density 1.0 A/cm^2; SRa=3.0

6.4.1.3. Effect of air stoichiometric ratio

The air stoichiometric ratio (SRa) is an important operating variable, and it has significant influence on the cell performance and compressor power. In addition, increasing the SRa will increase the air mass flow and hence increase the pressure drop of air loop and filtration demand since more air (and hence more contaminants) enters the system. Therefore, SRa is an important optimization parameter for the air supply system.

Increasing the SRa can increase the oxygen partial pressure and then increase the open-circuit voltage of the fuel cell, according to the Nernst equation. As observed in Figure 6.12 (a), the initial baseline cell voltage was improved with increasing SRa. However, when contaminants are present in the air stream, higher SRa can enhance the contamination effect on the cell performance. As shown in Figure 6.12 (b), the cell voltage loss caused by toluene contamination was increased from 67 to 87 mV when the SRa was increased from 2.0 to 4.0.

On the other hand, increasing SRa proportionally increases the total dose of contaminants and hence increases the requirement of filter capacity. Increasing the filter capacity requires increasing the thickness of the filter, which causes an increase in pressure drop. In addition, increasing SRa also proportionally increases the air flow rate and the pressure drop of the filter. Either the increased thickness of the filter or the increased flow rate requires higher pressure from the compressor. From the compressor performance chart, we know that higher-pressure ratios and mass flow rates will increase the compressor power. From the above discussion, we can conclude that increasing the SRa has many negative impacts on improving the net efficiency of the fuel cell system, although it can increase the open circuit voltage. Therefore, in practice (especially when contamination exists), a high SRa (>3) should be avoided.

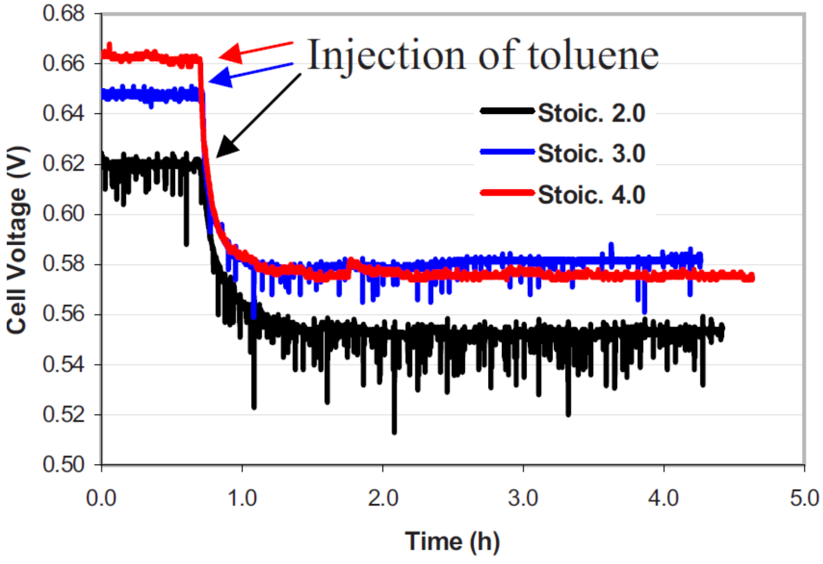

(a)

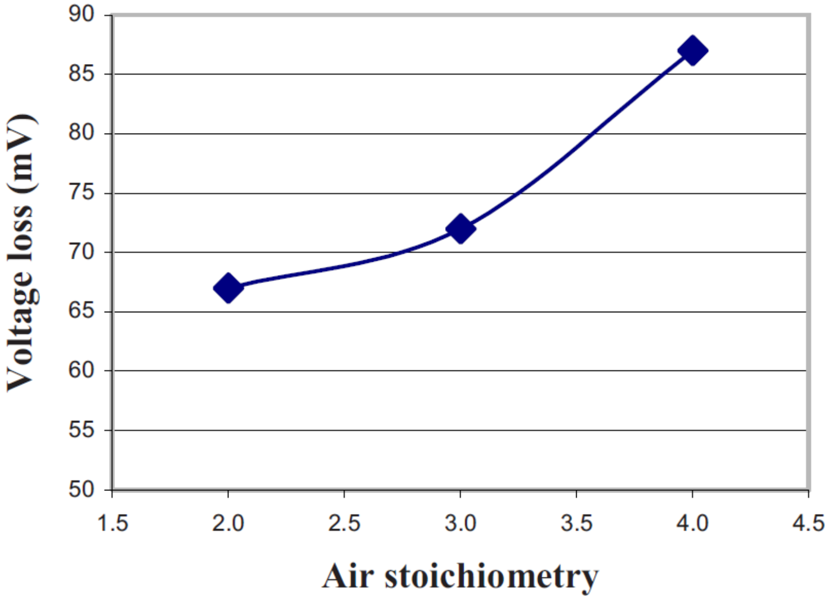

(b)

Figure 6.12 (a) Contamination effect on cell performance under various SRa. (b) steady-state cell voltage losses versus SRa. Operating conditions: toluene 5 ppm; current density 1.0 A/cm2; system pressure 30 psig.

6.5. Case study: application of cathode filter design to a 72 kW fuel cell

Cathode filter design methodology was applied to a 70 kW PEMFC system to compare filter design options for removal of hexane using activated carbon filter. The operation parameters are based on a realistic 70 kW stationary PEMFC system operated at the Akzo Nobel Chlor-alkali plant in Delfzijl, Netherlands [36]. Table 6.2 shows a summary of stack attributes and operating parameters. The rated power of system is 72 kW with a peak power of 120 kW. The system consists of 12 stacks with 75 cells for each stack. The new cells deliver, on average, 725 mV per cell at 80 A. The balance of plant consumes about 10 kW of power. The module electrical efficiency is 55%, and the total system efficiency is about 48%.

Four different filter options were considered for this fuel cell system. The first three options were different designs for panel (single) filter; they are traditional packed bed filter, microfibrous media, and composite bed filter. The fourth option is multi-element structured array (MESA) filter, consisting of multiple panel filters. The panel filters in the MESA also have the above-mentioned three options.

In order to demonstrate the unique advantage of microfibrous materials, the filtration requirement was set as the worst scenario, where both high logs of removal and high filtration capacity were required. In this study, it was set that the inlet concentration of hexane is 100 ppm, and the fuel cell tolerance is 0.1 ppm, i.e., the filter needs to provide a 99.9% removal efficiency or 3-logs removal.

Table 6.2 Summary of the operating conditions of the 70 kW PEM fuel cell power plant

Parameters	Value
Fuel cell power	50-72 kW
Fuel cell voltage	650-590 V
Fuel cell current	80-120 A
Number of stacks	12 in series
Number of cells per stack	75
Cell active area	200 cm^2
Airflow rate	300 m^3/h
RH of air	80%
Air pressure (after compression)	110 kPa (absolute)
Hydrogen flow (consumed)	36-52 m^3/h
Hydrogen flow (recirculated)	72 m^3/h
RH of hydrogen	80%
Hydrogen purity	99.95%
Average temperature stacks	65 ˚C
Air stoichiometry	2.8
Hydrogen stoichiometry	1.6

Table 6.3 Filter design parameters calculated from experimental data

Design parameter	Packed bed	MFES	Composite bed
Adsorption rate constant (K’)	$0.00132C_0\sqrt{V}$	$0.0144C_0\sqrt{V}$	$0.0029C_0\sqrt{V}$
Saturation capacity (τ)	$2397\frac{L_1}{VC_0}$	$799\frac{L_2}{VC_0}$	$2397\frac{L_1}{VC_0}+799\frac{L_2}{VC_0}$
Pressure drop (ΔP)	$(212V+156V^2)\cdot L_1$	$(262V+132V^2)\cdot L_2$	$(212V+156V^2)\cdot L_1 + (262V+132V^2)\cdot L_2$

Figure 6.13, Pilot 70 kW PEM fuel cells in container at the Akzo Nobel Chlor-alkali plant in Delfzijl, Netherlands.

Table 6.3 gives the filter design parameters calculated from the experimental breakthrough data. The packed bed used 12×20 mesh granular activated carbon, and the MFES media used 60×80 mesh activated carbon particles. The expressions for adsorption rate constant (K') and saturation capacity (τ) were based on the modified Wheeler's model and experimental breakthrough data. The pressure drop relationships for different beds were determined by the measurements in the laboratory. The face dimension of all filters is 24"×24", while the thickness of filters varies.

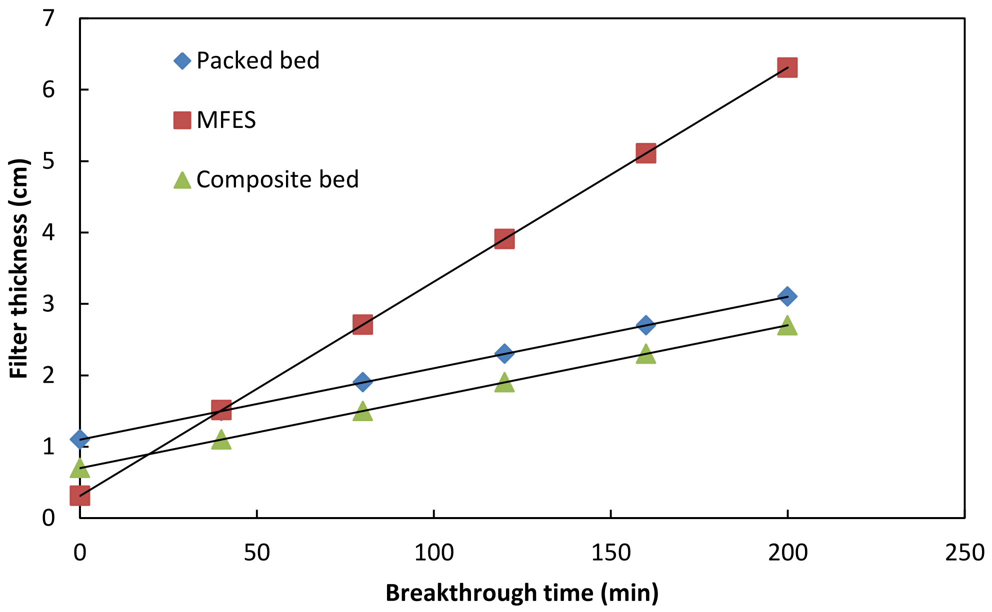

Figure 6.14. Predicted thickness for panel filter to meet required breakthrough time

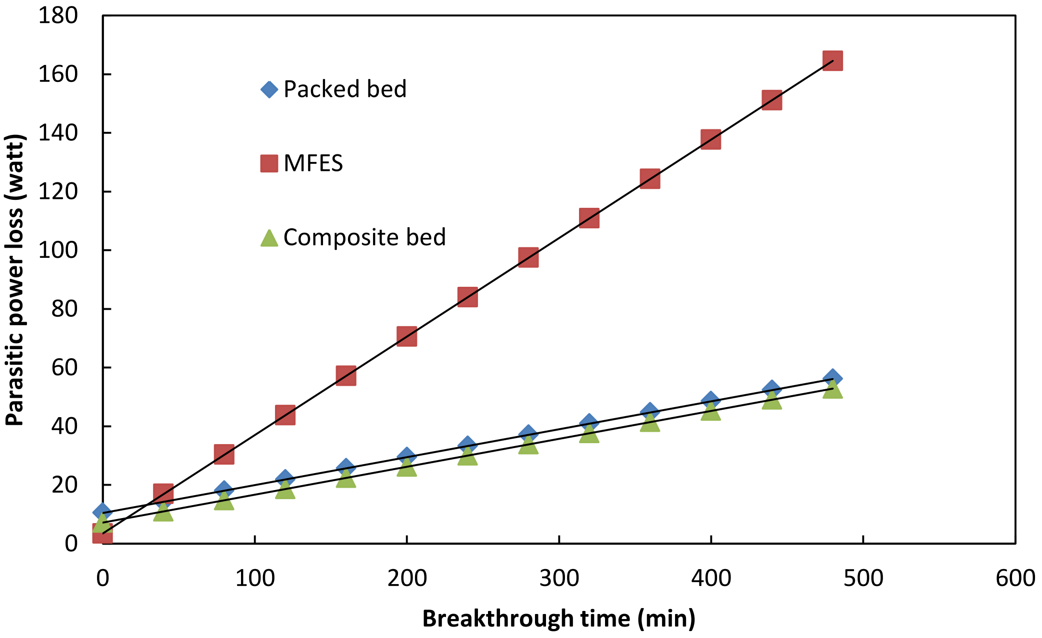

Figure 6.15. Predicted parasitic power loss for panel filter to meet required breakthrough time

Figure 6.14 shows the predicted thickness required for the panel filter to meet required breakthrough time. Due to the inherent high contacting efficiency of MFES, the MFES media has the least critical bed length among the three options. Therefore, for short-term protection, the

MFES requires least thickness of bed. However, although the sorbent load in MFES is much lower than in packed bed (about 20% load of PB), the benefit of the high contacting efficiency of MFES cannot offset the drawback of low sorbent load. As the required protection time increases, the required thickness of MFES increases sharply. Therefore, for long-term protection, the packed and composite beds are the better option. The composite bed can effectively reduce the critical bed length without losing the advantage of packed bed (high capacity). As shown in Figure 6.14, the composite bed filter is the best option in term of the total filter thickness.

Figure 6.15 shows the predicted parasitic power from panel filters to meet required breakthrough time. Longer protection time requiring a thicker filter increases the pressure drop of the filter and hence increases the parasitic power of compressor. It is evident that for long-term protection, the composite bed is the best solution with least parasitic power. For the same protection time, the MFES requires the thickest bed, and, meantime, its air permeability is lower than packed bed. These two factors result in the MFES having the most parasitic power.

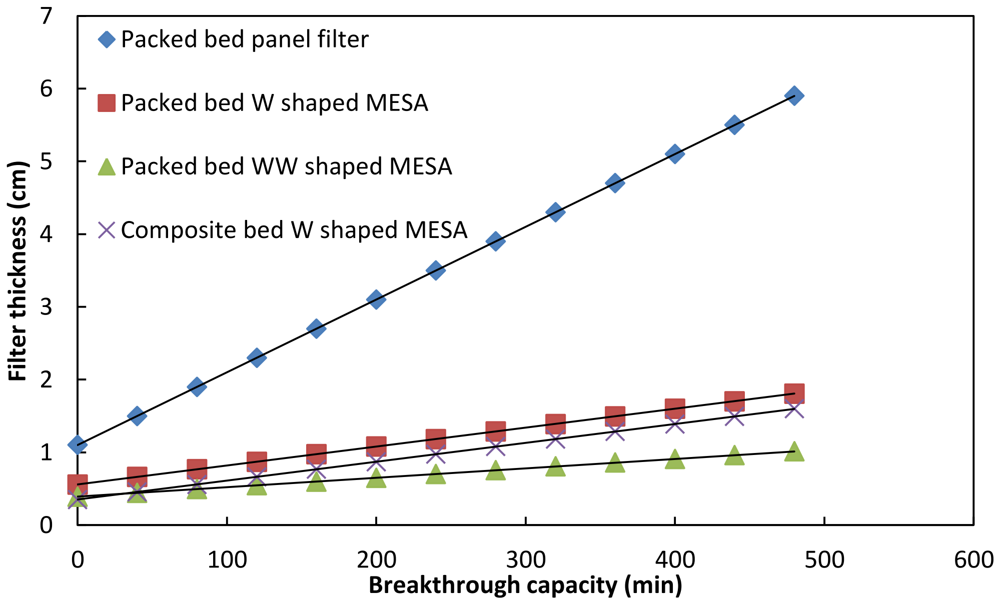

Figure 6.16. Predicted thickness for MESA filter to meet required breakthrough time

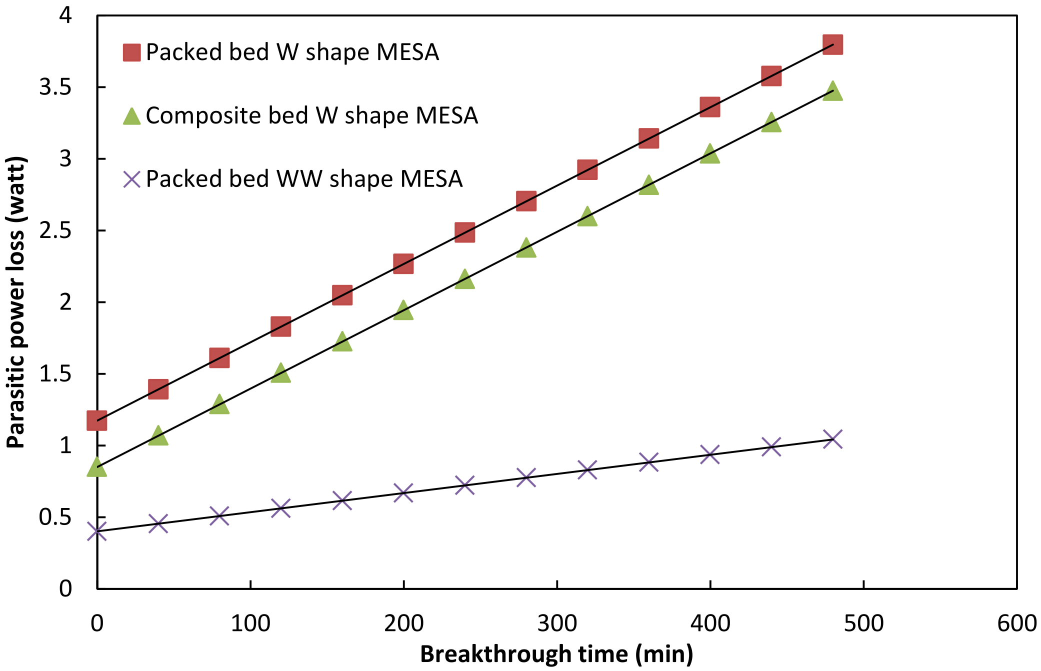

Figure 6.17 Predicted parasitic power loss for MESA filter to meet required breakthrough time

Figure 6.16 shows the predicted thickness for MESA filters to meet required breakthrough times. The element filter for MESA has two options, i.e., packed bed filter and composite bed filter. As shown in the figure, the required thickness for the panel filter increases sharply with the increase of required breakthrough time. In contrast, the required thickness for the MESA filter increases with a much smaller slope. The thickness difference (gap) between the panel filter and the MESA filter also increases with the increase in required breakthrough time, indicating that the advantage of the MESA filter becomes more significant when high capacity is needed. Because the thickness of the element filter in the MESA is much smaller than in a panel filter, along with reduced face velocity through the filter, the parasitic power for the MESA is significantly reduced.

Besides the MESA effect, the composite bed can also improve the filter design. The most important benefit of using composite bed is the reduction of critical bed length. This is extremely important when the total length of bed is small. In this scenario, the percentage of the critical bed length becomes remarkably large, resulting in low bed utilization. The element filter in the MESA is just in this scenario. Due to the configuration limitation of the MESA, the element filter is thin, typically less than 2 inches (1 inch filter is pretty common). This characteristic of the MESA filter requires minimizing the critical bed length as much as possible to reduce the waste of sorbent material. From Figure 6.16, we can see that in the W-shaped MESA filter, the composite bed has less thickness compared to the packed bed. The thickness difference shown in the figure only represents the difference between each element; the total thickness difference needs be multiplied by the factor of the count of elements (the count is four for a W-shaped MESA). The total thickness difference represents the benefit (saved sorbent material) of use of composite bed.

From Figure 6.16 and Figure 6.17, we can infer that the other important factor is the count of elements in the MESA. As shown in the figures, the WW-shaped MESA (count of 8) outperforms the W-shaped MESA in terms of thickness of filter and parasitic power.

6.6. Conclusions

The goal of this study is to provide a methodology to simulate (or predict) the performance of PEMFC under different operating conditions in a polluted air environment. To achieve this goal, theoretical models and experimental data need be combined. Some necessary models include the stack model, compressor model, contamination model, adsorption model, and pressure drop model, Depending on the application, more models, such as cooling model, might be needed. Some necessary experimental data include the polarization curve, adsorption curve, and contamination data. The simulation is useful to understand the interaction between the stack and its BoP components, eventually optimize the system design, and improve the overall system efficiency. The simulation is also useful to optimize cathode filter design based on specific application in fuel cells.

Reference

[1] Larminie J, Dicks A. Fuel Cell Systems Explained (Second Edition): Wiley; 2003.

[2] Mann RF, Amphlett JC, Hooper MAI, Jensen HM, Peppley BA, Roberge PR. Development and application of a generalised steady-state electrochemical model for a PEM fuel cell. Journal of Power Sources. 2000;86(1–2):173-80.

[3] Springer TE, Zawodzinski TA, Gottesfeld S. Polymer Electrolyte Fuel Cell Model. Journal of The Electrochemical Society. 1991;138(8):2334-42.

[4] Amphlett JC, Mann RF, Peppley BA, Roberge PR, Rodrigues A, Salvador JP. Simulation of a 250 kW diesel fuel processor/PEM fuel cell system. Journal of Power Sources. 1998;71(1–2):179-84.

[5] Laboratory NET, Energy USDo. Fuel Cell Handbook: University Press of the Pacific; 2005.

[6] Liu H, Li P, Wang K. Optimization of PEM fuel cell flow channel dimensions—Mathematic modeling analysis and experimental verification. International Journal of Hydrogen Energy. 2013;38(23):9835-46.

[7] Grujicic M, Zhao CL, Chittajallu KM, Ochterbeck JM. Cathode and interdigitated air distributor geometry optimization in polymer electrolyte membrane (PEM) fuel cells. Materials Science and Engineering: B. 2004;108(3):241-52.

[8] Grujicic M, Chittajallu KM. Optimization of the cathode geometry in polymer electrolyte membrane (PEM) fuel cells. Chemical Engineering Science. 2004;59(24):5883-95.

[9] Cunningham J. Air System Management for Fuel Cell Vehicle Application. Michigan State University, 1996.

[10] Wishart J, Dong Z, Secanell M. Optimization of a PEM fuel cell system based on empirical data and a generalized electrochemical semi-empirical model. Journal of Power Sources. 2006;161(2):1041-55.

[11] Zhang G, Kandlikar SG. A critical review of cooling techniques in proton exchange membrane fuel cell stacks. International Journal of Hydrogen Energy. 2012;37(3):2412-29.

[12] Faghri A, Guo Z. Challenges and opportunities of thermal management issues related to fuel cell technology and modeling. International Journal of Heat and Mass Transfer. 2005;48(19–20):3891-920.

[13] Sohn Y-J, Park G-G, Yang T-H, Yoon Y-G, Lee W-Y, Yim S-D, et al. Operating characteristics of an air-cooling PEMFC for portable applications. Journal of Power Sources. 2005;145(2):604-9.

[14] Büchi FN, Scherer GG. In-situ resistance measurements of Nafion® 117 membranes in polymer electrolyte fuel cells. Journal of Electroanalytical Chemistry. 1996;404(1):37-43.

[15] Bergman TL, Lavine AS. Introduction to Heat Transfer: Wiley; 2011.

[16] Amundson NR. A Note on the Mathematics of Adsorption in Beds. The Journal of Physical and Colloid Chemistry. 1948;52(7):1153-7.

[17] Yoon YH, Nelson JH. Application of Gas Adsorption Kinetics I. A Theoretical Model for Respirator Cartridge Service Life. American Industrial Hygiene Association Journal. 1984;45(8):509-16.

[18] Wheeler A, Robell AJ. Performance of fixed-bed catalytic reactors with poison in the feed. Journal of Catalysis. 1969;13(3):299-305.

[19] Cahela DR, Tatarchuk BJ. Permeability of sintered microfibrous composites for heterogeneous catalysis and other chemical processing opportunities. Catalysis Today. 2001;69(1–4):33-9.

[20] Springer TE, Rockward T, Zawodzinski TA, Gottesfeld S. Model for Polymer Electrolyte Fuel Cell Operation on Reformate Feed: Effects of CO, H;2 Dilution, and High Fuel Utilization. Journal of The Electrochemical Society. 2001;148(1):A11-A23.

[21] Wang X, Hsing IM, Leng Y-J, Yue P-L. Model interpretation of electrochemical impedance spectroscopy and polarization behavior of H2/CO mixture oxidation in polymer electrolyte fuel cells. Electrochimica Acta. 2001;46(28):4397-405.

[22] Bhatia KK, Wang C-Y. Transient carbon monoxide poisoning of a polymer electrolyte fuel cell operating on diluted hydrogen feed. Electrochimica Acta. 2004;49(14):2333-41.

[23] Chan SH, Goh SK, Jiang SP. A mathematical model of polymer electrolyte fuel cell with anode CO kinetics. Electrochimica Acta. 2003;48(13):1905-19.

[24] Zhang J, Wang H, Wilkinson DP, Song D, Shen J, Liu Z-S. Model for the contamination of fuel cell anode catalyst in the presence of fuel stream impurities. Journal of Power Sources. 2005;147(1–2):58-71.

[25] Shah AA, Sui PC, Kim GS, Ye S. A transient PEMFC model with CO poisoning and mitigation by O2 bleeding and Ru-containing catalyst. Journal of Power Sources. 2007;166(1):1-21.

[26] Shi Z, Song D, Zhang J, Liu Z-S, Knights S, Vohra R, et al. Transient Analysis of Hydrogen Sulfide Contamination on the Performance of a PEM Fuel Cell. Journal of The Electrochemical Society. 2007;154(7):B609-B15.

[27] Shah AA, Walsh FC. A model for hydrogen sulfide poisoning in proton exchange membrane fuel cells. Journal of Power Sources. 2008;185(1):287-301.

[28] Antoine O, Bultel Y, Durand R. Oxygen reduction reaction kinetics and mechanism on platinum nanoparticles inside Nafion®. Journal of Electroanalytical Chemistry. 2001;499(1):85-94.

[29] Kuhn H, Wokaun A, Scherer GG. Exploring single electrode reactions in polymer electrolyte fuel cells. Electrochimica Acta. 2007;52(6):2322-7.

[30] Du CY, Zhao TS, Xu C. Simultaneous oxygen-reduction and methanol-oxidation reactions at the cathode of a DMFC: A model-based electrochemical impedance spectroscopy study. Journal of Power Sources. 2007;167(2):265-71.

[31] Shi Z, Song D, Li H, Fatih K, Tang Y, Zhang J, et al. A general model for air-side proton exchange membrane fuel cell contamination. Journal of Power Sources. 2009;186(2):435-45.

[32] Li H, Zhang J, Fatih K, Wang Z, Tang Y, Shi Z, et al. Polymer electrolyte membrane fuel cell contamination: Testing and diagnosis of toluene-induced cathode degradation. Journal of Power Sources. 2008;185(1):272-9.

[33] Proton Exchange Membrane Fuel Cells: Contamination and Mitigation Strategies (Green Chemistry and Chemical Engineering): CRC Press; 2010.

[34] Li H, Zhang J, Shi Z, Song D, Fatih K, Wu S, et al. PEM Fuel Cell Contamination: Effects of Operating Conditions on Toluene-Induced Cathode Degradation. Journal of The Electrochemical Society. 2009;156(2):B252-B7.

[35] Friedman DJ. PEM Fuel Cell System Optimization.

[36] Verhage AJL, Coolegem JF, Mulder MJJ, Yildirim MH, de Bruijn FA. 30,000 h operation of a 70 kW stationary PEM fuel cell system using hydrogen from a chlorine factory. International Journal of Hydrogen Energy. 2013;38(11):4714-24.

Chapter 7

Conclusion and Future Work

7.1. Conclusions

A novel fibrous CNW, activated carbon fiber enhanced microfibrous entrapped sorbent media, was prepared via wet-lay and sintering process. A bicomponent fiber (LLDPE/PET) with a low melting temperature sheath was selected as the base fiber to facilitate the bonding of particles. A small amount of ACF (20 wt.% of total fiber) was added to improve the media's quality and adsorption performance. Wet end chemistry (dispersion aids, retention aids, and formation aids) was also added to improve the formation of the web.

Permeability test results evidenced that the pressure drop of ACF-MFES media is mainly contributed by the fiber rather than by the particles, even though the fiber's volume fraction is much lower than particles'. This is because the fiber diameter is one order of magnitude smaller than the particles, and hence the fiber's external surface area is much larger than particles'.

Hexane adsorption tests were performed to investigate the adsorption dynamics of ACF-MFES media, and its performance was also compared to other sorbent media. The conclusions drawn from the adsorption tests are as follows:

The ACF-MFES has a very high adsorption rate constant (3.03 min^{-1}), which is greater than packed bed (0.27 min^{-1}) and ACF cloth (1.45 min^{-1}), and slightly smaller than ACF felt (5.55 min^{-1}). The ACF-MFES media's high adsorption rate is mainly because of its small particles and uniform structure. On the other hand, the ACF-MFES media was found to be the most efficient sorbent in terms of heterogeneous contacting efficiency.

The overall volumetric mass transfer coefficient ($k_G\alpha$) in ACF-MFES is sensitive to the face velocity, indicating that the external mass transfer resistance is more dominant than the internal resistance. The $k_G\alpha$ for ACF-MFES reach up to about 30,000 min^{-1}, which is at least ten times higher than packed bed media.

Because of the ACF-MFES media's high contacting efficiency, it can be used as a polishing layer in a composite bed filter structure. The composite bed significantly improves the filter's breakthrough capacity (a 330% increase) and the adsorbent bed utilization (a 350% increase) compared to the packed bed filter. Three-layer composite bed design (capacity layer + guard layer + polishing layer) further improves the filter's performance in terms of pressure drop and adsorbent utilization.

The enhanced mass transfer characteristic of MFES structure was studied by theoretical and experimental methods, and compared with traditional packed bed structure. To measure the effective volumetric mass transfer coefficient in MFES structure, a physisorption (hexane adsorption onto activated carbon) was used as a probe reaction. First, a theoretical adsorption breakthrough model was established to analyze the experimental breakthrough data and calculate the adsorption rate constant, which is directly correlated to the mass transfer coefficient. In a comparison test, mass transfer rate in an MFES is more than 10 times higher than in packed bed. The mass transfer rate of MFES is also even comparable with ACF felt, whose fiber dimension is one order of magnitude smaller than particle dimension in MFEP.

To further understand the mass transfer in MFEP structure, a series of experiments with different particle size MFES was conducted. The contribution of three mass transfer resistances (including the external, internal mass transfer resistance, and axial dispersion) to the overall resistance varies with particle size in MFES structure. At relatively large particle size, both internal and external mass transfer resistances are important, while the axial dispersion effect is negligible. As particle size decreased, the internal mass transfer resistance was gradually eliminated, and the external mass transfer resistance becomes the controlling resistance. When the particle size was further decreased to near 100 μm, the external mass transfer resistance was also nearly eliminated, and the axial dispersion became the rate-limiting resistance. Since the axial dispersion effect is not sensitive to particle size, further decreasing the particle size can't effectively improve the mass transfer rate in MFES. In this study, 100 μm is the optimal particle size for MFES at which the mass transfer rate reaches its maximum value. The results also indicate that the ultra-fine fiber size (approximately 10 μm) in ACF felt is not necessary to enhance the mass transfer rate, and it is a waste of energy since the small dimension of fiber significantly increase the flow resistance.

For mass transfer limited heterogeneous processes like catalytic reaction or gas-solid adsorption, an MFES structure using micron-sized particles can significantly enhance the mass transfer rate and thereby the effective reaction rate. With a decreasing particle size, the MFES can effectively eliminate the external and internal mass transfer resistances; however, its effective mass transfer coefficient is eventually limited by the axial dispersion effect when ultra-fine particles are utilized in MFES structures.

7.2. Future work

7.2.1. Catalyst screening and kinetic study

MFEC technology also has great potential in catalyst screenings, catalyst tests, and kinetics studies due to its unique mass and heat transport characteristics. A lot of heterogeneous catalytic reactions involve mass/heat transfer limitation, couple of reaction kinetics with mass/heat transport, and slowness to reach steady state operation. For example, an FTS reaction in a traditional packed bed reactor takes days to reach a steady state; this is time costly in the initial catalyst screening step. In addition, because of the hot spot in the packed bed, the catalyst may undergo deactivation. Those issues make fast catalyst screening reaction kinetics studies become very difficult. The MFEC uses micro-sized particles that can significantly enhance the mass transfer rate causing the reaction to fall within the surface reaction control region. Eliminating the mass transport limitation is essential for reaction data collecting in order to study the intrinsic reaction kinetic on a specific catalyst. Furthermore, MFEC with high thermal conductivity metal fibers (such as Cu fiber) can effectively improve the bed’s radial heat transfer coefficient. The use of such an MFEC catalyst can effectively decrease the temperature gradient in the bed, prevent the occurrence of hot spots, and ultimately make the reaction reach the steady state in a much shorter time. Catalytic steam reforming is another example that can take advantage of the features of MFEC structure. Steaming reforming process is a highly endothermic reaction. The catalyst screening process involves the choice of various primary active species and promoters; therefore there exist hundreds of combinations of catalyst recipes. In the preliminary catalyst screening stage, the most concerning factor is the catalyst activity and selectivity. It is typically required to collect raw data when the reaction is already in the steady state. However, the traditional packed bed reactor takes a long time to reach a steady state. This challenge makes the catalyst screen very time-consuming if hundreds, or even thousands, of catalyst samples need be tested and compared. Using the MFEC, which has enhanced heat and mass transfer rates, can effectively perform a fast catalyst screening.

7.2.2. Mass transfer study

The mass transfer study for MFES structure was studied in present study. To investigate the mass transfer coefficient of MFES, activated carbon particle was selected, and the experiments were performed at a superficial velocity of 0.6 m/s. It was found that there exists a transition point for different mass transfer mechanisms near 100 μm particle size. However, this transition point may vary at different operating velocities. It is suggested to test at low face velocity (e.g. 0.1 m/s) and high face velocity (e.g. 2 m/s) to observe the impact of face velocity on the transition point. The relationship between the mass transfer coefficient and the particle size in MFES needs to be further studied at different superficial velocities. In the present study, only activated carbon particle was used. The pores in activated carbon were primarily micropore. It was suggested to perform a similar study using other sorbent-like activated alumina or silica, which have very different pore sizes and pore structures. It is interesting to know the impact of pore structure on the MFES's overall contacting efficiency. The MFES's mass transfer coefficient has been studied by the adsorption test; however, the results obtained from this study are also very valuable for catalyst systems. It is possible to predict whether the MFEC is in the mass transfer controlled region or in the surface reaction controlled region.